

Aqueous fluid advection: A plausible mechanism for heating the shallow crust to form HTLP metamorphic belts

Catherine A. Stuart



Thesis presented to the Department of Earth and Planetary Sciences in partial
fulfilment of the requirements for the degree of
Bachelor of Environmental Science (Honours)

Macquarie University

2012



STATEMENT OF ORIGINALITY

All the work submitted in this thesis is the original work of the author except where otherwise acknowledged. No part of this thesis has been previously submitted to any other university or institution.

Catherine A. Stuart

Date

- ACKNOWLEDGEMENTS -

I can't believe I'm finally writing this after the most fantastic year, through which I would never have made it alone. Each of the following people has helped me throughout the year and whether the contribution was big or small it is greatly appreciated.

First and foremost, to my two wonderful supervisors Nathan Daczko and Sandra Piazzolo: a million thanks! Nathan, without you I wouldn't be here in the first place. It was your classes and fieldtrips that got me hooked on geology and your enthusiasm continues to inspire me. Sandra if it wasn't for you I would not have made it through the last two weeks. Thank you for your never-ending patience with all my questions and emails, and your super speedy reading. Both Nathan and Sandra, I am thankful for your knowledge, patience, direction and support throughout this year. Thank you for the opportunity you've given me to work on this project, I have learnt so much from both of you.

To all the people in the Department and the Geochemical Analysis Unit who have taught me over the years, whether it be in lectures, pracs, or instructing me on using an instrument – thank you for having the patience and taking the time to teach me. Thanks go to the following people who have assisted me throughout the year in various aspects: Steve Craven for his input to this project, help with fieldwork, sample preparation, reviewing my introduction, LA-ICP-MS mount preparation, the fruitless search for zircons in the quartzite and for putting up with my general pestering; Manal Bebbington for the production of my thin sections; Kevin Grant for his tireless help with the SEM and patience with the seemingly ridiculous number of hours I spent using it; Peter Wieland for his help with whole rock chemistry sample preparation and his speedy organisation of XRF analysis of my samples at

USYD; and Will Powell for his help with the LA-ICP-MS and being happy to answer my many questions. Norman Pearson, Dick Flood, Juan Carlos Afonso and Simon George all provided comments and insights that helped to improve this thesis.

To James, Ristch, Tickle, Sam, Emma, Sarah, Rajat, Elyse, Mel and everyone in the demountable - we've had an excellent year of lunches, board games, complaining sessions, confusion, stress, support and laughs. Thanks guys for a brilliant year!

Vicki – I couldn't have done this without you. You've been there every step of the way this year, and your positivity and encouragement never ceases to amaze me. Thank you for all the coffees, lunches, laughs, yoga, and for being so amazing.

Thanks also need to go to my friends, for cheering me on and putting up with me this year. In particular, these four were fantastic: Alex - for letting me live vicariously through you this year; Darcy - for always being there on the other end of the phone; Peter - for getting me out of the house each week for baseball; and Dan - for being an excellent scribe and baking assistant. Love you guys!

Last, but most definitely not least, to Mum, Dad and Joey. Thank you for your never ending love, support, encouragement, chocolate, cups of tea, and for saving me dinner when I was working late at night. Special thanks go to my Mum for being a whizz on EndNote, Excel and formatting, and for always offering to help me. Most of all - thank you family for believing in me and my dreams.

ABSTRACT

The Wongwibinda Metamorphic Complex is a High-Temperature Low-Pressure metamorphic belt in the Southern New England Fold Belt composed of Carboniferous metapelitic schists, characterised by a steep ($<55\text{ }^{\circ}\text{C km}^{-1}$) metamorphic field gradient. While the regional metamorphism is well documented in literature, presently there is no suitable mechanism to explain the elevated temperatures of the crust.

A thermal anomaly is recognised in the centre of the complex, evident through the distribution of cordierite-bearing rock around folded quartzite units. Petrographic analysis reveals a vein network of complex mineralogy through the schists of the aureole.

From field relationships, the overall structure of the quartzite appears analogous to a large quartz vein sequence grown during regional deformation. EBSD mapping of banding in the quartzite reveals only slight similarities compared to the microstructure of a quartz vein in the schists. Using XRF data, attempts to classify the quartzite based on protolith were inconclusive.

Whole rock chemistry analysis revealed metasomatism through the aureole, characterised by Fe, Mn, K and heavy REE enrichment and Ca depletion compared to regional values.

Similar enrichment and depletion values are observed in the quartzite chemistry. Comparing mineral chemistry between the schists, veins in the schists and the quartzite allowed estimations of fluid-rock interaction which agreed with metasomatic changes in the schists. Following the evidence for metasomatism in the schists, the quartzite is established as a site of high fluid flux, with fluids driving the metamorphic evolution of this site.

An aqueous fluid advection model is proposed, whereby pulses of hot fluids migrate upwards through the crust and are focussed through the WMC. Upon reaching the complex, they are diverted and slowed, and phases begin to crystallise out of the fluid. Transported by the fluids, additional heat enters the surrounding meta-sedimentary sequences, driving metamorphism coeval with metasomatism driven by the pulses of fluid.

Whilst this is model best fits evidence found in this study it is by no means confirmed, and further research is suggested into both the thermal and metasomatic history of these rocks to further constrain the mechanisms driving HTLP metamorphism.

Contents

CHAPTER 1 - INTRODUCTION	1
High-Temperature Low-Pressure Metamorphism	1
Fluids as a heating mechanism	2
Wongwibinda Metamorphic Complex: A Natural Laboratory	5
Aims.....	9
CHAPTER 2: REGIONAL GEOLOGY	10
CHAPTER 3: FIELDWORK	15
Site selection	15
Field work and sample collection.....	16
Field relationships	19
Quartzite structure.....	23
CHAPTER 4 - PETROGRAPHY	25
Aims.....	25
Analytical Method	25
Results	25
Rampsbeck Schists	25
Rampsbeck Schist veins	29
Quartzite	37
CHAPTER 5 - MICROSTRUCTURE.....	41
Introduction.....	41
Aims.....	42
Analytical Methods	42
Results	45
W1204 – A large (>0.5 mm) vein in the Rampsbeck Schists.....	45
W1207g – A banded Quartzite sample	50
Interpretation.....	55
CHAPTER 6 - GEOCHEMISTRY	57
PART 1: WHOLE ROCK CHEMISTRY	57
Introduction.....	57
Aims.....	57

Analytical Methods	58
XRF	58
LA-ICP-MS.....	58
Previous analyses.....	59
Accuracy and Precision.....	60
Results	62
Rampsbeck Schists	64
Comparison with previous analyses	66
Quartzite	70
PART 2: MINERAL CHEMISTRY	74
Introduction.....	74
Aims.....	75
Analytical Methods	75
Results	76
Feldspars	76
Muscovite.....	82
Cordierite	84
Garnets.....	86
PART 3: INTERPRETATION	89
CHAPTER 7 - DISCUSSION.....	96
Achievement of aims.....	96
Origin of the spatial relation between the cordierite-in isograd and the quartzite.....	97
Model 1 - Enrichment of Mg from a meta-chert	97
Model 2 - Fluids as a catalyst	98
Model 3 - Aqueous fluid advection.....	98
Aqueous fluid advection as a best-fit model	100
Aqueous fluid advection – a model.....	102
Source of fluids	102
Migration of fluid through the crust.....	104
Fluids arrive at the WMC	105
Fluids are variably channelled through the schists.....	106
Fluids vary in composition	107

Suggestions for further research.....	108
Origin of the quartzite unit	108
Presence of fluids in the aureole	108
Metasomatism in the schists	109
Temperature gradients in the thermal anomaly	110
Role of the pegmatite	111
CHAPTER 8 - CONCLUSION.....	112
REFERENCES	114
APPENDICES	118
A – Whole rock chemistry raw data	119
I: LA-ICP-MS Run 1 Analyses of standards	119
II: LA-ICP-MS Run 1 Analyses of samples	121
III: LA-ICP-MS Run 2 Analyses of standards	127
IV: LA-ICP-MS Run 2 Analyses of samples.....	129
V: Database of major element whole rock chemistry analyses of low-grade Rampsbeck Schists (Henson, 2000).....	130
VI: Database of trace and rare earth element whole rock chemistry analyses of low-grade Rampsbeck Schists (Henson, 2000)	131
VII: Database of published whole rock chemistry results from quartz-rich rocks.....	133
B - Mineral Chemistry Raw Data	135
I: SEM-EDS raw data.....	135

LIST OF FIGURES

Figure	Description	Page
1.1	Silica solubility in water	3
1.2	Process of mobile hydrofracturing	4
1.3	Geological map of the WMC	6
2.1	Geological map of the Southern New England Fold Belt	10
3.1	Stereonet	15
3.2	Sample location map	18
3.3	Outcrop styles of quartzite	19
3.4	Bedding in the meta-pelite	20
3.5	Pegmatite/meta-pelite contact	21
3.6	Stereonet	21
3.7	Structural map of the study site	22
3.8	Structure of folded quartzite units	23
3.9	Textures displayed by the quartzite	24
4.1	Photomicrographs of Rampsbeck Schists	27
4.2	Cordierite grain size analysis	28
4.3	Photomicrograph of a small vein	30
4.4	Outcrop of sample W1204	31
4.5	Photomicrographs of sample W1204	32
4.6	Outcrop of sample W1221	33
4.7	Photomicrograph of sample W1221	34
4.8	Photomicrograph of sample W1221	36
4.9	Quartzite sampling transect	37
4.1	Photomicrograph of banding in the quartzite	38
4.11	Photomicrograph of garnets in the quartzite	38
4.12	Photomicrograph of banding in the quartzite	39
5.1	EBSD sample locations	44
5.2	Phase and band contrast map of W1204	46
5.3	Orientation map of W1204	46
5.4	Grain size statistics of sample W1204	47
5.5	Pole figures of quartz orientation in W1204	49
5.6	Phase and band contrast map of W1207g	51
5.7	Orientation map of W1207g	51
5.8	Grain size statistics of sample W1207g	52
5.9	Pole figures of quartz orientation in W1207g	53
6.1.1	Major element chemistry of Rampsbeck Schists	64
6.1.2	Trace element and REE chemistry of the Rampsbeck Schists	65
6.1.3	Chemistry of the aureole compared to regional values	67
6.1.4	Proxy of chemical change v distance	69
6.1.5	Chemistry of the quartzite compared to chemistry of the aureole	71
6.1.6	Major elements composition of quartz-rich rocks	72
6.1.7	Iron vs potassium in quartz-rich rocks	73
6.2.1	Feldspar ternary classification diagram	77

Figure	Description	Page
6.2.2	Plagioclase feldspar albite composition	78
6.2.3	K-feldspar orthoclase composition	79
6.2.4	Biotite ternary diagram	80
6.2.5	Biotite Mg composition	81
6.2.6	Muscovite Fe and paragonite composition	83
6.2.7	Muscovite Na composition	83
6.2.8	Cordierite Na composition	85
6.2.9	Cordierite Mg vs Na composition	85
6.2.10	Garnet ternary classification diagram	87
7.1	Model Figure 1	103
7.2	Model Figure 2	104
7.3	Model Figure 3	105
7.4	Model Figure 4	106
7.5	Model Figure 5	107

LIST OF TABLES

Table	Description	Page
3.1	Details of samples	17
4.1	Petrography of Rampsbeck Schists	26
4.2	Petrography of the quartzite	40
5.1	Acquisition details for EBSD mapping	43
6.1.1	LA-ICP-MS analysis of standards	61
6.1.2	XRF results	62
6.1.3	LA-ICP-MS results	63
6.1.4	Proxy for comparing chemical changes	69
6.3.1	Equilibrium/disequilibrium textures	95
7.1	Expected and observed features of three models	99

CHAPTER 1 - INTRODUCTION

High-Temperature Low-Pressure Metamorphism

High-temperature low-pressure (HTLP) metamorphic complexes are formed through specific metamorphic processes that result in steep metamorphic field gradients of over $35\text{ }^{\circ}\text{C km}^{-1}$ in shallow crustal levels (10-15 km depth). These conditions have been recognised in several complexes in Australia, including: the Cooma Complex, NSW (Flood and Vernon, 1978); the Forrest Creek granites at Walwa, Victoria; the Reynolds Range in Central Australia (Sandiford and Hand, 1998); Halls Creek Orogen, Northern Australia (Bodorkos et al., 1999); the Mopunga Range region of the Arunta Inlier, Central Australia (Scrimgeour et al., 2001); and the Tia (Dirks et al., 1992) and Wongwibinda (Binns, 1966) Metamorphic Complexes, NSW.

Four processes have been recognised to explain the formation of HTLP complexes through heating of the crust at shallow levels:

- advective heating due to the intrusion of mafic igneous rocks and/or granitoids (De Yoreo et al., 1991, Johnson, 1999, Richards and Collins, 2002, Bodorkos et al., 1999, Scrimgeour et al., 2001);
- advective heating due to the shallowing of a thermal boundary layer (Dirks et al., 1992, Langone et al., 2010);
- tectonic advective heat transfer from rapid denudation (Winslow et al., 1994), or diapiric drag of metamorphosed material from depth (Flood and Vernon, 1978);
- conductive heating from radioactive decay (Sandiford et al., 1998).

Fluids as a heating mechanism

Yet to be defined is a process whereby fluids significantly alter thermal regime to the extent that HTLP metamorphism occurs. While a fluid component is present in most metamorphic processes, improbable regional fluid fluxes would be required to drive the thermal development of a HTLP complex (Connolly, 1997), rendering this type of process unsuitable in most situations.

However if fluid flow is focussed into channels rather than flowing through a porous medium, flux rates on a local scale would be significantly increased, allowing heat advection and mass transfer to occur (Thompson and Connolly, 1992). The affect on the surrounding rock is dependent on spacing of the channels: small channel spacing results in a shallow lateral temperature gradient; as the channels become more widely spaced the thermal gradient becomes steeper and increasingly easier to discern with thermobarometry (Hoisch, 1991). Fluid flow operating on a scale of metres to kilometres therefore has the potential to isobarically heat regions, as long as fluid flux is concentrated into channels.

Several HTLP complexes have been studied and found to have sites of significantly higher temperature superimposed on the regional thermal high, either restricted to lithologies or confined to local 'hot spots' (Chamberlain and Rumble, 1988, Chamberlain and Rumble, 1989, Hoisch, 1987). These are inferred to be sites of high hot, metamorphic fluid flux, which has been channelled along fracture systems within particular units. In the case of central New Hampshire, USA, the thermal perturbation was found to be relatively short, in the order of 10^6 years, with a large fluid flux ($> 1 \times 10^{-9} \text{ m}^3$ of fluid per m^2s^{-1}) channelled through a highly fractured quartzite (Chamberlain and Rumble, 1989).

Evidence for regional fluid flow would be preserved in the presence of quartz veins throughout the terrain (Walther and Orville, 1982, Rumble, 1989). Quartz veins form as fluids supersaturated in silica are transported through rocks either by diffusional flow or by fluid flow, until they reach conditions under which the minerals are no longer soluble and precipitate out.

The solubility of silica is highly dependent on temperature (Figure 1.1), with supersaturation of silica occurring at high temperatures. Darcian advection of fluids (path 1) from their source deep in the crust (point C) is relatively slow, resulting in a loss of heat matching that of the geothermal gradient and precipitation of quartz at deep levels in the crust (point A), rather than at shallow levels in the crust where veins are commonly found. Therefore Darcian flow is too slow to maintain sufficient elevated temperatures required to heat the shallow crust (Bons, 2000).

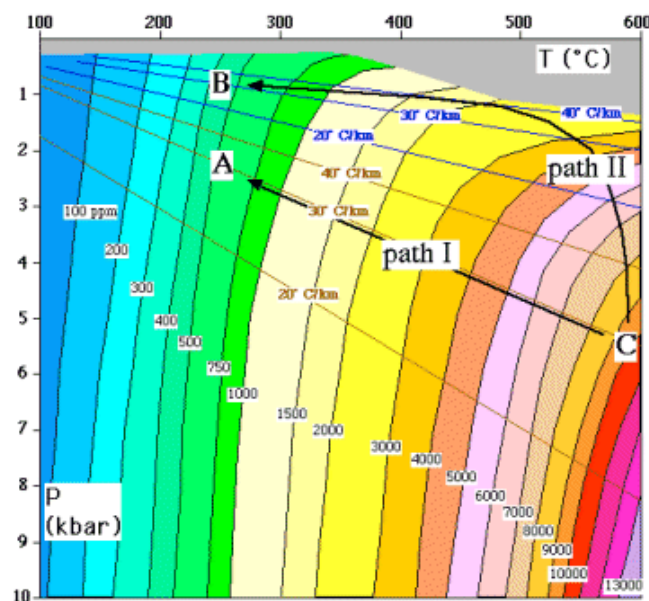


Figure 1.1: Silica solubility (ppm) in pure water as a function of temperature (x-axis) and pressure (y-axis). Path I describes the ascent of fluids through Darcian flow from source (C). Path II describes the ascent of fluids from the same source via mobile hydrofracturing. Taken from Bons (2000).

If metamorphic fluids are to heat the rocks to a sufficient temperature for metamorphism, a faster fluid transport mechanism is required. Mobile hydrofracturing allows rapid ascent of fluids through the crust, in the order of metres per second, delivering hot fluids that are supersaturated in silica to shallow depths (Figure 1.1, path II; (Bons, 2000)).

This process is a type of flow where a fluid body moves upwards with a fracture, as it expands at the top and closes at the bottom of the body of fluid. The fracture follows the direction of least perpendicular stress, in some cases following existing planes of weakness (Figure 1.2, stage I). In this way, a hot body of fluid could potentially rise as much as ten kilometres through the crust in a matter of hours, maintaining its temperature and therefore the supersaturation of silica, until it reaches an obstacle and becomes immobile (Figure 1.2, stage II). At this point in time the fluid begins to equilibrate with the host rock, cooling and quickly precipitating minerals held in solution, after which the fluid slowly escapes (Figure 1.2, stage III). Bons (2001) proposed this mechanism as the process forming large (100 – 1000 m) quartz veins, as it resolves the issues of the position of these veins in

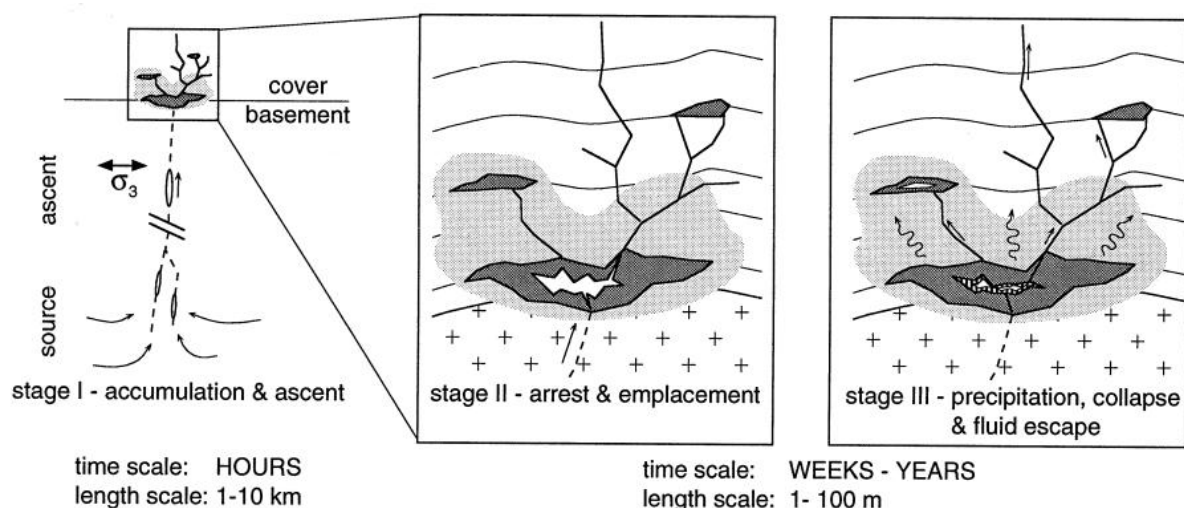


Figure 1.2: The three stages of quartz vein precipitation through the process of mobile hydrofracturing. Adapted from Bons, 2001.

the cooler shallow crust and the large fluid flux required if they were to form through Darcian flow (in the order of tens of kilometres cubed of fluid).

Quartz veins formed through precipitation following mobile hydrofracture are expected to show elongate blocky textures, with evidence for crack-sealing (parallel wall-rock inclusion trails). Supersaturation of silica in the fluids can cause ongoing nucleation as well as continued growth of 'seed grains' (pre-existing grains in the wall rock or grains formed during initial nucleation), producing a blocky texture (Bons, 2000). If the fluid was at such high temperatures we may also expect to find wall rock interaction involving metasomatism, with a decreasing temperature gradient distal to the site of fluid flux, as well as a spatial association between the inferred site of fluid flux and metamorphic field gradients.

Wongwibinda Metamorphic Complex: A Natural Laboratory

The Wongwibinda Metamorphic Complex (WMC) is a ~25km² HTLP regional aureole (Figure 1.3). Metasedimentary rocks increase in metamorphic grade from west to east, with very low-grade Gurrakool beds in the west grading into greenschist to upper amphibolite facies Rampsbeck Schists and Zone of Migmatites to the east. The highest grade rocks are adjacent to several intrusions from the Hillgrove Plutonic Suite, including the Abroi Granodiorite.

Previous work has constrained the pressure and temperature conditions of metamorphism, with temperature increasing from 350-450°C in the low grade rocks to 660°C in the highest grade rocks, and a maximum region-wide pressure of 3.5 kbar (Craven et al., 2012).

Initially the complex was interpreted to be a contact aureole around the Abroi Granodiorite (Binns, 1966, Vernon, 1982), which is consistent with the west to east increase in

Wongwibinda Metamorphic Complex Geological Map

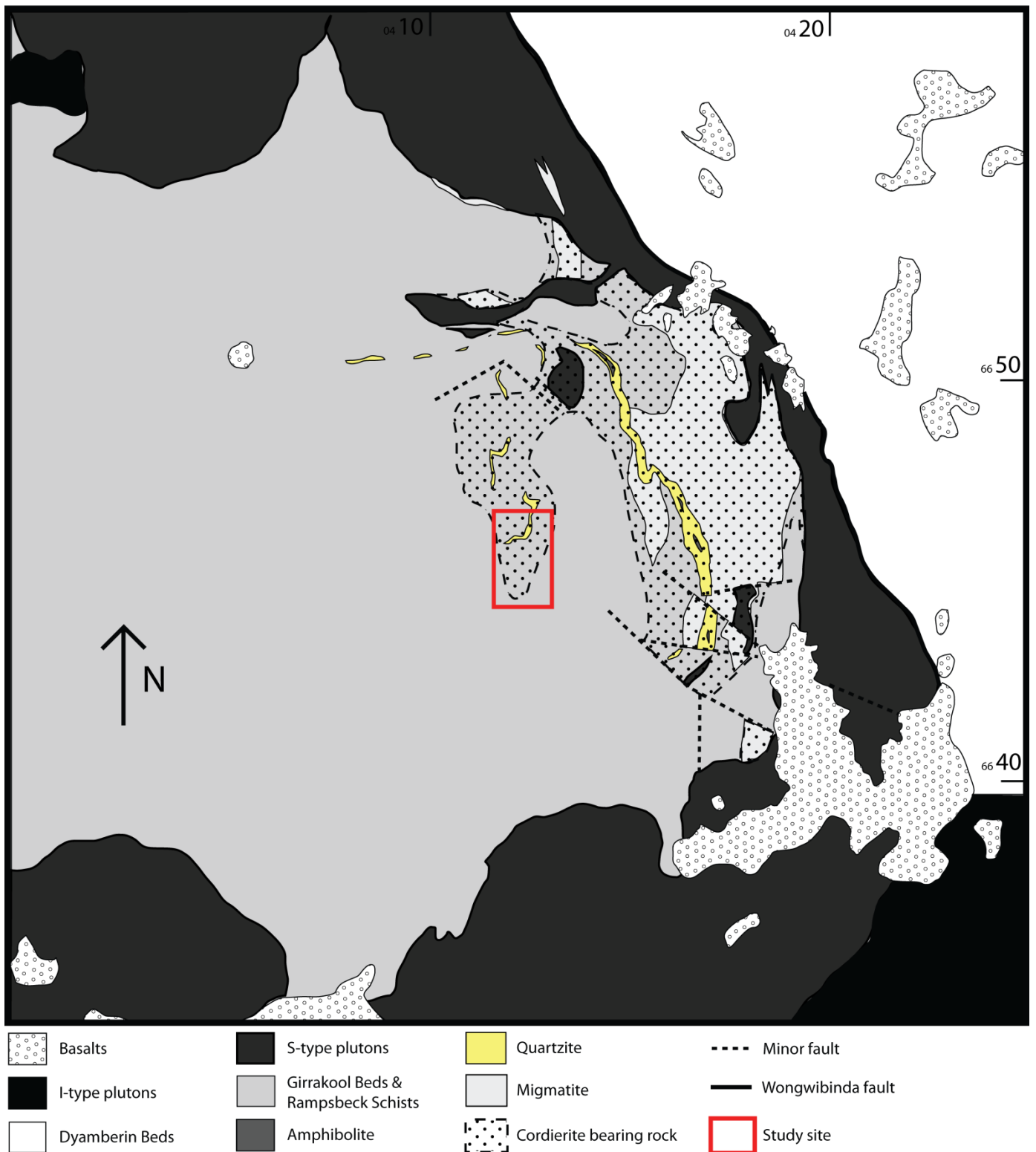


Figure 1.3: Geological map of the WMC

temperature. Subsequent mapping by Craven et al. (2012) has revealed that the exposed margins of the Abroi Granodiorite show no spatial relationship to metamorphic isograds in the complex, and in some places even cut the isograds. Dating work has shown that emplacement of the pluton post-dated the peak HTLP regional metamorphism by approximately 8 million years (Craven et al., 2012), and combined with the mapping this effectively rules out the Abroi Granodiorite as a heat source for regional HTLP metamorphism.

Most of the previously outlined processes can be ruled out by structural and temporal relationships. Diapiric drag of a high-grade envelope around a rising pluton (Flood and Vernon, 1978) and conductive heating from radioactive decay (Sandiford et al., 1998) can both be ruled out by the pluton emplacement post-dating HTLP metamorphism, as well as a lack of evidence for other suitable heat sources in geophysical data. There is no evidence of remnant high-pressure metamorphic mineralogy at Wongwibinda (Binns, 1966, Farrell, 1992), which excludes a rapid denudation and subsequent advective heat transfer scenario (Winslow et al., 1994).

The remaining scenario is conductive heating via shallowing of a thermal boundary layer. Regional geology of the New England Fold Belt does support a history of extension following the termination of the Keepit-Connors arc (~305 Ma) and the movement of magmatism forwards into the accretionary prism (Jenkins et al., 2002, Cawood et al., 2011). However conductive heating results in a broad metamorphic field gradient that would be smooth, continuous and on a scale of tens of kilometres. This is not the case at Wongwibinda, where Craven et al. (2012) found a steep (100°C/km) field gradient and patchy development of

high temperature rocks (on a kilometre scale), and so this scenario was also rejected. This poses a problem concerning the mechanism by which the shallow crust was heated.

Mapping of metamorphic isograds by Farrell (1992) and further work by Craven et al. (2012) reveals the cordierite-in isograd at Wongwibinda to have a spatial association with the quartzite units. This is especially evident in the centre of the complex, where an area of cordierite bearing rock is found in an aureole-like shape around a discontinuous, folded quartzite unit, which has previously been interpreted as a metamorphosed chert. Farrell (1992) described these quartzite units as massive and pure in some places and banded in others, with common psammitic laminations and, in places, grading into quartz-rich psammite. Due to the unique shape of the cordierite-in isograd and the presence of quartzite units in areas of higher metamorphic gradient, it is plausible that these quartzite units mark a site of high fluid influx, either providing planes of weakness for mobile hydrofracturing to occur or being formed during this process as large quartz veins.

Several cordierite phase equilibria have been extensively used as geothermobarometers (Richardson, 1968, Hensen, 1971, Mukhopadhyay and Holdaway, 1994, Vielzeuf, 1983, Wyhlidal et al., 2009), and so changes to cordierite mineral chemistry would be indicative of changing temperatures. A linear inverse relationship was found to exist between the Na content of Mg-cordierite and temperature (Kalt et al., 1998), and has been used as a geothermometer (Visser et al., 1994, Wyhlidal et al., 2009). Vielzeuf (1983) discovered that Fe-Mg exchange between cordierite and spinel is independent of pressure and this has also been successfully applied as a geothermometer (Ikeda et al., 2010). Following this work, it is expected that cordierites found distal to sites of fluid flux would show lower Fe and higher Mg and Na values compared to those proximal to the site of fluid flux.

Aims

This study aims to explore the role fluids have played in regional metamorphism at

Wongwibinda. This will involve:

1. Examining composition, macro- and microstructure of the quartzite as the site of fluid flux to classify it as either a meta-chert or a large quartz vein sequence
2. Characterising the mineralogy and chemistry of the rocks of the aureole in order to examine any changes or spatial patterns to the site of fluid flux

CHAPTER 2: REGIONAL GEOLOGY

Eastern Australian geology is comprised of the Tasmanides, five successive orogens which young from west to east. They record the sedimentary, magmatic and metamorphic history of the Eastern Gondwana boundary from the Neoproterozoic to the early Triassic. The Southern New England Fold Belt is one of the younger parts of the Tasmanides (350-240 Ma) and includes a fore-arc basin and accretionary subduction complex pair – the Tamworth Belt and Tablelands Complex, respectively – separated by the Peel-Manning Fault System (Figure 2.1). The region of study, the Wongwibinda Metamorphic Complex (WMC), is a high-temperature, low-pressure metamorphic terrane that lies within the Tablelands Complex.

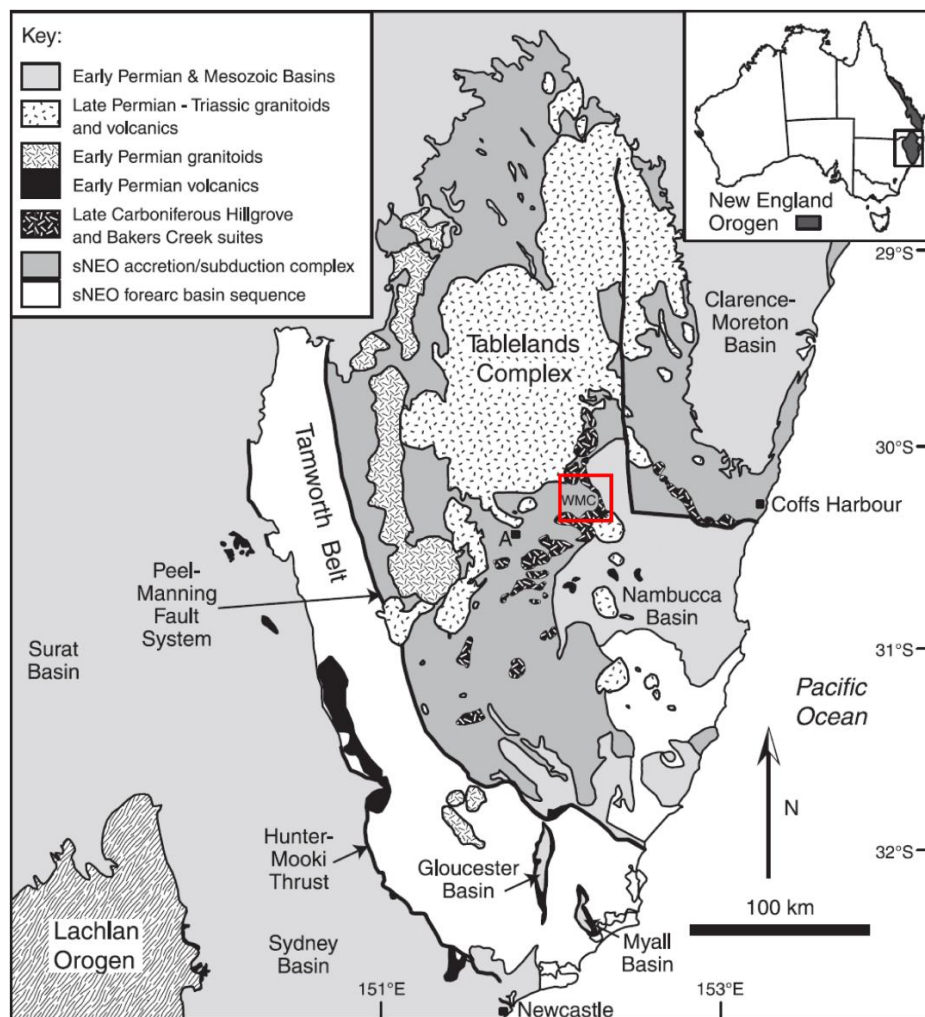


Figure 2.1: Geological map of the Southern New England Fold Belt. The WMC is highlighted by a red box.

The Tablelands Complex was formed in the mid- to late-Palaeozoic, as the accretionary prism of a west-dipping subduction zone (Leitch, 1975). A magmatic arc west of the Tablelands Complex (Keepit-Connors) was active and relatively stationary between 350 and 310 Ma, indicating moderate rates of convergence (Jenkins et al., 2002). Sourced from this arc, the sediments of the WMC are from a deep marine setting, dominantly composed of medium to fine grained siliceous turbidites which form the Girrakool Beds (Roberts et al., 2006). Prior to deformation, the sedimentary sequences of the Wongwibinda Complex faced west and were largely overturned, most likely due to formation of the accretionary prism (Farrell, 1992). The abundance of these sediments close to the volcanic centre indicates that the Keepit-Connors arc was at least partially submerged, similar to the contemporary Indonesian arc (Collins, 1991).

A change in the subduction system occurred between 310 and 305 Ma, as the initial stages of oroclinal bending began. The northern and southern ends of the subduction front moved east past the Tablelands Complex, bending around the central area where it was pinned (Rosenbaum et al., 2012). Due to the movement of the subduction front, magmatism in the Keepit-Connors arc ceased at 305 Ma (Roberts et al., 2006). This marks the beginning of the Tablelands Phase of orogenesis, which is characterised by widespread compressional deformation, magmatism (including the intrusion of S- and I-type granites), extension and sedimentation (Cawood et al., 2011).

After the migration of the subduction front, the Tablelands Complex - formerly under compressive, fore-arc conditions – experienced a short period of extension in the back-arc setting (Korsch et al., 2009). This resulted in the formation of a limited rift basin in the old and cold rocks (Buck et al., 1988), reflected in the geochemistry of the later-emplaced

Bakers Creek Suite, which progressively changes from an intraoceanic back-arc to a MORB signature between 290 and 280 Ma (Jenkins et al., 2002).

High-temperature low-pressure (HTLP) regional metamorphism occurred at WMC during this extensional period, with peak metamorphism dated at 296.8 ± 1.5 Ma (Craven et al., 2012). The complex is characterised by a steep geothermal gradient (at least $55^{\circ}\text{C km}^{-1}$), defined through mapping of metamorphic isograds from biotite-in isograd in the west, to the cordierite-in isograd through the centre and east of the complex (Figure 1.3). Peak metamorphic conditions have been constrained, with temperatures between $350\text{--}450^{\circ}\text{C}$ in the lowest grade rocks in the west, and $\sim 660^{\circ}\text{C}$ in the highest grade rocks in the east (Craven et al., 2012). Nowhere in the complex does the metamorphic pressure exceed 3.5kbar (Craven et al., 2012). While regional extension is linked spatially and temporally to HTLP metamorphism, as of yet there has been no proposed mechanism of heat transfer that satisfactorily explains the very steep metamorphic field gradients associated with an elevated thermal state of the crust during extension.

After a brief hiatus during the bending of the subduction system, subduction-related magmatism recommenced at 296 Ma, occurring 250 km east of the Keepit-Connors arc in the Tablelands Complex (Jenkins et al., 2002). The Hillgrove Suite (including the Abroi Granodiorite) is a set of S-type plutonic granites emplaced between 296 and 288 Ma, formed by the melting of clastic rocks in the lower crust (Flood and Shaw, 1977).

The first deformation event at the WMC was an intense, amphibolite facies deformation forming migmatites, folding sedimentary sequences (including quartzite and amphibolite layers, interpreted as a meta-chert and meta-basalt respectively) and producing a regional foliation (characterised by subvertical NW-SE axial planes and fold axes dipping steeply to

the east), which anastomoses around large porphyroblasts of cordierite, K-feldspar and garnet (Farrell, 1992). The porphyroblasts are attributed to a previous thermal event (Farrell, 1992), likely to be the peak HTLP metamorphism.

Immediately following this, the second deformation event developed initially through buckling and east-west shortening at amphibolite facies condition. Deformation from this event is mostly restricted to the higher grade rocks, particularly the migmatites, and characterised by isoclinal folding and rotation of cleavage from NE-SW to NNW-SSE (Farrell, 1992). The Abroi Granodiorite was emplaced during D₂, at 290.5 ± 1.5 Ma (Craven et al., 2012).

Another brief hiatus in magmatism, between 285 and 260 Ma, likely represents wide-scale plate reorganisation as oroclinal bending continued (Rosenbaum et al., 2012). The reorganisation caused a change from subduction to oblique convergence, accompanied by dextral strike-slip faults throughout the complex (Offler and Foster, 2008).

The Hunter-Bowen Orogeny commenced at 265 Ma, and is characterised by E-W compressive deformation, westward-propagating thrusting, folding, metamorphism and silicic magmatism (Cawood et al., 2011). This is contemporaneous with D₃ in WMC, characterised by uplift via ductile movement along steeply dipping thrust faults and shear zones, such as the Wongwibinda Fault (Farrell, 1988). Simple shear occurred under amphibolite facies conditions, forming the steeply dipping to sub-vertical Wongwibinda and Glen Bluff Shear Zones in areas intensely deformed during D₂. Wongwibinda Fault shows evidence for displacement of several kilometres in both the vertical and horizontal components, as the complex was thrust over Permian sequences to the east (Farrell, 1992).

Uplift during D₃ exhumed the WMC, juxtaposing the migmatites against the lower grade Nambucca Block of Permian sediments (Binns, 1966).

Shearing terminated at 260 Ma (Landenberger et al., 1995), marking the end of major deformation in this area and the cooling of the WMC, which occurred between 266 and 256 Ma (Farrell, 1992).

CHAPTER 3: FIELDWORK

Site selection

A field site was chosen where a quartzite unit lies within the cordierite-in isograd, allowing observations of potential thermal gradient to be made along a transect perpendicular to the quartzite boundary out into the country rock. The site is sufficiently distal from the D₃ shear zones, removing potential overprinting of metamorphic features.

This specific location was selected based on fieldwork conducted in November 2011 by Steven Craven, Nathan Daczko, Sandra Piazzolo and myself, during which a relationship between cordierite porphyroblasts in the meta-pelites and distance from the quartzite unit was observed, and the tie between quartzite units and the 'aqueous fluid advection' theory proposed. In particular a decrease in cordierite size was observed with distance from the quartzite, as well as multiple quartz veins throughout the meta-pelites. Measurements were taken that appeared to highlight discordance between the meta-pelite and the quartzite (Figure 3.1).

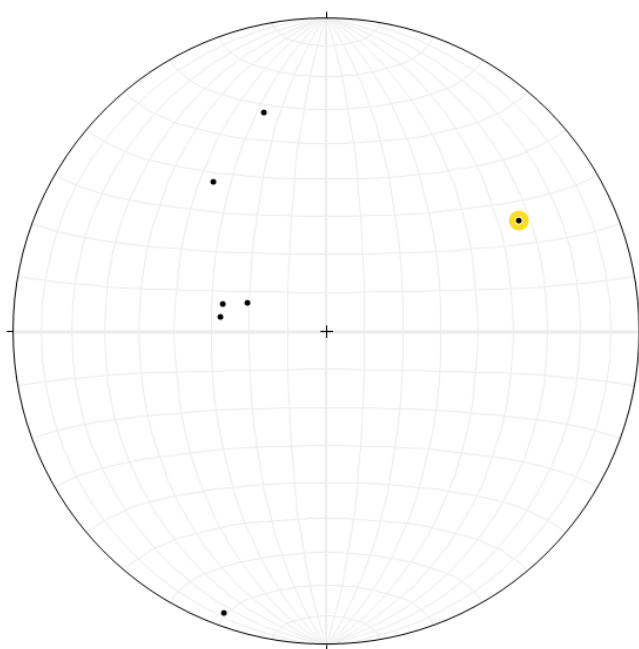


Figure 3.1: Stereonet of structural data collected in November 2011. Plotted poles for both bedding and cleavage. Measurement taken in quartzite is highlighted.

Field work and sample collection

Fieldwork was conducted over three days, April 17th – 19th, along the boundary between the Lynoch and Lyndhurst properties in the Wongwibinda Metamorphic Complex by myself and Steven Craven. The aim of the fieldwork was: to gather samples in order to determine changes to cordierite size and composition with distance from the quartzite; measure structural aspects to look for discordance between the quartzite and the country rock; gather samples to look for vein structures within the quartzite; and to look for evidence of metasomatism within 20-30 metres of the quartzite boundary.

Fieldwork included a transect perpendicular to the strike of the quartzite along the boundary fence line from the Lynoch driveway north, as well as detailed sampling, mapping and measurements through the quartzite unit and in the adjacent country rock. Samples were collected from thirty two locations in the field area including ten large samples for XRF analysis. Samples were removed from the outcrop by chisel and hammer, labelled and subsequently bagged. The location of each outcrop was recorded using a GPS with accuracies equal to or less than 10 metres. Significant features were noted, structural aspects such as bedding, foliation, fold axes and lineation were measured, and estimations made as to the size of any quartz veins and cordierite minerals present.

The location of samples collected is shown in Figure 3.2. For the purpose of investigating relationships between sample properties and position within the aureole, distance from the quartzite has been calculated by measuring the perpendicular distance from the schist-quartzite contact to the sample. Measurements, along with the type of analyses performed on the samples, are presented in Table 3.1.

Table 3.1: Details of samples used for analysis in this study

Sample	Unit	Veins	Distance to quartzite (km)	Analytical Method		
				SEM-EBSD	SEM-EDS	XRF & LA-ICP- MS
W1201	Rampsbeck Schist	Small	0.03		X	X
W1204	Rampsbeck Schist	Large	0.02	X	X	
W1207d	Quartzite	Small			X	
W1207e	Quartzite	Small			X	X
W1207g	Quartzite	Small		X		
W1207h	Quartzite	Small			X	
W1209	Rampsbeck Schist		0.03		X	
W1211a	Rampsbeck Schist	Small	0.52		X	X
W1213c	Rampsbeck Schist		0.35		X	X
W1214a	Rampsbeck Schist	Small	0.18		X	X
W1215	Rampsbeck Schist		0.15		X	X
W1216	Rampsbeck Schist	Small	0.08		X	X
W1218	Rampsbeck Schist		0.03		X	X
W1219	Rampsbeck Schist		0.02		X	X
W1221	Rampsbeck Schist	Large	0.03		X	
W1223a	Rampsbeck Schist	Small	0.07		X	X
W1225	Rampsbeck Schist	Small	0.2		X	
W1228	Rampsbeck Schist	Small	0.04		X	
W1229	Rampsbeck Schist		0.05		X	X
W1122	Rampsbeck Schist		1.14		X	
W0903*	Rampsbeck Schist	Small	1.82		X	

- Sample collected in 2009 by Elizabeth Teague.

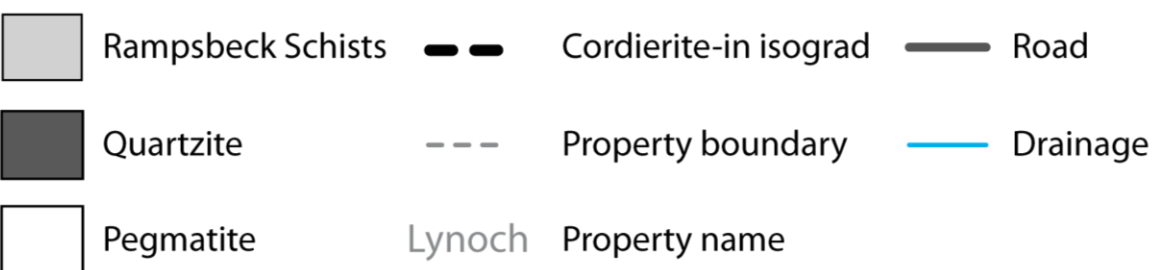
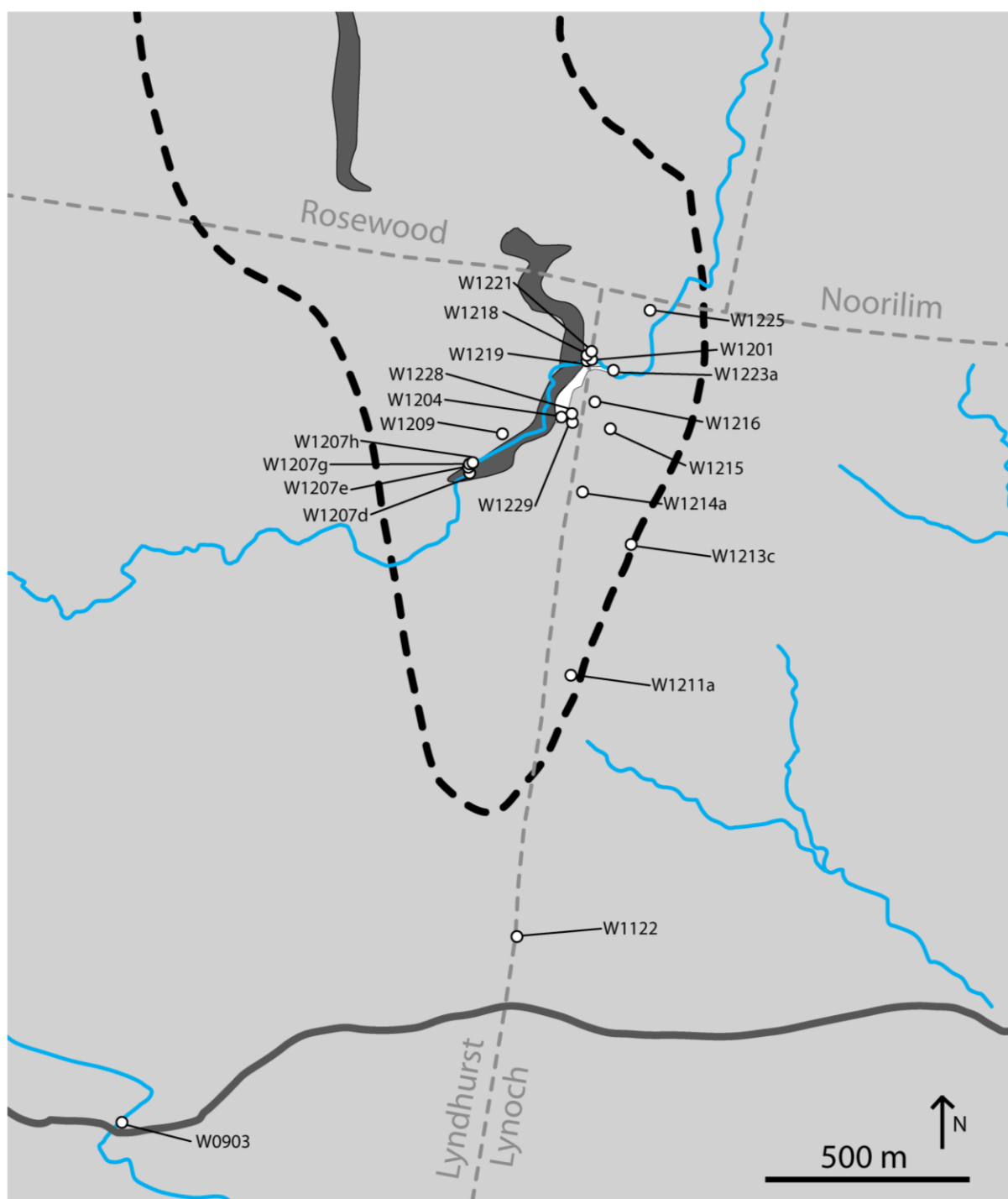


Figure 3.2: Geological map of the field site showing the location of samples collected.

Field relationships

Three main geological units lie within the field site: meta-pelite, quartzite and pegmatite.

The quartzite unit outcrops mostly within a section of the creek which runs roughly north-east to south-west. The quartzite begins outcropping close to where the creek crosses the Lynoch-Lyndhurst boundary fence, where it occurs as massive, rounded outcrops (Figure 3.3A). Moving downstream along strike, the outcrops become larger, more common and increasingly layered. The layers mostly have sharp boundaries defined by cleavage/joints, however in some places outcrops lack cleavage/jointing. Here the layers are defined by colour changes and the boundaries appear diffuse (Figure 3.3B). In one outcrop these layers are folded in small scale (20-30 cm) z-type folds, with fold axes and axial planes clearly defined, and possible evidence of shearing. At the southern end of the field area, the creek turns to the south and cuts across strike. At this location (W1207) the quartzite is roughly 30m wide, with layers 0.5-15 cm wide (Figure 3.3C).

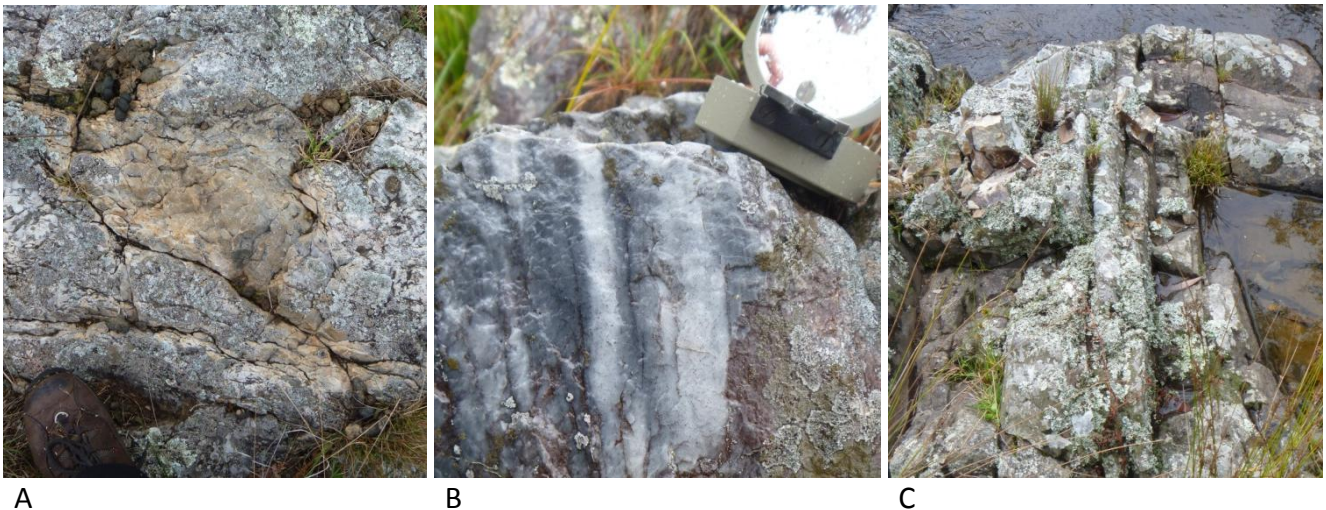


Figure 3.3: Various outcropping styles of quartzite. A: massive, rounded outcrop approximately halfway along the length of the creek studied. B: layered outcrop with layers defined by colour changes. C: layered quartzite at the southern-most outcrop studied, with joints/cleavage defining the layer boundaries.

The meta-pelite comprises the majority of the landscape, outcropping sparsely through the field area. Bedding was difficult to distinguish, but in some places defined by the juxtaposition of cordierite-rich and cordierite-poor layers (Figure 3.4). Fabric within the meta-pelite is weakly formed to non-existent in hand sample. Quartz veins are ubiquitous throughout the field area, often folded on small scales (<5 cm) and often appearing in conjugate pairs close to the quartzite. Cordierite crystals generally increase in size towards the quartzite, from less than 5 mm approximately 1.3 km south of the quartzite, up to as large as 20 mm adjacent to the quartzite. In some locations there appears to be a decrease in crystal size but an increase in the number of crystals within the rock.



Figure 3.4: Bedding in the meta-pelite distinguished by the juxtaposition of cordierite-rich and cordierite-poor layers. Lens cap for scale.

The pegmatite features prominently in the landscape, forming a ridge along the southern bank of the creek, following the boundary of the quartzite. Outcropping as large, rounded masses, it consists of quartz, feldspar, orthoclase, biotite and tourmaline, in places displaying a sub-vertical foliation defined by biotite which highlights small scale folds. The contact between the pegmatite and meta-pelite was easily distinguished and located in several outcrops and boulders along strike. At these locations discordance between the meta-pelite and the pegmatite was clearly visible (Figure 3.5). The contact between the

quartzite and the pegmatite was harder to distinguish, appearing almost diffuse in some locations.



Figure 3.5: Boulder displaying the pegmatite/meta-pelite contact, highlighting the discordance. FOV: 30 cm.

Structural measurements taken in 2012 were mapped and analysed by stereonet to look for discordance between the quartzite unit and the meta-pelite (Figure 3.6).

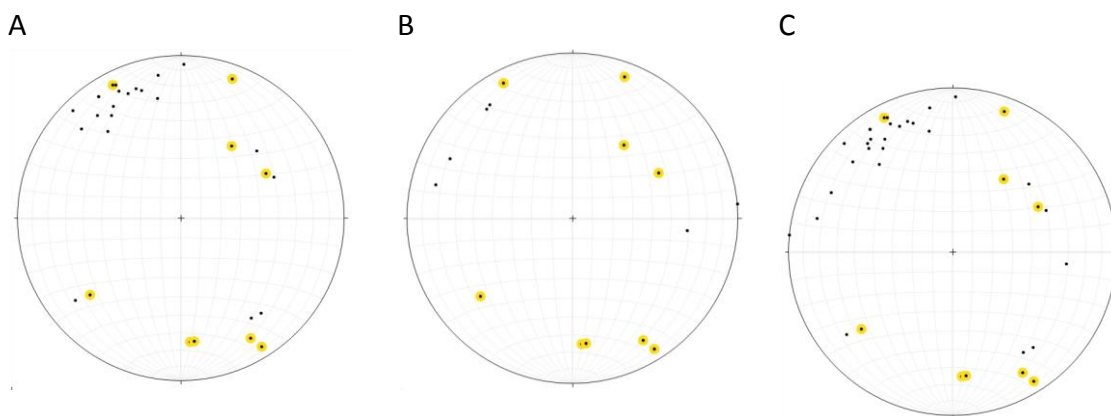


Figure 3.6: Stereonet analysis of measurements taken in 2012. A: Meta-pelite (highlighted) and quartzite; B: Meta-pelite (highlighted) and quartz veins; C: Measurements from all rock types, meta-pelite measurements highlighted.

Results are not consistent along the length of the quartzite unit. Structural measurements at the south-western end show the strike of the quartzite conforms to S_1 fabrics in the aureole however measurements at the north-eastern end of the unit highlight discordance where bedding is at a high angle to the quartzite-schist contact (Figure 3.7).

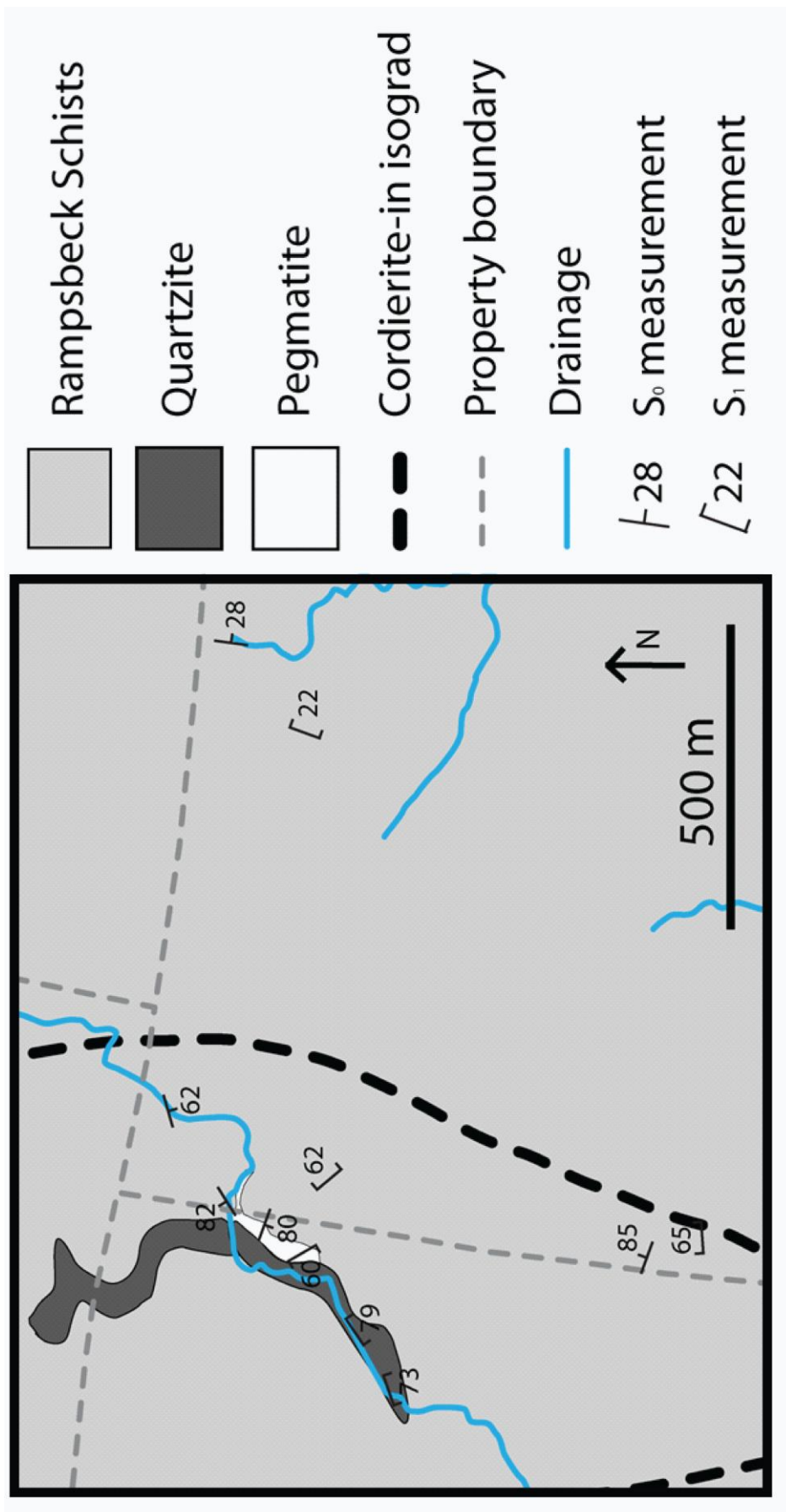


Figure 3.7: Geological map of the study site showing the trends of bedding and cleavage.

Quartzite structure

The quartzite units through the middle of the complex appear to trace out folds with axial planes trending NW-SE (Figure 3.8), roughly consistent with folds recognised as D₁ structures (Korsch, 1981).

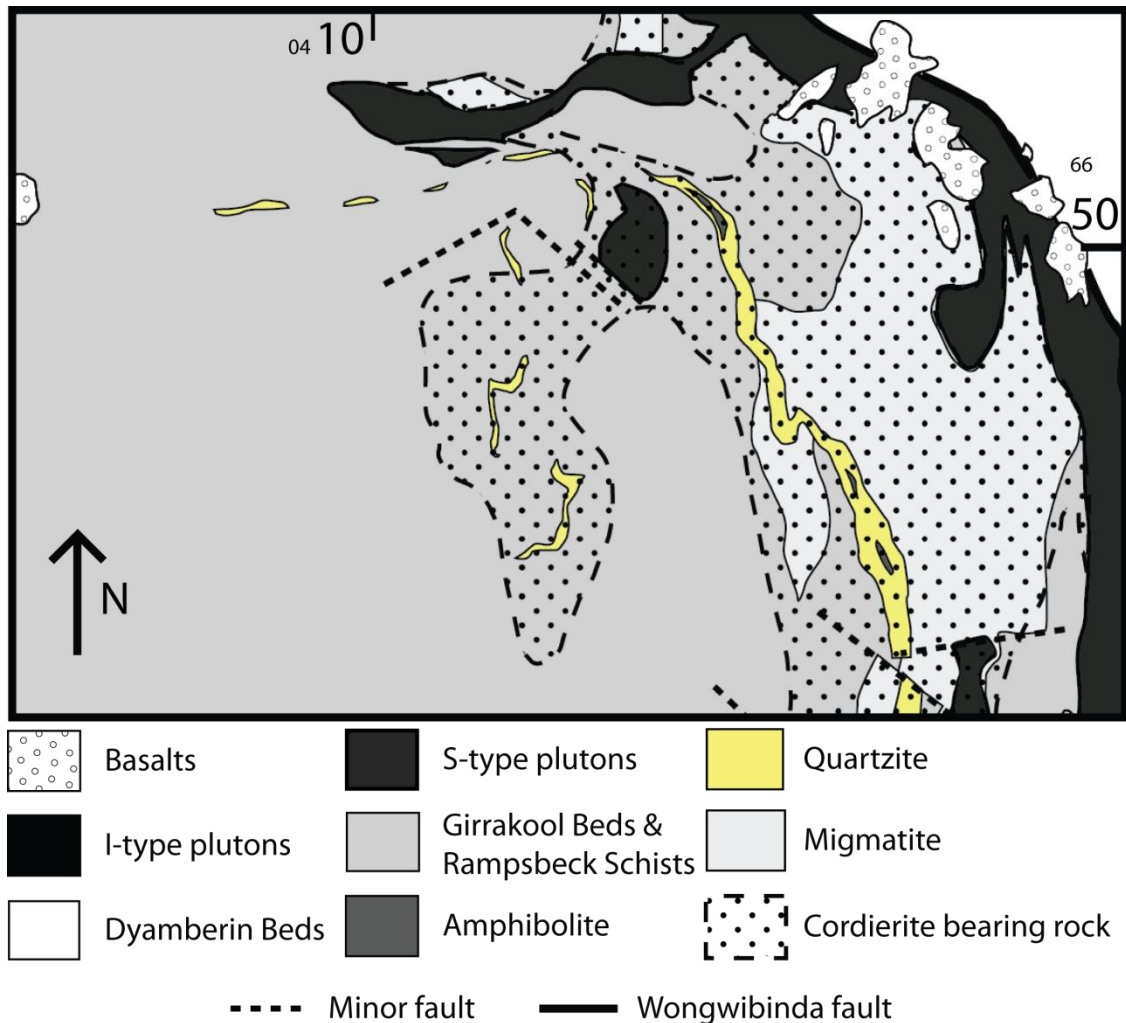


Figure 3.8: Geological map of the WMC, highlighting the structure of the folded quartzite units through the centre of the complex.

Textures of the quartzite (Figure 3.9) are suggestive of vein growth textures. At the hinge of the folded quartzite, the quartz has a massive, vuggy-like structure to it, similar to that of a saddle reef. Towards the limbs it appears increasingly blocky and banded, as in a more typical vein formed through crack-seal processes. Examples of these textures in outcrops are shown below in Figure 3.9.



Figure 3.9: Textures displayed by the quartzite. On the left is an example from the hinge of the fold, where outcrops lack any obvious textures. On the right is an example from the southern limb of the fold, where the quartz shows a pervasive banding.

These changing textures along strike of the quartzite, as well as the general orientation of the limbs parallel to bedding suggests that this is a vein sequence, formed as folding of the bedding created a cavity at the hinge for fluid to accumulate. The conformity of this unit to D_1 fold structures in the WMC suggests that the veins were emplaced syn- or post- D_1 (characterised by subvertical NW-SE axial planes and fold axes dipping steeply to the east) but prior to D_2 (coeval with E-W shortening, characterised by isoclinal folding and rotation of cleavage from NE-SW to NNW-SSE). Vein growth textures revealed through petrographic and microstructural analysis would shed more light on any relative movement of vein walls during growth and therefore the timing of vein formation.

CHAPTER 4 - PETROGRAPHY

Aims

This chapter examines the petrography of the three different rock types involved in this study. The aim is to identify changes to mineral assemblages and microstructures that will aid in the identification of thermal and/or chemical changes in the study area. This chapter will attempt to characterise the samples as a representative of each rock unit, rather than providing detailed descriptions of each thin section. Detailed descriptions of individual thin sections are provided in the appendix, with locations of samples shown in Figure 3.2.

Analytical Method

Thirty five samples were mounted on glass slides and polished to a thickness of 30 μm , including twenty seven from the Rampsbeck Schists, and eight from the Quartzite unit. These were examined under a petrographic microscope using PPL, XPL, as well as a gypsum plate and reflected light where appropriate, and are described below.

Results

Rampsbeck Schists

Twenty seven samples from the Rampsbeck Schists were examined, sixteen of which were cordierite bearing.

The Rampsbeck Schists are very fine grained ($<100\ \mu\text{m}$) meta-pelitic schists comprised of quartz, biotite, plagioclase feldspar and k-feldspar \pm muscovite, with minor minerals zircon, monazite, apatite, titanite, xenotime, and opaques (hematite, pyrrhotite, pyrite, ilmenite

and rutile). Small garnets were present in one sample (W1209). Mode percentages of the mineralogy are summarised in Table 4.1.

Table 4.1: Summary of Ramspeck Schists Samples. Mode percentages of three representative samples at different distances from the quartzite unit calculated from backscatter images and photomicrographs obtained in this study.

Mineral	Mode			Notes
	W1211 0.52 km	W1214 0.18 km	W1229 0.05 km	
Quartz	30	25	15	Anhedral, 40 μm , grain boundary shape determined by the surrounding minerals. Some grains show undulose extinction.
Plagioclase feldspar	20	17	11	Anhedral, 50 μm , grain boundary shape determined by the surrounding minerals.
K-feldspar	20	17	26	Two populations: matrix grains tend to be irregular and anhedral with curved edges; poikiloblasts are anhedral and form sub-equant oval shapes (200-1300 μm).
Biotite	29	25	15	Two populations (60 μm): platy, which align to form S_1 , commonly found as inclusions in Crd poikiloblasts and throughout the matrix; and irregular and anhedral, commonly found in the matrix.
Muscovite	1	3	6	Two populations: matrix grains are lobate (100 μm); poikiloblasts are platy, with euhedral edges parallel to the c-axis, and lobate ends with embayments of matrix minerals (700-100 μm).
Cordierite	-	13	27	Crystals are poikiloblastic and anhedral. Some samples show equant grains, and in others cordierites appear flattened. Range in size from 300 – 14500 μm .
Opaques, Zircon, Monazite, Apatite, Titanite, Xenotime	Minor and accessory			

Two foliations are weakly defined by fine grained micas only discernible in thin section, with S_1 defined by biotite, and S_2 defined by muscovite. In the field, bedding was distinguished in places by cordierite rich versus cordierite poor layers. In thin section however this is not visible, with poikiloblasts distributed evenly throughout the samples.

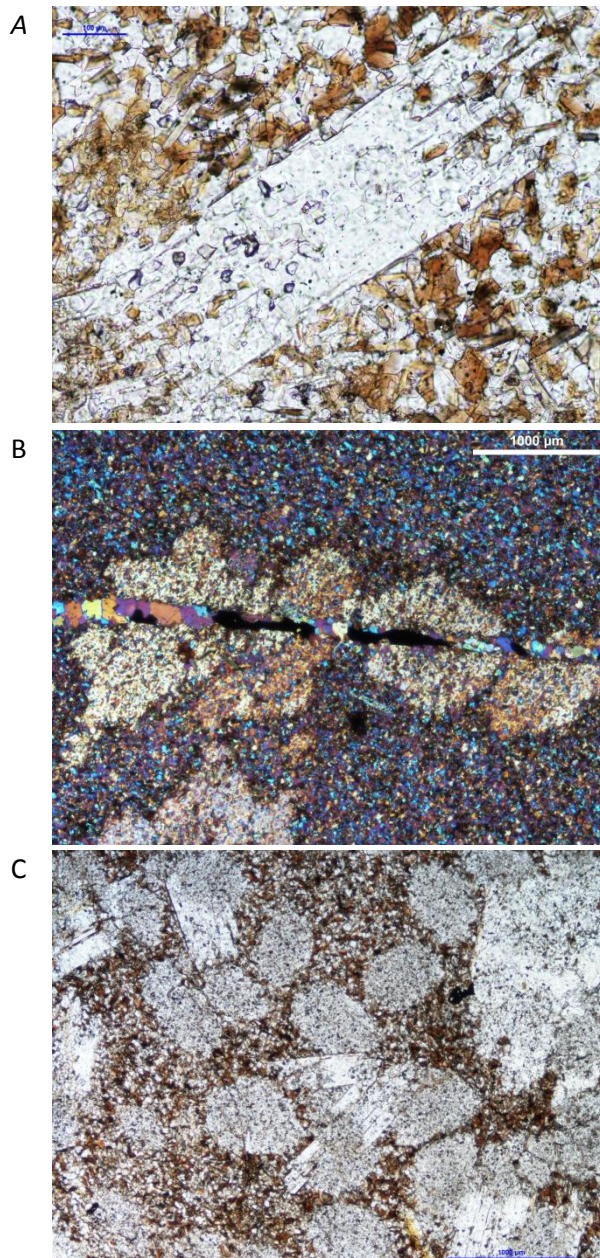


Figure 4.1: Photomicrographs of samples W1216 (A and B, 0.08 km from quartzite boundary) and W1229 (C, 0.05 km from quartzite boundary), two typical examples of Rampsbeck Schists.

(A) A muscovite poikiloblast with inclusions of biotite and quartz, in PPL. The poikiloblast is surrounded by a typical matrix of quartz, plagioclase feldspar, biotite, k-feldspar and muscovite. Scale bar in the top left is 100 μm.

(B) Photomicrograph in XPL with a gypsum plate, showing cordierite poikiloblasts with a vein cutting through the centre. The poikiloblasts have inclusions of biotite and quartz. The vein shows a complex mineralogy, with quartz, sulphides (black) and biotite. Scale bar in the top right is 1000 μm.

(C) Photomicrograph in PPL of muscovite (platy) and k-feldspar (round) poikiloblasts within the schist. Inclusions consist of biotite and quartz. K-feldspars bottom centre and top left seem to replace muscovite. Scale bar bottom right is 1000 μm.

This reveals a decrease in the largest grain size in the first 75 metres away from the quartzite boundary; however samples further than 75 metres from the boundary contain outliers that interrupt this general trend. A wide spread of sizes within each sample is also revealed, especially in samples closer to the quartzite unit.

Most of the samples were altered, showing evidence for seritisation and pseudomorphing of cordierite by pinitite. Alteration occurs preferentially along fractures and around some cordierite crystals.

Rampsbeck Schist veins

The Rampsbeck Schists contain a network of veins, which is present throughout the aureole. In the field these veins are pervasive through the outcrops, and sets of veins are commonly seen to cross each other at an angle. In thin section the veins show a complex mineralogy, with quartz as a major constituent, but also containing a wide range of minor minerals including silicates, oxides and sulphides.

Veins examined in this project are divided into two groups based on width. Small veins (≤ 5 mm) are found throughout the aureole, whereas large veins (> 5 mm) were found within outcrops of schists less than 50 m from the quartzite.

Small veins (≤ 5 mm)

Typically these veins are between 100 and 500 μm in width, consisting of quartz \pm plagioclase feldspar, k-feldspar, muscovite and biotite, with accessory phases titanite, apatite, zircon, monazite and opaques (hematite, pyrrhotite, pyrite, ilmenite and rutile).

Rather than forming straight lines by fracturing individual grains, edges of the veins trace paths along grain boundaries, giving the veins a jagged appearance (Figure 4.3, yellow outline). The veins show a blocky growth texture, with no obvious growth direction, and hence are likely to be asymmetrical syntaxial veins with ongoing nucleation and growth occurring on one side of the fracture outwards towards the other.

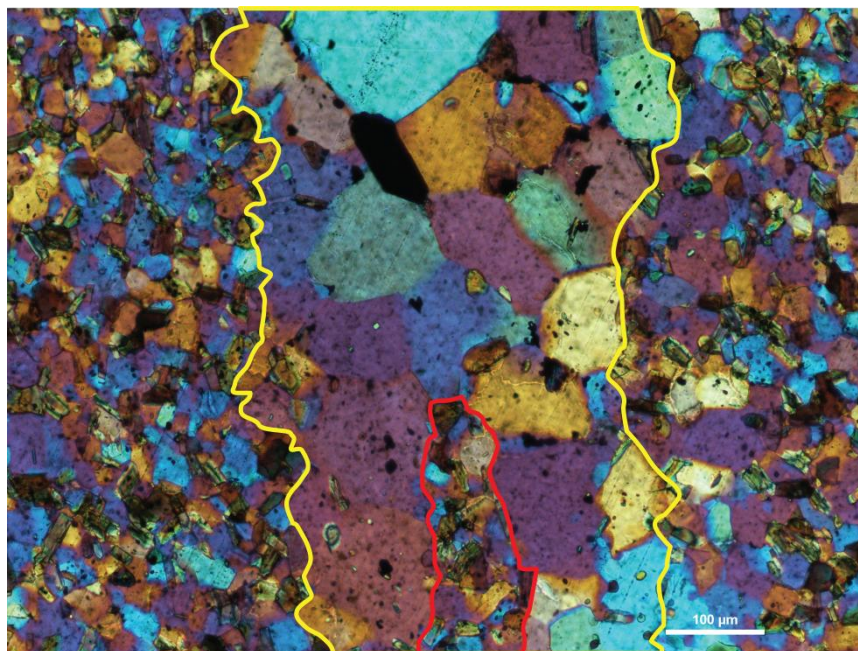


Figure 4.3: Photomicrograph in XPL with a gypsum plate, of sample W1216 (0.08 km from quartzite boundary), representative of a quartz vein in the schist. Edge of the vein is outlined in yellow, showing the vein boundary following grain boundaries, as well as a wall rock inclusion outlined in red. Scale bar in the bottom right is 100 μm .

Inclusions of wall rock are also seen in these veins (Figure 4.3, red outline), distinguished from vein mineralogy by crystal habit and the occurrence of minor phases clustered together, as opposed to phases crystallised from vein fluid which occur as one or two minor phases surrounded by large quartz crystals.

Veins cut through cordierite poikiloblasts and the matrix with no discernible change or alteration to the host rock (Figure 4.1B), indicating that they formed in equilibrium with the host rock.

Large veins (> 5 mm)

Sample W1204

This sample was collected from an outcrop twenty metres from the quartzite boundary, featuring a quartz vein splitting into two around a large inclusion of wall rock, with a thin section cut from the point where the vein splits (Figure 4.4).



Figure 4.4: Outcrop from which sample W1204 was collected, with the quartz vein running horizontally through the outcrop and the large wall rock inclusion to the left. Red box shows approximate position of the thin section within the sample. Compass dial is 6.5 cm diameter.

The vein is composed dominantly of quartz. Banding defined by grain size is visible under the microscope, with coarse (250 μm) and fine ($\leq 100 \mu\text{m}$) bands of quartz alternating across the vein. Quartz grains display sutured grain boundaries and undulose extinction (Figure 4.5A).

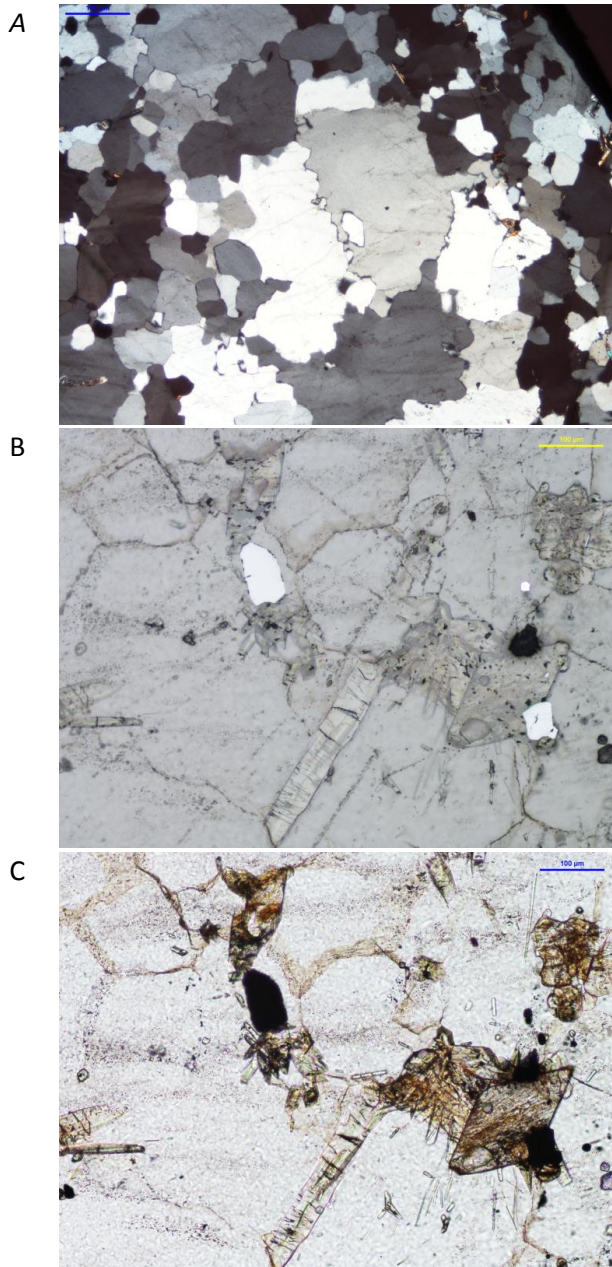


*Figure 4.5:
Photomicrographs of a
typical quartz vein close
(0.02 km) to the quartzite
contact. Sample W1204, (A)
in XPL, (B) in reflected light
and (C) in PPL.*

*(A) Quartz crystals from the
vein displaying sutured grain
boundaries and blocky
texture. Quartz grain centre
left showing undulose
extinction. Scale bar in top
left is 100 μm .*

*(B) Hematite with wall rock
material surrounded by vein
quartz grains. Scale bar in
top right is 100 μm .*

*(C) Same view as (B), in PPL.
Above both hematites are
euhedral amphibole crystals,
and throughout the slide are
small, platy muscovites.
Blocky quartz crystals show
iron-weathering along grain
boundaries and parallel
bands of inclusions
horizontally across the field
of view. Scale bar in top right
is 100 μm .*

Thin slivers of wall rock inclusions are incorporated in the vein, indicating multiple episodes of fracturing and mineralisation. These host rock fragments consist of amphibole, muscovite, garnet, apatite and opaques (Figure 4.5, B and C).

Sample W1221

This sample is a 2.5 cm wide quartz vein within an outcrop of schist thirty metres from the quartzite boundary (Figure 4.6A). Although bedding and cleavage were not discernible in this outcrop, the strike and dip of this vein ($052^{\circ}/73^{\circ}/E$) is comparable to bedding measurements in an outcrop 10-20 m away (S_0 : $058^{\circ}/82^{\circ}/W$). This particular outcrop also featured several large veins cross cutting each other (Figure 4.6B). Some of these veins were not linear, curving across the outcrop.

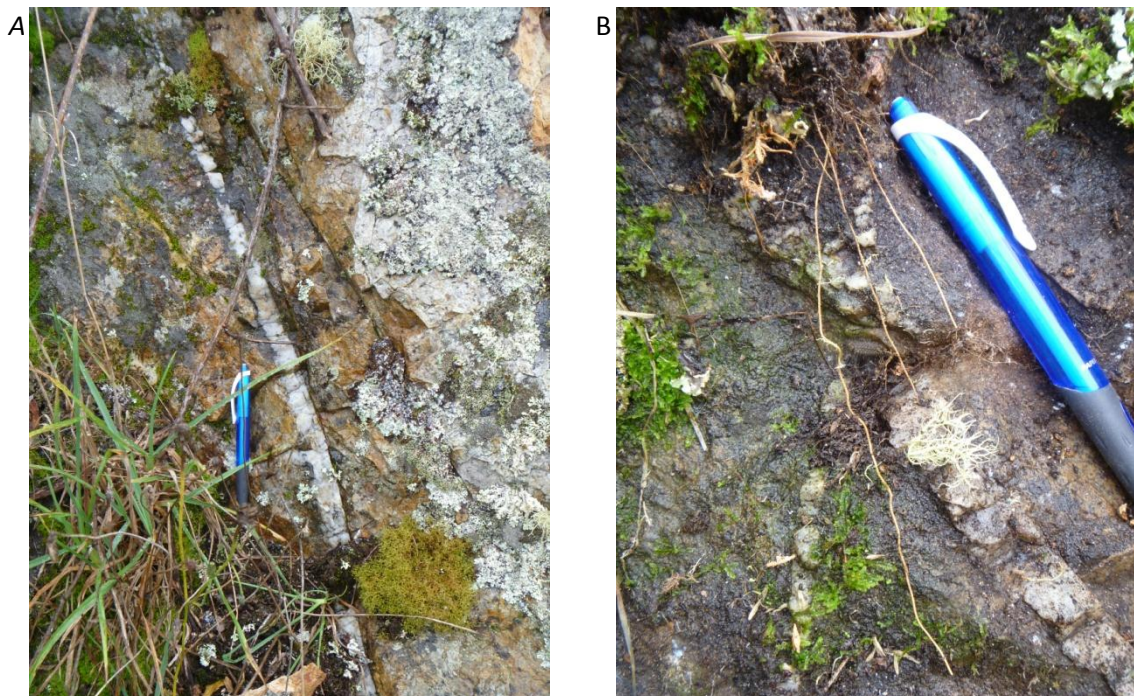


Figure 4.6: Outcrop from which sample W1221 was collected, showing (A) width of vein in the schist, and (B) the cross-cutting relationship of veins. Thin section cut from vein shown in (A).

Pencil is 14 cm long.

In thin section this vein displays two growth textures: blocky (Figure 4.7B) and fibrous (Figure 4.7D). This texture change, along with wall rock fragments included in the centre of the vein indicates multiple opening events and subsequent episodes of vein growth.

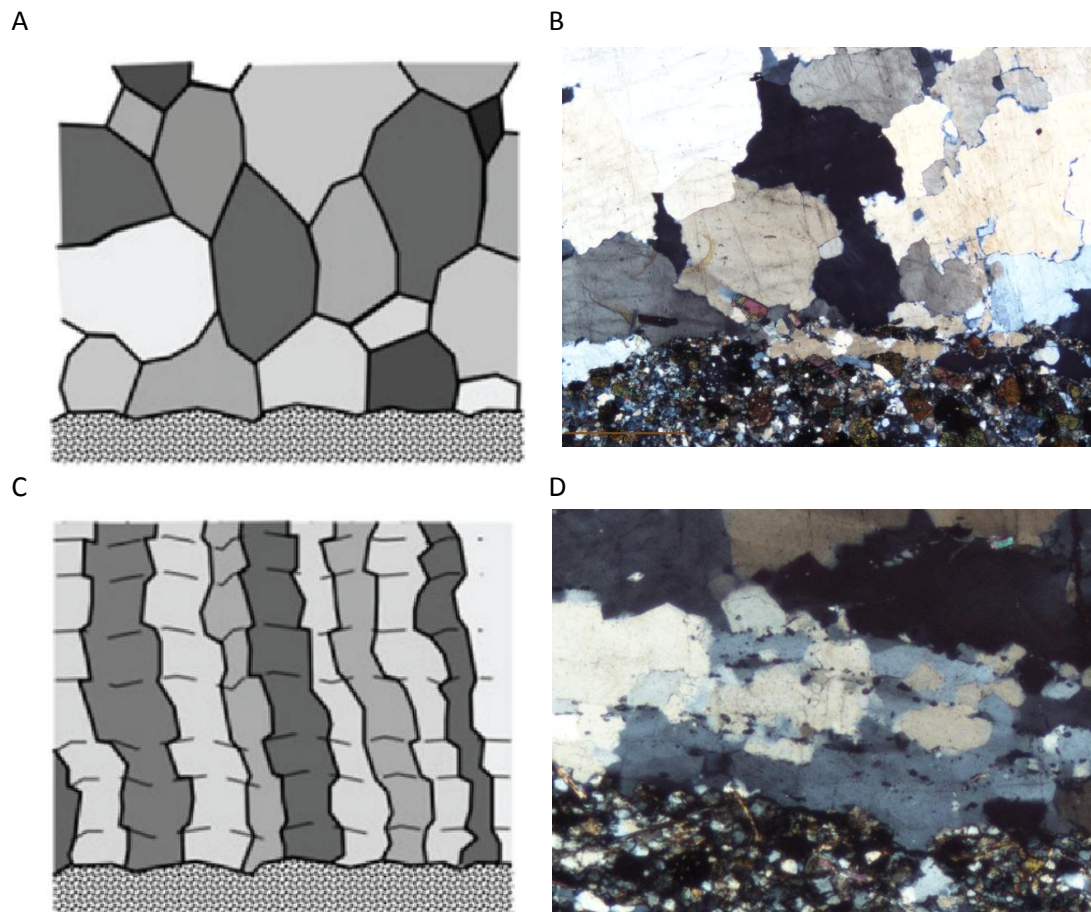


Figure 4.7: Varying growth textures in sample W1221. (A) and (C) show typical crystal morphology with respect to vein wall in blocky and stretched vein types respectively. (B) and (D) are photomicrographs of sample W1221 in XPL showing corresponding examples of these textures. Photos oriented with the vein wall at the bottom. (B) Field of view 7.41 mm across, (D) Field of view 3.09 mm across. (A) and (C) adapted from Bons et al. (2012).

These textures are indicative of two distinct vein formation processes. The first is syntaxial vein growth, in which a crack forms and crystals grow from the one side of the crack towards the centre, ongoing nucleation of minerals within the vein producing equant quartz crystals and sealing the crack (Figure 4.7, A and B). The second process is stretching vein growth. This is similar to syntaxial growth in that it occurs by crack-sealing, however the

crack plane cuts through previously precipitated crystals (instead of along the growth plane, as in syntaxial growth). Precipitation then occurs by epitaxial growth on the same minerals, forming “stretched crystals” (Figure 4.7, C and D).

Quartz grains displaying blocky growth texture also display undulose extinction and presence of sub-grains. The wall rock fragments within this section of the vein consist of k-feldspar, tourmaline, plagioclase feldspar and muscovite, with accessory zircon.

Quartz grains displaying fibrous growth texture are oriented parallel to the vein boundary, and show a preferred orientation under XPL using a gypsum plate. These grains also have fine grained wall rock inclusions, which form trails parallel to the vein boundary (Figure 4.7D).

The host rock is composed of quartz, plagioclase feldspar, k-feldspar and tourmaline with accessory phases apatite, rutile and xenotime. Tourmaline crystals increase in size from 150 to 450 μm towards the vein, potentially indicating crystallisation from the vein fluid. K-feldspar and tourmaline crystals are poikiloblastic, with inclusions of quartz and mica. At the vein boundary there are more wall rock fragments within the vein, of the same mineralogy.

Small, irregular offshoot quartz veins have formed within the host rock, perpendicular to the large vein. These offshoot veins are similar to the small veins within the schists, being dominantly composed of quartz, with blocky growth texture indicative of an asymmetrical syntaxial vein (Figure 4.8).

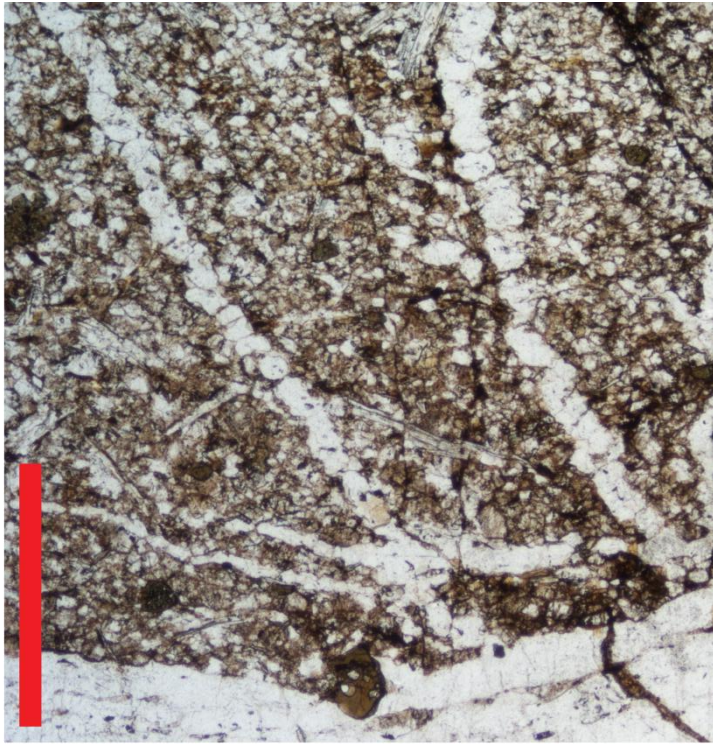


Figure 4.8: Photomicrograph of sample W1221, showing offshoot veins from a large quartz vein close to the quartzite contact. Photomicrograph oriented with the vein wall running horizontally across the bottom. Blocky vein texture is apparent as individual quartz grains are picked out by weathering along boundaries. Scale bar bottom right is 1000 μm .

Quartzite

Eight samples from the quartzite were examined, arranged in a transect across the width of the unit (Figure 4.9).

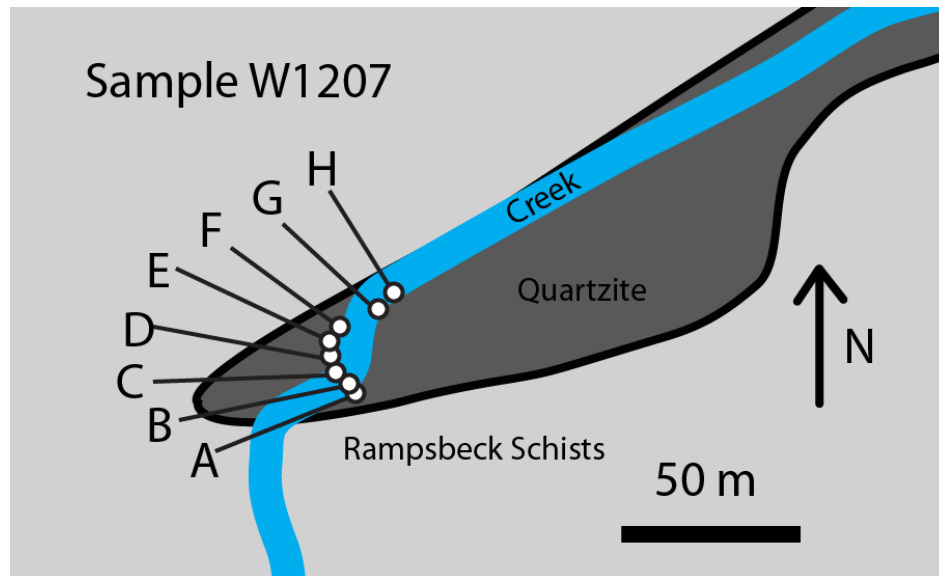


Figure 4.9: Quartzite sampling transect location map.

The mineralogy is 90-99% quartz, which ranges from 10-100 μm in size. Minor minerals present include muscovite, biotite, plagioclase feldspar, garnet, and opaques (ilmenite and hematite). Modal percentages from a representative sample are shown in Table 4.2.

Banding is visible in thin section, with alternating light and dark bands between 50 and 100 mm in width. The banding is subparallel to the boundaries of the quartzite with the surrounding rock units. Banding is defined by mineralogy and grain size contrasts: dark bands are characterised by 90% quartz (<100 μm) with muscovite (100 μm), biotite (20 μm), garnet (20 μm), plagioclase feldspar (40 μm) and opaques (10 μm) totalling 10%; whereas light bands are characterised by 99% quartz (~100 μm) and minor amounts of biotite (<20 μm) (Figure 4.10).

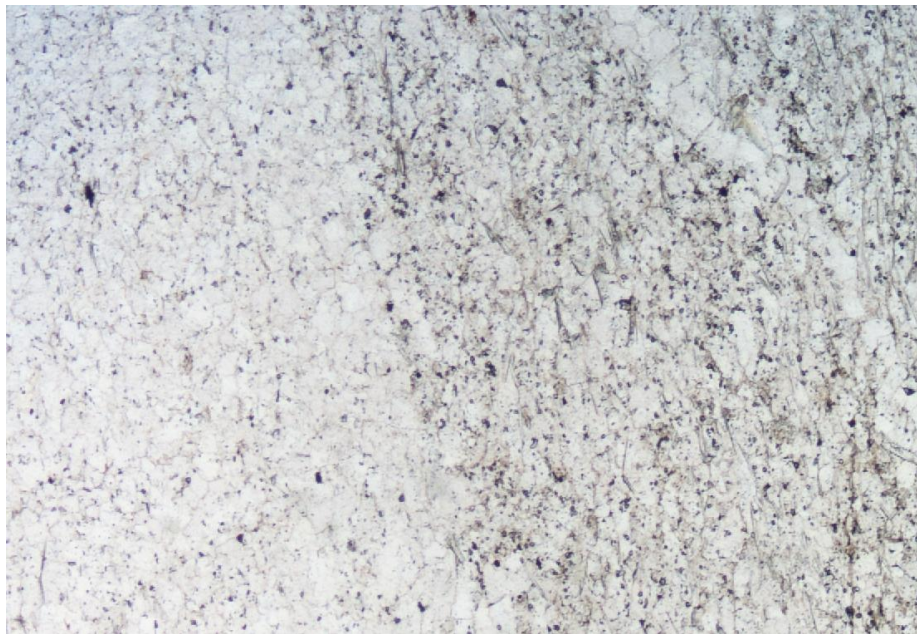


Figure 4.10: Photomicrograph of sample W1207h in PPL, showing banding defined by mineralogy. Light band is on the left, with mostly pure quartz. Dark band is on the right, showing more complex mineralogy with fine, platy micas and small high relief garnets giving it a dark colour. A small quartz vein in the top right cuts across the dark band. FOV 12.8 mm.

Biotite and muscovite in the dark bands show foliation (S_1 and S_2 respectively) which is subparallel to banding. Within the dark bands quartz grain boundaries meet the long axes of the micas at $\sim 90^\circ$ angles, resulting in small grain sizes compared to those in the light bands. Darker trails parallel to the banding and foliation form from concentrations of small, high relief garnets within dark bands (Figure 4.11).

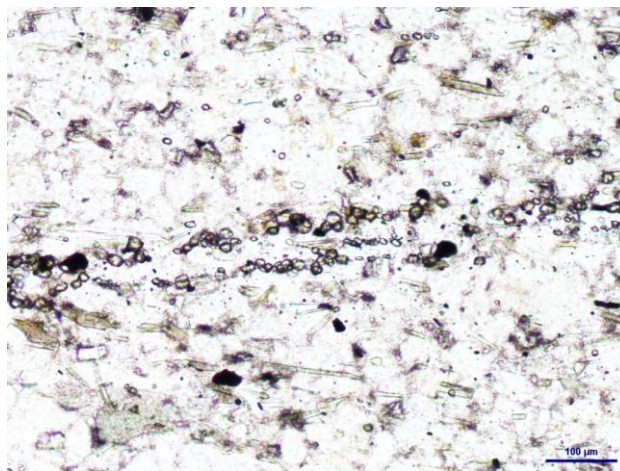


Figure 4.11: Photomicrograph of sample W1207e in PPL, showing concentrations of garnets forming trails parallel to foliation, which is defined by biotite and muscovite. Scale bar in bottom right is 100 μm .

Quartz grains rarely display undulose extinction, but commonly exhibit bulging irregular grain boundaries interpreted as evidence of grain boundary migration. Examining orientations using a gypsum plate on the petrographic microscope reveals a weak association between banding and alignment of crystals (Figure 4.12).

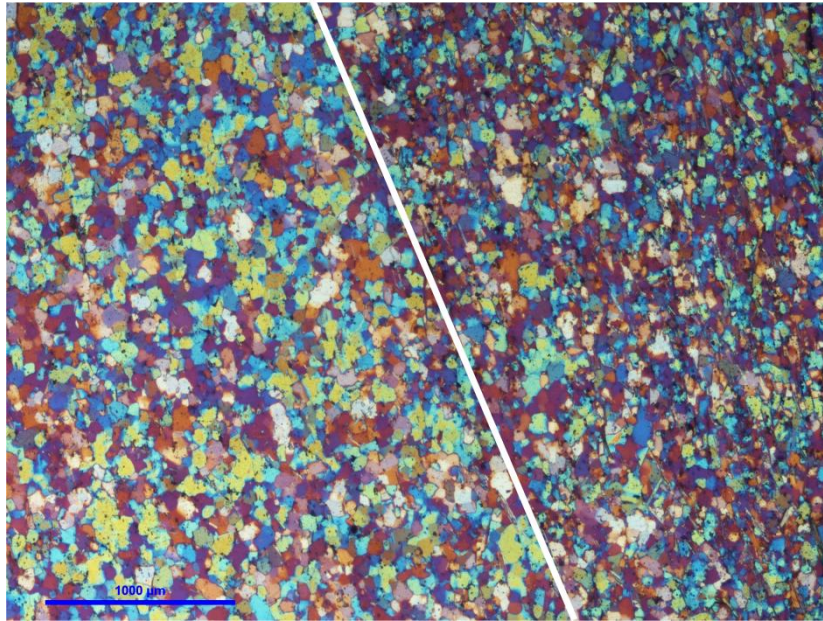


Figure 4.12: Photomicrograph of sample W1207g in XPL with a gypsum plate, showing the weak association between banding (defined by the white line) and crystal orientation (defined by colour of grains). The dark band on the right shows darker pink and purple colours, whereas the light band on the left shows more yellows and blues. Scale bar at the bottom left is 1000 μm .

Small distinct quartz veins, approximately 150 μm in width, are common throughout the quartzite unit. These veins are at varying angles to the banding; in some places they are oriented roughly parallel to the bands however they generally form at an angle to the banding (Figure 4.10). Similar to veins in the schist, veins in the quartzite commonly cross-cut each other and show blocky textures consistent with asymmetrical syntaxial growth.

Table 4.2: Summary of the quartzite. Mode percentages determined by SEM-EBSD mapping of Sample W1207g.

Mineral	Mode (%)	Size (μm)	Notes
Quartz	95	100	Crystals are irregular and form 120° triple junctions. Undulose extinction is rare, but evidence for grain boundary migration is common.
Muscovite	0.6	100	Crystals form in thin plates, and align to form S_2 .
Biotite	0.7	20	Biotite ranges in form from euhedral platy crystals to anhedral, irregular crystals. Euhedral crystals are aligned, forming S_1 .
Plagioclase feldspar	3	40	Crystals are anhedral and irregular. No oscillatory zoning or twinning is evident.
Garnet	0.3	20	Garnets form equant crystals, which commonly cluster together to form garnet trails parallel to banding.
K-feldspar Opakes	Minor and accessory		

CHAPTER 5 - MICROSTRUCTURE

Introduction

Veins exhibit a range of internal structures dependant on the specific fracture mechanics, deformation kinematics and fluid composition at the time of formation. Due to the specific growth patterns, the study of vein textures can be valuable in determining previous metamorphic conditions, especially through comparison of a range of veins within a complex (Vearncombe, 1993, Pennacchioni et al., 2010, Bons et al., 2012) .

Discovered through petrographic analysis, veins in the WMC are commonly formed through a crack-seal process, with one or more episodes of mineral growth producing veins of varying size. Large veins within the Rampsbeck Schist exhibit multiple growth textures, indicative of this process. During each episode of mineral growth, growth competition results in the formation of a crystallographic preferred orientation (Hilgers et al., 2001), with c-axes generally forming at a high angle to the vein wall (Cox and Etheridge, 1983). Initially, lateral and outward growth results in c-axes at oblique angles to the vein wall however with prolonged growth crystals with c-axes perpendicular to the vein wall will dominate (Bons and Bons, 2003). Repeated episodes of mineral growth within one vein can then form 'bands' of minerals at different orientations.

Also discovered through petrographic analysis, the quartzite unit displays grain size and mineralogy banding, which is weakly associated with orientation of quartz crystals. These microstructural properties are reminiscent of those 'bands' of differently oriented minerals seen in small quartz veins. Quartz grains in the quartzite have been recrystallised during an

episode of regional metamorphism, obscuring original textural relationships, however orientation of the grains in these bands may provide clues as to its original formation.

Aims

This chapter aims to characterise crystallographic orientation and microstructure within a large quartz vein from the Rampsbeck Schists, in order to constrain mineral growth conditions and vein formation processes.

This will then be compared to crystallographic orientations within a sample from the quartzite unit, with an aim to better constrain the origin of this unit.

Analytical Methods

Representative sites for EBSD mapping were chosen in two samples in order to obtain data across two areas of differing microstructure: in sample W1204 bands of contrasting grain size within the vein were mapped, and in sample W1207g both light and dark bands, as well as a small quartz vein, were mapped (Figure 5.1).

Electron Backscatter Diffraction (EBSD) analysis was undertaken on a Zeiss Scanning Electron Microscope (SEM) with a HKL NordleysNano high sensitivity EBSD detector, using the HKL CHANNEL5 analysis software from Oxford Instruments. Data was collected from mechanically polished thin sections with a final mechanochemical polish using colloidal silica. Thin sections were subsequently coated with ~3 nm of carbon. The SEM was run at a high vacuum with an accelerating voltage of 20 kV, a beam current of 8.0 nA, and with an aperture of 30 μm . The sample was tilted to an angle of 70°, with tilt correction applied in the Zeiss SEM software. EBSPs were processed with 2 frame averaging, 4x4 binning, ~55 theoretical reflectors and 8-11 bands. Specifics for both samples are shown in Table 5.1.

Table 5.1: Acquisition and processing details for EBSD maps run

	W1204	W1207g
Mechanochemical polishing time	3.5 min	5.5 min
Accelerating voltage	20.00 kV	20.00 kV
Specimen tilt	70°	70°
Working distance	24.3 mm	14.8 mm
Number of channels	2048	1024
Energy range	20 keV	10 keV
Energy per channel	10.0 eV	10.0 eV
Detector type	X-Max	X-Max
Pulse Pile Up Correction	Succeeded	Succeeded
Frame averaging	2	2
Step size	3 μ m	3 μ m

Obtained from the mapping sequence, several maps were produced displaying different properties of the sample. Band contrast maps display data quality, with lighter colours showing areas of good quality patterns and dark lines representing grain boundaries in these maps. Phase maps are coloured by the identification of the mineral by the software, based on crystallographic properties. Orientation maps are also produced, with colour of grains on the map corresponding to orientation within the sample. Two different colour schemes are used: the Inverse Pole Figure (IPF) colouring scheme, which is based on the orientation of the sample axes relative to the crystal unit cell; and the All Euler angle scheme, which is based on the angle through which each axis of the sample must be rotated until it coincides with those of the crystal.

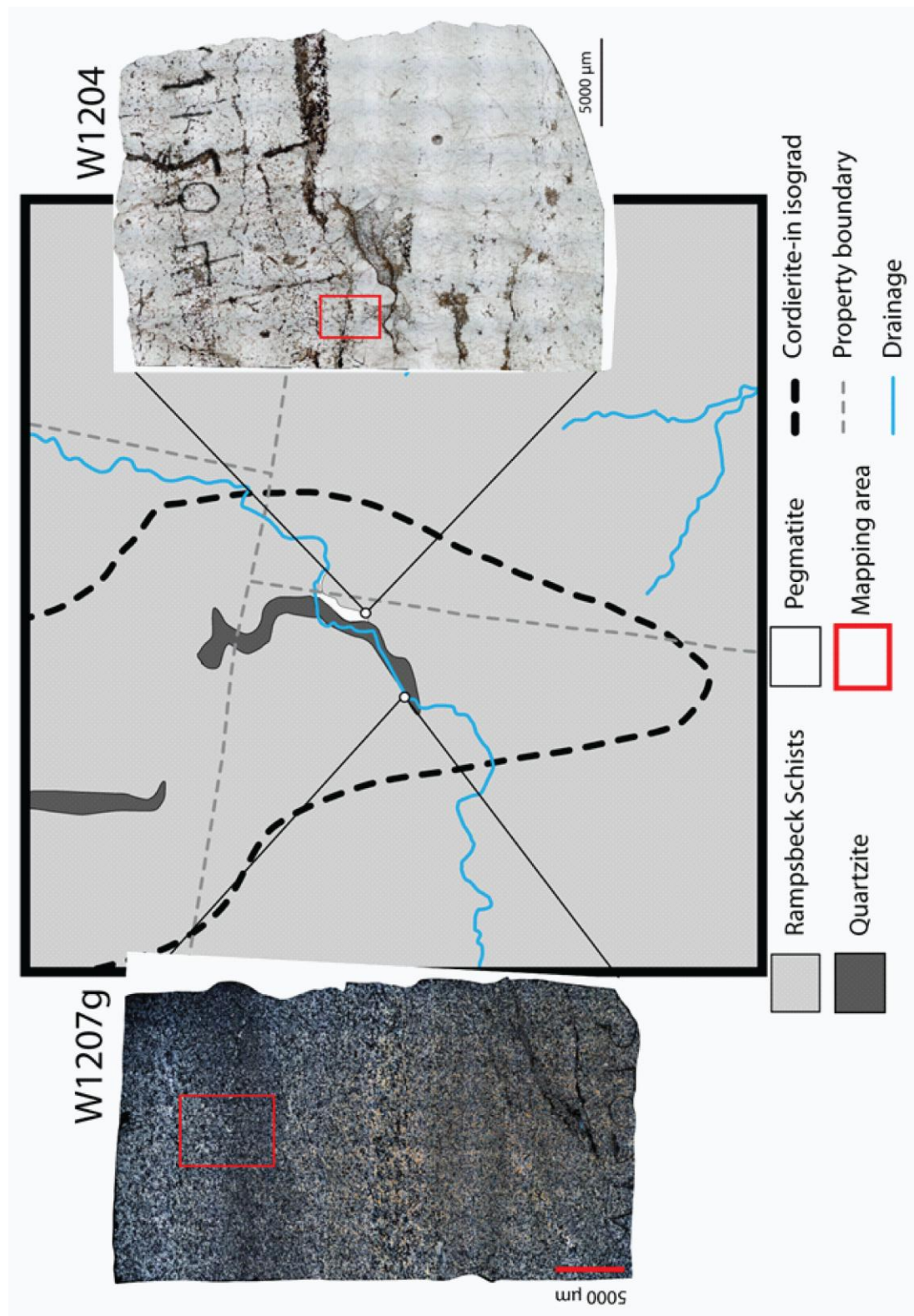


Figure 5.1: Geological map of the study site, showing the location of samples chosen for EBSD mapping. Insets show the location of the mapping area on each thin section. Photomicrograph of W1207g is in XPL, W1204 is in PPL.

Post-acquisition data processing was undertaken using CHANNEL5 software suite. This included removal of non-indexed points through the removal of wild spikes and then extrapolation of points from neighbouring data points (up to 4 neighbouring data points).

Crystallographic orientation information is presented in the form of pole figures (equal area, lower hemisphere projections), with each figure representing the orientation of a specific crystal axis in the sample coordinate system where x is horizontal, y is vertical and z is perpendicular to the sample surface. This information is also shown as contoured plots.

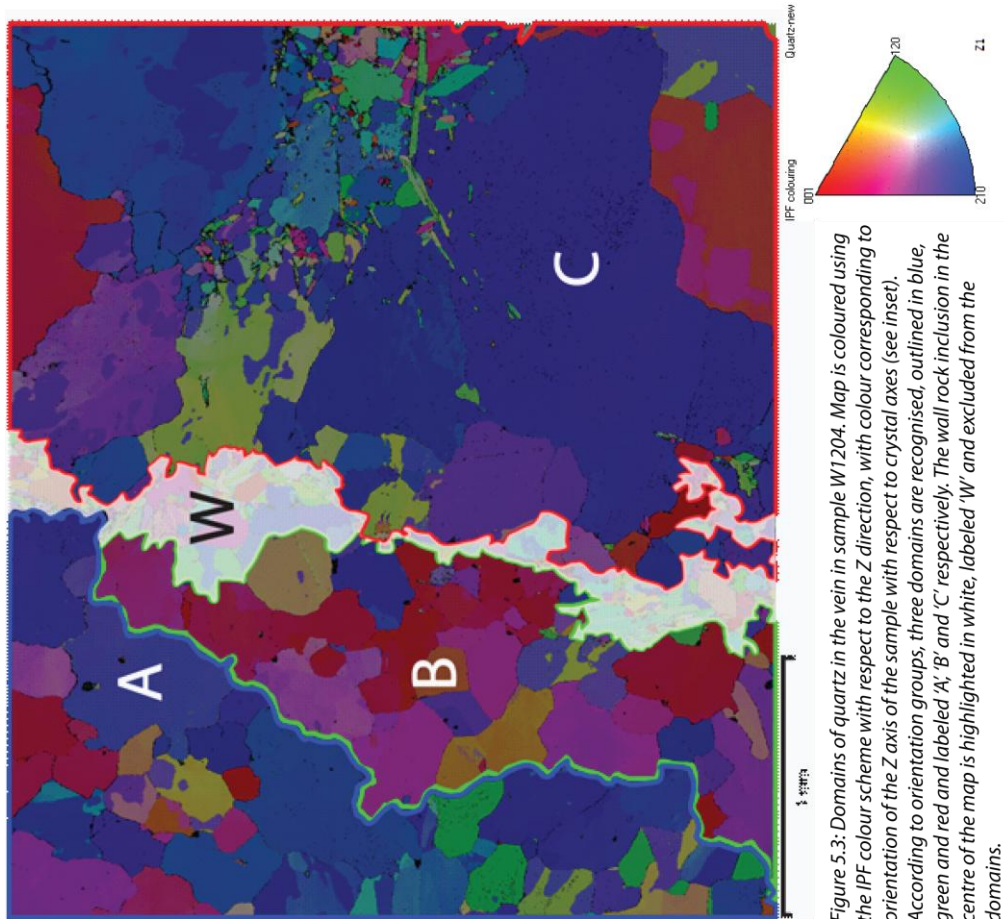
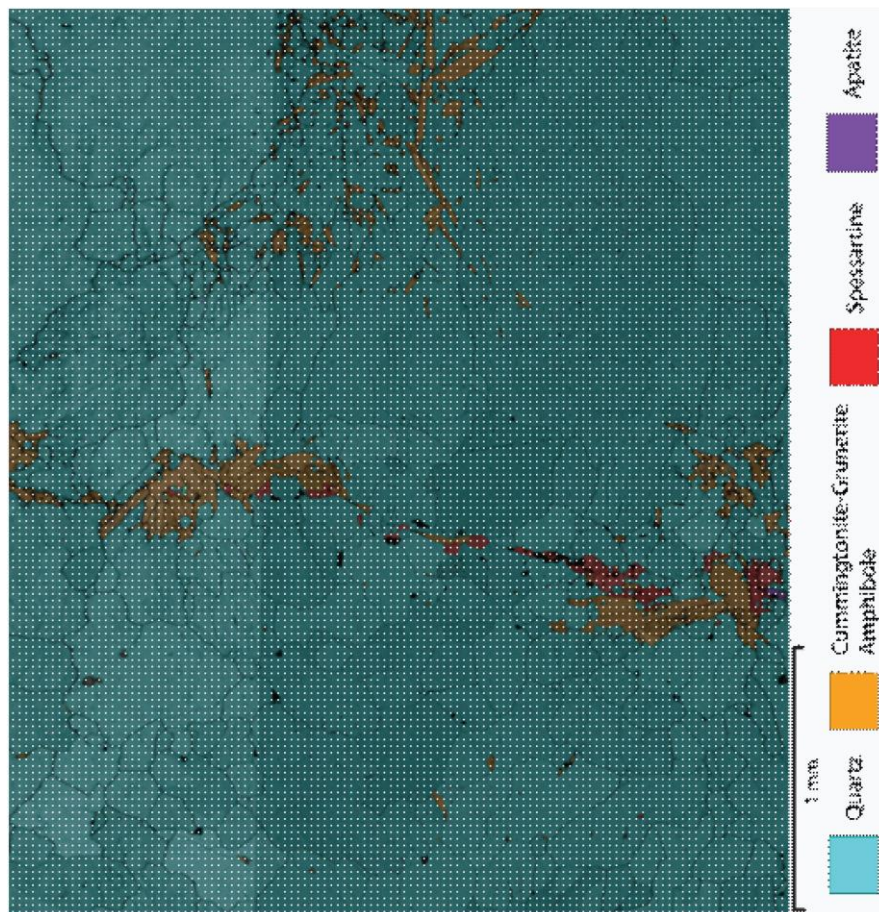
Results

W1204 – A large (>0.5 mm) vein in the Rampsbeck Schists

Figure 5.2 shows the phase and band contrast map for Sample W1204. The band contrast shows a range in pattern quality, however overall the quality was good.

EBSD mapping reveals the vein from Sample 1204 to consist of quartz. Initially, the map can be divided into two quartz domains, based on visually determined grain size changes. These are defined by large grains to the right and smaller grains to the left, with a wall rock inclusion delineating the boundary. The wall rock inclusion runs vertically through the centre of the map area, with apatite, Fe-Mn rich amphibole and garnet grains.

Figure 5.3 shows crystallographic orientation mapped based on IPF colouring for the Z axis. This represents the orientation of the Z axis of the sample, with respect to the crystal unit cell.



To the right of the wall rock inclusion (labelled W) the vein material shows dominantly blue colours. This is labelled as domain C (Figure 5.3). Material to the left of the wall rock was thought to be indicative of a single, separate domain. Mapping of orientation reveals here that this section can be divided into two domains, with domain A showing dominantly blue colours and domain B dominantly red colours.

Graphing of grain size confirms visual estimates, showing the domains are separated by grain size changes (Figure 5.4). Domains A and B show similar profiles of grain size, separated from domain C which shows a higher frequency of larger grains.

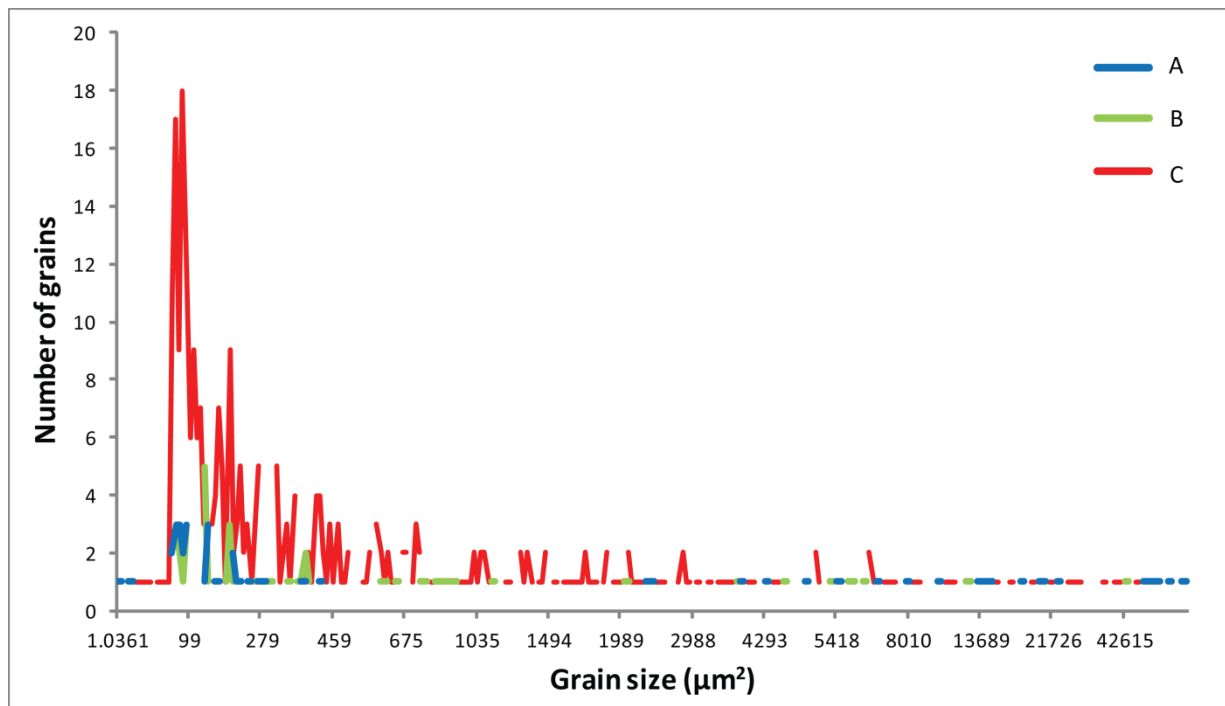


Figure 5.4: Grain size (by area) of the three domains in sample W1204.

Plotting orientations of quartz grains in the three domains onto pole figures reveals patterns of preferred orientation (Figure 5.5).

Domain A shows a preferred orientation of the $\langle 0001 \rangle$ axis to the Y axis of the sample, represented in the point maxima on the right of the contoured pole figure (Figure 5.5A). The two other axes plotted show varied orientation, with the $\langle 10\bar{1}0 \rangle$ axis and the $\langle 11\bar{2}0 \rangle$ axis showing orientation in girdles around the $\langle 0001 \rangle$ axis.

Domain C shows a strong orientation of the $\langle 0001 \rangle$ axis to the X axis of the sample, represented by the point maxima in the centre of the pole figure (Figure 5.5C). Correlating with this, the $\langle 10\bar{1}0 \rangle$ and $\langle 11\bar{2}0 \rangle$ axes show variable rotation around the X-axis of the sample, represented on the pole figures by the higher density of data at the edge of the figure compared to the lower densities in the centre.

Pole figures for Domain B show that the $\langle 0001 \rangle$ axis appears to be oriented with the Z axis of the sample, seen through the point maxima at the top and bottom of the figure, and an absence of data across the centre (Figure 5.5B). The $\langle 10\bar{1}0 \rangle$ and $\langle 11\bar{2}0 \rangle$ axes show opposite trends, with girdle structures running across the centre of the figures, particularly in points coloured in shades of red. Quartz grains in this domain therefore have strong orientation of $\langle 0001 \rangle$ axes to the Z axis of the sample, with variable rotation of grains around the $\langle 0001 \rangle$ axis.

In summary, the division into three domains reveals a pattern of orientation in quartz grains across the sample, with $\langle 0001 \rangle$ axes in neighbouring domains oriented at 90° to each other, and the $\langle 10\bar{1}0 \rangle$ and $\langle 11\bar{2}0 \rangle$ axes oriented variably around the $\langle 0001 \rangle$ axis.

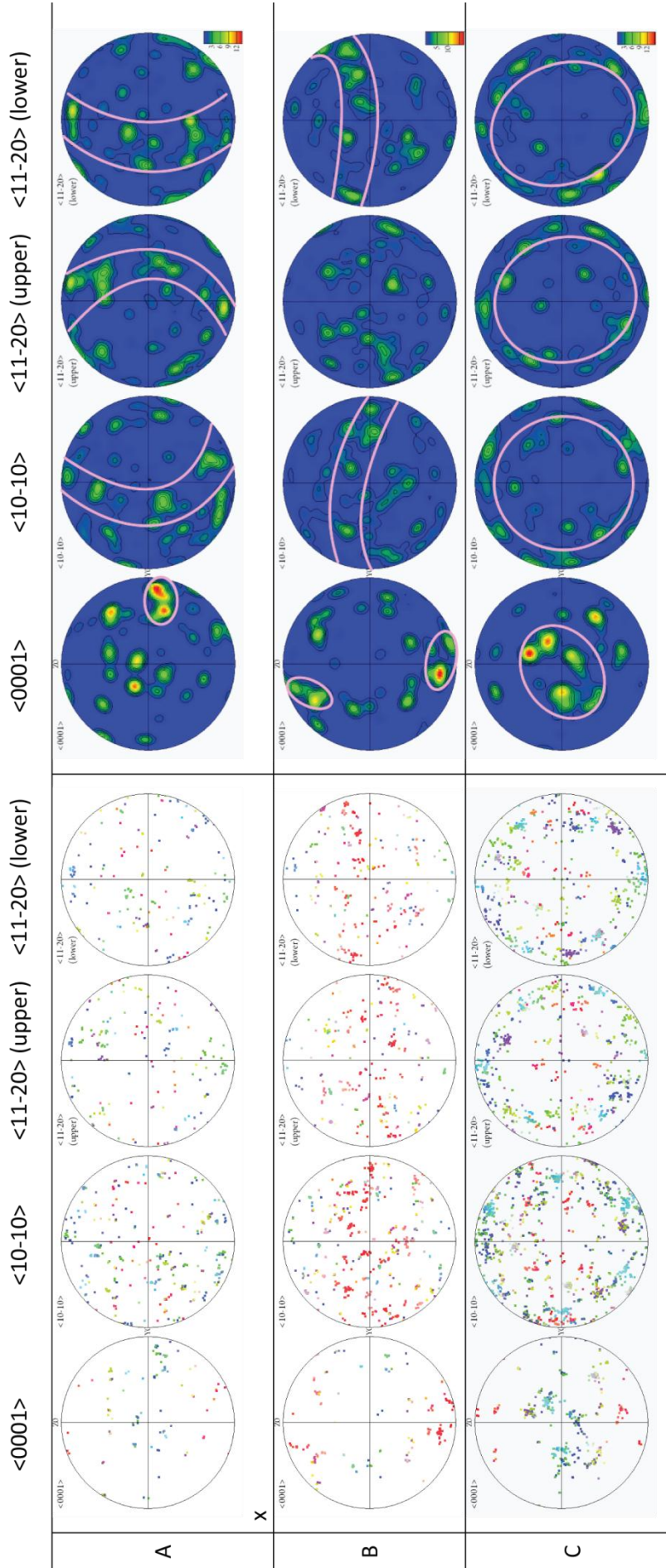


Figure 5.5: Pole figures showing orientation of quartz axes from the three domains in sample W1204. Left to right, the four figures represent the <0001>, <10-10>, and <11-20> (upper and lower) axes, plotted onto equal area, lower hemisphere projections. Scattered data coloured by IPF sample Z colouring (left), and data contoured by colour and contour lines (right), annotated with circles and bands to highlight point maxima and girdles respectively. Pole figures arranged with sample axes Z vertical, Y horizontal and X perpendicular to the page.

W1207g – A banded Quartzite sample

Figure 5.6 shows the phase and band contrast map for sample W1207g. Overall, quartz grains display good quality patterns. Due to poor pattern quality some other minerals were not identified and these are shown in black. Based on the shape of these minerals they are likely to be micas, such as muscovite or biotite, which were removed through the polishing process.

As previously discussed in Chapter 4, the quartzite unit displays banding on a centimetre scale, defined as changes to grain size and mineralogy. Changes to mineralogy are reflected in Figures 5, with the light band on the right dominantly composed of large grained quartz, and the dark band on the left with smaller quartz grains and a more complex mineralogy.

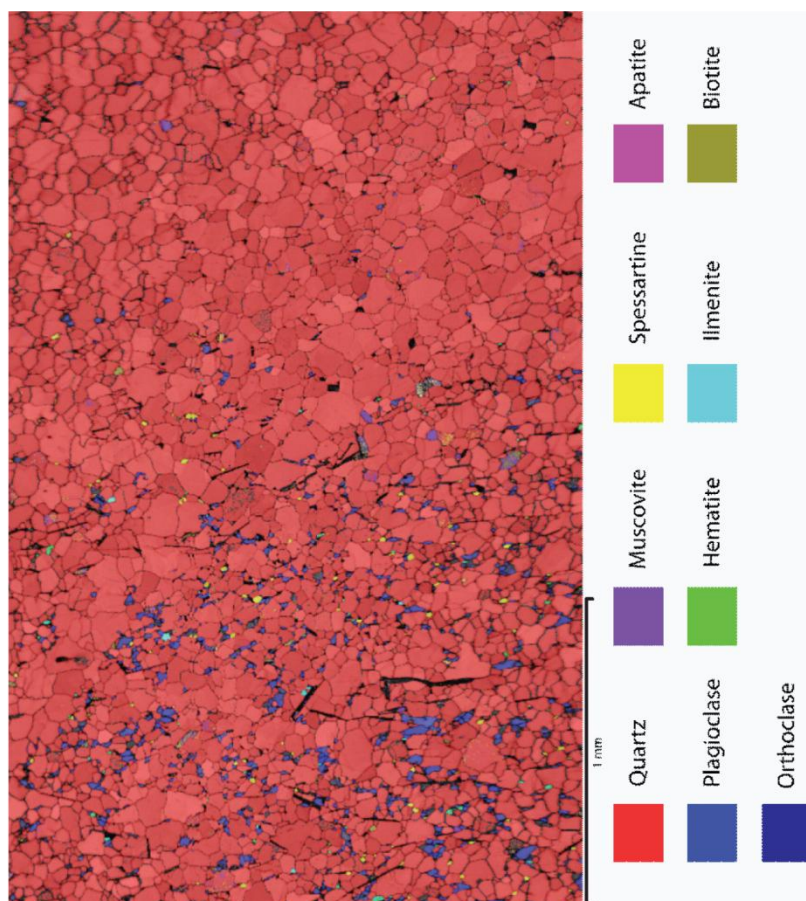


Figure 5.6: Phase and band contrast map for Sample W1207g. Band contrast map shows the pattern quality, with lighter areas corresponding to patterns of higher quality, dark lines represent grain boundaries. Overlain on top of the band contrast map, the phase map is coloured based on mineralogy showing the quartzite is dominantly composed of quartz, with a more complex mineralogy in the darker band (left), including a significant component of feldspars and spessartine garnets.

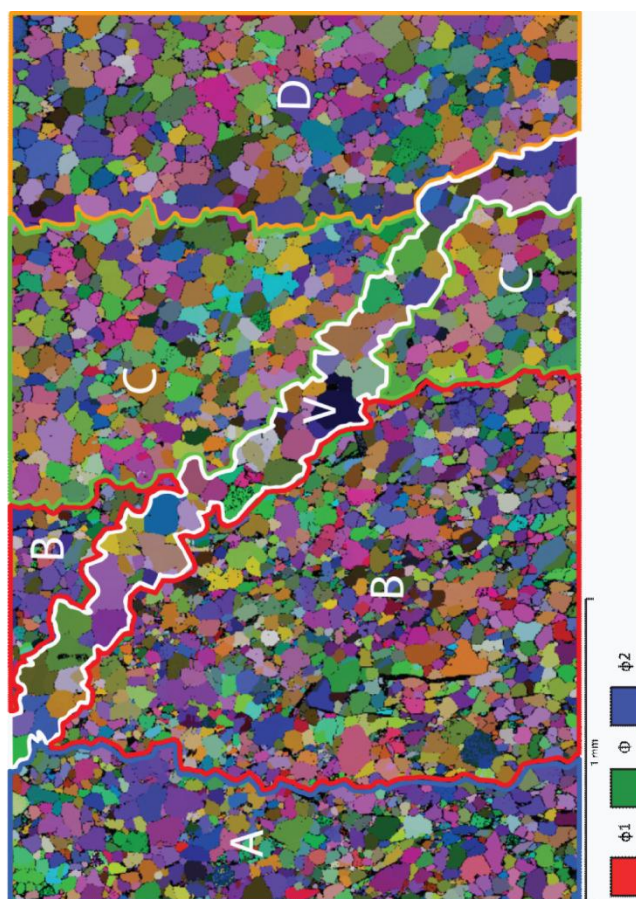


Figure 5.7: Domains of quartz in sample W1207g from the quartzite. Domains are distinguished based on orientation, grain size and the presence of other phases. Map is coloured using the composite of All Euler angles, with colour corresponding to orientation within the sample. Four domains are recognised, outlined in blue, red, green and orange, labeled 'A', 'B', 'C' and 'D' respectively. The small vein in the centre of the map is outlined in white, labeled 'V' and excluded from the domains.

Based on amount of other phases and orientations mapped by All Euler angles, four quartz domains are recognised (Figure 5.7). This has divided both the light band and the dark band into two domains each, as well as a separate domain for the small quartz vein that cross-cuts these bands.

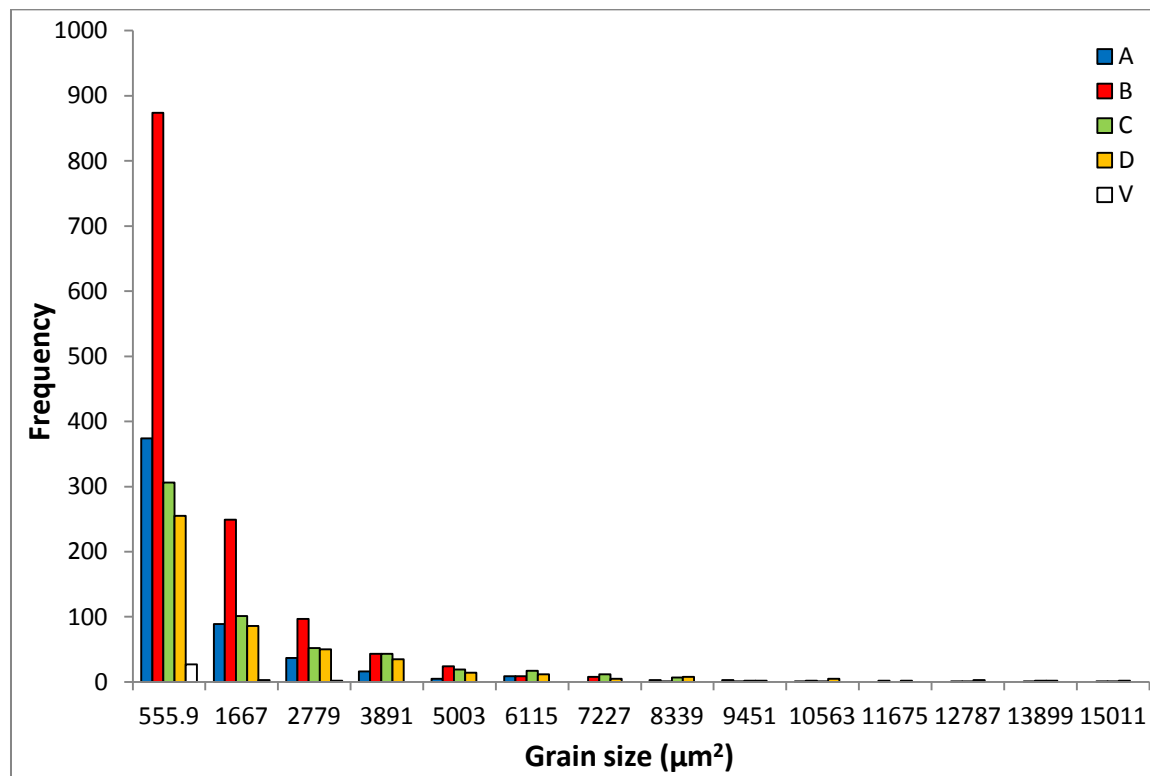


Figure 5.8: Grain size (by area) of the three domains in sample W1207g.

Domains were determined initially by visually determined grain size changes which are here affirmed by grain size statistics (Figure 5.8). Domain A and B show smaller grain sizes, and domains C and D show similar grain size profiles, with larger grains.

Plotting orientations of quartz grains for each of the five domains reveals patterns of preferred orientation, more complex in this sample compared to those in sample W1204 (Figure 5.9).

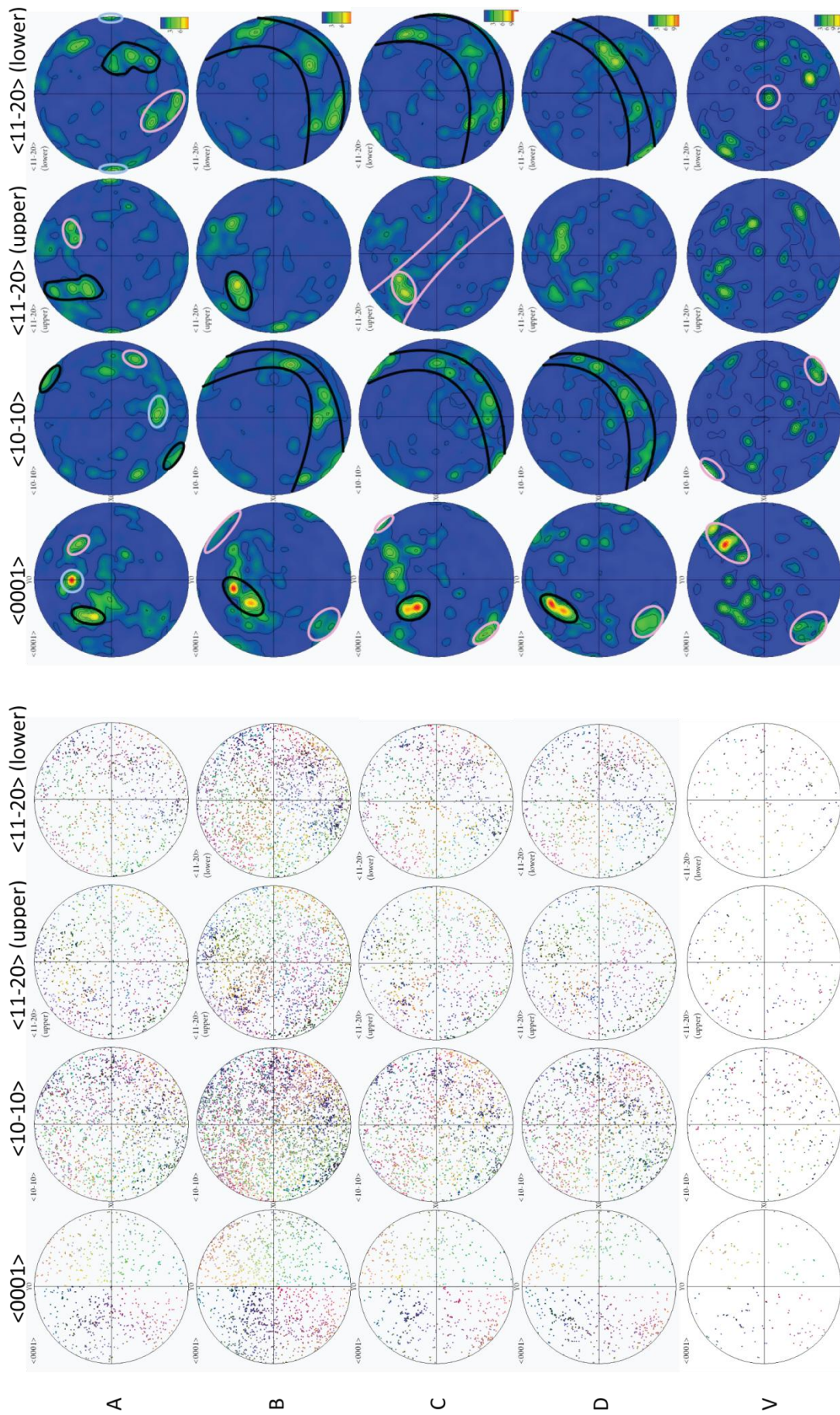


Figure 5.9: Pole figures showing orientation of quartz axes from the three domains in sample W1207g. Left to right, the four figures represent the $\langle 0001 \rangle$, $\langle 10-10 \rangle$, and $\langle 11-20 \rangle$ (upper and lower) axes, plotted onto equal area, lower hemisphere projections. Scattered data coloured by All Euler angles (left), and data contoured by colour and contour lines (right), annotated with circles and bands to highlight point maxima and girdles respectively. Pole figures arranged with sample axes Y vertical, X horizontal and Z perpendicular to the page.

Domains A-D all show similar point maxima for the $\langle 0001 \rangle$ axis, highlighted by black circles on the contoured pole figures (Figure 5.9). Following this, each domain shows varying strength of orientation in the other axes, with domain A showing strongly orientations in the point maxima for both $\langle 10\bar{1}0 \rangle$ and $\langle 11\bar{2}0 \rangle$ pole figures, domains B, C and D showing girdles across both $\langle 10\bar{1}0 \rangle$ and $\langle 11\bar{2}0 \rangle$ axes.

A second preferred orientation across the sample is seen in the contoured pole figures, which show common point maxima on $\langle 0001 \rangle$ plots in domains B, C, D and V (Figure 5.9, pink circles). Plots for the other axes show them to be oriented variably around the $\langle 0001 \rangle$ axis (Figure 5.9, pink circles and bands). This is also seen in domain A, however here it is not as strongly aligned as seen in the other domains. This may be a result of the common orientation being closely aligned to a second orientation in this domain in which the $\langle 0001 \rangle$ axis lies close to the X axis of the sample.

Each domain differs in how variable the orientations are. Domains C and D, from the light band, show stronger and more specific orientations, with points better clustered around the point maxima. Domains A and B, from the dark band, show more smeared orientations, with orientations defined by two or three point maxima aligned closely to each other and data points scattered around them.

In summary, W1207g shows two common orientations throughout the sample, one of which is coincident with the preferred orientation of grains in the small quartz vein within the mapping area. Domains A-D all show differing strength in orientation, domains C and D showing stronger orientations than domains A and B.

Interpretation

Sample W1204 is known to be a quartz vein from field relationships, petrography and now also microstructure. The domains of differing orientations are indicative of episodes of vein growth. Each episode involves the formation of a crack, through which fluids migrate. New vein material crystallises from these fluids, filling up the void created by the crack.

In the case of the boundary between domains B and C, this crack formed at the vein/host rock boundary, tearing off a sliver of wall rock with minerals such as amphiboles and garnets, now forming the wall rock inclusion. New vein material then crystallised in the crack. This process is known as ataxial vein growth.

In comparison, the boundary between domains A and B lacks wall rock material and is indicative of syntaxial growth. It is likely that domain B was once much wider. At some point in time a crack formed through it, through which fluids flowed. Material forming domain A then crystallised from fluids flowing through this crack, in the middle of domain B.

In the case of Sample W1207h from the quartzite unit, contrasting orientations between domains are not as strongly defined. Each domain exhibits two preferred orientations, comparable to the regional cleavage development during D_1 and D_2 . Therefore these two preferred orientations are likely artefacts of regional deformation and recrystallisation of this unit.

Although they are not strong, small differences in the pole figures distinguish each domain from the other. The differences are mainly divided by the strength of the orientation of the $\langle 0001 \rangle$ axis, with domains A and B showing stronger orientations than domains C and D,

which have more smeared data points. Other differences also lie in the strength of orientation through the other two axes.

In comparison, both samples analysed can be divided into domains based on orientation of quartz grains. Analysis of the large quartz vein reveals contrasting orientation changes between domains, representing different episodes of vein growth. Banding in the quartzite can be divided into domains by mapping orientation, but comparing the domains through analysis of pole figures reveals only slight differences. The differences between the domains hint at a possible vein-like crystallisation of material in this unit, however significant recrystallisation post HTLP metamorphism has masked any potential original orientation contrasts.

CHAPTER 6 - GEOCHEMISTRY

PART 1: WHOLE ROCK CHEMISTRY

Introduction

Fluids are important mobile elements within the crust, facilitating mass transfer of soluble material. During migration of fluid, exchange of material can occur with the host rock, resulting in addition or depletion of elements and causing replacement of pre-existing minerals with the growth of new minerals. These chemical changes in an open system are defined as metasomatism.

The exchange of material will be evident through changes to whole rock chemistry. In this way, the presence of fluids and a history of metasomatism can be inferred through changes seen in whole rock chemistry.

Aims

This chapter aims to characterise the whole rock chemistry of the aureole and compare it to values for the Rampsbeck Schists from low-grade areas of the complex in order to examine variations from the regional norm.

Similarly, whole rock chemistry of the quartzite unit will be characterised and compared to published values for quartz-rich rocks (such as quartzites, cherts and oozes) in an attempt to better constrain an origin for the unit.

Analytical Methods

Eleven samples were selected for whole rock chemistry analysis (Table 3.1). These were first processed by using a circular diamond saw to remove weathered and altered surfaces.

Samples were then mechanically crushed using a hammer and a hydraulic press with tungsten carbide plates. The freshest pieces obtained from the crushing were then milled in a TEMA tungsten carbide mill to a very fine, homogenous powder. To avoid contamination between samples, the mill was cleaned using ethanol and purified water before each sample was processed.

XRF

X-Ray Fluorescence (XRF) was used to analyse major and trace elements, conducted at the Mark Wainwright Analytical Centre, at the University of New South Wales, Sydney, Australia. Analyses were performed using a Phillips PW2400 XRF, with an Rh end-window tube.

For major element analysis, sample rock powders were fused with a flux into 40 mm glass discs, at a ratio of 1:10 sample/flux. Calibration was performed using the WROXI standards. Oxides analysed were: SiO₂, TiO₂, Al₂O₃, Fe₂O₃, MnO, MgO, CaO, Na₂O, K₂O, P₂O₅, and SO₃, with results presented in wt% oxide.

LA-ICP-MS

Trace and rare earth element (REE) analyses were conducted using Laser Ablation Inductively Coupled Plasma Mass Spectrometry (LA-ICP-MS) at the Geochemical Analysis Unit (GAU), in the Australian Research Council (ARC) National Key Centre for Geochemical Evolution and Metallogeny of Continents (GEMOC), in the Department of Earth and Planetary Sciences at Macquarie University, Australia.

Rock powders were fused into glass discs, prepared using ~0.5 g of rock powder and ~1.5 g of flux. The discs were stacked and mounted in resin, after which the stack was cut in half to expose sections through all eleven discs on a flat surface, used for analysis.

Samples were analysed using an Agilent 7700 ICP-MS, a quadrupole mass-spectrometer fitted with an Excimer laser for sample ablation. The laser was run at a wavelength of 193 nm, at an intensity of 13.7 J/cm^2 and a frequency of 5 Hz.

Analyses of Rampsbeck Schist samples were performed using spot sizes of 65 μm , and analyses of the quartzite sample with a spot size of 85 μm . All analyses were run with the laser beam rastered at 1 micron per second. Total acquisition time for each run was 180 seconds, with 60 seconds of background measurement and 120 seconds of analysis. Data reduction was performed using GLITTER software. This data is presented in Tables II and IV in Appendix A.

Previous analyses

Previous analyses of Rampsbeck Schist samples for whole rock chemistry were undertaken at the GAU at Macquarie University (Henson, 2000). The same sample preparation techniques as outlined above were employed, with the addition of digestion by hydrofluoric acid in order to homogenise the samples.

XRF analyses were performed on a Siemens SRS XRF Spectrometer, with a gas flow proportional counter detector (containing an argon plasma) and a scintillation detector. Blanks and standards were run before and after the analyses to calibrate the instrument.

Samples for ICP-MS analysis were digested and then placed into solution, in order to be nebulised into the ICP-MS. Analyses were conducted on an Agilent 7500, using an argon plasma at atmospheric pressure. This analysis was performed using procedures and

operating conditions outlined in literature (Norman et al., 1996). Blanks and standards were analysed every 5 samples in order to apply drift corrections. Data reduction was performed using 'GLITTER' software, including drift corrections, memory effects, and background and matrix interferences. Data is presented in Tables V and VI in Appendix A.

A database of whole rock chemistry for quartz-rich rocks has been compiled from published values. Rock types include red cherts (Thurston, 1972, Leggett and Smith, 1980), green cherts (Hara et al., 2010, Thurston, 1972, Swindon, 1976), a bedded chert (Yongzhang et al., 1994), oozes (Wakeel and Riley, 1961, Cressman, 1962), quartzites (Chudy et al., 2008, Makrygina and Suvorova, 2011) and radiolarites (Barrett, 1981, Leoni, 1974, Audley-Charles, 1965). Data is presented in Table VII in Appendix A.

Accuracy and Precision

Standards were measured at the beginning and end of the runs for calibration, measurement of sensitivity and for the application of a drift correction. Presented in Table 6.1.1 are observed measurements compared to published values (Wilson, 1997, Norman et al., 1996) for the standards NIST610 and BCR-2, which are representative of the accuracy and precision of analyses performed on the LA-ICP-MS. Analyses of all standards are presented in Appendix A in Tables I and III.

The standard NIST610 shows relatively consistent results between the expected and observed values from analyses during the run, and was used for the application of a drift correction performed using GLITTER software. The standard BCR-2 shows greater variation in the accuracy of element concentrations using one standard deviation, with 16 elements falling outside the range of accepted values. Comparing these values using two standard deviations increases the relative accuracy, with only 4 elements (Cr, Fe, P and Rb) falling outside accepted values.

Table 6.1.1: Published and observed concentrations (ppm) of two standards analysed by LA-ICP-MS.

Element	NIST610				BCR-2				
	Expected	Observed	1 sigma	Within range	Expected	1 sigma	Observed	1 sigma	Within range
Al	10053.47	10120.62	314.96	Yes	71400	1000	77729.2	2421.09	No
Ba	446	446.75	13.51	Yes	683	28	678.23	21.36	Yes
Be	460.7	465.26	15.61	Yes	-	-	-	-	-
Ca	81905.31	82079.05	2490.31	No	50900	800	51276.72	1562.23	Yes
Ce	446	445.94	13.43	Yes	53	2	50.44	1.54	Yes
Co	388	389.91	11.95	Yes	37	3	32.41	1.02	No
Cr	388	386.57	11.8	Yes	18	2	32.28	1.35	No
Cs	361	360.66	11.05	Yes	1.1	0.1	0.88	0.046	No
Cu	432.9	433.68	13.23	Yes	19	2	16.16	0.6	No
Dy	453	457.03	14.5	Yes	-	-	-	-	-
Er	463	467.15	14.73	Yes	-	-	-	-	-
Eu	452	453.92	13.94	Yes	2	0.1	2.039	0.09	Yes
Fe	453.1	462.12	17.03	Yes	96600	1500	66663.61	2449.05	No
Ga	431	431.67	13.01	Yes	23	2	20.45	0.67	No
Gd	450	452.08	13.83	Yes	6.8	0.3	6.86	0.32	Yes
Hf	458	462.69	14.79	Yes	4.8	0.2	5.16	0.22	Yes
Ho	475	478.78	14.94	Yes	1.33	0.06	1.367	0.06	Yes
K	463.1	461.96	14.04	Yes	14900	400	13632.46	414.31	No
La	440	440.82	13.33	Yes	25	1	25.29	0.79	Yes
Lu	467	470.95	14.77	Yes	0.51	0.02	0.529	0.03	Yes
Mg	455	456.69	13.95	Yes	21600	300	20174.72	613.87	No
Mn	436.4	439.31	13.58	Yes	28	2	30.38	1.03	Yes
Na	97190.21	96770.89	2945.76	No	23400	800	20764.33	632.38	No
Nb	512	513.38	15.65	Yes	-	-	-	-	-
Nd	454	454.36	13.7	Yes	-	-	-	-	-
Ni	415	415.72	13	Yes	-	-	-	-	-
P	342.5	343.46	15.15	Yes	1500	100	1182.91	52.34	No
Pb	419.1	419.6	12.66	Yes	11	2	8.89	0.3	Yes
Pr	468	470.57	14.46	Yes	6.8	0.3	7.21	0.24	Yes
Rb	430	429.4	12.96	Yes	48	2	40.9	1.27	No
Sc	450	452.8	14	Yes	33	2	35.66	1.14	Yes
Si	334048	334048.1	10564.55	Yes	253000	4000	252884.7	8001.71	Yes
Sm	463	466.84	14.66	Yes	6.7	0.3	7.01	0.33	Yes
Sr	525	525.74	15.93	Yes	346	14	338.71	10.66	Yes
Ta	490.6	496.26	16.12	Yes	-	-	-	-	-
Tb	442	445.16	13.79	Yes	1.07	0.04	0.926	0.045	No
Th	481	484.38	15.02	Yes	6.2	0.7	6.29	0.22	Yes
Ti	476	478.19	14.78	Yes	13500	300	14828.09	455.86	No
Tm	454	458.84	14.7	Yes	0.54	-	0.523	0.03	No
U	487	486.23	14.63	Yes	1.69	0.19	1.63	0.063	Yes
V	444	441.18	13.64	Yes	416	14	398.16	12.34	Yes
Y	490	492.62	15.14	Yes	37	2	34.7	1.1	Yes
Yb	479	483.9	15.55	Yes	3.5	0.2	3.72	0.2	Yes
Zn	429.3	430.49	13.15	Yes	127	9	124.62	3.95	Yes
Zr	490	493.59	15.47	Yes	188	16	201.73	6.39	Yes

Results

Major, trace and REE concentrations from XRF analysis of 11 samples are presented in Tables 6.1.2 and 6.1.3. Samples from the schist are similar in composition, with high SiO₂ (63.42 – 66.76 wt%), moderate Al₂O₃ (14.51 – 16.97 wt%) and K₂O values systematically higher than Na₂O values. In contrast to this, the composition of the quartzite unit is dominantly SiO₂ (91.73 wt%), with minor amounts of Al₂O₃ (2.37 wt%). The quartzite unit also has relatively high concentrations of MnO (0.31 wt%) compared to the schists (0.06 – 0.18 wt%). Schists have varied trends in trace and rare earth element compositions, being similar in concentrations of elements such as La and Eu, but showing great variation in elements such as Ba, Cu and Ni. The quartzite unit has heavy trace and rare earth element values an order of magnitude smaller than those of the schists, however it is more enriched in lighter elements such as Ni and Co.

Table 6.1.2: Major element results from XRF analysis of representative samples of quartzite (W1207e) and Rampsbeck Schists. Data presented in wt%.

Sample	W1207e	W1219	W1218	W1201	W1229	W1223a	W1216	W1215	W1214b	W1213	W1211a
Distance to quartzite (km)	0.00 (quartzite)	0.02	0.03	0.03	0.05	0.07	0.08	0.15	0.18	0.35	0.52
SiO ₂	91.73	65.2	65.91	65.3	65.29	66.76	65.17	63.58	66.62	64.00	63.42
TiO ₂	0.06	0.76	0.73	0.73	0.71	0.56	0.71	0.79	0.76	0.75	0.81
Al ₂ O ₃	2.37	15.49	15.28	15.70	15.62	14.51	15.73	16.16	15.15	16.29	16.97
Fe ₂ O ₃	0.79	5.77	5.36	5.78	6.02	5.74	5.57	6.59	5.26	6.29	6.10
MnO	0.31	0.10	0.08	0.08	0.06	0.12	0.07	0.18	0.09	0.10	0.12
MgO	0.71	2.12	1.87	1.92	2.31	2.12	2.02	2.26	1.78	2.07	2.15
CaO	0.11	2.56	1.02	1.04	0.64	0.73	1.39	1.36	2.06	1.28	0.93
Na ₂ O	0.48	3.12	3.16	3.13	1.08	1.96	3.10	2.47	3.27	2.91	2.14
K ₂ O	0.50	2.93	3.71	3.91	5.16	4.49	4.06	4.43	3.31	3.96	4.69
P ₂ O ₅	0.03	0.16	0.17	0.16	0.12	0.10	0.15	0.14	0.27	0.14	0.15
SO ₃	< 0.01	< 0.01	< 0.01	< 0.01	0.15	< 0.01	0.12	0.04	0.17	< 0.01	0.09
L.O.I.	0.0377	0.1106	0.1196	0.1318	0.1021	0.1207	0.0796	0.1144	0.0776	0.1131	0.1484
TOTAL	97.09	98.21	97.29	97.75	97.16	97.09	98.09	98.00	98.74	97.79	97.57

Loss on ignition (L.O.I.) at 1050°C. Concentrations below the lower limit of detection (LLD) are reported here with the symbol < next to the LLD value.

Table 6.1.3: Averaged trace and rare earth element data from LA-ICP-MS analysis of representative samples of quartzite (W1207e, n=4) and Rampsbeck Schists (n=2). Data presented in ppm.

Sample Distance to quartzite (km)	W1207e	W1219	W1218	W1201	W1229	W1223a	W1216	W1215	W1214b	W1213	W1211a
	0.00	0.02	0.03	0.03	0.05	0.07	0.08	0.15	0.18	0.35	0.52
⁹ Be	1.39	3.14	4.41	2.90	2.31	3.43	3.36	2.17	1.96	3.51	3.38
⁴⁵ Sc	6.53	19.28	17.74	18.39	17.52	15.00	17.14	19.64	19.35	19.15	20.04
⁵¹ V	43.20	111.51	101.44	108.65	118.85	93.36	93.55	125.26	110.19	118.24	122.68
⁵³ Cr	35.41	53.79	50.20	72.54	75.82	48.74	48.53	69.93	91.03	77.04	87.44
⁵⁹ Co	85.19	30.57	32.63	33.01	38.28	43.71	22.22	23.26	32.84	41.86	14.37
⁶⁰ Ni	59.86	32.73	31.55	70.65	38.38	37.11	35.50	66.75	99.52	66.68	84.80
⁶² Ni	55.74	33.74	31.92	69.49	37.51	37.87	34.23	67.94	100.04	67.13	80.56
⁶³ Cu	7.53	31.39	8.55	23.59	23.48	13.44	13.38	25.18	63.47	23.61	15.98
⁶⁵ Cu	7.27	32.74	8.51	24.60	24.67	13.91	13.51	25.05	64.17	24.86	16.37
⁶⁶ Zn	41.48	105.55	91.77	103.42	97.35	100.46	95.01	105.49	92.19	100.57	95.26
⁶⁹ Ga	7.21	112.81	81.87	88.07	87.85	72.05	56.44	58.67	50.11	66.37	95.41
⁷¹ Ga	3.62	20.04	20.12	19.82	20.81	20.08	20.20	21.16	19.03	20.27	22.96
⁸⁵ Rb	20.77	129.22	114.61	112.35	176.35	187.23	134.17	144.78	136.37	123.54	142.57
⁸⁶ Sr	21.24	163.43	158.10	162.07	75.47	127.91	187.97	168.30	183.90	198.69	138.81
⁸⁸ Sr	17.13	166.14	163.65	168.88	79.62	130.00	184.85	170.82	187.16	200.31	142.09
⁸⁹ Y	2.46	32.40	30.95	31.83	25.91	25.88	28.30	31.64	34.25	29.18	31.40
⁹⁰ Zr	13.45	164.87	176.68	172.94	153.22	158.12	188.02	177.68	173.62	176.03	190.79
⁹³ Nb	1.64	12.14	11.94	12.77	16.38	11.74	12.32	13.77	12.49	13.13	13.54
¹³³ Cs	1.68	24.95	16.53	6.35	8.84	13.93	8.26	11.64	8.45	19.02	7.77
¹³⁷ Ba	63.85	1382.59	949.93	1000.11	1011.25	788.82	561.30	586.60	493.32	697.14	1069.58
¹³⁸ Ba	62.27	1370.12	940.90	983.47	1017.68	790.10	554.96	580.42	492.06	683.50	1062.42
¹³⁹ La	3.78	27.31	28.94	30.74	27.33	29.67	28.32	29.28	32.00	28.56	29.51
¹⁴⁰ Ce	13.52	56.15	61.56	65.07	59.12	62.80	59.86	63.06	64.97	61.38	64.52
¹⁴¹ Pr	0.87	7.03	7.65	8.19	6.92	7.29	7.32	7.87	7.94	7.43	7.95
¹⁴⁶ Nd	3.48	27.56	30.80	32.33	27.47	28.46	30.35	30.87	31.84	29.09	31.66
¹⁴⁷ Sm	0.76	5.54	6.54	6.57	5.69	5.60	6.04	6.48	6.42	6.19	6.77
¹⁵³ Eu	0.15	1.55	1.32	1.39	1.19	1.18	1.34	1.35	1.44	1.19	1.26
¹⁵⁷ Gd	0.65	5.20	5.17	6.05	4.96	4.75	5.58	5.79	5.75	5.65	5.67
¹⁵⁹ Tb	0.08	0.81	0.86	0.89	0.71	0.78	0.82	0.85	0.91	0.77	0.96
¹⁶¹ Dy	0.60	5.84	5.37	5.95	4.69	5.14	4.95	5.62	5.43	5.36	5.74
¹⁶⁵ Ho	0.12	1.11	1.09	1.17	0.92	1.04	1.05	1.18	1.22	1.05	1.16
¹⁶⁷ Er	0.32	3.28	3.21	3.26	2.63	2.71	3.22	3.19	3.33	2.98	3.28
¹⁶⁹ Tm	0.04	0.47	0.50	0.50	0.39	0.41	0.41	0.43	0.50	0.44	0.50
¹⁷³ Yb	0.33	3.51	3.36	3.31	2.84	3.15	3.04	3.11	3.84	2.86	3.45
¹⁷⁵ Lu	0.06	0.52	0.49	0.52	0.42	0.45	0.45	0.51	0.49	0.46	0.48
¹⁷⁸ Hf	0.46	4.46	4.78	4.76	4.15	4.22	5.20	4.74	4.43	4.77	5.27
¹⁸¹ Ta	0.94	1.11	1.20	1.31	1.52	1.35	1.16	1.19	1.09	1.52	1.10
²⁰⁸ Pb	5.04	19.42	20.56	21.15	20.26	23.08	19.46	20.51	16.00	18.91	14.73
²³² Th	1.44	11.66	11.65	12.60	13.65	12.28	12.16	12.13	11.16	12.82	13.48
²³⁸ U	1.05	2.97	3.08	3.26	2.54	2.48	2.78	2.64	3.39	2.83	2.60

Rampsbeck Schists

Data for the 10 samples of Rampsbeck Schists have been plotted against distance from the quartzite, with a conservative uncertainty of $\pm 5\%$ (Figure 6.1.1). With distance SiO_2 values are within uncertainty of each other, showing a range of ~ 3 wt%. Oxides such as MnO , TiO_2 and K_2O show weak trends of increasing concentrations with distance. Proximal to the quartzite (in the first ~ 200 m) this trend is not well defined, with wider spread of data.

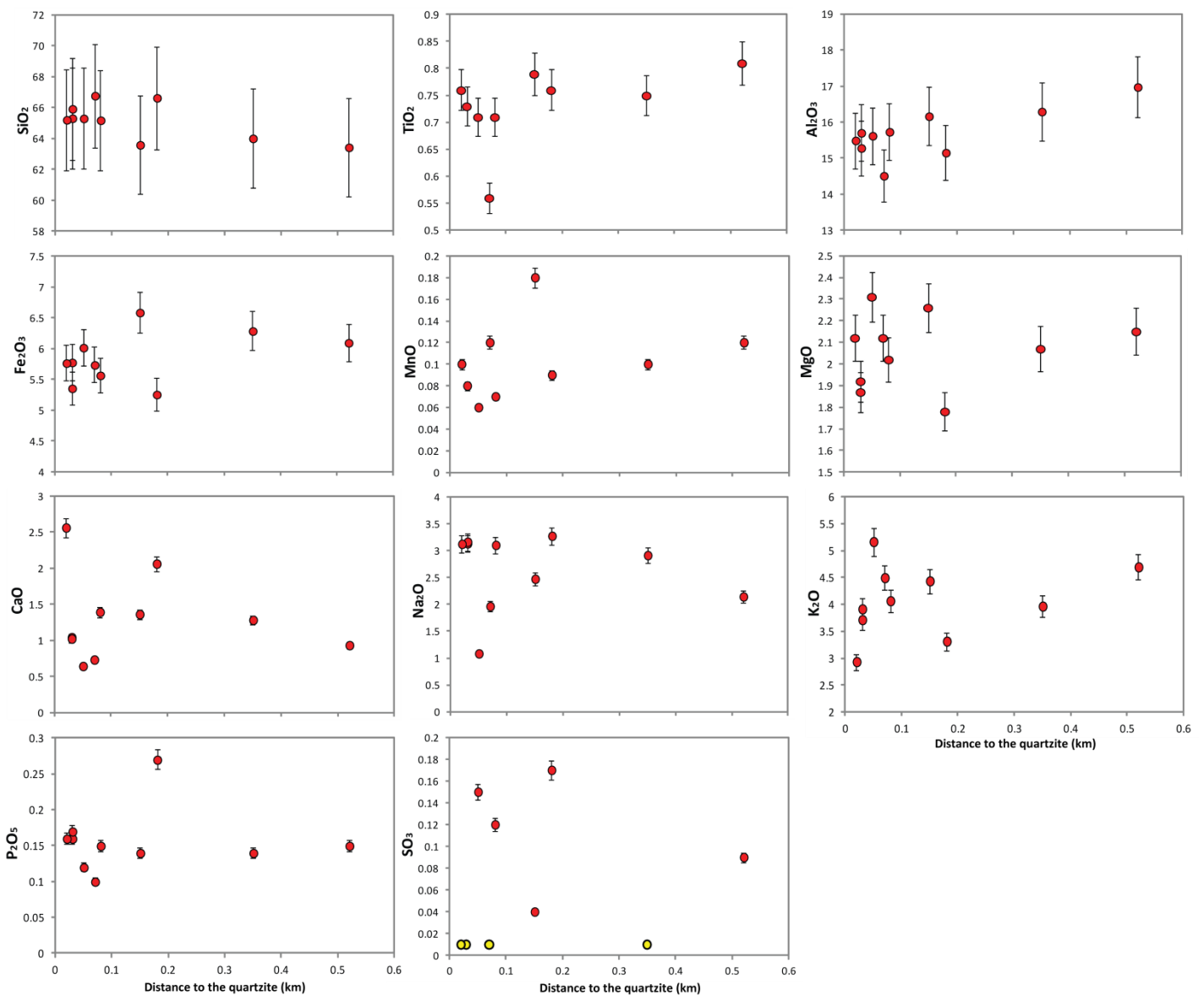


Figure 6.1.1: Major element chemistry of ten Rampsbeck Schist samples from the aureole. Oxide is plotted on the y-axis in wt%, against distance from the quartzite on the x-axis. Data points have 5% error bars. Data points in yellow represent a result less than the lower limit of detection.

Results for oxides such as Na_2O and Fe_2O_3 show no obvious trends, with samples variably spread through the range of values.

Major element abundances differ between samples however these changes do not appear to be strongly correlated to spatial distribution.

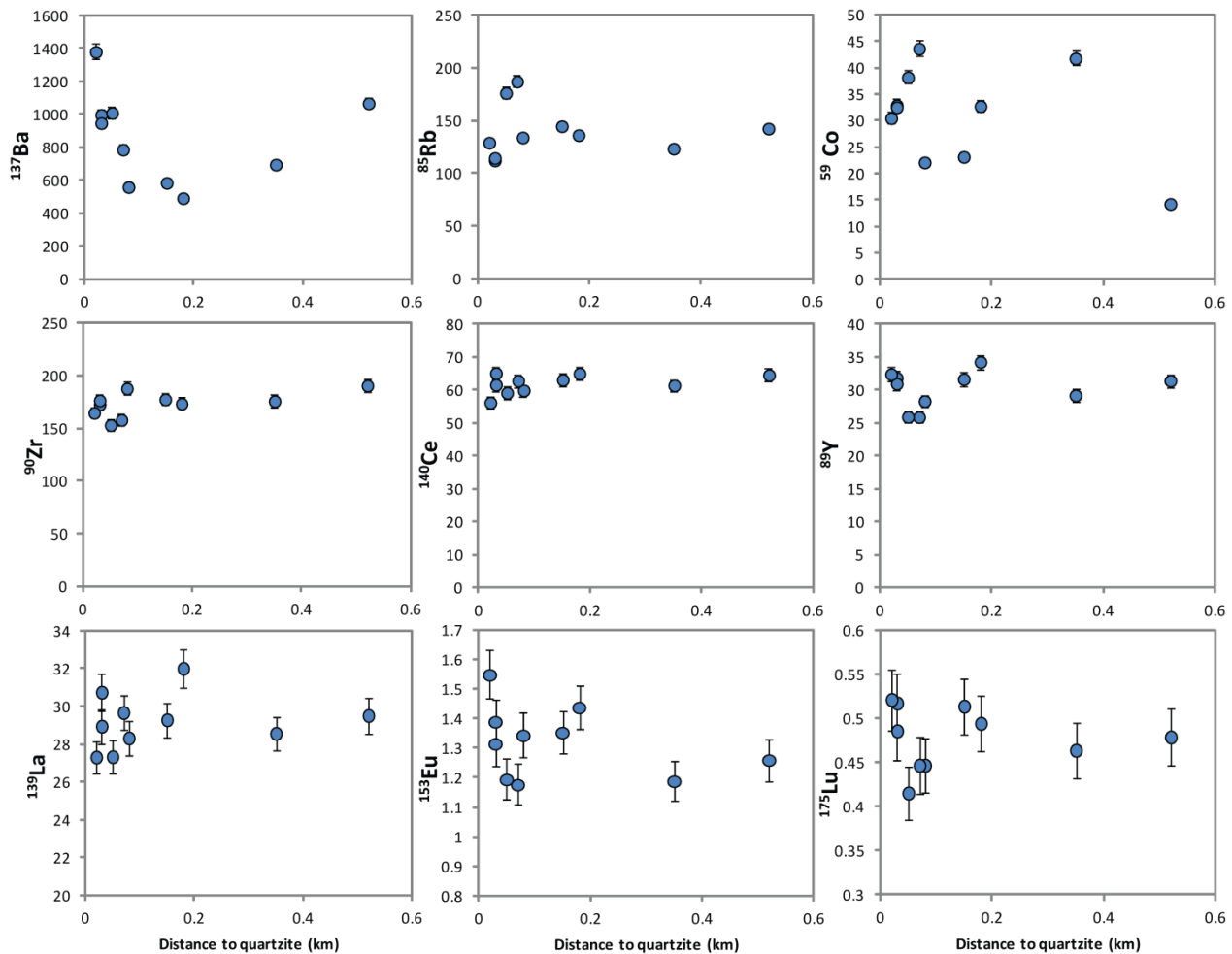


Figure 6.1.2: Representative graphs of trace and rare earth element data of ten Rampsbeck Schist samples. Plotted by distance from the quartzite unit on the x-axis (km) and element abundance on the y-axis (ppm), with 1 sigma error bars. On some data points, error is encompassed by the symbol.

Trace element data show similar relationships when plotted against distance from the quartzite (Figure 6.1.2). Representative elements are presented here, to characterise trace and rare earth element abundance through the aureole.

Graphs of Rb, Ba and Co show three typical trends in abundance. The top three graphs in Figure 6.1.3 show these three typical trends in trace element data: (1) element abundance highest in the most distal sample, initially decreasing towards the quartzite and then increasing within the ~100 m proximal to the quartzite, displayed by Ba; (2) element abundance relatively equal throughout the aureole, with some spread close to the quartzite as displayed by Rb; and (3) a wide spread in elemental abundance with no obvious spatial relationship as displayed by Co.

Accessory phases in the Rampsbeck Schists include zircon, monazite and xenotime.

Graphing the major cations from these phases (Zr, Ce and Y respectively) reveals similar trends in these cations to that shown by Rb, with similar concentrations throughout the aureole and some spread in data proximal to the quartzite (Figure 6.1.2).

Representative REE plots are shown in the bottom of Figure 6.1.2. No obvious spatial trends are observed, with values showing spread close to the quartzite and the two most distal samples within range of each other.

Comparison with previous analyses

In order to examine any changes that have occurred, the whole rock chemistry of the aureole is compared with that of a 'background' signal, representative of the protolith. The whole rock chemistry of the WMC was characterised in a previous honours study (Henson, 2000). The background signal has been constructed using analyses performed on low grade rocks from this suite of data, excluding those with anomalous results. An average was taken from these analyses (three from the Girrikool Beds, seven from the Transitional Schists and six from the Low Grade Rampsbeck Schists) and data obtained in this study was normalised to these values (Figure 6.1.3).

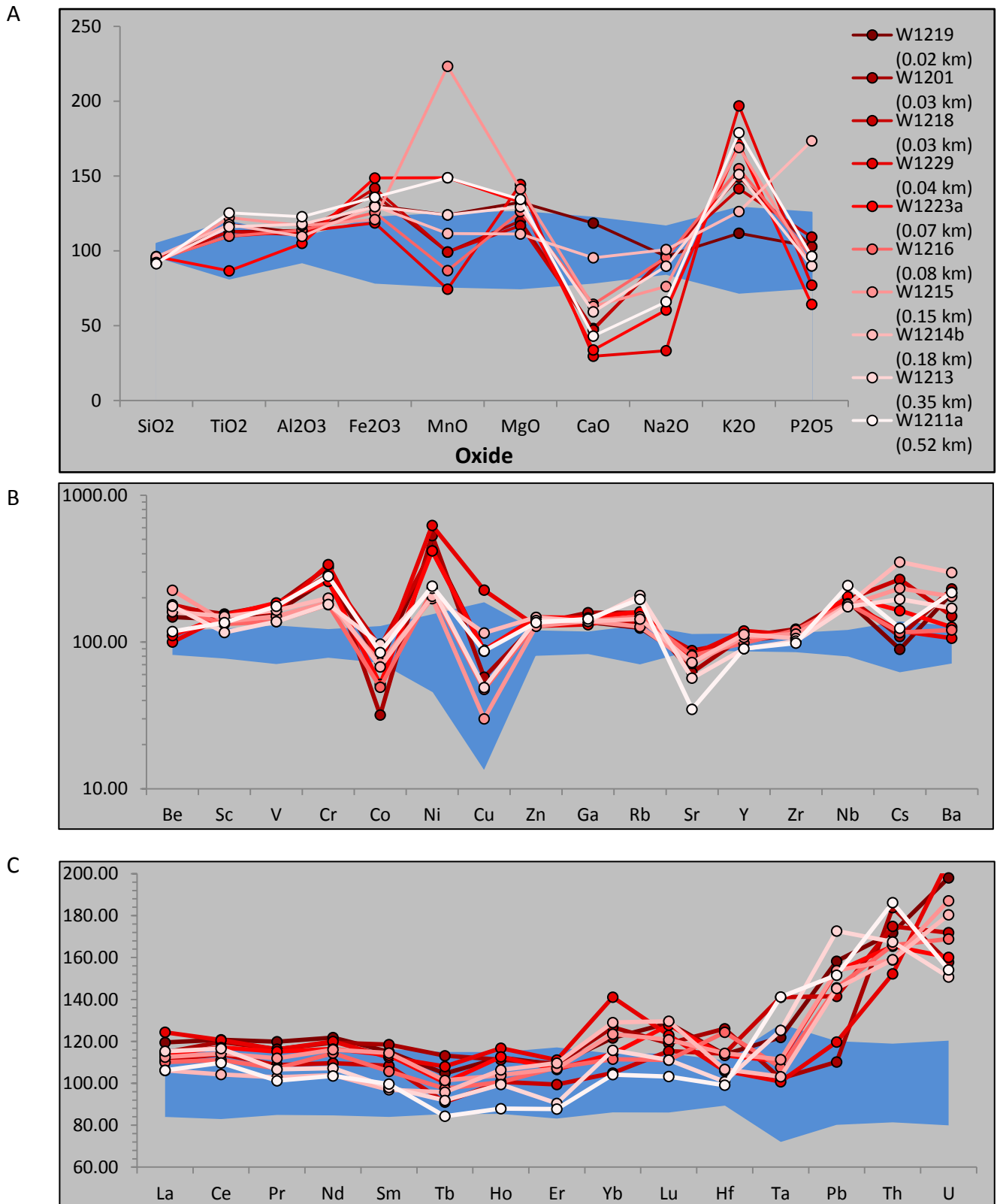


Figure 6.1.3: Major (A), trace (B) and rare earth element (C) spidergrams of ten representative Rampsebeck Schist samples from the aureole, normalised to a background signal represented by the blue field (mean \pm 1sd). Samples colour coded by distance from the quartzite, with the sample coloured in the strongest red closest to the quartzite and the sample coloured white furthest from the quartzite.

Significant changes to bulk rock chemistry have occurred within the aureole, through the depletion of SiO_2 , CaO , Na_2O and P_2O_5 , and the enrichment of TiO_2 , Al_2O_3 , Fe_2O_3 , MnO , MgO and K_2O compared to regional values (Figure 6.1.3A). Trace elements also show variation from the regional average, particularly through enrichment in Cr, Ni and Cs (Figure 6.1.3B). The light and mid-REE are within the regional average range, however heavy REE are enriched, particularly U, Pb and Th (Figure 6.1.3C). Rare earth elements appear to show some spatial trends, seen best in the lighter elements (Figure 6.1.3C), although when graphed against distance (Figure 6.1.2) these trends are shown to be weak.

There appears to be no general trends with distance from the quartzite as samples show varied changes throughout the aureole. This is demonstrated by results for P_2O_5 , where the sample closest to the quartzite sits next to a sample from the edge of the aureole within the background signal range, and sample W1223c (0.07 km from the quartzite) shows the highest depletion in P_2O_5 (Figure 6.1.3).

Although there are no obvious spatial trends, samples do tend to show a pattern in terms of the degree of enrichment or depletion of major elements. Because of the large variation in values, this is demonstrated best in the results for calcium and potassium oxides. The sample most depleted in calcium oxide (W1229) is also the sample most enriched in potassium oxide. Similarly, sample W1219 is the least depleted in calcium oxide, and the least enriched in potassium oxide. Other samples follow similar patterns between these two oxides, as well as in calcium oxide values.

Due the wide spread of values, and the pattern in sample distribution through major element values, calcium depletion and potassium enrichment can be used as indicators of the degree of chemical changes a sample has undergone. A proxy has been constructed by

dividing K_2O by CaO in order to obtain a value representative of the degree of chemical changes in a sample (Table 6.1.4), where a high proxy value signifies high chemical change relative to the general regional Rampsbeck schist composition. As samples show no obvious trends with distance from the quartzite (Figure 6.1.4), this proxy will be used when comparing other properties of the samples in order to look for trends.

Table 6.1.4: Proxy for comparing the degree of chemical changes between samples of Rampsbeck Schists in the aureole. The higher the proxy the higher the chemical change relative to the regional Rampsbeck schist composition.

Sample	Proxy
W1219	1.14
W1201	3.76
W1218	3.64
W1229	8.06
W1223a	6.15
W1216	2.92
W1215	3.26
W1214b	1.61
W1213	3.09
W1211a	5.04

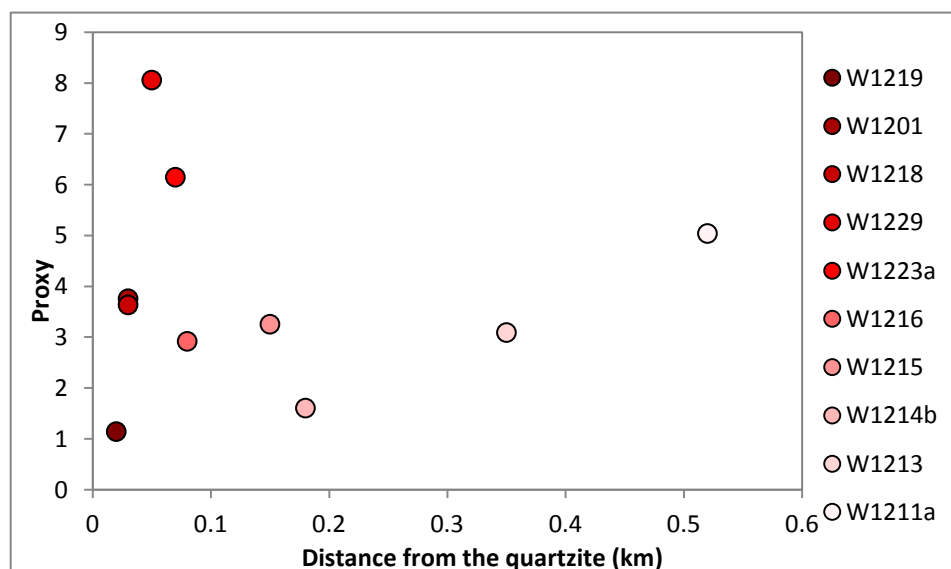


Figure 6.1.4: Proxy for the degree of chemical change within a sample against distance of the sample from the quartzite. Samples colour coded by distance from the quartzite, with the sample coloured in the strongest red closest to the quartzite and the sample coloured white furthest from the quartzite.

Quartzite

Whole rock chemistry of the quartzite unit is vastly different to that of the Rampsbeck Schists, both in major element abundance, as well as trace and rare earth element patterns (Tables 6.1.2 and 6.1.3).

Throughout the major, trace and rare earth element abundances, the quartzite shows similar patterns of enrichment and depletion to those in the schists, but with most elements occurring at concentrations lower by approximately an order of magnitude (Figure 6.1.5). In particular, the quartzite has high potassium values and lower calcium values, consistent with the pattern in the schists and the parameters used to construct the proxy above. Silica dominates the chemistry of the quartzite however manganese is present in a high concentration compared to that of the schists.

Trace elements in the quartzite mostly follow similar patterns to those in the schists, except for elements between Co and Cu (Figure 6.1.5). These elements fall either within, or on the border of, the Rampsbeck Schist field, indicating enrichment relative to other elements within the quartzite. In the schists, the ranges of concentrations for these elements are comparatively larger than those for other elements, indicating variable enrichment throughout the aureole.

REE patterns in the quartzite are also very similar to those in the schists, following the saw-tooth like pattern (Figure 6.1.5). The heavy REE are enriched in the schists (Figure 6.1.3C) and this pattern is also seen in the quartzite, particularly in Ta.

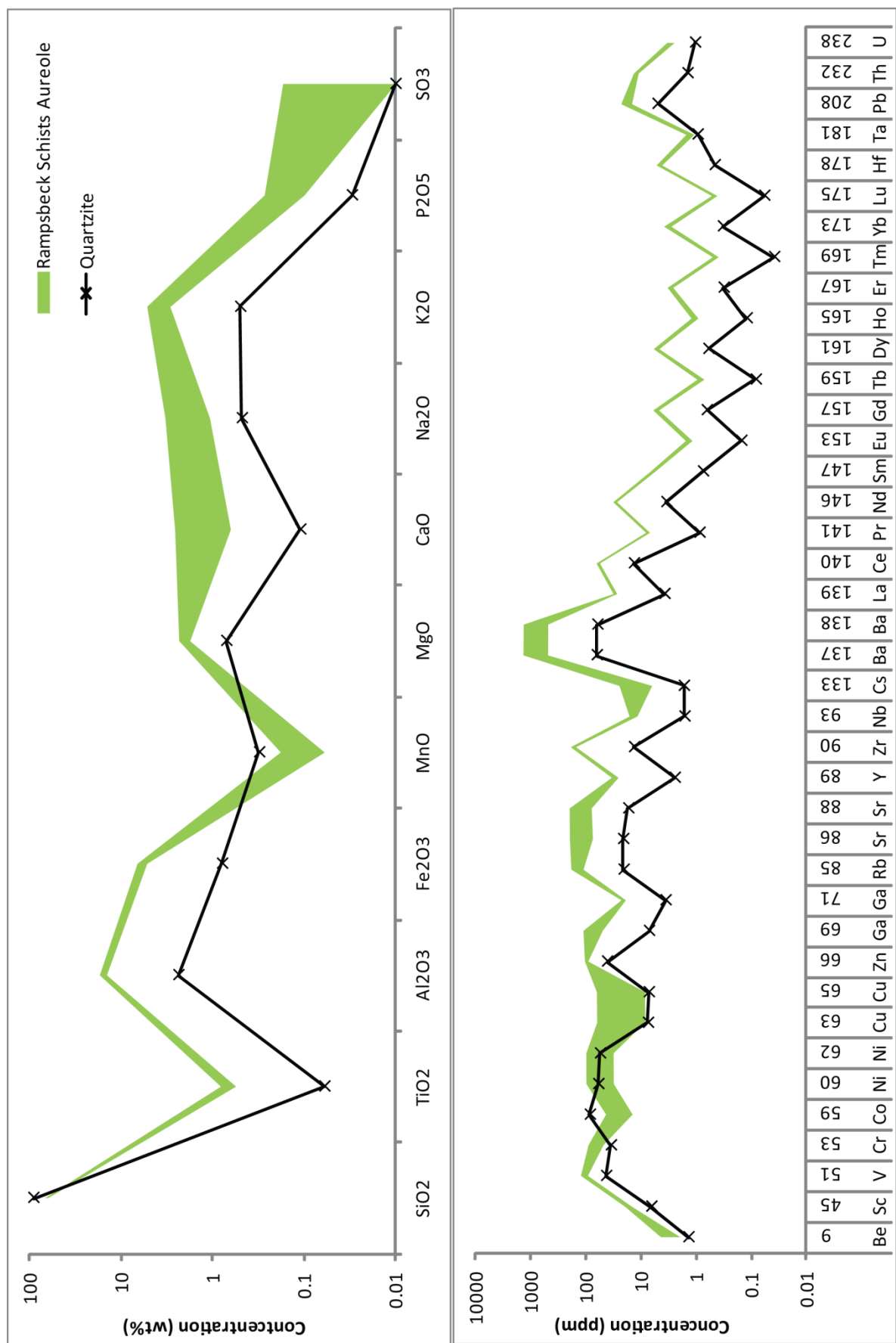


Figure 6.1.5: Comparison on the major (top), trace and rare earth element compositions of the quartzite and Rampsebeck Schists of the aureole. On the x-axes are the elements analysed, and they y-axes show concentration on a logarithmic scale. The green field represents the range of values in the ten samples analysed from the aureole.

Chemical studies of the quartzite present in the region have not been previously performed, and so these initial results will be used as an overview to characterise this unit in comparison to other quartz-rich rocks known from literature.

Excluding SiO_2 , major element oxides show some patterns based on rock type (Figure 6.1.6). Both oozes (blue) and quartzites (i.e. metamorphosed sandstone, purple) show comparatively higher abundances of major elements, with oozes rich in magnesium and quartzites rich in calcium. Radiolarites (yellow) follow similar trends to each other, generally plotting with the smallest values. Red cherts show high iron values, green cherts are spread variably throughout the data range.

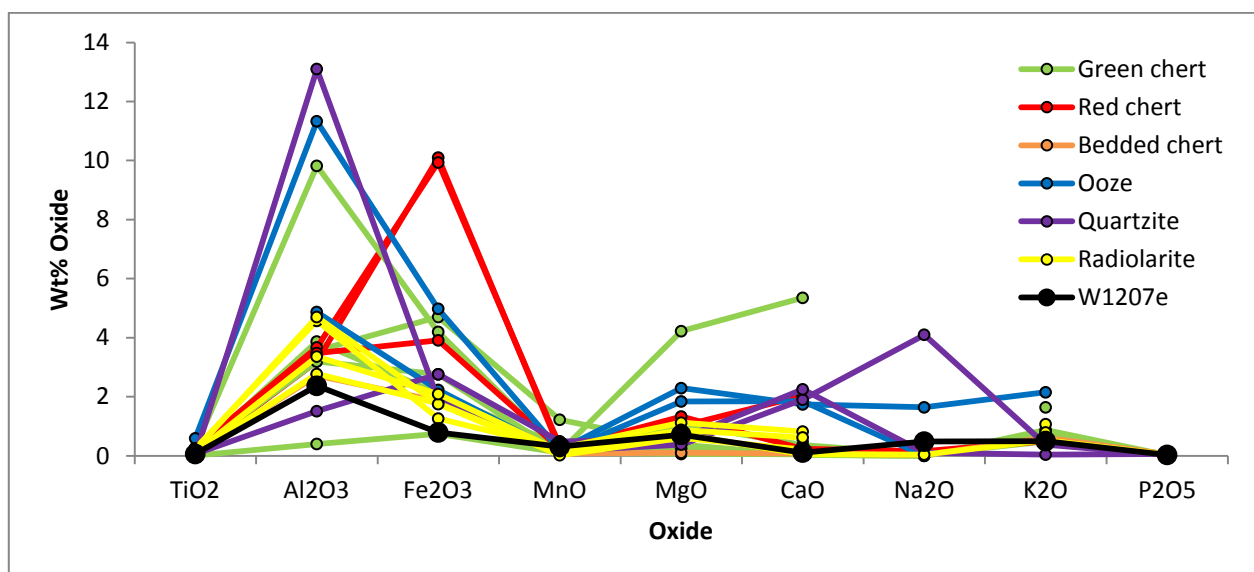


Figure 6.1.6: Major element spidergram for whole rock chemistry analysis of quartz-rich rocks. Data is colour coded by rock type; sample W1207e from this study is black.

Sample W1207e from this study (plotted in black) shows similar patterns to those of the radiolarites, plotting with low values for major elements, however due to the spread throughout the graph, it is not possible to define specific fields and designate a range of values of major elements for each rock type. Therefore, based on major element abundance patterns W1207e cannot be confidently grouped with any rock type.

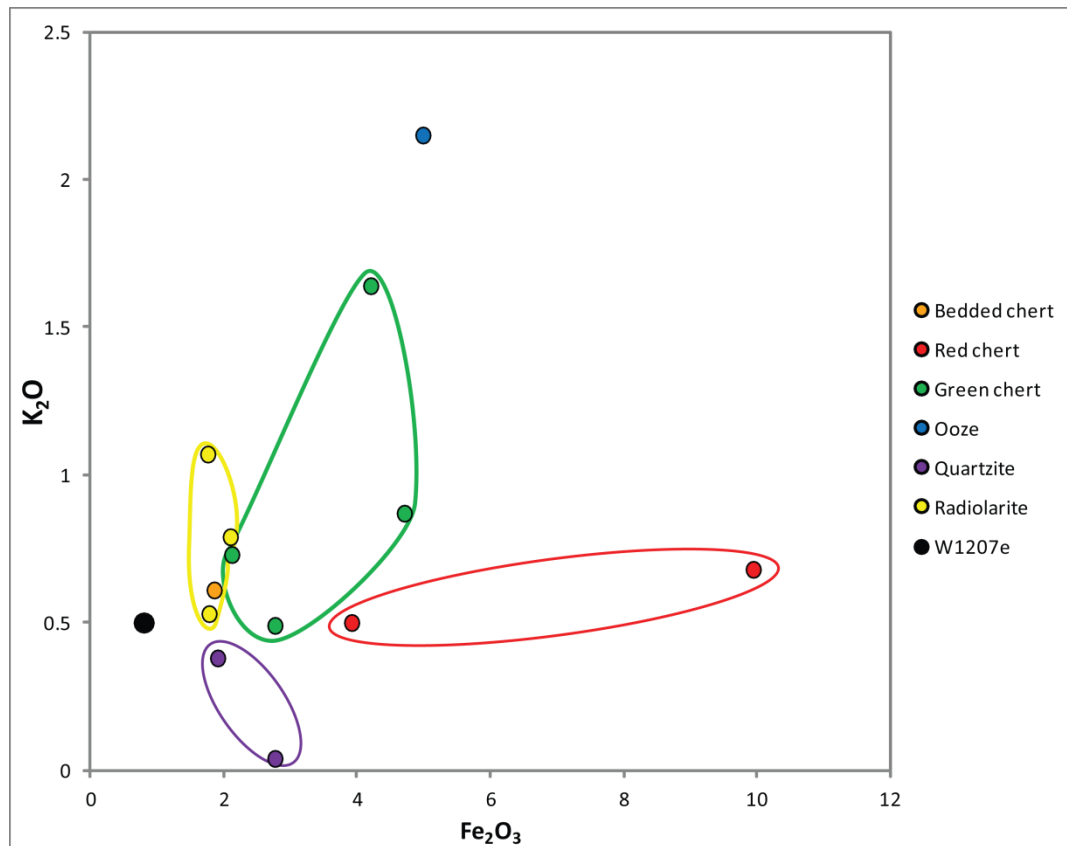


Figure 6.1.7: Fe_2O_3 vs K_2O plot for quartz rich rocks. Data points coloured by rock type, with Sample W1207e from this study in black. Circles denote approximate fields for each rock type, coloured accordingly.

Specific fields for each rock type are more easily visualised by comparing values for two major elements (Figure 6.1.7). Grouping of data points on the graph has been used to create fields to approximate characteristic chemical signatures for the rock types. Quartzite from the WMC has a low iron component, placing it outside the range of these fields.

PART 2: MINERAL CHEMISTRY

Introduction

Based on changes to mineral phase equilibria with temperature and pressure, geothermobarometers are widely used in geological studies to constrain metamorphic conditions. As peak metamorphic conditions at Wongwibinda have been found to be isobaric with pressures of no more than 3.5 kbar, changes to mineral chemistry through the complex can be interpreted as evidence for changing temperature.

In the previous section of this chapter, evidence for chemical change was discovered through whole rock chemistry. Throughout this section of the chapter, phases from the quartzite, the Rampsbeck Schists and the network of veins of the aureole will be examined, in order to look for changes to mineral chemistry correlating with these whole rock chemical changes, using the proxy constructed in the previous chapter to characterise the samples.

A possible explanation for the spatial distribution of Cordierite abundance observed during fieldwork and in thin section (Figure 4.1B) is that metamorphic processes driven by the thermal anomaly resulted in the growth of these cordierite porphyroblasts in the Rampsbeck Schists, forming the observed aureole (Figure 3.2). Several geothermobarometers use the cordierite phase equilibria, showing decreasing sodium content and increasing iron content with increasing temperature. As the cordierite phase may be a direct result of this local heating, examining chemistry of this phase may provide insight into temperature gradients through the aureole.

Complex mineralogy displayed by both the quartzite and the veins through the schists allow for comparison of mineral chemistry with the Rampsbeck Schists. Several different phases are used for this, including biotite and muscovite, feldspars and garnets.

Aims

This chapter aims to describe mineral chemistry throughout the aureole. Chemistry of the schists, the quartzite, and veins found in the schists will be compared. Selected components of mineral chemistry within the Rampsbeck Schists will be compared to changes in whole rock chemistry discovered in the previous chapter, to build an overall picture of the chemical profile of the aureole.

Scanning electron microscopy is employed to (1) determine major element compositions of minerals and (2) map elemental concentrations at selected sites in samples.

Analytical Methods

Nineteen representative samples were chosen for analysis - three from the transect across the quartzite unit (Figure 4.9), and sixteen Rampsbeck Schist samples including eight of the XRF samples, many of which displayed quartz veining. Sample locations are shown in Figure 3.2.

Mineral chemistry analysis was performed using Scanning Electron Microscopy at the Geochemical Analysis Unit (GAU), in the Australian Research Council (ARC) National Key Centre for Geochemical Evolution and Metallogeny of Continents (GEMOC), in the Department of Earth and Planetary Sciences at Macquarie University, Australia.

Energy Dispersive Spectrometry (EDS) analysis was undertaken on a Zeiss Scanning Electron Microscope (SEM) with an X-Max EDS detector, using the HKL AZtec analysis software from Oxford Instruments. Data was collected from mechanically polished thin sections with ~10 nm of carbon coating. The SEM was run at a high vacuum with an accelerating voltage of 20 kV, a beam current of 8.0 – 10.0 nA, and with an aperture of 30 µm. The samples were at

working distances between 11 and 13 mm. Analyses were performed using 1024 channels with 10 eV per channel, and an automated counting time (acquisition continuing until enough counts are collected in the spectrum for quantification).

Raw data is presented in Appendix B.

Results

Feldspars

Feldspars from the quartzite, the Rampsbeck Schists and large and small veins found in the schists were analysed. End member proportions were obtained from the SEM analyses, first by calculation of cations per formula unit from normalized data and then using these values, calculation of the end members:

$$\text{Albite } X_{\text{Ab}} = \frac{Na}{(Na+Ca+K)}$$

$$\text{Anorthite } X_{\text{An}} = \frac{Ca}{(Na+Ca+K)}$$

$$\text{Orthoclase } X_{\text{Or}} = \frac{K}{(Na+Ca+K)}$$

Feldspars are found throughout the field area, in all rock types. In the schists, plagioclase feldspar and k-feldspar both are found in the matrix, and in some samples large porphyroblasts of k-feldspar are seen. Small veins in the schists contain grains of both plagioclase feldspar and k-feldspar, as minor modal percentages. Dark bands in the quartzite unit have grains of plagioclase.

Results show a range in feldspar composition with two main populations in the aureole, one occupying the albite-rich corner and one occupying the orthoclase-rich corner of the diagram (Figure 6.2.1).

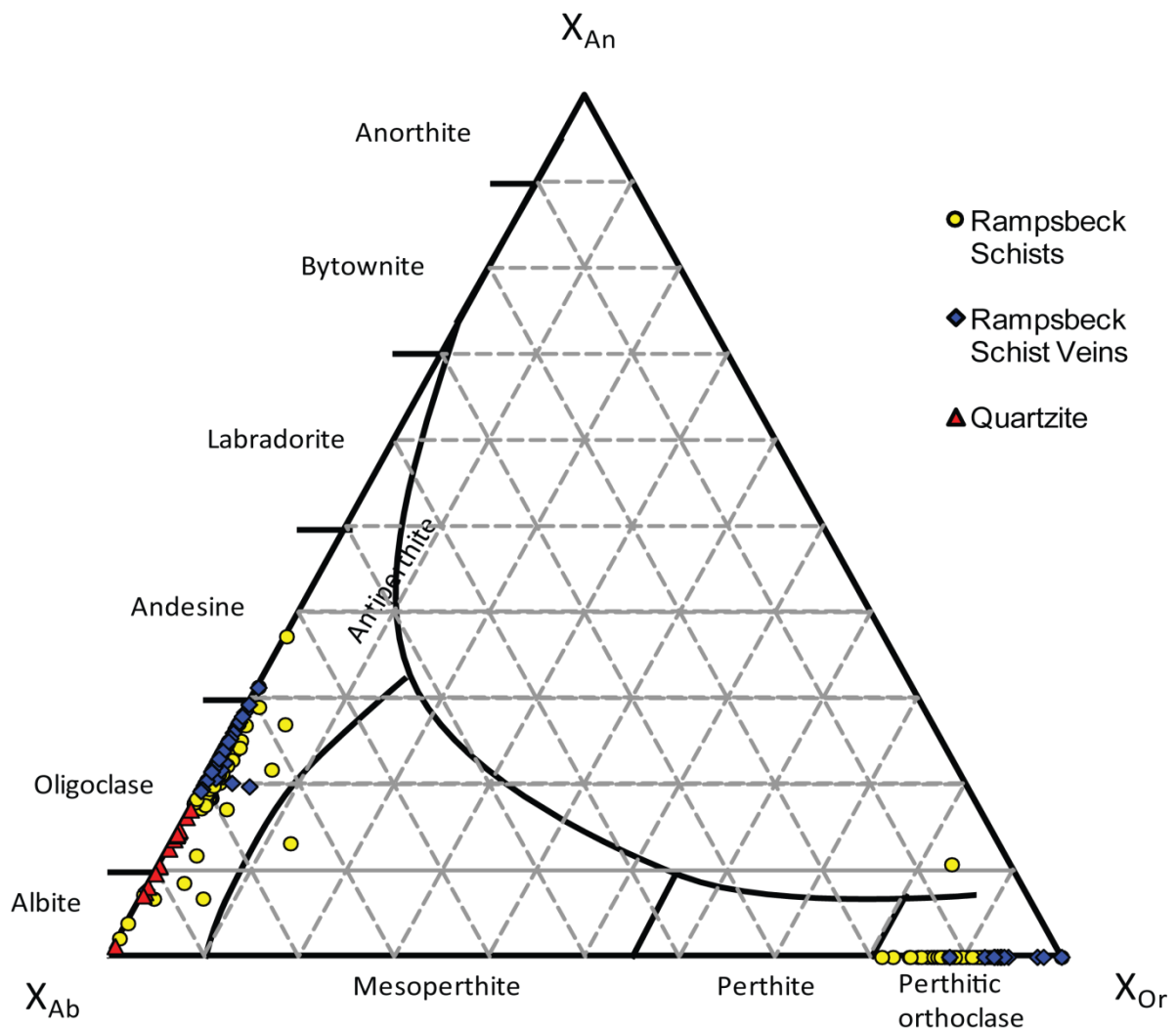


Figure 6.2.1: Feldspar ternary classification diagram with analyses plotted by lithology.

The plagioclase feldspars comprise one of these populations, occupying the albite rich corner of the classification diagram, with varying proportions of albite and anorthite (Figure 6.2.1). Throughout this population, feldspars from the quartzite (shown in red) plot closer to pure albite with higher sodium contents; those from veins in the schists (shown in blue) plot with more anorthitic compositions, indicating higher calcium content; those from the schist (shown in yellow) show greater spread, spanning the range in composition shown by feldspars from the quartzite and the veins, from nearly pure albite down to nearly 40% anorthite. Samples from the schist also show small amounts of potassium, uncommon to those from the quartzite and the veins.

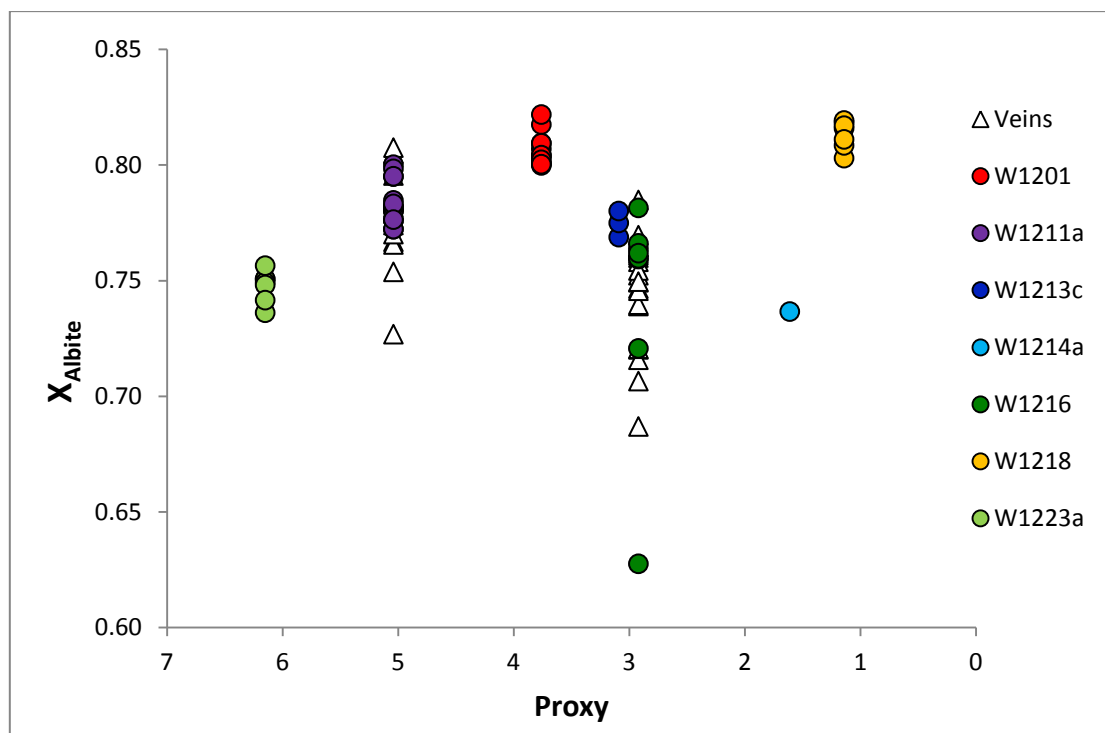


Figure 6.2.2: Plagioclase feldspar albite compositions from samples against a proxy representative of the degree of chemical changes in a sample, determined through whole rock chemistry analysis. Plotted are analyses of grains from the schists (coloured circles) as well as analyses of grains from small veins in these samples (white triangles).

The overlap of composition between grains in the schist and grains in the veins is also seen within individual samples (Figure 6.2.2). Most samples show tightly clustered albite

compositions, with a spread of 0.05 or less. There are no strong trends between plagioclase feldspar composition and the degree of chemical change within a sample.

The second population occupies the orthoclase-rich corner of the diagram, with grains from the schist and from veins in the schist (Figure 6.2.1). Similar to the first population, this population shows separation based on rock type, with varying proportions of orthoclase and albite. Feldspars from the veins plot closer to the pure orthoclase corner, with a range in orthoclase composition from ~90 - 100%. Feldspars from the schists plot with higher sodium contents, having albite compositions ranging from ~10 – 20%.

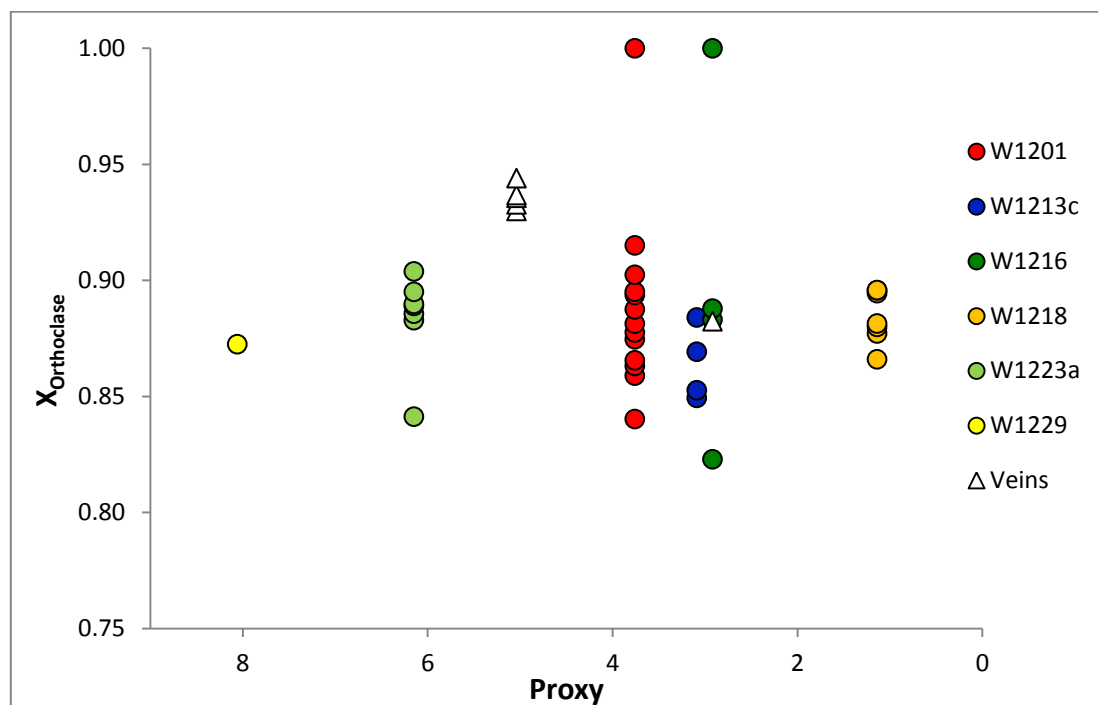


Figure 6.2.3: K-feldspar orthoclase compositions from samples against a proxy representative of the degree of chemical changes in a sample, determined through whole rock chemistry analysis. Plotted are analyses of grains from the schists (coloured circles) as well as analyses of grains from small veins in these samples (white triangles).

K-feldspar grains within samples show larger ranges in composition than plagioclase grains, with orthoclase composition ranging over 0.15 or more in samples W1201 and W1216. Once again, the overlap in composition between the schists and the veins is also seen within

individual samples (Figure 6.2.3), with no obvious trends in relation to the degree of chemical change in the sample. Two veins analysed exhibit higher orthoclase components than the schists, further confirming trends shown in Figure 6.2.1.

Biotite

Biotite was analysed in samples from both the quartzite and the schists, as well as in small veins from schist samples. Results from the SEM were converted into cations per formula unit, from which the magnesium proportion was calculated:

$$X_{\text{Mg}} = \frac{\text{Mg}}{(\text{Mg} + \text{Fe})}$$

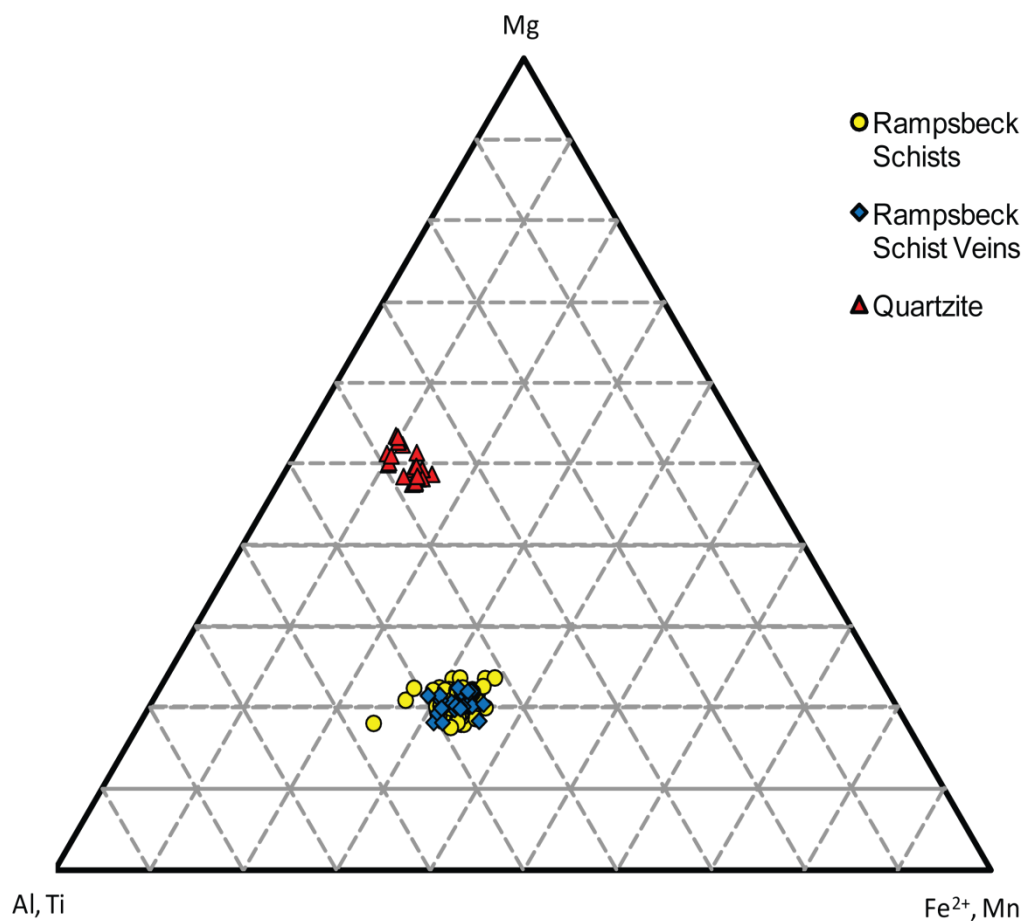


Figure 6.2.4: Biotite ternary diagram (following Foster, 1960) with analyses plotted by lithology.

Analyses of biotite are separated into two groups based on lithologies, as biotite from the quartzite has higher proportions of magnesium and lower of aluminium and iron than those in the schists (Figure 6.2.4). Data for each lithology are tightly clustered together, with vein biotite analyses overlapping with biotites from the schists.

This overlap is reflected in analyses from individual samples (Figure 6.2.5). X_{Mg} shows significant spread within each sample in both the veins and the schists, and there is a weak trend of increasing spread within samples of schist with increasing degrees of chemical change, as well as a weak trend of increase in the highest XMg value in each sample with increasing degrees of chemical change.

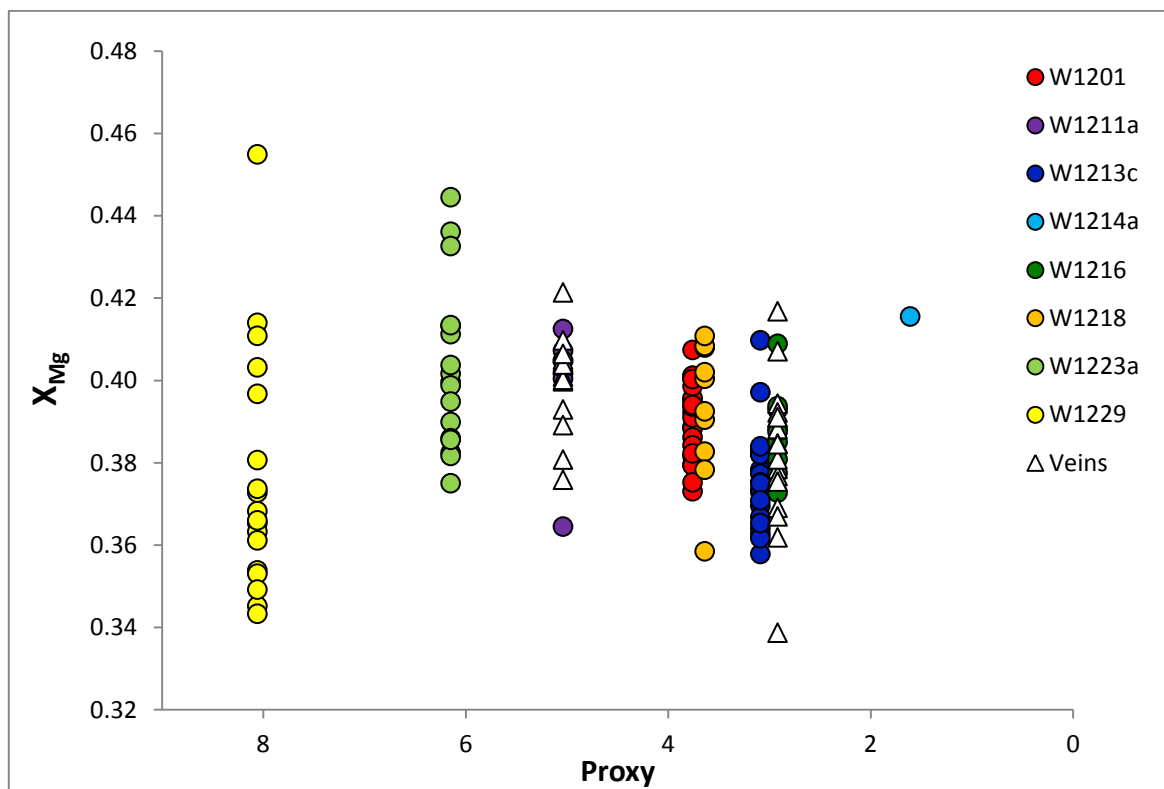


Figure 6.2.5: Biotite X_{Mg} compositions from samples against a proxy representative of the degree of chemical changes in a sample, determined through whole rock chemistry analysis. Plotted are analyses of grains from the schists (coloured circles) as well as analyses of grains from small veins in these samples (white triangles).

Muscovite

Muscovite is found throughout the aureole in the schists, the quartzite and small veins in the schists. Grains form two populations – small grains in the matrix and veins of the schist and the quartzite, and platy poikiloblasts in the schists – both appearing to be secondary minerals formed through metamorphic processes, as observed through petrographic analysis (Figure 4.1A).

Normalized results from the SEM were converted to cations per formula unit (based on 22 oxygens per unit), from which X_{Fe} and a paragonite component were calculated:

$$X_{Fe} = \frac{Fe}{(Mg+Fe)}$$

$$\text{Paragonite component} = \frac{Na}{(Na+K)}$$

The paragonite component is formed due to K replacement by Na within the muscovite lattice. In solid solution, muscovite can have a paragonite component of up to 20%.

These two components have been used to graph analyses by lithology (Figure 6.2.6). This shows muscovites in the schists and veins from the schists to be constant in the paragonite component, at values of approximately 0.05. Analyses from the quartzite show both higher values and a wider spread, between ~ 0.10 and 0.20. As well as this, muscovites from the quartzite unit have higher X_{Fe} values than the majority of analyses from the schists. From Figure 6.2.6, it can be seen that overall, muscovites from the quartzite are chemically different to those found in the schists and in veins from the schists, which show similar chemistries.

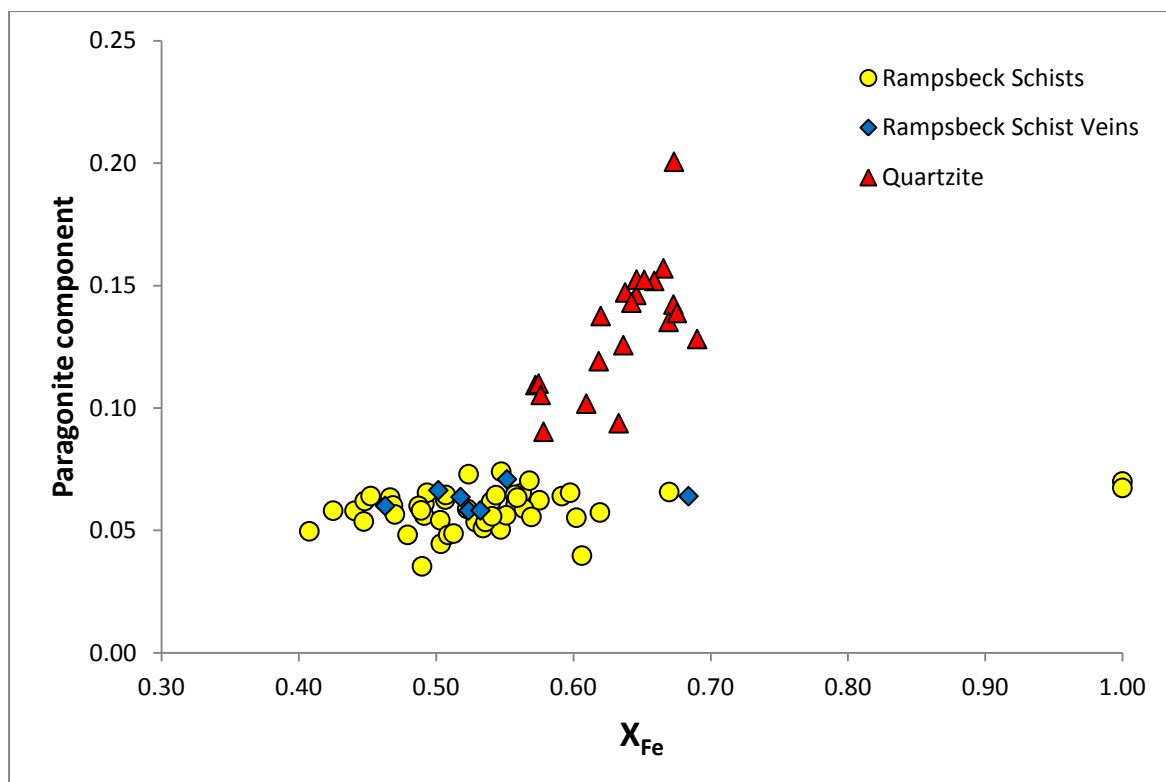


Figure 6.2.6: Muscovite analyses plotted by lithologies. X_{Fe} and Paragonite components calculated as per equations above.

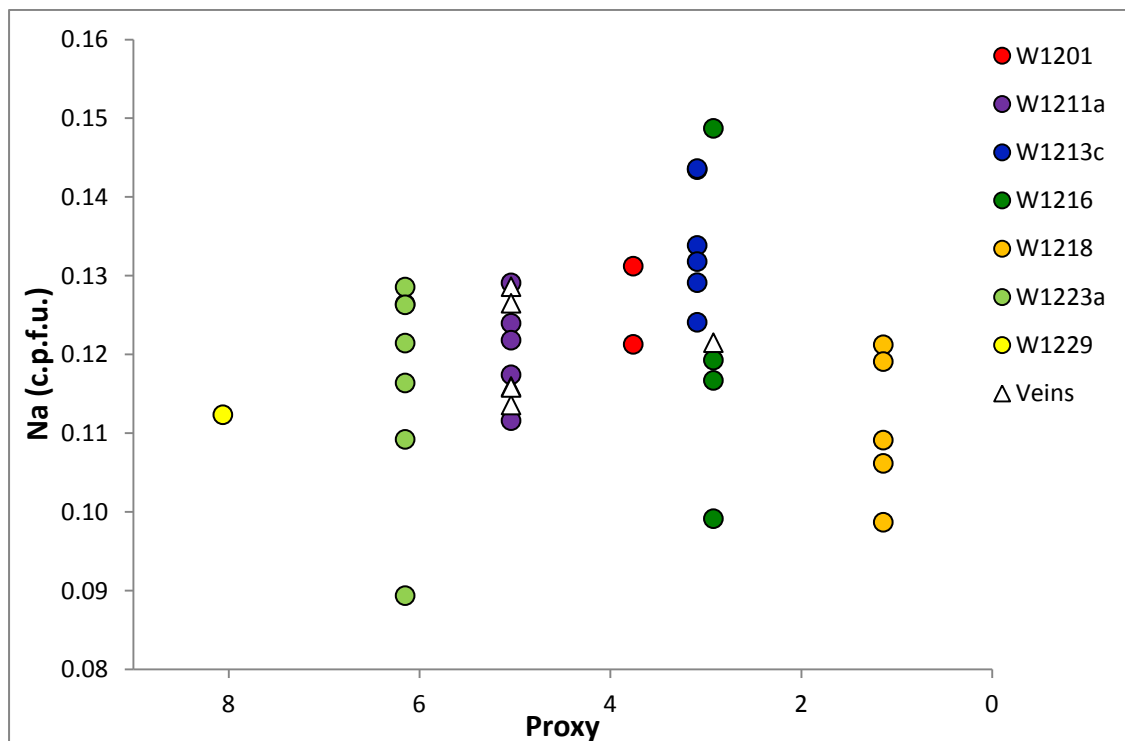


Figure 6.2.7: Muscovite sodium composition from samples against a proxy representative of the degree of chemical changes in a sample, determined through whole rock chemistry analysis. Plotted are analyses of grains from the schists (coloured circles) as well as analyses of grains from small veins in these samples (white triangles).

Examining analyses sample-by-sample reveals a weak trend of decreasing sodium content with increasing whole rock chemical changes (Figure 6.2.7), consistent with patterns in the whole rock chemistry results. Each sample shows a spread in sodium values. Analyses of muscovite grains from veins show similar chemical compositions to those in the schist, and in the case of sample W1211a, a similar range in values.

Cordierite

Cordierite poikiloblasts were found in samples of Rampsbeck Schists throughout the aureole, with the exception of sample W1211a on the very edge of the cordierite-in isograd. Normalized results from the SEM were calculated to cations per formula unit, from which the X_{Mg} was calculated using the following formula:

$$X_{Mg} = \frac{Mg}{(Mg+Fe)}$$

Cordierite grains throughout the aureole are Mg-cordierites, with a range in X_{Mg} values from 0.51 – 0.59. Following the use of Mg-cordierites in the Na in cordierite geothermobarometer (Kalt et al 1998), Figure 6.2.8 shows the Na content of cordierites against the proxy for the degree of chemical change in the sample.

The majority of cordierites in the aureole show very low Na compositions between 0.05 and 0.10 c.p.f.u. and many analyses below the LLD. Cordierite grains in sample W1201 are especially rich in sodium and show considerable spread compared to analyses from other samples. Overall there are no strong trends in this data.

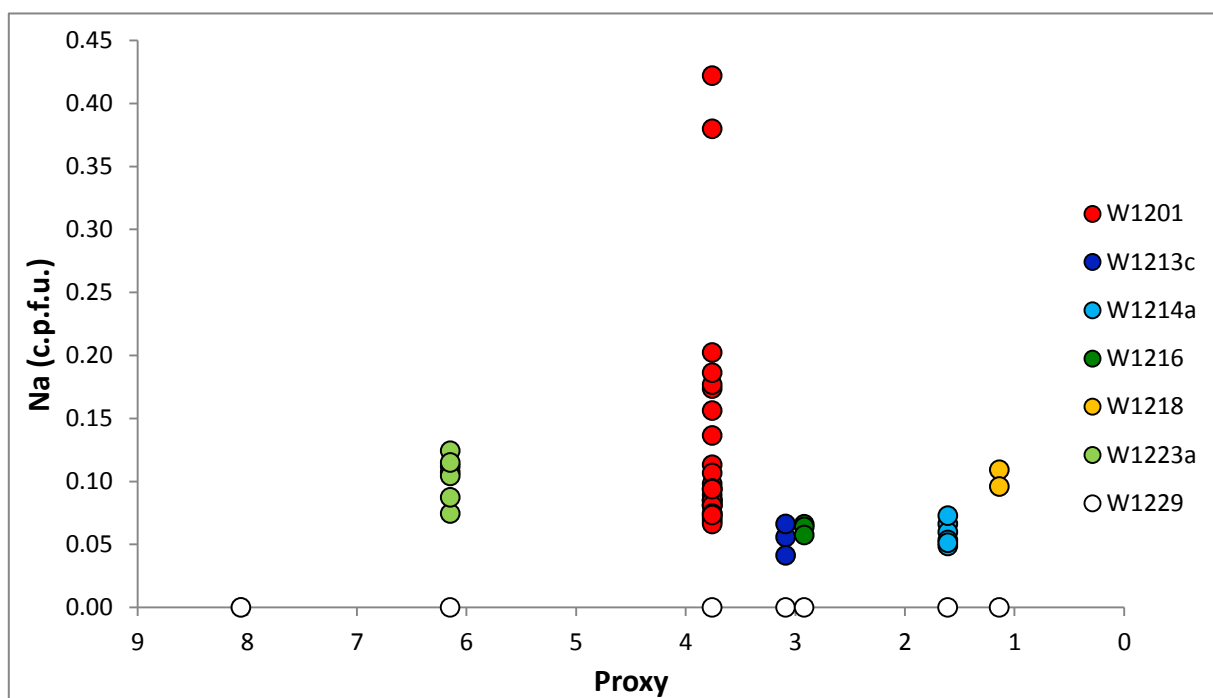


Figure 6.2.8: Cordierite sodium composition from samples against a proxy representative of the degree of chemical changes in a sample, determined through whole rock chemistry analysis. Plotted are analyses of grains from the schists (coloured circles), with analyses below the lower limit of detection represented by white circles.

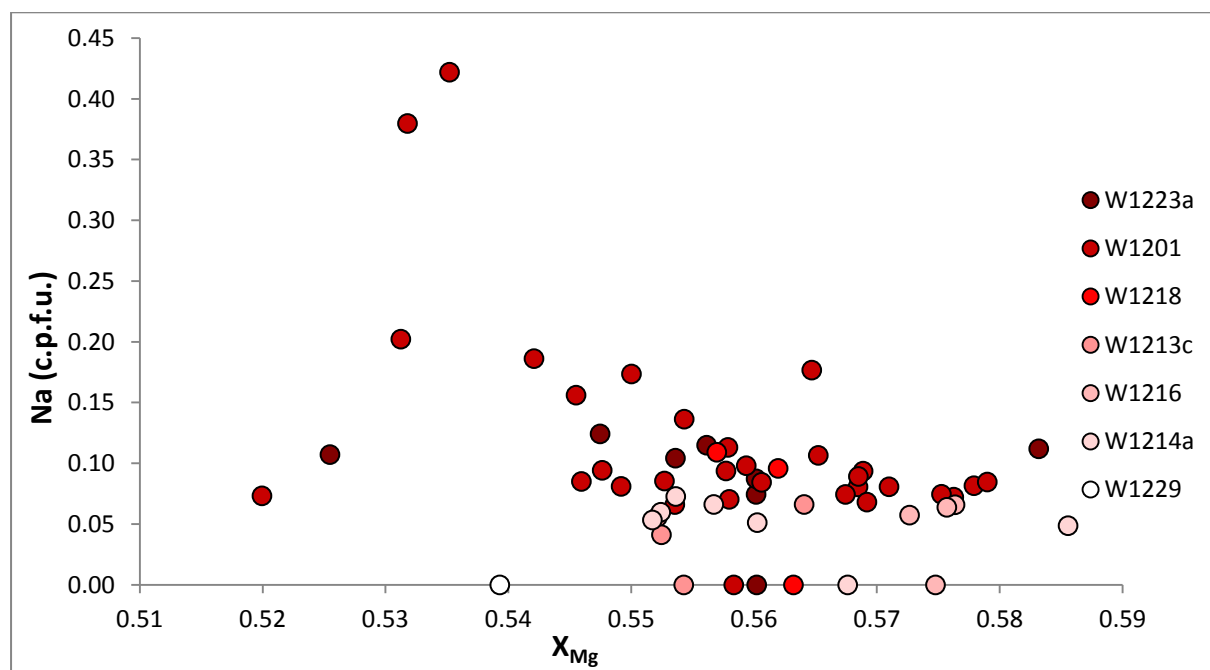


Figure 6.2.9: Cordierite X_{Mg} vs sodium composition. Samples coloured using a proxy representative of the degree of chemical changes in a sample, determined through whole rock chemistry analysis. Samples with a high proxy value are coloured in dark red, and samples with low proxy values are coloured in pinks, with analyses below the lower limit of detection represented by white circles.

A weak trend is observed between X_{Mg} and sodium content of the cordierites (Figure 6.2.9). Colouring data points by proxy value reveals those samples with higher degrees of chemical change show higher sodium content and a spread of X_{Mg} values from $\sim 0.52 - 0.585$. Those samples with lesser degrees of chemical change display lower sodium values, and a smaller range of X_{Mg} values in the higher range, between 0.55 and 0.59.

Garnets

Garnets are found within very restricted areas in the aureole. Small garnets are abundant throughout the quartzite, found in all samples that were examined. Within the schists, only two samples were found to contain garnets: W1209, a fine-grained schist found within 20m of the quartzite boundary; and W1204 (Figure 5.1), a large (~ 2.5 cm wide) vein found in an outcrop of schist also within 20m of the quartzite boundary, with garnets found in wall rock inclusions throughout the vein.

Results from the SEM were calculated to cations per formula unit, from which garnet end members were calculated using the following equations:

$$\text{Almandine } X_{Alm} = \frac{Fe}{(Fe+Mg+Mn+Ca)} \times 100$$

$$\text{Pyrope } X_{Py} = \frac{Mg}{(Fe+Mg+Mn+Ca)} \times 100$$

$$\text{Grossular } X_{Gr} = \frac{Ca}{(Fe+Mg+Mn+Ca)} \times 100$$

$$\text{Spessartine } X_{Sps} = \frac{Mn}{(Fe+Mg+Mn+Ca)} \times 100$$

Garnets in both the quartzite and inclusions in the vein were found to be spessartine-rich, with X_{SpS} values of 60 – 75 in the vein (W1204), and 68 – 80 in the quartzite (W1207d, e and h). Garnets in the schist showed more iron rich chemistries, with X_{Alm} values between 60 and 67. Plotting these onto a ternary diagram clearly distinguishes these two populations from each other (Figure 6.2.10).

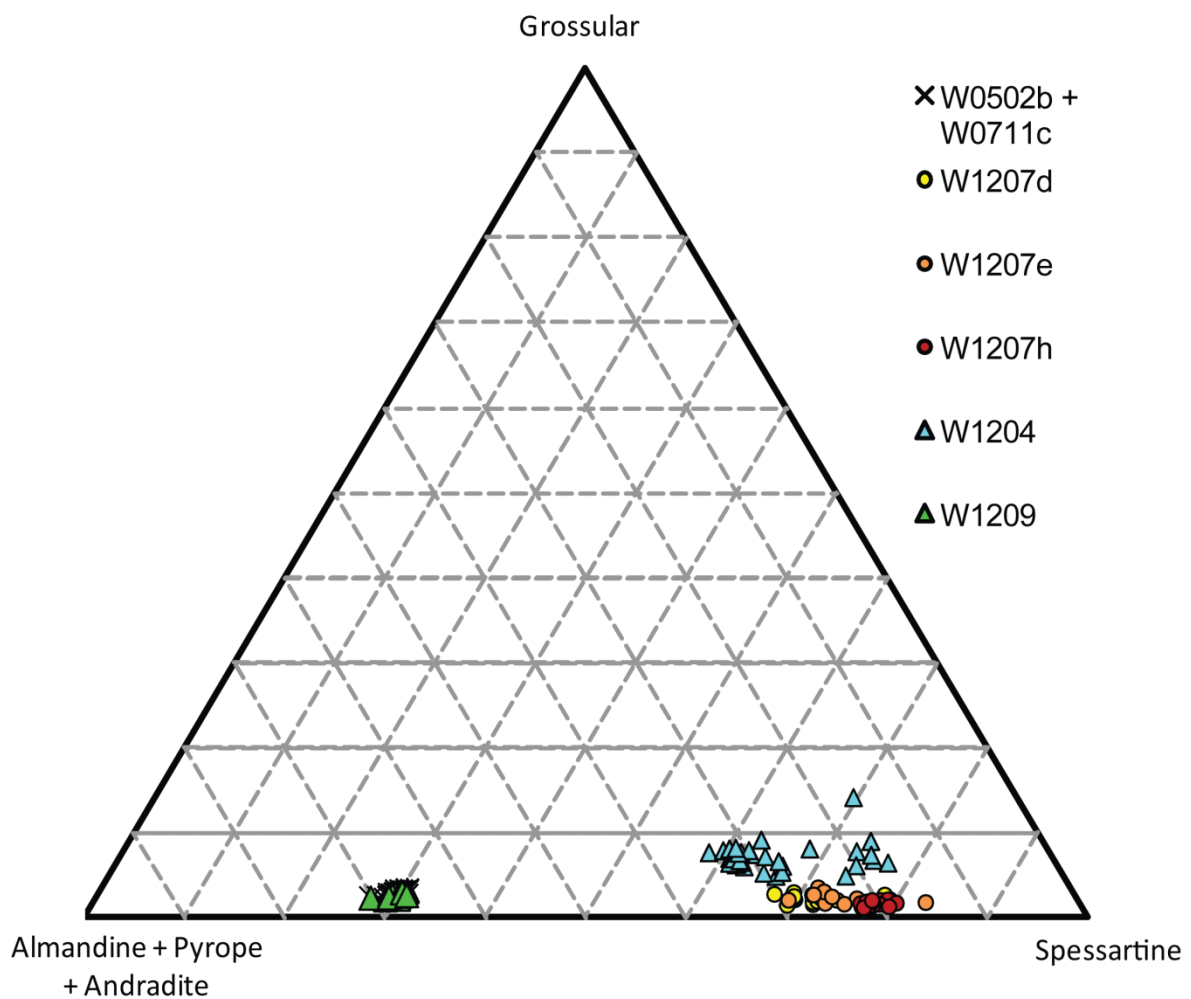


Figure 6.2.10: Garnet ternary diagram. Analyses plotted by lithology, with round data points quartzite samples, and triangular data points schist samples. Note, W1204 is the vein within the Rampsbeck schist. Also plotted are analyses previously performed on garnets found in the Rampsbeck Schists (W0502b + W0711c) from various locations through the WMC (Craven et al, 2012).

Garnets found in the Rampsbeck Schists plot over the top of previous analyses of garnets from elsewhere in the complex (Figure 6.2.10). This population is clearly distinguished from the spessartine-rich garnets found in the quartzite and in association with veins.

Samples W1207d, W1207e and W1207h are three samples from a transect across the width of the quartzite unit, with W1207h taken close to the quartzite boundary, and W1207d and W1207e from the centre of the unit. Compositions of garnets show a weak trend with sample position in the quartzite, as garnets from the outer edge have higher X_{Sps} , and those from the centre of the quartzite have lower X_{Sps} . This is not a clearly defined continuum, as outliers create overlap between samples.

Garnets from small schist inclusions in the vein (W1204) also show high X_{Sps} , showing considerable spread across the spessartine values seen in the quartzite unit. Although these garnets are found within a vein within a sample of Rampsbeck Schist, chemically they are more characteristic of those in the quartzite.

PART 3: INTERPRETATION

Compared to values for the region, the Rampsbeck Schists of the aureole have altered chemical signatures, which are evident in specific elements (Figure 6.1.3). In general, the changes are characterised by depletion in Ca, Na, Co and Sr, and enrichment in Fe, K, Cr, Cs, Ba, Ni, heavy REEs, and to a lesser extent Mg. Similar patterns in whole rock chemistry of the quartzite indicate that it was influenced by the same system, linking metamorphism of the schists to the quartzite.

Interpretation of the systematic chemical changes as metasomatism involves the movement of fluids through the system. The shape of the aureole, formed by the metamorphic isograd, as well as the occurrence of large quartz veins in the centre and smaller veins on the edges of the aureole points to the quartzite as the site of high flux, from which fluids were introduced outwards into the schists.

Under pervasive fluid flow conditions, chemistry of the rocks would change in a gradient with distance from the site of fluid flux. Close to the site of flux, the host rock would have a chemical signature highly influenced by that of the fluid. With distance, fluid-rock interactions result in the fluid chemistry becoming progressively more like that of the schist, until such a distance is reached that no chemical changes are evident in the host rock.

Changes to whole rock chemistry within the aureole have no obvious spatial controls (Figure 6.1.1). Instead, metasomatism has occurred in varying degrees in the samples collected, indicating patchy distribution of fluid. The patchy distribution of metasomatism and apparent steep thermal gradient across the aureole are features expected from the channelling of fluids. In the event of channelised flow, rocks at the edge of the aureole can

experience a greater degree of those closer to the site of fluid flux, depending on direction and frequency of channelling, and the volume of fluid passing through the channels.

The proxy constructed from the degree of chemical changes experienced by a sample is therefore an approximate measure of the volume of fluid that has passed through the sample, as well as giving an indication of the extent of the channelling. Sample W1211a sits in the vicinity the cordierite-in isograd (Figure 3.2), itself lacking the cordierite poikiloblasts that highlight the shape of the aureole. Although poikiloblast growth has not occurred at this location, this sample exhibits whole rock chemistry indicative of a high degree of metasomatism, indicating the channelling of fluids to the edge of the aureole.

Examining changes to mineral chemistry and correlating with the degree of metasomatism can therefore give an indication as to the evolving chemistry of the fluid. Veins are important in this study as they mark the passage of fluids through the rocks, with vein material crystallising from the fluid. Comparisons between mineral chemistry of the veins and the host rock can be used to interpret the changing chemistry of the fluid as it moves through the aureole.

Several important trends are revealed through mineral chemistry analysis:

1. Minerals in the Rampsbeck Schists have similar chemical compositions to those in small veins in the schists. This trend is demonstrated in biotite, muscovite, and feldspar compositions.
2. Minerals in the quartzite are chemically different to those in the schists and small veins. Muscovites and (to a lesser extent) feldspars show enrichment in sodium, and biotites show enrichment in magnesium.

3. Garnets in the large vein analysed are similar to those found in the quartzite, showing similar ranges in composition. They are distinct from the Rampsbeck Schist garnets.

This signifies two chemical populations: (1) Rampsbeck Schists of the aureole and small veins in the schists; and (2) the quartzite and large veins in the Rampsbeck Schists. The origin of these populations are likely to be products of fluid-rock interactions, based on the fluid:rock ratio.

In the large veins the fluid:rock ratio is higher and the composition of the fluid would be less influenced by the whole rock chemistry of the surrounding host rock. Vein minerals crystallising directly from the fluid without much fluid rock interaction will largely preserve compositions of the fluids; in particular, the veins appear to have preserved a high Mn/Mg ratio in the garnet chemistry (Figure 6.2.10), also seen in the Fe/Mn-rich amphiboles of the wall rock inclusions in Sample W1204 (Figure 5.2), as well as a silica rich chemistry through the dominance of quartz in vein material.

Taking into account that fluid flux occurred at a high rate in the quartzite, as well as the coincidence of garnet composition from the quartzite with garnet composition from the large veins, the quartzite is likely to have experienced very high fluid:rock ratios. Minerals in the quartzite therefore have preserved the chemical signature of the fluid as it entered this area. Abundance of quartz, Mn-rich garnets, high Na values in the feldspar and muscovite, high Fe in muscovite and high Mg in biotite suggest that the fluid from the veins was higher in Si, Mn, Na and Fe, and high in Mg relative to the surrounding Rampsbeck schists.

With these conditions in sites of high fluid flux, we would expect to see patterns of metasomatism correlating in the Rampsbeck Schists.

Although bulk rock Fe shows enrichment from the regional background, these are only small changes and so the significance is not strong (Figure 6.1.3). In comparison with the schists, the quartzite has a slightly higher Fe/Mg ratio (Figure 6.1.5), indicating fluids with high Fe component which might have been responsible for the observed Fe enrichment in fluid affected schists through metasomatism.

On a smaller scale, variation to the Fe/Mg ratio in minerals is controlled by assemblage. In the quartzite, contemporaneous growth of garnets and biotite resulted in biotite with a lower Fe/Mg ratio than in schists or veins (Figure 6.2.4). A lack of garnet in the schists results in more iron available when biotite crystallises, and so they have a relatively higher Fe/Mg ratio. Vein forming fluids (i.e. with significant interaction with the schists) have similar Fe/Mg ratios as biotite compositions with the schists themselves, supporting the influence of country rock on vein composition.

Commonly, Fe/Mg ratios in ferromagnesian minerals are used as geothermometers, and so changes to these values in the schists can be indicators of temperature differences. Biotite X_{Mg} in the schists shows large spread within samples, and little differences between samples (Figure 6.2.5). Cordierite X_{Mg} shows similar patterns to those in biotites from the schists and the veins (Figure 6.2.9). The spread shown within samples is unusual, as it is expected if equilibrium conditions were attained throughout the sample that minerals in one sample formed under the same temperature conditions; thus showing the same Fe/Mg reactions. Therefore another factor is influencing the growth of cordierite; perhaps cordierites of different chemical composition form as various pulses of fluid affect the sample. Changes to fluid temperature, equilibrium-disequilibrium, chemistry and subsequent changes to whole rock chemistry are all possible explanations of the spread in X_{Mg} within a sample.

Examining whole rock data reveals the quartzite to be depleted in Ca (Figure 6.1.5), indicating Ca-poor fluid chemistry. Because the schists have a higher concentration of Ca than the fluid, fluid-rock interactions will result in depletion of Ca from the schists as it is taken up by the fluid. This is reflected in feldspar chemistry (Figure 6.2.1) and garnet chemistry (Figure 6.2.10), which both indicate higher Ca values in veins relative to the quartzite. This is also demonstrated in Sample W1204, a large vein from the schists where large apatite grains are growing in the vein and in wall rock inclusions.

The depletion of Ca is supported by inverse patterns in K component of K-feldspar chemistry (Figure 6.2.1). These reveal trends tending towards a continuum as feldspars in the schists spread from high Ca, low K composition towards those in the veins, which have low Ca, high K compositions. Here the veins have preserved high K component present in the chemistry of the fluids, indicating metasomatism involved the enrichment of K in the schists. This is supported by a general enrichment of K throughout the aureole. Where exactly the K comes from remains unclear as the quartzite shows low K values.

Similarly, whole rock chemistry for the quartzite reveals it to be enriched in the heavy REEs, such as tantalum, lead, thorium and uranium, indicating an enrichment of these in the fluid (Figure 6.1.5). This pattern is repeated through the schists, which show increased concentrations from the regional values, especially in Th and U (Figure 6.1.3). This pattern is repeated with several other trace elements, such as Cr and Ni, both of which show substantial enrichment in the schists.

Within the aureole, fluid-rock interactions have a great impact on chemistry, with the fluid taking on a high chemical signature from the schists which masks its original composition. In general, the original chemistry of the fluid can be estimated by characterising samples which

have experienced high fluid:rock ratios. From whole rock and mineral chemistry, there is strong evidence for Fe-Mn (+ Cr + Ni + Th + U) rich, Ca-poor fluids moving in channelised flow through the aureole and metasomatising the Rampsbeck Schists.

Fluid-rock interactions such as this must occur over short amounts of time and space in order to result in these distinct changes between rock types and vein sizes, which occur within 20m of the quartzite boundary. Sample W1204 preserves evidence for these interactions, seen in textural relationships between garnet and amphiboles (Figure 6.3.1A) in which the garnet grains show inclusions and embayments of amphibole and quartz.

Here the Mn-rich garnets have crystallised first, preserving the Mn-rich chemistry of the fluids. After significant fluid-rock interactions and evolution of fluid chemistry, the garnets are no longer in equilibrium with the fluid, out of which feldspars are crystallising.

Disequilibrium from the fluid-rock interaction causes the garnets to react with the fluid and feldspars to form amphibole and quartz.

In comparison with this the quartzite has garnets in equilibrium with the surrounding material (Figure 6.3.1B), where a garnet sits next to a muscovite grain with a straight edge, exhibiting equilibrium conditions. The garnet-fluid reaction caused by disequilibrium seen in W1204 is not present in this sample. As disequilibrium conditions are a result of fluid-rock exchanges, evidence for which is not seen in the quartzite, it is likely that little to no fluid-rock interaction occurred in this unit.

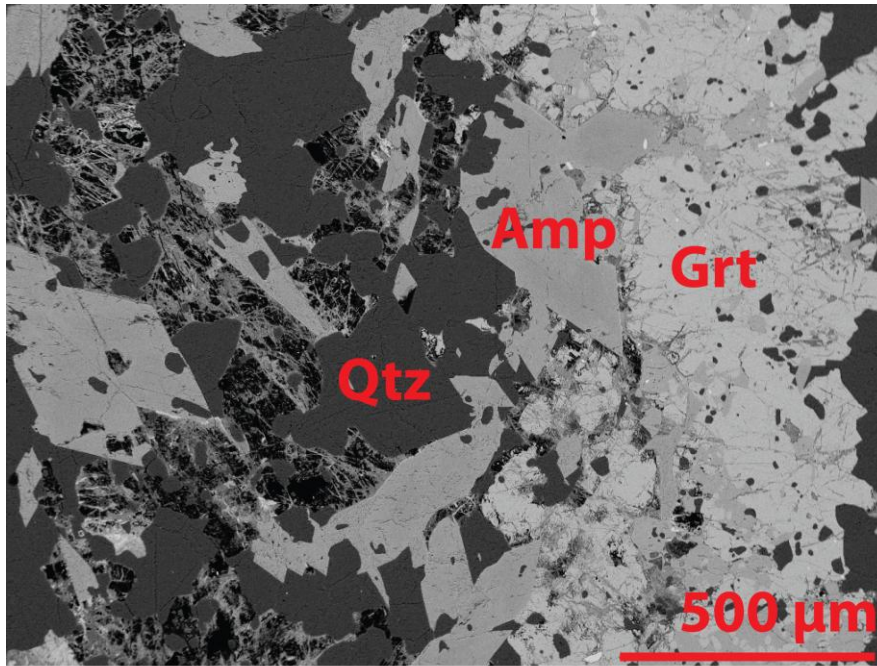
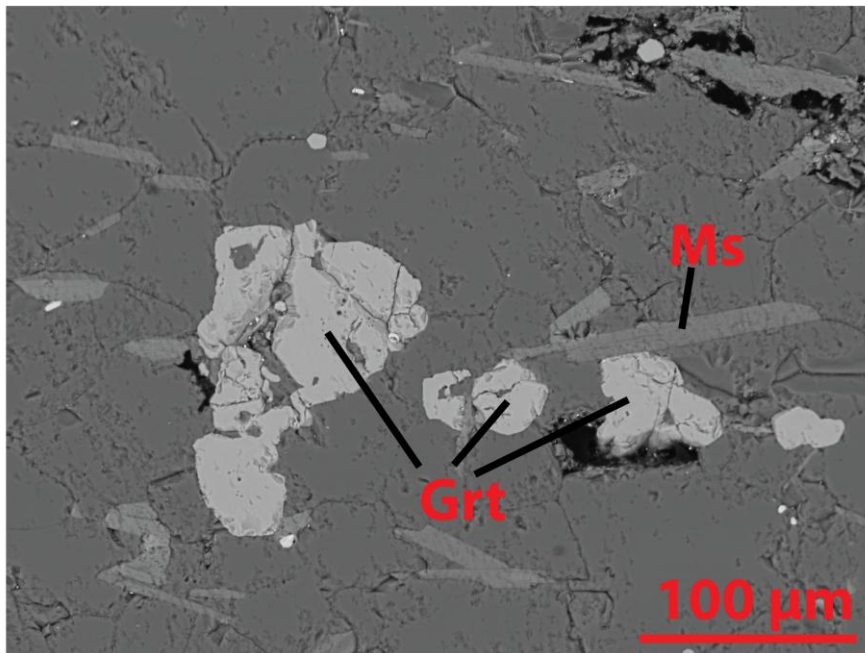


Figure 6.3.1:
Backscatter images of
representative
garnets in a large
vein (A) and in the
quartzite (B).

(A) Sample W1204,
displaying garnet in
disequilibrium with
the surrounding wall
rock and vein forming
material.



(B) Sample W1207d,
displaying garnet in
equilibrium with the
surrounding material.

CHAPTER 7 - DISCUSSION

Achievement of aims

Mapping of metamorphic isograds outlines inconsistencies between the cordierite-in isograd and the regional metamorphic gradient. Seen through field relationships in this study, cordierite growth is spatially related to quartzite units in the complex, occurring in aureole-like patterns around quartzites through the centre of the complex, as well as those in the shear zone to the east. The study site represents an example of this spatial relationship in a low strain area.

Chemical characterisation of the quartzite was inconclusive in terms of categorising it among other quartz-rich rocks. Differences between this unit and published values for other rocks were evident, especially through Fe content.

Microstructural analysis of the quartzite revealed it is weakly banded on a small scale, related to the mineralogical and grain size banding. A quartz vein analysed showed domains of quartz at high angles to each other, clearly separated on the basis of orientation. In comparison with this vein, the quartzite shows very few similarities as neighbouring domains show similar orientations throughout, only differentiated by the strength of the orientations. Significant recrystallisation has occurred in this unit and so it is possible that these slight differences are remnants of pre-existing orientation contrasts that have been masked by later deformation. A vein origin for this unit cannot be conclusively proved or disproved.

Chemical analyses reveal anomalies within the schists. Compared to regional values, the schists of the aureole are enriched in Fe, K and heavy REEs, and depleted in Ca. Whole rock chemistry of the quartzite follows similar patterns to the schists, as well as showing further enrichment in Mn.

Mineral chemistry differences divide the lithologies into separate populations: (1) the quartzite unit and large veins in the Rampsbeck Schists through high Mg, Na and Mn components compared to (2) the Rampsbeck Schists and the small veins in the schists. Trends between these groups are interpreted as the result of fluid-rock interaction, with Fe, Ca and K components following the enrichment patterns seen in whole rock chemistry.

Origin of the spatial relation between the cordierite-in isograd and the quartzite

There are three possible models which can explain the spatial relationship between the cordierite-in isograd and the quartzite unit. These are presented and further explored below.

Model 1 - Enrichment of Mg from a meta-chert

In previous studies, the quartzite has been interpreted as a meta-chert. As a seafloor deposit, this unit could have high Mg, Mn and Fe components through the formation of crusts or nodules on the seafloor (Makrygina and Suvorova, 2011), forming a quartzite enriched in these elements compared to the surrounding sequences.

During regional metamorphism these components may have become mobile, moving outwards into the schists and supplying Mg for the growth of cordierite. Regionally, whole

rock chemistry is unsuited to cordierite growth even at higher temperatures, hence the cordierite is only able to grow adjacent to the meta-cherts, where the Mg is available.

Model 2 - Fluids as a catalyst

Acting on the assumption that the metasedimentary sequence was metastable, this model involves migration of pulses of fluids up through the crust to the WMC. When fluids reached the complex, migration was stalled and crystallisation from the dissolved species in the fluid occurred, forming a large vein sequence at the site of fluid flux. The fluids acted purely as catalysts for the nucleation and growth of cordierite in the metastable country rock.

Subsequent recrystallisation of the vein sequence during regional deformation masked any vein growth textures.

Model 3 - Aqueous fluid advection

This model occurs in a similar fashion to the second model, with fluids migrating in pulses upwards through the crust and being focussed at this point in the WMC. When the fluid reached the complex migration was stalled and phases began to crystallise from the fluid, forming a large sequence of veins at the site of high fluid flux.

Where this model differs though, is in the fact that the fluids are not in equilibrium with the surrounding schists and advecting heat to this site. Chemistry of the fluids interacts with that of the schists, driving metasomatism in an aureole around the site of high flux. Added heat from the fluid drives local metamorphic reactions, resulting in the growth of cordierite in an aureole around the site of high fluid flux.

Specific features are to be expected for each model. These are outlined in Table 7.1, along with the accompanying evidence (or lack thereof) found in this study. Table 7.1: Three

models presented to form a spatial relationship between the cordierite-in isograd and the quartzite units, with expected and observed evidence for each.

Table 7.1: Three models presented to form a spatial relationship between the cordierite-in isograd and the quartzite units, with expected and observed evidence for each.

Model	<i>1. Enrichment from a meta-chert</i>	<i>2. Fluids as a catalyst</i>	<i>3. Aqueous fluid advection</i>
Expected features	<ul style="list-style-type: none"> • Spatially controlled cordierite-in isograd, matching with quartzite geometry • Enrichment, but not depletion in the aureole • Chemical signature of the quartzite in agreement with published values for cherts 	<ul style="list-style-type: none"> • Cordierite-in isograd spatially associated with the quartzite unit • Vein structures and growth textures at the site of fluid flux, discordant with bedding • Similar chemical signatures within the aureole to those of the region • Outside the aureole, equal metamorphic conditions throughout the region 	<ul style="list-style-type: none"> • Cordierite-in isograd spatially associated with the quartzite unit • Vein structures and growth textures at the site of fluid flux, discordant with bedding • Evidence for metasomatism in the aureole • Evidence for disequilibrium between fluids and the schists • Thermal anomaly overprinting the regional gradient
Observed features	<ul style="list-style-type: none"> • In the field site, the cordierite-in isograd matches with quartzite geometry. However this is not consistent along the length of the unit, as in the north, the cordierite-in isograd cross-cuts a quartzite unit which is approximately stratiform with the studied quartzite • Enrichment and depletion throughout the aureole • Chemically characterising the quartzite gave inconclusive results 	<ul style="list-style-type: none"> • All patches of cordierite-bearing rock are associated with quartzite units • Microstructural analysis of the quartzite proved inconclusive due to strain in the sample; however in places the strike of the unit appears at an angle with bedding in the schist and a vein origin for this unit has not been ruled out • Schists within the aureole show variation in whole rock chemistry from regional averages • Regionally (with the exception of this aureole) the Rampsbeck Schists display a smooth, west to east metamorphic gradient 	<ul style="list-style-type: none"> • All patches of cordierite-bearing rock are associated with quartzite units • Microstructural analysis of the quartzite proved inconclusive due to strain in the sample; however in places the strike of the unit appears at an angle with bedding in the schist and a vein origin for this unit has not been ruled out • Schists within the aureole show evidence for metasomatism in the aureole, altered from that of the regional averages • The aureole is an anomaly in the complex-wide metamorphic gradient

Aqueous fluid advection as a best-fit model

Based on evidence presented in this thesis, models 1 and 2 are deemed unfit to explain the metamorphic evolution of the aureole.

Model 1 is based upon the assumption that the quartzite is a metamorphosed chert which supplies the Mg for cordierite growth. If this was the case then we would expect cordierite growth to occur around all quartzite units that are stratiform with the one studied. We would also expect enrichment of elements through the aureole. Although enrichment is seen through whole rock chemistry data, this model has been excluded depletion in the aureole is also quantified. As well as this, the cordierite-in isograd cross-cuts an outcrop of a stratiform quartzite unit to the north, indicating that cordierite growth does not require contribution from the quartzite.

Model two is based upon the assumption that the sedimentary sequence was metastable at the time of fluid flux, acting purely as catalysts for cordierite growth around the site of fluid flux. This model can be ruled out based on the regional metamorphic gradient across the complex, indicating that the region was not metastable, and the evidence for metasomatism through the aureole, indicating that the fluids acted as reactants rather than catalysts.

Of the three models presented above, heating and metasomatism from aqueous fluid advection best fits the metamorphic evolution of the aureole, based on the evidence obtained in this study.

There is insufficient data to prove the quartzite is a vein sequence, however there is also insufficient data to definitively rule it out, and so it is considered a possibility. The quartzite does show a chemical affinity to large veins in the Rampsbeck Schists. Estimations of fluid

chemistry from these samples match trends to chemistry within the schists of the aureole, which are not spatially related but do show evidence of fluid-rock interactions throughout the aureole. Metasomatism in whole rock chemistry correlates with trends seen in mineral chemistry, which further confirms the role of fluids in the metamorphic history of this area.

Fluid pulses of changing chemistry can sufficiently explain the variable metasomatism and heating throughout the aureole. Similarly, fluid pulses of different temperature and composition can explain the spatial distribution of cordierite throughout the complex. In the northern WMC, outcrops of quartzite are seen lacking the cordierite aureoles. These may mark sites of high fluid flux at temperatures insufficient to cause the growth of cordierite.

Aqueous fluid advection – a model

Presented below is a model of the metamorphic evolution of the thermal aureole.

Source of fluids

Large quartz veins with gold and sulphide mineralisation are hosted within the Hill End Anticline, a regionally deformed turbidite sequence. These quartz veins display growth textures indicative of syn- and post-deformation formation, with bedding-parallel, banded veins on the limbs of the fold and massive, saddle reef veins in the hinge zone. Accompanied by vein growth, the turbidite sequences have experienced metasomatism concentrated in the hinge zone of the anticline (Windh, 1995).

The outcrop-scale structures of veins at Hill End are similar to those found in the quartzite here in Wongwibinda, which were previously explored in Chapter 3. Although Wongwibinda has not experienced economic mineralisation, significant metasomatism has been found surrounding the quartzite unit.

In the case of Hill End, the source of the sulphides and gold was found to be the underlying turbidite sequences. The dissolved species were from a significantly large area of the underlying rock, and were channelled by fault systems from the source area into the overlying structures.

In general a “Hill End type model” could be a viable model for fluid source and transport at Wongwibinda, as D_1 folds are thought to have formed above a basal detachment fault at depth (Collins, 1991). This fault later propagated upwards to form the Hunter Thrust and subsidiary faults.

This basal detachment fault could act as a path for fluids, increasing connectivity through the accretionary prism and acting as a collection point, sourcing fluids from a large area of rock undergoing prograde metamorphism at depth (Figure 7.1, fault highlighted with a red line). Here the fluids are at higher temperatures and so will have a larger dissolved silica concentration.

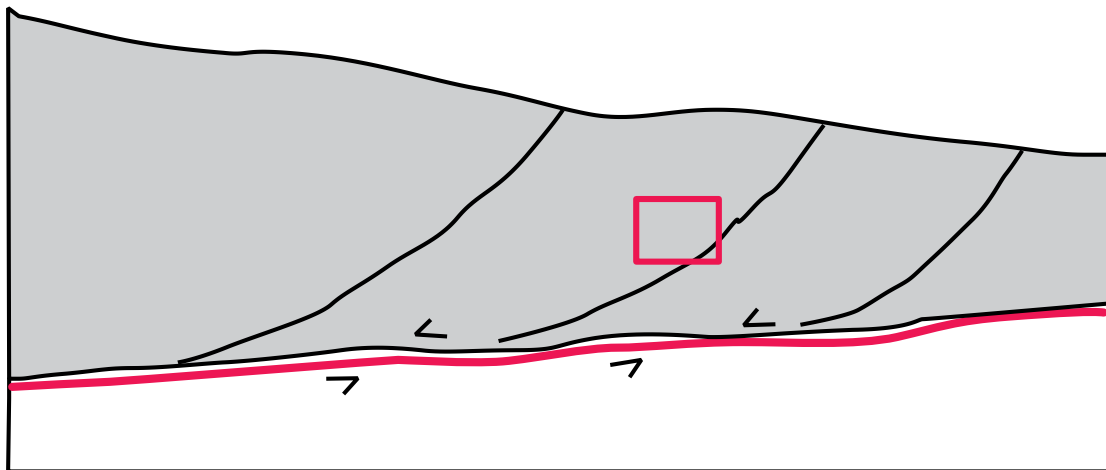


Figure 7.1: Source of fluids. The red line highlights a basal detachment fault, a potential collection point for fluids. The red box approximates the position of the WMC.

The Wongwibinda Complex is bound to the east by the Wongwibinda Fault (Figure 1.3), a subsidiary of the Hunter Bowen Thrust Fault (Collins, 1991). The last activity along the Wongwibinda Fault was during the Hunter Bowen Orogeny (260Ma), which was thrust movement at greenschist facies grade. If the Wongwibinda Fault was active as a normal fault at the time of HTLP metamorphism during the Carboniferous, it could act as a preferred path for the transport of fluids upwards through the crust to the WMC (Figure 7.1, red box).

Migration of fluid through the crust

In order to maintain heat and the silica content necessary to metasomatise and form a quartz vein sequence as large as the quartzite, the fluids will have to migrate quickly through the crust to the WMC.

The general process for forming quartz veins is for fluids to flow through an open fracture (Bons, 2001) (Figure 7.2, inset I). This process can be slow, following the path of continental geotherm. Silica content is highly dependent on temperature, and following this path (I) it would rapidly precipitate out at depth, losing silica and heat until by the time the fluids reach the WMC the concentration is too low to form large quartz vein sequences.

Mobile hydrofracturing (Weertman, 1971, Bons, 2001) is a process that would allow pulses of fluid to rapidly ascend through the crust. A pocket of fluid forms at depth, and pressure

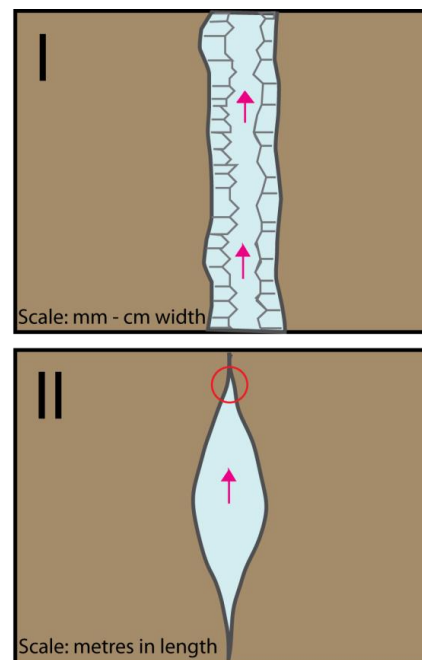
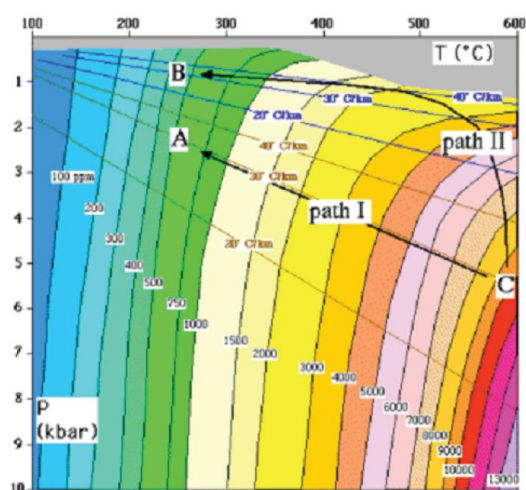


Figure 7.2: Left - Silica solubility in fluid with temperature and pressure (adapted from Bons, 2001). Path I describes ascent along the geotherm, through mechanisms such as flow through a fracture (inset I). Path II describes rapid ascent through the crust, through a mobile hydrofracturing method (inset II).

differences result in a concentration of stress at the tip of this pocket (Figure 7.2, inset II, red circle), causing the rock to fracture. The fluid moves upwards with the fracture as it opens at the top and closes at the bottom. This kind of process has been estimated to move as fast as 1m/s, translating to 10km in 3 hours, delivering hot and silica rich fluids to the complex.

Fluids arrive at the WMC

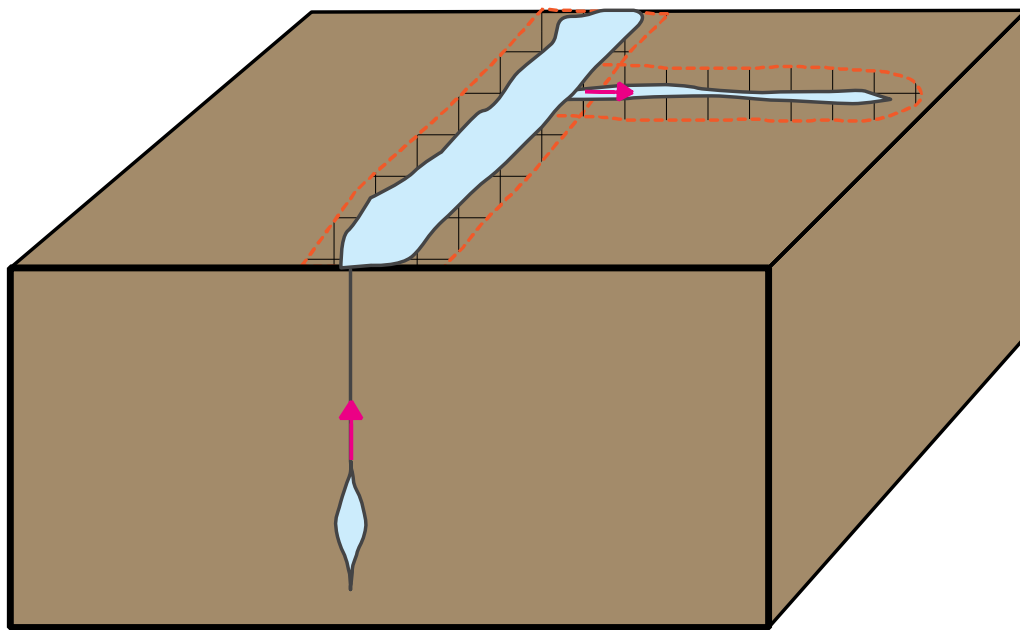


Figure 7.3: Fluids arrive at the WMC. Crystallisation of fluids occurs, forming the quartz vein sequence (central blue stripe). Following this, fluids are channelled out into the surrounding schists (horizontal blue stripe). Fluid-rock interactions occur with fluid migration (patterned area of schist). Pink arrows indicate direction of fluid movement.

Some geological feature, such as a fracture plane in the complex or the fluid passing the brittle-ductile boundary, results in the pocket of fluid being diverted off its upwards trajectory, slowing it down.

At this point it will start losing heat at a faster pace, precipitating quartz and forming a large quartz vein sequence (Bons, 2001) (Figure 7.3). Depending on its composition, the fluid will

continue to precipitate minerals and, through fluid-rock interactions, metasomatise the host rock as it is diverted and channelled outwards into the surrounding schists. Enrichment and depletion will occur following the channels of fluid.

Fluids are variably channelled through the schists

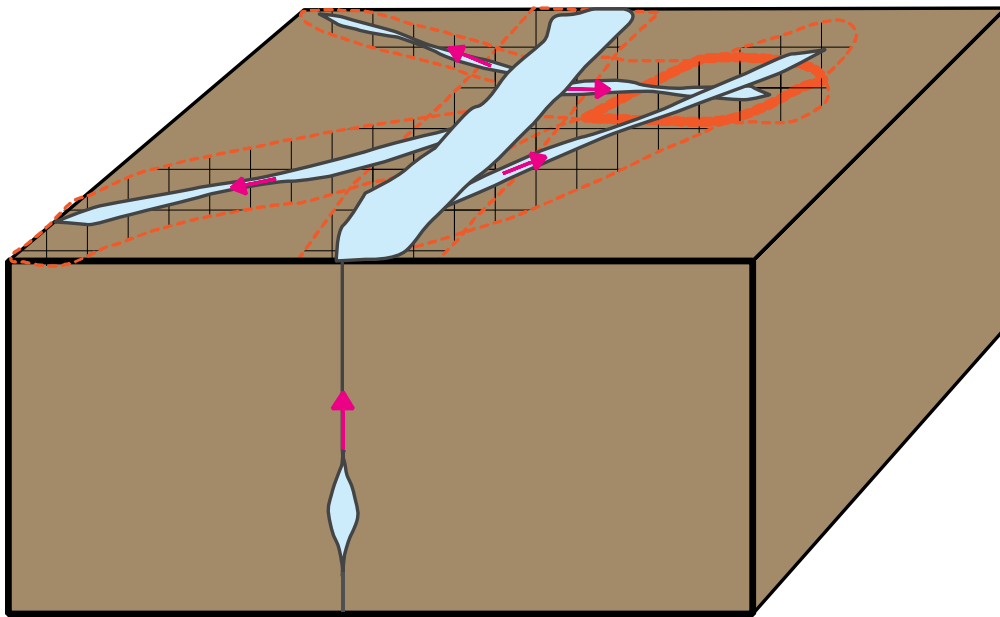


Figure 7.4: Fluids are variably channelled through the schists. As each pulse of fluid arrives in the WMC it is diverted through the schists along different paths, causing metasomatism along these channels. Areas of rock may experience greater rates of metasomatism if they experience multiple pulses of fluids, represented here by the crossing of two channels.

Multiple pulses of fluids exploit the plane of weakness that the initial pocket moved along, being channelled to this site. The site of high flux experiences multiple pulses of fluid of different volumes, which are diverted and channelled outwards. Pulses of differing volumes will affect different volumes of rock; large pulses of fluid may be channelled further out, whereas smaller pulses may only affect rocks adjacent to the large quartz vein/quartzite.

If the channels were to intersect, or if multiple pulses of fluid are diverted along the same channel, then at this point the rocks would undergo several pulses of metasomatism. In this way a patchy distribution of metasomatism can form.

Fluids vary in composition

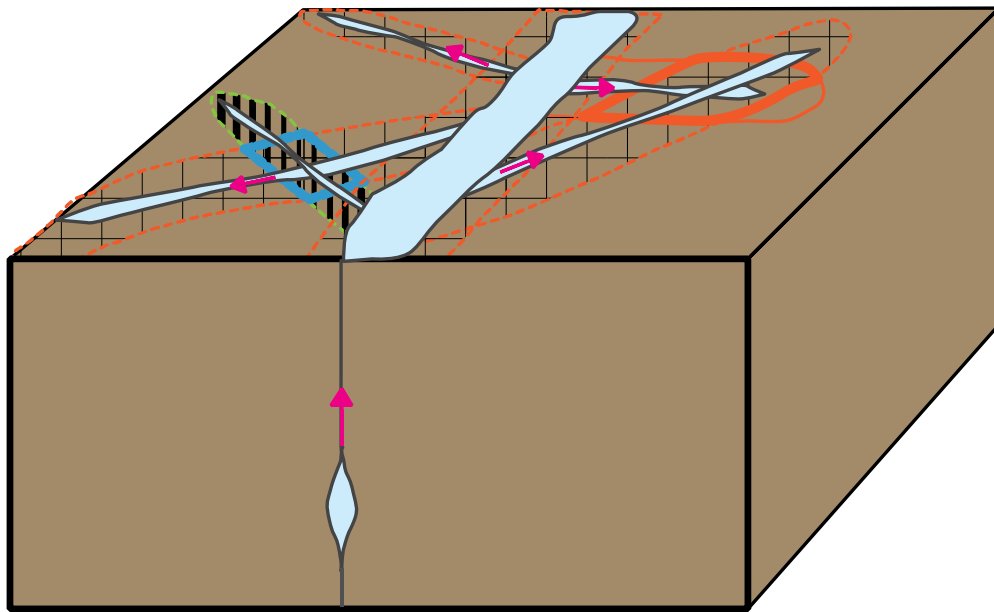


Figure 7.5: Pulses of fluid arriving in the WMC may vary in composition. As these are channelled out into the surrounding rock, patches of metasomatism will occur with different chemical signatures (green stripy halo around the channel).

Pulses of fluid can vary not only in volume but also in chemical composition. In this way each pulse can have a unique affect on the host rock, causing further variation to the degree of metasomatism but also causing a patchy distribution of chemical changes (Figure 7.5). Changes to fluid:rock ratios can have similar effects in terms of patchy metasomatism and chemical changes.

Suggestions for further research

Origin of the quartzite unit

Analyses of the quartzite unit in this study were limited to one or two samples per technique. Further research should perform microstructure analysis on a greater range of samples of the quartzite, especially in lower strain samples including samples from the hinge zone and limbs of a quartzite unit.

This study analysed the differing orientations between one dark and one light band within the quartzite. Results from this study were inconclusive however this was a restricted sample size. Analyses of several bands in the one sample are recommended, in order to better quantify differences between them.

Further mapping work both at this study site and around the quartzites immediately to the north are recommended. In particular the boundary between the quartzite and the schist should be studied to look for conformity, or lack thereof, between bedding in the schist and the boundary of the quartzite.

Presence of fluids in the aureole

Further studies of fluids through the aureole would benefit from isotopic studies, which were unavailable during the course of this study. These would be useful in determining several features:

- Homogenisation of oxygen isotope signatures in the aureole compared to the regional values would be strong evidence for the presence of fluids (Chamberlain and Rumble, 1988);

- Furthermore, the isotopic composition of veins can be used to constrain an origin for the fluid (marine, meteoric, magmatic, metamorphic, or formation brines) by comparing oxygen isotope ratios from fluids of known origins (Kerrick, 1986, Kerrich and Feng, 1992);
- Studies of sulphides in small veins may also be useful in constraining the source of fluids, however unless the fluids are sourced from outside the accretionary prism sediments, inconclusive results are expected (Andrew et al., 1993)

Also not explored in this study, fluid inclusions could be used to determine chemical composition of the fluids (Andrew et al., 1993, Boiron et al., 1999) which can then be related to metasomatism and changes to mineral chemistry.

Metasomatism in the schists

Outcrops of schists were scarce along the transect performed in this study, limiting the range of samples collected with distance to the quartzite. This low data density through the aureole inhibits effective mapping of degrees of metasomatism. A more systematic sampling method, such as sampling in a grid pattern, could be employed in order to map metasomatism through the aureole.

More detailed studies on the fluid-rock interaction would be beneficial in constraining fluid chemistry and the contribution to chemistry of schists from the fluids. In particular this can be determined through comparing REE and trace element compositions of quartz between vein and wall rock material (Wagner et al., 2010).

Temperature gradients in the thermal anomaly

As the cordierite isograd highlights a thermal anomaly around the quartzite, correlating temperature increases are to be expected through the aureole. Cordierite grain size was analysed in this study, with no obvious spatial relationships. Further investigation of cordierite mode percent in hand samples may give a better handle on temperature variations.

Similarly, electron microprobe analysis of garnets in the quartzite, veins and schists could be used in the application of thermodynamic calculations, such as the program THERMOCALC (Powell and Holland, 1988). As garnets are only found at and adjacent to the site of fluid flux (and therefore heat advection), analyses such as these would provide a maximum temperature for the aureole.

Using such a program, with inputs of XRF data and the assemblage of schists in the aureole, P-T pseudosections can be calculated such as those constructed for other areas in the complex (Craven et al., 2012, Danis et al., 2010). Pseudosections are used to provide estimates of P-T conditions, through which metamorphic grades of the aureole could be mapped on a large scale to examine patterns to regional fluid flux.

On a smaller scale, detailed examination and chemical characterisation of a small and well exposed outcrop should be performed to record local changes. Such analyses can be employed to better constrain the local variability of fluid flux and the resulting metamorphic reactions.

Role of the pegmatite

The pegmatite unit within the study site was not explored in this study beyond mapping and structural measurements. As this unit forms from melt, it would have introduced heat to the surrounding schists. Dating of the pegmatite would be useful in determining the timing and therefore possible influence on HTLP metamorphism in the area.

Analyses of mineral chemistry could also be useful in examining the influence of the pegmatite in the area. Enrichment of K in the schists is documented through both whole rock and mineral chemistry, however this is not supported by corresponding high K values in the quartzite. The pegmatite could be a source of K for the aureole, as large orthoclase grains were observed in this unit. Similarly, large tourmaline grains had formed here, which were also observed in a large vein in the schists (W1221). Other studies have observed Mn-rich garnets forming from Mn-rich fluids exsolving from pegmatite bodies (Harrison, Whitworth). Therefore the intrusion of the pegmatite-forming melt was likely accompanied by the addition of solute rich fluids to the surrounding schists, possibly forming Mn-rich garnets in veins and enriching the schists in K.

CHAPTER 8 - CONCLUSION

Due to spatial and temporal relationships, yet to be presented is an effective mechanism to explain the thermal elevation of the crust to form the HTLP metamorphic belt at Wongwibinda. Presented in this thesis is a model of aqueous fluid advection, whereby fluids are focussed through the WMC and drive the thermal evolution of the complex.

Field relationships highlight an association between cordierite-bearing rock and folded quartzite units through the region. Through this spatial relationship and comparable mineral chemistry with large quartz veins in the Rampsbeck Schists, the quartzite unit is determined as a site of high fluid flux. Outcrop patterns and structural data suggest the quartzite is potentially a large quartz vein sequence and not a sedimentary feature however efforts to classify the chemistry and microstructure of this rock were inconclusive.

Mineralogy and whole rock chemistry of cordierite-bearing rock from an aureole around a quartzite unit reveals a complex, local metasomatic history involving enrichment of Si, Fe, K and heavy REEs, as well as depletion of Ca. Metasomatism does not occur in smooth gradients with distance from the site of fluid flux; rather, patchy metasomatism has occurred through the channelling of pulses fluids.

Further studies could better constrain the presence of fluid and fluid chemistry through isotopic studies. The role of the pegmatite unit in both a thermal and metasomatic capacity has not yet been investigated. As well as this, modelling of peak P-T conditions and mapping of metasomatic activity could aid in quantifying the thermal history of this aureole.

Evidence from the quartzite studied and its thermal aureole point towards a significant role of fluids in altering the local thermal regime, leading to the proposal of aqueous fluid

advection as a plausible mechanism for heating the shallow crust. In this situation, this model involves fast migration of fluid pulses through the crust to the WMC, followed by slowing of the fluid migration and vein growth. Variable channelling of fluid pulses occurs outwards from the site of high flux, forming a network of veins and causing metasomatism and thermal elevation in the surrounding schists.

REFERENCES

- ANDREW, A. S., GULSON, B. L. & MIZON, K. J. (1993) Nature and evolution of metamorphic fluids associated with turbidite-hosted gold deposits: Hill End goldfield, NSW, Australia. *Mineralogical Magazine*, 57, 423-436.
- AUDLEY-CHARLES, M. G. (1965) Some aspects of the chemistry of Cretaceous siliceous sedimentary rocks from eastern Timor. *Geochimica et Cosmochimica Acta*, 29, 1175-1192.
- BARRETT, T. J. (1981) Chemistry and mineralogy of Jurassic bedded chert overlying ophiolites in the North Apennines, Italy. *Chemical Geology*, 34, 289-317.
- BINNS, R. A. (1966) Granitic intrusions and regional metamorphic rocks of Permian Age from the Wongwibinda District, north-eastern New South Wales. *Journal and Proceedings, Royal Society of New South Wales*, 99, 5-36.
- BODORKOS, S., OLIVER, N. H. S. & CAWOOD, P. A. (1999) Thermal evolution of the central Halls Creek Orogen, northern Australia. *Australian Journal of Earth Sciences*, 46, 453-465.
- BOIRON, M.-C., MOISSETTE, A., CATHELIN, M., BANKS, D., MONNIN, C. & DUBESSY, J. (1999) Detailed determination of palaeofluid chemistry: an integrated study of sulphate-volatile rich brines and aquo-carbonic fluids in quartz veins from Ouro Fino (Brazil). *Chemical Geology*, 154, 179-192.
- BONS, A.-J. & BONS, P. D. (2003) The development of oblique preferred orientations in zeolite films and membranes. *Microporous and Mesoporous Materials*, 62, 9-16.
- BONS, P. D. (2000) The formation of veins and their microstructures. In: Stress, Strain and Structure, A volume in honour of W D Means. IN JESSELL, M. W. & URAI, J. L. (Eds.) *Journal of the Virtual Explorer*.
- BONS, P. D. (2001) The formation of large quartz veins by rapid ascent of fluids in mobile hydrofractures. *Tectonophysics*, 336, 1-17.
- BONS, P. D., ELBURG, M. A. & GOMEZ-RIVAS, E. (2012) A review of the formation of tectonic veins and their microstructures. *Journal of Structural Geology*, 43, 33-62.
- BUCK, W. R., MARTINEZ, F., STECKLER, M. S. & COCHRAN, J. R. (1988) Thermal consequences of lithospheric extension: Pure and simple. *Tectonics*, 7, 213-234.
- CAWOOD, P. A., LEITCH, E. C., MERLE, R. E. & NEMCHIN, A. A. (2011) Orogenesis without collision: Stabilizing the Terra Australis accretionary orogen, eastern Australia. *Geological Society of America Bulletin*, 123, 2240-2255.
- CHAMBERLAIN, C. P. & RUMBLE, D. (1988) Thermal anomalies in a regional metamorphic terrane: An isotopic study of the role of fluids. *Journal of Petrology*, 29, 1215-1232.
- CHAMBERLAIN, C. P. & RUMBLE, D. (1989) The influence of fluids on the thermal history of a metamorphic terrain: New Hampshire, USA. *Geological Society, London, Special Publications*, 43, 203-213.
- CHUDY, T. C., ZEH, A., GERDES, A., KLEMD, R. & BARTON JR, J. M. (2008) Palaeoarchaeon (3.3 Ga) mafic magmatism and Palaeoproterozoic (2.02 Ga) amphibolite-facies metamorphism in the Central Zone of the Limpopo Belt: New geochronological, petrological and geochemical constraints from metabasic and metapelitic rocks from. *South African Journal of Geology*, 111, 387-408.
- COLLINS, W. J. (1991) A reassessment of the 'Hunter-Bowen Orogeny': Tectonic implications for the southern New England fold belt. *Australian Journal of Earth Sciences*, 38, 409-423.
- CONNOLLY, J. A. D. (1997) Mid-crustal focussed fluid movement: thermal consequences and silica transport. IN JAMTVEIT, B. & YARDLEY, B. W. (Eds.) *Fluid Flow and Transport in Rocks*. London, Chapman & Hall.
- COX, S. F. & ETHERIDGE, M. A. (1983) Crack-seal fibre growth mechanisms and their significance in the development of oriented layer silicate microstructures. *Tectonophysics*, 92, 147-170.

- CRAVEN, S. J., DACZKO, N. R. & HALPIN, J. A. (2012) Thermal gradient and timing of high-T–low-P metamorphism in the Wongwibinda Metamorphic Complex, southern New England Orogen, Australia. *Journal of Metamorphic Geology*, 30, 3-20.
- CRESSMAN, E. R. (1962) Data of Geochemistry, Ch T: Non-detrital siliceous sediments (6th ed.). *U.S. Geological Survey Professional Papers*, 440-T, 23.
- DANIS, C. R., DACZKO, N. R., LACKIE, M. A. & CRAVEN, S. J. (2010) Retrograde metamorphism of the Wongwibinda Complex, New England Fold Belt and the implications of 2.5D subsurface geophysical structure for the metamorphic history. *Australian Journal of Earth Sciences*, 57, 357-375.
- DE YOREO, J. J., LUX, D. R. & GUIDOTTI, C. V. (1991) Thermal modelling in low-pressure/high-temperature metamorphic belts. *Tectonophysics*, 188, 209-238.
- DIRKS, P. H. G. M., HAND, M., COLLINS, W. J. & OFFLER, R. (1992) Structural-metamorphic evolution of the Tia Complex, New England Fold Belt; Thermal overprint of an accretion-subduction complex in a compressional back-arc setting. *Journal of Structural Geology*, 14, 669-688.
- FARRELL, T. R. (1988) Structural geology and tectonic development of the Wongwibinda Metamorphic Complex. IN KLEEMAN, J. D. (Ed.) *New England Orogen: tectonics and metallogenesis*. Department of Geology & Geophysics, University of New England.
- FARRELL, T. R. (1992) Deformation, Metamorphism, and Migmatite Genesis in the Wongwibinda Metamorphic Complex, Eastern Australia. Newcastle, University of Newcastle.
- FLOOD, R. H. & SHAW, S. E. (1977) Two “S-type” granite suites with low initial $^{87}\text{Sr}/^{86}\text{Sr}$ ratios from the New England Batholith, Australia. *Contributions to Mineralogy and Petrology*, 61, 163-173.
- FLOOD, R. H. & VERNON, R. H. (1978) The Cooma Granodiorite, Australia: An example of in situ crustal anatexis? *Geology*, 6, 81-84.
- HARA, H., KURIHARA, T., KURODA, J., ADACHI, Y., KURITA, H., WAKITA, K., HISADA, K.-I., CHARUSIRI, P., CHAROENTITIRAT, T. & CHAODUMRONG, P. (2010) Geological and geochemical aspects of a Devonian siliceous succession in northern Thailand: Implications for the opening of the Paleo-Tethys. *Palaeogeography, Palaeoclimatology, Palaeoecology*, 297, 452-464.
- HENSEN, B. J. (1971) Theoretical phase relations involving cordierite and garnet in the system $\text{MgO-FeO-Al}_2\text{O}_3\text{-SiO}_2$. *Contributions to Mineralogy and Petrology*, 33, 191-214.
- HENSON, A. (2000) A geochemical study of the metasediments of the Wongwibinda Metamorphic Complex, Southern NEFB, Australia. *Honours Thesis, Department of Earth and Planetary Sciences, Macquarie University*.
- HILGERS, C., KOEHN, D., BONS, P. D. & URAI, J. L. (2001) Development of crystal morphology during uniaxial growth in a progressively widening vein: II. Numerical simulations of the evolution of antitaxial fibrous veins. *Journal of Structural Geology*, 23, 873-885.
- HOISCH, T. D. (1987) Heat transport by fluids during Late Cretaceous regional metamorphism in the Big Maria Mountains, southeastern California. *Geological Society of America Bulletin*, 98, 549-553.
- HOISCH, T. D. (1991) The thermal effects of pervasive and channelized fluid flow in the deep crust. *The Journal of Geology*, 99, 69-80.
- IKEDA, T., HIRAMINE, A. & ONOUE, T. (2010) Orthopyroxene–cordierite mafic gneiss from the Nomamisaki metamorphic rocks, Southern Kyushu, Japan: Implication for western continuation of the Usuki–Yatsushiro Tectonic Line. *Island Arc*, 19, 230-242.
- JENKINS, R. B., LANDENBERGER, B. & COLLINS, W. J. (2002) Late Palaeozoic retreating and advancing subduction boundary in the New England Fold Belt, New South Wales. *Australian Journal of Earth Sciences*, 49, 467-489.
- JOHNSON, S. E. (1999) Deformation and possible origins of the Cooma Complex, southeastern Lachlan Fold Belt, New South Wales. *Australian Journal of Earth Sciences*, 46, 429-442.
- KALT, A., ALTHERR, R. & LUDWIG, T. (1998) Contact metamorphism in Pelitic rocks on the Island of Kos (Greece, Eastern Aegean Sea): A test for the Na-in-Cordierite thermometer. *Journal of Petrology*, 39, 663-688.

- KERRICH, R. (1986) Fluid infiltration into fault zones: Chemical, isotopic, and mechanical effects. *Pure and Applied Geophysics*, 124, 225-268.
- KERRICH, R. & FENG, R. (1992) Archean geodynamics and the Abitibi-Pontiac collision: implications for advection of fluids at transpressive collisional boundaries and the origin of giant quartz vein systems. *Earth-Science Reviews*, 32, 33-60.
- KORSCH, R. J., TOTTERDELL, J. M., CATHRO, D. L. & NICOLL, M. G. (2009) Early Permian East Australian Rift System. *Australian Journal of Earth Sciences*, 56, 381-400.
- LANDENBERGER, B., FARRELL, T. R., OFFLER, R., COLLINS, W. J. & WHITFORD, D. J. (1995) Tectonic implications of Rb-Sr biotite ages for the Hillgrove Plutonic Suite, New England Fold Belt, N.S.W., Australia. *Precambrian Research*, 71, 251-263.
- LANGONE, A., GODARD, G., PROSSER, G., CAGGIANELLI, A., ROTTURA, A. & TIEPOLO, M. (2010) P-T-t path of the Hercynian low-pressure rocks from the Mandatoriccio complex (Sila Massif, Calabria, Italy): new insights for crustal evolution. *Journal of Metamorphic Geology*, 28, 137-162.
- LEGGETT, J. K. & SMITH, T. K. (1980) Fe-rich deposits associated with Ordovician basalts in the Southern Uplands of Scotland: Possible lower Palaeozoic equivalents of modern active ridge sediments. *Earth and Planetary Science Letters*, 47, 431-440.
- LEITCH, E. C. (1975) Plate Tectonic Interpretation of the Paleozoic History of the New England Fold Belt. *Geological Society of America Bulletin*, 86, 141-144.
- LEONI, L. (1974) Le rocce silicee non detritiche dell'Appennino centro-settentrionale. *Atti della Società Toscana di Scienze Naturali, residente in Pisa*, Ser. A, 81, 187-221.
- MAKRYGINA, V. A. & SUVOROVA, L. F. (2011) Spessartine in the greenschist facies: Crystallization conditions. *Geochemistry International*, 49, 299-308.
- MUKHOPADHYAY, B. & HOLDAWAY, M. J. (1994) Cordierite-garnet-sillimanite-quartz equilibrium: I. New experimental calibration in the system FeO-Al₂O₃-SiO₂-H₂O and certain P-T-X_{H₂O} relations. *Contributions to Mineralogy and Petrology*, 116, 462-472.
- NORMAN, M. D., PEARSON, N. J., SHARMA, A. & GRIFFIN, W. L. (1996) Quantitative analysis of trace elements in geological materials by Laser Ablation ICPMS: Instrumental operating conditions and calibration values of NIST glasses. *Geostandards Newsletter*, 20, 247-261.
- OFFLER, R. & FOSTER, D. A. (2008) Timing and development of oroclinal in the southern New England Orogen, New South Wales. *Australian Journal of Earth Sciences*, 55, 331-340.
- PENNACCHIONI, G., MENEGON, L., LEISS, B., NESTOLA, F. & BROMILEY, G. (2010) Development of crystallographic preferred orientation and microstructure during plastic deformation of natural coarse-grained quartz veins. *J. Geophys. Res.*, 115, B12405.
- POWELL, R. & HOLLAND, T. J. B. (1988) An internally consistent dataset with uncertainties and correlations: 3. Applications to geobarometry, worked examples and a computer program. *Journal of Metamorphic Geology*, 6, 173-204.
- RICHARDS, S. W. & COLLINS, W. J. (2002) The Cooma Metamorphic Complex, a low-P, high-T (LPHT) regional aureole beneath the Murrumbidgee Batholith. *Journal of Metamorphic Geology*, 20, 119-134.
- RICHARDSON, S. W. (1968) Staurolite stability in a part of the system Fe-Al-Si-O-H. *Journal of Petrology*, 9, 467-488.
- ROBERTS, J., OFFLER, R. & FANNING, M. (2006) Carboniferous to Lower Permian stratigraphy of the southern Tamworth Belt, southern New England Orogen, Australia: Boundary sequences of the Werrie and Rouchel blocks. *Australian Journal of Earth Sciences*, 53, 249-284.
- ROSENBAUM, G., LI, P. & RUBATTO, D. (2012) The contorted New England Orogen (eastern Australia): New evidence from U-Pb geochronology of early Permian granitoids. *Tectonics*, 31, TC1006.
- RUMBLE, D. (1989) Evidence of fluid flow during regional metamorphism. *European Journal of Mineralogy*, 1, 731-737.
- SANDIFORD, M. & HAND, M. (1998) Australian Proterozoic high-temperature, low-pressure metamorphism in the conductive limit. *Geological Society, London, Special Publications*, 138, 109-120.

- SANDIFORD, M., HAND, M. & MCLAREN, S. (1998) High geothermal gradient metamorphism during thermal subsidence. *Earth and Planetary Science Letters*, 163, 149-165.
- SCRIMGEOUR, I., SMITH, J. B. & RAITH, J. G. (2001) Palaeoproterozoic high-T, low-P metamorphism and dehydration melting in metapelites from the Mopunga Range, Arunta Inlier, central Australia. *Journal of Metamorphic Geology*, 19, 739-757.
- SWINDON, H. S. (1976) Chemical sedimentation associated with Mid-Paleozoic volcanism in Central Newfoundland. *M.Sc. Thesis*. Memorial University, St. John's, Newfoundland.
- THOMPSON, A. B. & CONNOLLY, J. A. D. (1992) Migration of metamorphic fluid: some aspects of mass and heat transfer. *Earth-Science Reviews*, 32, 107-121.
- THURSTON, D. (1972) Studies on bedded cherts. *Contributions to Mineralogy and Petrology*, 36, 329-334.
- VEARNCOMBE, J. R. (1993) Quartz vein morphology and implications for formation depth and classification of Archaean gold-vein deposits. *Ore Geology Reviews*, 8, 407-424.
- VERNON, R. H. (1982) Isobaric cooling of two regional metamorphic complexes related to igneous intrusions in southeastern Australia. *Geology*, 10, 76-81.
- VIELZEUF, D. (1983) The spinel and quartz associations in high grade xenoliths from Tallante (S.E. Spain) and their potential use in geothermometry and barometry. *Contributions to Mineralogy and Petrology*, 82, 301-311.
- VISSER, D., KLOPROGGE, J. T. & MAIJER, C. (1994) An infrared spectroscopic (IR) and light element (Li, Be, Na) study of cordierites from the Bamble Sector, south Norway. *Lithos*, 32, 95-107.
- WAGNER, T., BOYCE, A. J. & ERZINGER, J. R. (2010) Fluid-rock interaction during formation of metamorphic quartz veins: A REE and stable isotope study from the Rhenish Massif, Germany. *American Journal of Science*, 310, 645-682.
- WAKEEL, S. K. E. & RILEY, J. P. (1961) Chemical and mineralogical studies of deep-sea sediments. *Geochimica et Cosmochimica Acta*, 25, 110-146.
- WALTHER, J. V. & ORVILLE, P. M. (1982) Volatile production and transport in regional metamorphism. *Contributions to Mineralogy and Petrology*, 79, 252-257.
- WEERTMAN, J. (1971) Theory of Water-Filled Crevasses in Glaciers Applied to Vertical Magma Transport beneath Oceanic Ridges. *J. Geophys. Res.*, 76, 1171-1183.
- WILSON, S. A. (1997) The collection, preparation, and testing of USGS reference material BCR-2, Columbia River, Basalt. *U.S. Geological Survey Open-File Report 98-xxx*.
- WINDH, J. (1995) Saddle reef and related gold mineralization, Hill End gold field, Australia; evolution of an auriferous vein system during progressive deformation. *Economic Geology*, 90, 1764-1775.
- WINSLOW, D. M., ZEITLER, P. K., CHAMBERLAIN, C. P. & HOLLISTER, L. S. (1994) Direct evidence for a steep geotherm under conditions of rapid denudation, Western Himalaya, Pakistan. *Geology*, 22, 1075-1078.
- WYHLIDAL, S., TROPPER, P., THÖNY, W. & KAINDL, R. (2009) Minor element and carbonaceous material thermometry of high-grade metapelites from the Sauwald Zone, Southern Bohemian Massif (Upper Austria). *Mineralogy and Petrology*, 97, 61-74.
- YONGZHANG, Z., GUANGCHI, T., CHOWN, E., GUHA, J. & HUANZHANG, L. (1994) Petrologic and geochemical characteristics and origin of Gusui cherts, Guangdong Province, China. *Chinese Journal of Geochemistry*, 13, 118-131.

APPENDICES



A – Whole rock chemistry raw data

I: LA-ICP-MS Run 1 Analyses of standards

(ppm)	STD610-01	1 sigma	STD610-02	1 sigma	AGV-R2-9	1 sigma	BCR-R2-9	1 sigma
Be9	465.26	15.61	455.95	15.3	3.12	0.19	3.15	0.19
Na23	96770.89	2945.76	97641.98	2972.25	27045.52	823.59	20764.33	632.38
Mg25	456.69	13.95	453.21	13.85	9929.2	302.31	20174.72	613.87
Al27	10120.62	314.96	9983.42	310.71	99655.16	3103.04	77729.2	2421.09
Si29	334048.1	10564.55	334048.1	10564.58	277191.5	8771.28	252884.7	8001.71
P31	343.46	15.15	341.57	15.08	1509.11	66.7	1182.91	52.34
K39	461.96	14.04	464.26	14.11	21565.03	655.34	13632.46	414.31
Ca42	82079.05	2490.31	81714.67	2479.23	37066.39	1133.95	51276.72	1562.23
Ca43	82037.77	2482.12	81766.95	2474.07	47126.38	1456.82	58332.16	1788.28
Sc45	452.8	14	447.05	13.82	16.6	0.56	35.66	1.14
Ti47	478.19	14.78	473.73	14.65	6892.61	212.2	14828.09	455.86
V51	441.18	13.64	447.07	13.82	113.62	3.55	398.16	12.34
Cr53	386.57	11.8	389.53	11.89	64.92	2.38	32.28	1.35
Mn55	439.31	13.58	433.35	13.4	703.6	21.79	1400.61	43.36
Fe57	462.12	17.03	443.88	16.41	32659.93	1195.87	66663.61	2449.05
Co59	389.91	11.95	385.96	11.83	13.58	0.45	32.41	1.02
Ni60	418.99	13.4	410.88	13.15	42.19	1.49	28.77	1.04
Ni62	415.72	13	414.15	12.96	42.95	2.11	30.24	1.57
Cu63	434.34	13.21	431.38	13.13	48.31	1.54	15.23	0.52
Cu65	433.68	13.23	432.13	13.19	47.07	1.57	16.16	0.6
Zn66	430.49	13.15	428.01	13.07	88.88	2.88	124.62	3.95
Ga69	431.67	13.01	430.28	12.97	121.51	3.7	76.43	2.34
Ga71	429.03	13.08	433.11	13.21	19.67	0.66	20.45	0.67
Rb85	429.4	12.96	430.63	13	56.06	1.73	40.9	1.27
Sr86	525.74	15.93	524.18	15.89	667.1	20.56	338.71	10.66
Sr88	526.26	15.94	523.62	15.86	673.84	20.44	350.1	10.63
Y89	492.62	15.14	487.22	14.97	18.64	0.61	34.7	1.1
Zr90	493.59	15.47	486.18	15.24	244.8	7.75	201.73	6.39
Nb93	513.38	15.65	510.49	15.57	16.32	0.54	14.62	0.48
Cs133	360.66	11.05	361.29	11.07	0.792	0.048	0.88	0.046
Ba137	448.95	14.04	442.84	13.86	1121.41	35.22	678.23	21.36
Ba138	446.75	13.51	445.17	13.46	1120.56	33.91	669.79	20.28
La139	440.82	13.33	439.11	13.28	38.52	1.2	25.29	0.79
Ce140	445.94	13.43	446.09	13.44	66.08	2.02	50.44	1.54
Pr141	470.57	14.46	465.25	14.29	8.26	0.28	7.21	0.24
Nd146	454.36	13.7	453.62	13.68	32.76	1.12	30.38	1.03
Sm147	466.84	14.66	458.95	14.42	5.63	0.3	7.01	0.33
Eu153	453.92	13.94	449.91	13.81	1.662	0.081	2.039	0.09
Gd157	452.08	13.83	447.78	13.7	4.1	0.24	6.86	0.32
Tb159	445.16	13.79	438.69	13.59	0.583	0.034	0.926	0.045
Dy161	457.03	14.5	448.73	14.24	3.64	0.21	6.46	0.29
Ho165	478.78	14.94	471.04	14.7	0.63	0.037	1.367	0.06
Er167	467.15	14.73	458.66	14.46	1.94	0.13	3.59	0.18
Tm169	458.84	14.7	448.97	14.39	0.26	0.021	0.523	0.03
Yb173	483.9	15.55	473.83	15.22	1.75	0.13	3.72	0.2
Lu175	470.95	14.77	462.85	14.52	0.243	0.02	0.529	0.03
Hf178	462.69	14.79	453.09	14.48	5.72	0.25	5.16	0.22
Ta181	496.26	16.12	484.69	15.74	0.949	0.051	0.88	0.046
Pb208	419.6	12.66	418.6	12.63	12.15	0.4	8.89	0.3
Th232	484.38	15.02	477.47	14.8	6.78	0.24	6.29	0.22
U238	486.23	14.63	487.82	14.68	1.872	0.073	1.63	0.063

Element	BHVOR2-9	1 sigma	GSP-R2-9	1 sigma	STD610-3	1 sigma	STD610-4	1 sigma
Be9	1.77	0.14	1.94	0.15	460.25	17.01	461.32	17.16
Na23	14671.54	446.94	18387.18	560.27	97318.63	3031.24	97050.72	3027.73
Mg25	41378.2	1258.99	5594.8	170.65	455.02	14.16	455.05	14.17
Al27	77952.55	2429.33	87224.95	2719.95	10054.62	329.17	10055.22	330.35
Si29	233252.3	7381.14	314212.8	9942.93	334048.1	10564.78	334048.1	10564.75
P31	916.34	40.68	930.45	41.51	339.93	15.57	344.96	15.84
K39	3933.73	119.6	39074.54	1187.85	464.52	14.33	461.73	14.26
Ca42	84525.43	2570.54	14897.36	470.46	82141.35	2521.8	81691.11	2510.04
Ca43	89635.24	2735.91	21602.94	715.62	81823.4	2486.3	81987.91	2491.8
Sc45	33.69	1.08	9.79	0.37	450.26	14.5	449.87	14.53
Ti47	17765	546.26	4782.57	147.63	474.47	15.17	477.55	15.3
V51	306.14	9.5	53.25	1.69	443.26	14.37	444.58	14.46
Cr53	265.44	8.38	37.94	1.67	388.21	12.11	387.74	12.11
Mn55	1216.48	37.69	277.83	8.65	436.36	14.25	436.56	14.31
Fe57	60569.74	2235.82	21701.47	806.4	452.5	23.45	454.04	23.99
Co59	38.78	1.22	42.44	1.34	388.88	12.38	387.26	12.37
Ni60	119.08	3.94	48.98	1.74	413.59	15	416.51	15.24
Ni62	120.28	4.54	49.06	2.44	417.97	13.87	412.26	13.73
Cu63	108.32	3.35	30.55	1.01	432.85	13.44	433.01	13.46
Cu65	109.62	3.46	30.89	1.1	431.07	13.51	434.68	13.65
Zn66	91.23	2.94	105.25	3.41	430.24	13.34	428.47	13.3
Ga69	29.59	0.93	123.74	3.78	431.52	13.08	430.54	13.05
Ga71	20.2	0.67	32.19	1.05	431.44	13.53	430.5	13.53
Rb85	8.28	0.29	206.96	6.3	430.54	13.04	429.47	13.01
Sr86	418.8	13.06	236	7.89	525.81	16.01	524.27	15.97
Sr88	417.25	12.67	234.33	7.14	526.18	16.11	523.94	16.05
Y89	25.89	0.83	26.19	0.85	490.59	15.56	489.55	15.56
Zr90	180.77	5.74	671.56	21.17	491.67	16.39	488.59	16.35
Nb93	20.63	0.66	32.78	1.05	513.75	15.95	510.42	15.87
Cs133	0.095	0.019	0.961	0.054	363.27	11.52	358.87	11.41
Ba137	131.53	4.31	1285.58	40.44	448.12	14.88	444.14	14.8
Ba138	133.47	4.07	1294.1	39.17	447.08	13.63	445.02	13.57
La139	15.58	0.5	191.23	5.82	440.69	13.4	439.39	13.36
Ce140	36.44	1.12	435.94	13.16	445.14	13.45	446.82	13.51
Pr141	5.67	0.19	57.88	1.81	469.28	14.98	466.91	14.94
Nd146	25.39	0.89	220.45	6.8	453.79	13.7	454.21	13.71
Sm147	6.44	0.31	27.64	1.04	463.92	15.66	462.3	15.68
Eu153	2.105	0.093	2.31	0.11	454.17	14.5	450.05	14.4
Gd157	6.24	0.3	12.06	0.53	451.01	14.2	449.13	14.16
Tb159	0.839	0.042	1.299	0.062	441.9	14.41	442.23	14.47
Dy161	5.31	0.26	5.59	0.29	454.8	15.74	451.48	15.71
Ho165	1.051	0.05	1.016	0.053	475.18	15.8	474.99	15.87
Er167	2.61	0.15	2.24	0.15	462.94	15.76	463.23	15.85
Tm169	0.309	0.022	0.297	0.025	453.79	16.15	454.4	16.28
Yb173	2.45	0.15	2.01	0.15	480.85	17.21	477.47	17.21
Lu175	0.282	0.021	0.245	0.022	467.72	15.74	466.49	15.78
Hf178	4.43	0.2	16.72	0.62	458.85	16.08	457.4	16.12
Ta181	1.258	0.06	1.633	0.078	491.83	17.88	489.69	17.93
Pb208	1.908	0.085	41.2	1.28	418	12.72	420.17	12.79
Th232	1.417	0.065	121.74	3.81	480.46	15.65	481.65	15.74
U238	0.46	0.026	2.48	0.094	487.13	14.7	486.84	14.69

II: LA-ICP-MS Run 1 Analyses of samples

Element	Results in ppm							
	W1201-1	1 sigma	W1201-2	1 sigma	W1207e-1	1 sigma	W1207e-2	1 sigma
Be9	2.96	0.2	2.83	0.2	0.69	0.32	0.85	0.38
Na23	18266.49	556.78	18092.86	551.69	2527.63	77.51	2522.37	77.39
Mg25	10501.45	320.01	10530.42	320.97	3217.89	101.46	3521.77	110.42
Al27	88614.28	2765.37	88786.6	2773.16	10597.69	332.46	11297.1	354.77
Si29	305237.9	9659.14	305237.9	9658.96	428782.1	13617.96	428782.2	13621.81
P31	534.31	24.25	545.92	24.73	173.7	24.16	186.04	31.29
K39	27752.74	843.87	28145.36	856.01	4021.79	123.14	4461.24	136.68
Ca42	6236	219.34	6723.47	230.06	2230.76	516.92	<1794.05	675.1
Ca43	12629.01	451.5	10112.45	405.52	<3199.73	1304.31	<4185.15	1570.11
Sc45	18.59	0.63	18.18	0.62	5.76	0.75	6.05	0.91
Ti47	4882.52	150.77	4807.79	148.55	493.94	23.21	580.51	24.99
V51	109.42	3.43	107.88	3.38	44.04	1.64	44.57	1.64
Cr53	72.25	2.66	72.82	2.68	21.4	4.88	18.87	5.87
Mn55	515.59	16.03	513.7	15.98	2004.72	62.7	2043.32	63.97
Fe57	27831.94	1040.48	28146.91	1059.85	4318.34	174.11	4392.81	178.34
Co59	33.25	1.06	32.76	1.05	79.3	2.74	75.59	2.6
Ni60	69.25	2.4	72.04	2.49	52.14	2.74	54.69	2.79
Ni62	69.73	3.15	69.24	3.15	39.54	5.48	47.28	5.31
Cu63	24.12	0.81	23.05	0.78	6.51	0.74	8.27	0.87
Cu65	25.05	0.92	24.14	0.89	9.7	1.09	7.68	1.18
Zn66	104.1	3.38	102.73	3.33	44.42	2.65	51.88	2.84
Ga69	88.45	2.72	87.69	2.69	6.83	0.49	8.06	0.52
Ga71	19.73	0.67	19.9	0.68	3.23	0.47	2.84	0.47
Rb85	111.65	3.42	113.04	3.46	18.05	0.87	21.68	0.94
Sr86	162.79	5.81	161.35	5.74	31.55	13.14	<47.07	17.53
Sr88	168.94	5.16	168.81	5.16	16.99	0.78	18.88	0.81
Y89	31.58	1.02	32.07	1.03	2.21	0.24	2.75	0.25
Zr90	171.75	5.49	174.12	5.57	17.97	1.08	15.91	0.97
Nb93	12.83	0.44	12.71	0.43	1.95	0.22	1.79	0.21
Cs133	6.41	0.23	6.29	0.22	1.38	0.16	1.66	0.18
Ba137	997.41	31.46	1002.81	31.66	62.65	3.52	63.85	3.42
Ba138	985.79	29.85	981.14	29.71	58.44	2.09	64.87	2.25
La139	30.24	0.95	31.23	0.98	3.65	0.29	3.29	0.26
Ce140	64.87	1.98	65.27	2	13.18	0.59	13.83	0.59
Pr141	8.22	0.28	8.16	0.28	0.99	0.12	0.91	0.12
Nd146	31.67	1.11	32.98	1.15	4.76	0.64	3.43	0.51
Sm147	6.91	0.36	6.23	0.33	<0.53	0.25	<0.95	0.37
Eu153	1.415	0.077	1.364	0.074	0.043	0.03	0.282	0.1
Gd157	6.06	0.33	6.04	0.33	1.19	0.33	0.48	0.2
Tb159	0.823	0.045	0.95	0.049	0.116	0.039	0.046	0.023
Dy161	5.63	0.29	6.26	0.31	0.73	0.23	<0.61	0.25
Ho165	1.179	0.059	1.169	0.058	0.166	0.048	0.123	0.039
Er167	3.31	0.19	3.2	0.18	0.58	0.18	<0.34	0.17
Tm169	0.46	0.031	0.544	0.034	<0.072	0.022	<0.105	0.041
Yb173	3.38	0.21	3.24	0.21	0.51	0.2	0.65	0.21
Lu175	0.523	0.034	0.511	0.033	0.052	0.026	<0.077	0.04
Hf178	4.54	0.22	4.97	0.23	0.27	0.14	0.49	0.2
Ta181	1.344	0.068	1.283	0.065	1.05	0.13	1.23	0.14
Pb208	20.9	0.67	21.4	0.69	4.31	0.35	4.71	0.38
Th232	12.65	0.43	12.54	0.42	1.1	0.14	1.43	0.15
U238	3.24	0.12	3.28	0.12	1.09	0.11	1.31	0.11

Element	W1211a-1	1 sigma	W1211a-2	1 sigma	W1213c-1	1 sigma	W1213c-2	1 sigma
Be9	3.54	0.23	3.21	0.21	3.46	0.21	3.56	0.22
Na23	12464.02	380.66	12417.18	379.48	17344.02	530.37	17367.6	531.5
Mg25	11547.73	352.36	11682.35	356.64	11233.91	343.08	11233.97	343.28
Al27	95421.67	2990.7	95444.91	2995.66	91071.04	2862.62	91073.98	2867.49
Si29	296450.1	9381.28	296450.1	9381.48	299161.2	9466.4	299161.2	9466.53
P31	537.97	24.48	535.15	24.39	503.53	22.94	510.36	23.27
K39	34322.09	1044.9	34044.43	1036.88	28663.41	873.34	28741.73	876.16
Ca42	5625.45	202.24	5758.43	206.05	8023.14	264.1	8267.42	271.4
Ca43	11407.59	430.03	10328.43	425.36	12095.82	457.28	12431.73	471.55
Sc45	19.69	0.67	20.39	0.69	19.02	0.65	19.27	0.66
Ti47	5418.62	167.71	5365.24	166.24	4902.77	152.04	4951.29	153.72
V51	123.07	3.87	122.29	3.85	116.9	3.68	119.58	3.77
Cr53	89.54	3.21	85.33	3.09	81.33	2.9	72.74	2.66
Mn55	748.14	23.34	747.55	23.36	634.49	19.86	639.94	20.07
Fe57	30129.6	1165.16	30548.81	1193.88	31278.72	1236.09	31676.82	1267.01
Co59	14.44	0.48	14.3	0.48	42.13	1.34	41.58	1.32
Ni60	83.67	2.89	85.93	2.98	67.64	2.37	65.72	2.32
Ni62	78.31	3.47	82.8	3.63	72.54	3.2	61.72	2.88
Cu63	16.18	0.57	15.77	0.56	24.56	0.82	22.66	0.77
Cu65	16.17	0.65	16.56	0.67	25.58	0.93	24.14	0.89
Zn66	94.52	3.09	95.99	3.15	101.42	3.29	99.72	3.24
Ga69	94.73	2.91	96.09	2.95	67.56	2.08	65.18	2.01
Ga71	22.78	0.77	23.14	0.78	20.29	0.69	20.25	0.69
Rb85	141.84	4.33	143.29	4.38	122.36	3.74	124.71	3.81
Sr86	140.46	5.18	137.15	5.14	198.49	6.69	198.88	6.73
Sr88	142.18	4.35	142	4.35	201.18	6.14	199.44	6.09
Y89	30.79	1	32.01	1.04	29.56	0.96	28.79	0.93
Zr90	190.89	6.12	190.69	6.13	175.97	5.66	176.09	5.68
Nb93	13.61	0.46	13.47	0.46	13	0.44	13.26	0.45
Cs133	7.86	0.27	7.67	0.27	19.13	0.62	18.91	0.61
Ba137	1064.94	33.75	1074.22	34.1	701.81	22.39	692.47	22.14
Ba138	1056.31	32	1068.52	32.38	681.75	20.67	685.24	20.79
La139	30.17	0.95	28.84	0.91	28.49	0.9	28.63	0.9
Ce140	64.91	1.99	64.13	1.96	62.07	1.9	60.68	1.86
Pr141	7.92	0.27	7.97	0.27	7.32	0.25	7.54	0.26
Nd146	31.98	1.12	31.34	1.11	29.61	1.04	28.56	1.01
Sm147	6.98	0.36	6.55	0.35	6.13	0.32	6.24	0.33
Eu153	1.394	0.076	1.126	0.067	1.117	0.064	1.26	0.07
Gd157	5.32	0.3	6.02	0.33	5.5	0.3	5.8	0.31
Tb159	0.937	0.049	0.978	0.052	0.758	0.042	0.783	0.043
Dy161	5.41	0.29	6.07	0.31	5.36	0.28	5.36	0.28
Ho165	1.14	0.058	1.187	0.06	1.001	0.052	1.105	0.056
Er167	3.26	0.19	3.29	0.19	2.88	0.17	3.07	0.18
Tm169	0.507	0.033	0.491	0.033	0.431	0.029	0.458	0.03
Yb173	3.43	0.21	3.47	0.22	2.69	0.18	3.02	0.19
Lu175	0.51	0.033	0.447	0.032	0.442	0.03	0.485	0.032
Hf178	5.04	0.24	5.5	0.26	4.97	0.23	4.57	0.22
Ta181	1.121	0.06	1.084	0.059	1.672	0.078	1.368	0.068
Pb208	14.53	0.48	14.92	0.49	19.1	0.61	18.72	0.6
Th232	13.58	0.46	13.37	0.45	13.05	0.44	12.59	0.43
U238	2.73	0.1	2.465	0.094	2.84	0.1	2.82	0.1

Element	W1214a-1	1 sigma	W1214a-2	1 sigma	W1215-1	1 sigma	W1215-2	1 sigma
Be9	2.04	0.16	1.87	0.16	2.19	0.16	2.14	0.16
Na23	19333.54	592.13	19418.86	595.27	14123.31	433.35	14234.64	437.19
Mg25	9662.31	295.47	9571.49	292.88	12230.77	374.38	12377.01	379.12
Al27	85138.8	2685.36	85135.99	2690.41	90350.59	2861.01	90923.13	2885.34
Si29	311408.1	9853.62	311408.1	9853.63	297198	9403.96	297198	9403.84
P31	919.36	41.29	910.11	40.94	521.63	23.78	527.83	24.07
K39	24042.29	733.27	24260.81	740.35	32519.09	992.94	32480.79	992.4
Ca42	13924.04	437.27	13977.11	438.95	8721.88	282.39	9105.92	292.98
Ca43	17148.56	599.17	17153.39	600.75	11840.56	454.45	12355.19	467.97
Sc45	19.64	0.67	19.05	0.65	19.46	0.66	19.81	0.67
Ti47	4991.69	155.13	5024.2	156.32	5164.7	160.86	5102.69	159.14
V51	111.06	3.51	109.31	3.46	123.55	3.91	126.97	4.03
Cr53	90.09	3.17	91.97	3.23	69.04	2.53	70.81	2.58
Mn55	581.25	18.26	591.94	18.64	1164.02	36.69	1175.2	37.13
Fe57	26853.67	1088.03	27146.16	1114.78	33358.82	1389.12	34146.31	1443.04
Co59	32.5	1.04	33.17	1.06	23.38	0.76	23.14	0.75
Ni60	98.16	3.4	100.87	3.5	67.17	2.39	66.32	2.37
Ni62	97.72	4.03	102.36	4.2	68.51	3.05	67.37	3
Cu63	64.11	2.03	62.83	1.99	25.22	0.84	25.13	0.84
Cu65	65.32	2.15	63.02	2.09	24.62	0.9	25.47	0.92
Zn66	93.02	3.04	91.36	2.99	105.57	3.41	105.4	3.41
Ga69	50.33	1.56	49.89	1.55	59.01	1.82	58.32	1.8
Ga71	18.57	0.64	19.48	0.66	21.01	0.71	21.31	0.72
Rb85	135.64	4.14	137.09	4.19	145.13	4.43	144.42	4.41
Sr86	180.98	6.18	186.81	6.36	167.87	5.76	168.72	5.77
Sr88	186.96	5.71	187.35	5.73	170	5.2	171.64	5.25
Y89	33.94	1.09	34.55	1.11	32.03	1.03	31.24	1.01
Zr90	172.76	5.58	174.47	5.65	175.84	5.71	179.51	5.84
Nb93	12.43	0.42	12.55	0.43	13.79	0.46	13.74	0.46
Cs133	8.4	0.29	8.5	0.29	11.54	0.38	11.74	0.39
Ba137	491.47	15.82	495.16	15.97	583.49	18.8	589.7	19.04
Ba138	490.86	14.9	493.26	14.98	579.49	17.6	581.34	17.66
La139	32.05	1	31.95	1	29.35	0.92	29.21	0.92
Ce140	64.91	1.98	65.03	1.99	63.09	1.93	63.02	1.93
Pr141	7.93	0.27	7.95	0.27	7.86	0.27	7.88	0.27
Nd146	31.98	1.11	31.69	1.1	30.68	1.06	31.06	1.07
Sm147	6.47	0.34	6.37	0.34	6.1	0.32	6.85	0.34
Eu153	1.408	0.074	1.468	0.076	1.305	0.07	1.401	0.073
Gd157	5.46	0.3	6.03	0.32	5.77	0.3	5.81	0.3
Tb159	0.908	0.047	0.92	0.048	0.847	0.044	0.851	0.044
Dy161	5.52	0.28	5.33	0.28	5.59	0.28	5.65	0.28
Ho165	1.311	0.062	1.131	0.056	1.12	0.055	1.235	0.059
Er167	3.1	0.18	3.55	0.19	3.05	0.17	3.33	0.18
Tm169	0.519	0.033	0.488	0.031	0.409	0.028	0.445	0.03
Yb173	3.78	0.22	3.9	0.23	3.23	0.2	2.98	0.19
Lu175	0.504	0.032	0.484	0.031	0.522	0.032	0.505	0.031
Hf178	4.57	0.22	4.29	0.21	4.72	0.22	4.76	0.22
Ta181	1.105	0.058	1.066	0.056	1.199	0.061	1.184	0.06
Pb208	15.7	0.51	16.3	0.53	20.1	0.64	20.91	0.67
Th232	11.2	0.38	11.12	0.38	12.32	0.42	11.93	0.4
U238	3.32	0.12	3.46	0.12	2.602	0.095	2.67	0.097

Element	W1216-1	1 sigma	W1216-2	1 sigma	W1218-1	1 sigma	W1218-2	1 sigma
Be9	3.34	0.23	3.37	0.22	4.35	0.27	4.46	0.27
Na23	17710.23	544.54	17470.63	537.76	19010.3	585.83	18562.24	572.72
Mg25	11008.59	337.61	11011.91	337.98	10326.85	317.27	10221.62	314.32
Al27	88699.08	2821.39	88644.58	2826.42	87280.13	2789.94	87495.12	2804.2
Si29	304630.3	9640.34	304630.3	9640.25	308089.3	9749.82	308089.3	9749.88
P31	537.32	24.73	528.95	24.39	605.83	27.86	604.3	27.85
K39	29919.48	914.84	29541.83	903.93	27625.92	845.94	27162.12	832.39
Ca42	9311.22	305.76	8984.7	296.06	6401.69	224.13	6521.05	227.69
Ca43	12384.39	510.99	12068.47	500.57	9471.14	448.54	9471.02	449.14
Sc45	16.67	0.59	17.61	0.62	18.24	0.64	17.24	0.61
Ti47	4692.15	146.74	4697.38	147.12	4766.57	149.54	4717.97	148.27
V51	94.3	3.01	92.8	2.97	101.3	3.25	101.57	3.27
Cr53	48.93	2.06	48.12	2.04	50.58	2.14	49.82	2.12
Mn55	425.57	13.51	424.76	13.52	537.89	17.15	528.2	16.89
Fe57	29080.28	1248.43	29227.39	1274.9	28828.42	1278.45	29115.4	1313.3
Co59	22.56	0.74	21.87	0.72	33.39	1.09	31.87	1.04
Ni60	35.78	1.38	35.21	1.37	31.83	1.26	31.27	1.25
Ni62	33.7	2.05	34.76	2.03	32.91	1.99	30.93	1.94
Cu63	13.41	0.5	13.35	0.5	8.1	0.34	8.99	0.36
Cu65	13.42	0.58	13.6	0.59	8.91	0.45	8.11	0.42
Zn66	95.88	3.16	94.14	3.11	89.28	2.97	94.26	3.12
Ga69	56.18	1.75	56.69	1.76	81.84	2.53	81.9	2.53
Ga71	19.96	0.69	20.43	0.7	19.96	0.69	20.27	0.7
Rb85	135.8	4.16	132.53	4.06	114.77	3.52	114.44	3.51
Sr86	186.4	6.5	189.53	6.57	160.31	5.82	155.88	5.72
Sr88	185.39	5.68	184.3	5.65	164.31	5.05	162.99	5.01
Y89	28.07	0.92	28.53	0.94	30.52	1	31.37	1.03
Zr90	186.08	6.08	189.95	6.22	175.11	5.76	178.25	5.88
Nb93	12.26	0.42	12.37	0.43	12.02	0.42	11.86	0.41
Cs133	8.35	0.29	8.16	0.29	16.48	0.55	16.57	0.55
Ba137	560.93	18.23	561.67	18.3	945.89	30.73	953.96	31.08
Ba138	558.24	16.98	551.67	16.78	941.94	28.63	939.85	28.58
La139	28.03	0.89	28.6	0.91	29.01	0.92	28.87	0.92
Ce140	60.55	1.86	59.16	1.82	61.64	1.89	61.47	1.89
Pr141	7.3	0.26	7.34	0.26	7.79	0.27	7.51	0.26
Nd146	30.66	1.09	30.04	1.07	30.9	1.1	30.69	1.09
Sm147	5.71	0.33	6.36	0.35	6.4	0.35	6.67	0.36
Eu153	1.4	0.078	1.287	0.073	1.35	0.077	1.28	0.074
Gd157	5.84	0.32	5.32	0.3	5.62	0.32	4.72	0.29
Tb159	0.831	0.046	0.818	0.047	0.837	0.047	0.879	0.048
Dy161	4.82	0.27	5.08	0.28	5.13	0.29	5.61	0.3
Ho165	1.112	0.059	0.99	0.054	1.016	0.055	1.156	0.06
Er167	3.39	0.2	3.05	0.19	3.19	0.19	3.22	0.19
Tm169	0.373	0.029	0.44	0.031	0.503	0.034	0.489	0.034
Yb173	2.98	0.2	3.09	0.2	3.53	0.22	3.19	0.21
Lu175	0.44	0.031	0.453	0.032	0.505	0.034	0.466	0.033
Hf178	5.24	0.25	5.16	0.25	5.1	0.25	4.46	0.23
Ta181	1.199	0.065	1.12	0.061	1.298	0.069	1.101	0.061
Pb208	19.39	0.63	19.52	0.63	20.47	0.66	20.65	0.67
Th232	12.48	0.43	11.84	0.41	11.46	0.4	11.83	0.41
U238	2.81	0.1	2.75	0.1	3.11	0.11	3.05	0.11

Element	W1219-1	1 sigma	W1219-2	1 sigma	W1223-1	1 sigma	W1223-2	1 sigma
Be9	2.94	0.2	3.34	0.22	3.41	0.23	3.45	0.23
Na23	18499.9	571.5	18448.55	570.67	11161.96	345.75	11136.38	345.45
Mg25	11418.4	351.36	11574.51	356.52	11151.74	343.86	11256.79	347.48
Al27	87679.75	2817.79	88091.35	2839.15	78887.4	2550.06	81063.16	2628.5
Si29	304770.5	9644.44	304770.5	9644.59	312062.6	9875.18	312062.6	9875.37
P31	595.19	27.42	597.7	27.59	366.67	17.44	384.58	18.27
K39	21615.49	662.95	21266.86	652.82	32370.07	994.5	33249.67	1022.47
Ca42	17282.75	541.62	17481.13	548.19	4440.88	169.33	4476.17	171.65
Ca43	20420.28	709.46	21102.23	730.79	7327.8	391.96	7504.54	402.1
Sc45	19.07	0.66	19.48	0.68	15.19	0.54	14.81	0.54
Ti47	4943.38	155.55	4955.59	156.23	3680.28	116.42	3718.98	117.89
V51	111.48	3.59	111.53	3.6	93.42	3.03	93.29	3.03
Cr53	52.84	2.16	54.73	2.2	47.26	2.03	50.21	2.09
Mn55	649.37	20.82	642.25	20.65	807.68	26.04	823.95	26.66
Fe57	31222.52	1432.98	31181.14	1456.97	30975.95	1474.12	31413.29	1523.15
Co59	31.05	1.01	30.08	0.99	43.67	1.42	43.74	1.42
Ni60	32.24	1.28	33.21	1.32	37.32	1.48	36.89	1.48
Ni62	31.32	1.96	36.16	2.1	38.04	2.21	37.7	2.2
Cu63	31.91	1.07	30.87	1.04	13.55	0.51	13.33	0.5
Cu65	33.95	1.22	31.53	1.15	13.63	0.6	14.19	0.62
Zn66	104.28	3.42	106.81	3.51	101.28	3.34	99.63	3.3
Ga69	112.52	3.45	113.1	3.47	71.92	2.23	72.17	2.24
Ga71	19.78	0.68	20.29	0.7	20.36	0.71	19.79	0.69
Rb85	129.31	3.96	129.13	3.96	188.67	5.76	185.79	5.67
Sr86	161.76	5.78	165.1	5.87	124.69	4.8	131.13	4.98
Sr88	163.26	5.02	169.01	5.2	127.97	3.95	132.02	4.08
Y89	32.27	1.06	32.52	1.07	25.36	0.84	26.39	0.88
Zr90	163.23	5.41	166.51	5.54	154.95	5.18	161.29	5.4
Nb93	12.07	0.42	12.2	0.42	11.69	0.41	11.78	0.41
Cs133	25.07	0.82	24.82	0.81	13.66	0.46	14.2	0.48
Ba137	1389.07	45.25	1376.1	44.99	777.93	25.64	799.7	26.44
Ba138	1361.76	41.41	1378.48	41.94	782.43	23.83	797.76	24.31
La139	27.78	0.88	26.83	0.85	29.44	0.93	29.89	0.95
Ce140	56.14	1.72	56.15	1.73	62.53	1.92	63.07	1.94
Pr141	6.86	0.24	7.19	0.25	7.18	0.25	7.39	0.26
Nd146	27.75	1	27.37	0.99	27.64	1	29.27	1.05
Sm147	6	0.33	5.07	0.3	4.9	0.3	6.29	0.35
Eu153	1.544	0.082	1.553	0.083	1.2	0.07	1.153	0.068
Gd157	5.49	0.31	4.91	0.29	4.71	0.28	4.78	0.29
Tb159	0.778	0.044	0.843	0.047	0.805	0.045	0.749	0.044
Dy161	5.87	0.31	5.81	0.31	5.31	0.29	4.97	0.28
Ho165	1.082	0.056	1.143	0.059	1.077	0.057	1.003	0.055
Er167	3.2	0.19	3.36	0.2	2.58	0.16	2.83	0.18
Tm169	0.493	0.034	0.445	0.032	0.423	0.03	0.394	0.03
Yb173	3.62	0.23	3.4	0.22	3.17	0.21	3.13	0.21
Lu175	0.534	0.035	0.508	0.034	0.444	0.032	0.449	0.032
Hf178	4.23	0.22	4.69	0.23	4.07	0.21	4.36	0.22
Ta181	1.102	0.061	1.121	0.062	1.377	0.071	1.323	0.07
Pb208	19.4	0.63	19.43	0.63	23.12	0.74	23.03	0.74
Th232	11.5	0.4	11.81	0.41	12.02	0.42	12.53	0.44
U238	3.03	0.11	2.91	0.11	2.441	0.093	2.522	0.096

Element	W1229-1	1 sigma	W1229-2	1 sigma
Be9	2.27	0.17	2.34	0.18
Na23	5695.62	176.95	5676.59	176.62
Mg25	12071.28	372.97	12085.26	373.84
Al27	86652	2818.66	87340.96	2850.45
Si29	305191.2	9657.76	305191.2	9657.79
P31	428.23	20.2	450.18	21.21
K39	37927.34	1167.41	37793.87	1164.45
Ca42	3867.4	153.39	3951.21	155.12
Ca43	6479.78	371.98	7539.68	390.97
Sc45	17.61	0.62	17.42	0.62
Ti47	4612.81	146.32	4596.45	146.11
V51	119.38	3.88	118.31	3.86
Cr53	77.04	2.87	74.59	2.8
Mn55	368.62	11.99	366.55	11.97
Fe57	32967.21	1629.09	33142.84	1669.76
Co59	38.35	1.26	38.21	1.25
Ni60	37.47	1.5	39.29	1.58
Ni62	36.98	2.12	38.04	2.19
Cu63	22.89	0.79	24.07	0.83
Cu65	25.07	0.95	24.27	0.93
Zn66	97.56	3.23	97.13	3.22
Ga69	88.46	2.73	87.24	2.69
Ga71	21.04	0.73	20.57	0.72
Rb85	175.42	5.36	177.28	5.42
Sr86	72.79	3.51	78.14	3.63
Sr88	79.49	2.47	79.75	2.48
Y89	25.77	0.86	26.05	0.87
Zr90	154.4	5.19	152.03	5.13
Nb93	16.17	0.55	16.58	0.56
Cs133	8.59	0.3	9.08	0.32
Ba137	1006.69	33.32	1015.81	33.75
Ba138	1014.23	30.91	1021.12	31.14
La139	26.93	0.86	27.72	0.88
Ce140	59.3	1.82	58.93	1.81
Pr141	6.75	0.24	7.08	0.25
Nd146	27.91	1	27.02	0.97
Sm147	5.75	0.33	5.63	0.32
Eu153	1.289	0.072	1.1	0.066
Gd157	5.03	0.29	4.88	0.29
Tb159	0.668	0.04	0.759	0.043
Dy161	5.06	0.28	4.31	0.25
Ho165	0.871	0.049	0.967	0.053
Er167	2.76	0.17	2.49	0.16
Tm169	0.426	0.03	0.357	0.027
Yb173	3	0.2	2.67	0.19
Lu175	0.415	0.03	0.415	0.03
Hf178	4.21	0.22	4.08	0.21
Ta181	1.452	0.074	1.591	0.08
Pb208	20.11	0.65	20.41	0.66
Th232	13.57	0.47	13.73	0.48
U238	2.45	0.093	2.625	0.098

III: LA-ICP-MS Run 2 Analyses of standards

Element	Results in ppm							
	STD610-5	1 sigma	STD610-6	1 sigma	BCRR2-10	1 sigma	BHVR2-10	1 sigma
Be9	464.81	15.02	466.58	15.08	3.43	0.18	2.03	0.12
Na23	95423.11	2902.61	94970.91	2889.75	20717.22	631.09	14508.91	442.68
Mg25	466.63	14.23	463.93	14.15	20972.34	637.98	42251.71	1286.38
Al27	9997.56	305.81	10019.05	306.54	80180.05	2455.07	79654.49	2441.45
Si29	328328.9	10383.37	328328.9	10383.37	252884.7	8000.11	233252.3	7379.31
P31	341.58	15.4	343.17	15.48	1284.37	58.07	976.35	44.32
K39	485.33	14.66	487	14.71	14905.19	450.29	4330.57	130.88
Ca42	81869.44	2486.76	81832.48	2486.19	52872.11	1610.99	85499.95	2605.4
Ca43	81384.42	2509.25	82351.05	2540.56	58153.02	1812.4	88706.22	2764.05
Sc45	440.45	13.34	441.9	13.39	35.33	1.1	32.42	1.01
Ti47	435.57	13.34	432.36	13.25	13856.91	423.26	16592.13	507.53
V51	441.47	13.33	441.84	13.35	396.97	12.01	301.72	9.14
Cr53	406.32	12.74	404.36	12.69	39.26	1.48	283.25	9.15
Mn55	433.47	13.07	433.07	13.06	1450.88	43.76	1258.05	37.95
Fe57	456.97	14.4	456.79	14.41	79197.89	2470.02	71343.58	2234.53
Co59	406.16	12.35	403.62	12.27	34.55	1.07	41.08	1.27
Ni60	445.3	13.62	442.23	13.53	39.25	1.3	129.83	4.08
Ni62	441.43	13.83	446.83	14.01	43.03	1.94	134.96	4.87
Cu63	424.1	23.28	435.05	24.09	15.22	0.89	109.2	6.49
Cu65	425.39	22.68	433.59	23.3	16	0.93	111.43	6.43
Zn66	456.75	13.88	455.84	13.85	137.22	4.28	99.02	3.12
Ga69	438.4	13.26	437.93	13.25	65.9	2.02	28.63	0.89
Ga71	438.87	13.29	437.4	13.25	21.82	0.7	21.21	0.68
Rb85	431.01	13.01	431.31	13.02	42.75	1.32	8.78	0.29
Sr86	497.29	15.1	497.74	15.12	334.92	10.4	392.54	12.14
Sr88	496.94	15	498.04	15.03	338.17	10.23	397.89	12.04
Y89	448.17	13.68	451.93	13.8	32.08	1	23.78	0.75
Zr90	438.92	13.3	441.05	13.37	184.18	5.63	165	5.05
Nb93	418.98	12.7	420.03	12.73	12.14	0.39	17.29	0.54
Cs133	361.21	11.17	360.89	11.17	0.895	0.044	0.069	0.018
Ba137	423.35	12.9	425.15	12.96	652.33	19.99	125.79	3.97
Ba138	423.88	12.97	424.65	13	649.86	19.94	128.36	3.97
La139	456.69	13.81	458.29	13.86	27.07	0.84	16.53	0.52
Ce140	447.74	13.47	447.81	13.47	50.94	1.55	37.04	1.13
Pr141	428.29	12.99	431.55	13.09	6.67	0.22	5.07	0.17
Nd146	431.12	13	430.51	12.98	30.08	0.99	25.01	0.83
Sm147	448.77	13.72	452.62	13.84	6.9	0.29	6.19	0.27
Eu153	460.91	13.93	461.5	13.95	2.043	0.082	2.183	0.087
Gd157	418.65	12.69	421.25	12.77	6.4	0.27	5.67	0.25
Tb159	440.81	13.45	445.11	13.59	1.044	0.044	0.903	0.039
Dy161	423.72	13.14	429.62	13.33	6.4	0.26	5.2	0.22
Ho165	446.68	13.78	452.5	13.97	1.283	0.052	0.977	0.042
Er167	424.25	12.92	428.01	13.04	3.48	0.15	2.37	0.12
Tm169	417.93	12.8	422.6	12.95	0.47	0.024	0.298	0.018
Yb173	459.33	14.04	463.93	14.18	3.48	0.17	1.97	0.11
Lu175	433.06	13.15	436.58	13.26	0.518	0.026	0.258	0.016
Hf178	416.17	12.66	419.52	12.77	5.03	0.19	4.28	0.17
Ta181	375.45	11.38	377.97	11.46	0.678	0.031	1.004	0.041
Pb208	414.23	12.78	412.61	12.74	9.17	0.3	1.776	0.074
Th232	449.27	13.6	452.1	13.69	6.24	0.2	1.236	0.052
U238	457.33	13.8	456.67	13.78	1.482	0.053	0.33	0.017

Element	BHVOR2-9	1 sigma	GSP-R2-9	1 sigma	STD610-3	1 sigma	STD610-4	1 sigma
Be9	1.77	0.14	1.94	0.15	460.25	17.01	461.32	17.16
Na23	14671.54	446.94	18387.18	560.27	97318.63	3031.24	97050.72	3027.73
Mg25	41378.2	1258.99	5594.8	170.65	455.02	14.16	455.05	14.17
Al27	77952.55	2429.33	87224.95	2719.95	10054.62	329.17	10055.22	330.35
Si29	233252.3	7381.14	314212.8	9942.93	334048.1	10564.78	334048.1	10564.75
P31	916.34	40.68	930.45	41.51	339.93	15.57	344.96	15.84
K39	3933.73	119.6	39074.54	1187.85	464.52	14.33	461.73	14.26
Ca42	84525.43	2570.54	14897.36	470.46	82141.35	2521.8	81691.11	2510.04
Ca43	89635.24	2735.91	21602.94	715.62	81823.4	2486.3	81987.91	2491.8
Sc45	33.69	1.08	9.79	0.37	450.26	14.5	449.87	14.53
Ti47	17765	546.26	4782.57	147.63	474.47	15.17	477.55	15.3
V51	306.14	9.5	53.25	1.69	443.26	14.37	444.58	14.46
Cr53	265.44	8.38	37.94	1.67	388.21	12.11	387.74	12.11
Mn55	1216.48	37.69	277.83	8.65	436.36	14.25	436.56	14.31
Fe57	60569.74	2235.82	21701.47	806.4	452.5	23.45	454.04	23.99
Co59	38.78	1.22	42.44	1.34	388.88	12.38	387.26	12.37
Ni60	119.08	3.94	48.98	1.74	413.59	15	416.51	15.24
Ni62	120.28	4.54	49.06	2.44	417.97	13.87	412.26	13.73
Cu63	108.32	3.35	30.55	1.01	432.85	13.44	433.01	13.46
Cu65	109.62	3.46	30.89	1.1	431.07	13.51	434.68	13.65
Zn66	91.23	2.94	105.25	3.41	430.24	13.34	428.47	13.3
Ga69	29.59	0.93	123.74	3.78	431.52	13.08	430.54	13.05
Ga71	20.2	0.67	32.19	1.05	431.44	13.53	430.5	13.53
Rb85	8.28	0.29	206.96	6.3	430.54	13.04	429.47	13.01
Sr86	418.8	13.06	236	7.89	525.81	16.01	524.27	15.97
Sr88	417.25	12.67	234.33	7.14	526.18	16.11	523.94	16.05
Y89	25.89	0.83	26.19	0.85	490.59	15.56	489.55	15.56
Zr90	180.77	5.74	671.56	21.17	491.67	16.39	488.59	16.35
Nb93	20.63	0.66	32.78	1.05	513.75	15.95	510.42	15.87
Cs133	0.095	0.019	0.961	0.054	363.27	11.52	358.87	11.41
Ba137	131.53	4.31	1285.58	40.44	448.12	14.88	444.14	14.8
Ba138	133.47	4.07	1294.1	39.17	447.08	13.63	445.02	13.57
La139	15.58	0.5	191.23	5.82	440.69	13.4	439.39	13.36
Ce140	36.44	1.12	435.94	13.16	445.14	13.45	446.82	13.51
Pr141	5.67	0.19	57.88	1.81	469.28	14.98	466.91	14.94
Nd146	25.39	0.89	220.45	6.8	453.79	13.7	454.21	13.71
Sm147	6.44	0.31	27.64	1.04	463.92	15.66	462.3	15.68
Eu153	2.105	0.093	2.31	0.11	454.17	14.5	450.05	14.4
Gd157	6.24	0.3	12.06	0.53	451.01	14.2	449.13	14.16
Tb159	0.839	0.042	1.299	0.062	441.9	14.41	442.23	14.47
Dy161	5.31	0.26	5.59	0.29	454.8	15.74	451.48	15.71
Ho165	1.051	0.05	1.016	0.053	475.18	15.8	474.99	15.87
Er167	2.61	0.15	2.24	0.15	462.94	15.76	463.23	15.85
Tm169	0.309	0.022	0.297	0.025	453.79	16.15	454.4	16.28
Yb173	2.45	0.15	2.01	0.15	480.85	17.21	477.47	17.21
Lu175	0.282	0.021	0.245	0.022	467.72	15.74	466.49	15.78
Hf178	4.43	0.2	16.72	0.62	458.85	16.08	457.4	16.12
Ta181	1.258	0.06	1.633	0.078	491.83	17.88	489.69	17.93
Pb208	1.908	0.085	41.2	1.28	418	12.72	420.17	12.79
Th232	1.417	0.065	121.74	3.81	480.46	15.65	481.65	15.74
U238	0.46	0.026	2.48	0.094	487.13	14.7	486.84	14.69

IV: LA-ICP-MS Run 2 Analyses of samples

Element	Results in ppm							
	W1207e-3	1 sigma	W1207e-4	1 sigma	W1207e-5	1 sigma	W1207e-6	1 sigma
Be9	1.36	0.21	1.34	0.23	1.7	0.2	1.15	0.22
Na23	2553.93	78.2	2595.59	79.7	2530.41	77.94	2510.97	77.65
Mg25	3675.39	113.22	3778.09	116.57	3747.93	115.69	3666.61	113.53
Al27	12127.37	372.56	11627.66	357.85	11922.58	367.63	11781.59	364.21
Si29	428782.2	13576.64	428782.2	13577.4	428782.2	13574.04	428782.2	13574.43
P31	153.6	12.75	179.77	14.33	162.14	12.31	168.54	12.38
K39	4378.21	132.57	4555.16	138	4340.37	131.53	4331.63	131.36
Ca42	<561.15	214.18	<636.92	239.06	<541.02	201.54	<517.40	195.77
Ca43	4171.6	594.93	2933.29	666.65	2935.12	555.77	3451.89	541.02
Sc45	6.36	0.39	6.15	0.4	7.08	0.37	6.54	0.37
Ti47	529.58	18.06	536.61	18.47	507.5	17.26	527.78	18.01
V51	44.1	1.43	44.38	1.44	42.75	1.38	41.57	1.34
Cr53	34.77	2.8	36.99	2.9	33.02	2.57	36.85	2.59
Mn55	2162.85	65.34	2181.74	65.92	2173.14	65.64	2137.72	64.59
Fe57	5065.49	164.16	5292.69	172.68	5135.09	168.23	5036.65	166.86
Co59	85.83	2.73	84.92	2.71	84.7	2.69	85.3	2.72
Ni60	59.98	2.33	59.7	2.34	60.96	2.3	58.8	2.26
Ni62	51.72	3.84	53.38	4.11	54.92	3.75	62.92	4.11
Cu63	8.14	0.64	7.77	0.66	7.76	0.66	6.43	0.59
Cu65	7.79	0.73	7.62	0.76	7.44	0.72	6.21	0.68
Zn66	41.3	1.78	40.3	1.77	46.44	1.89	37.87	1.62
Ga69	7.23	0.34	7.22	0.34	7.19	0.32	7.19	0.32
Ga71	4.25	0.28	3.19	0.25	3.66	0.25	3.36	0.24
Rb85	20.66	0.75	20.78	0.75	20.67	0.73	20.95	0.74
Sr86	<14.84	5.66	<16.50	6.21	21.83	5.29	20.65	5.06
Sr88	17.65	0.63	17.07	0.61	17.13	0.6	16.68	0.59
Y89	2.41	0.15	2.41	0.15	2.48	0.14	2.55	0.15
Zr90	13.57	0.6	13.23	0.59	13.47	0.57	13.54	0.58
Nb93	1.63	0.11	1.59	0.11	1.68	0.11	1.64	0.11
Cs133	1.78	0.12	1.77	0.13	1.59	0.11	1.58	0.11
Ba137	64.77	2.58	63.92	2.56	63.46	2.46	63.26	2.48
Ba138	64.69	2.1	61.78	2.02	62.62	2.03	59.97	1.96
La139	3.71	0.19	3.66	0.19	3.88	0.19	3.88	0.19
Ce140	13.51	0.48	13.55	0.48	13.15	0.46	13.85	0.48
Pr141	0.924	0.069	0.817	0.064	0.98	0.066	0.778	0.057
Nd146	4.41	0.36	2.88	0.29	3.71	0.3	2.93	0.27
Sm147	0.64	0.16	1.01	0.18	0.58	0.15	0.79	0.15
Eu153	0.125	0.035	0.162	0.035	0.171	0.033	0.153	0.032
Gd157	0.69	0.14	0.7	0.14	0.53	0.11	0.66	0.14
Tb159	0.12	0.023	0.043	0.014	0.075	0.021	0.095	0.026
Dy161	0.46	0.1	0.54	0.11	0.68	0.13	0.73	0.12
Ho165	0.128	0.024	0.102	0.029	0.13	0.022	0.128	0.025
Er167	0.341	0.079	0.328	0.078	0.303	0.068	0.301	0.079
Tm169	<0.040	0.02	0.039	0.016	0.049	0.013	0.028	0.013
Yb173	0.361	0.094	0.29	0.12	0.305	0.079	0.36	0.088
Lu175	0.052	0.015	0.064	0.022	0.051	0.013	0.067	0.016
Hf178	0.35	0.11	0.91	0.12	0.281	0.066	0.308	0.075
Ta181	0.95	0.067	0.948	0.067	0.939	0.063	0.933	0.064
Pb208	5.28	0.25	4.72	0.24	5.23	0.25	4.92	0.23
Th232	1.295	0.091	1.301	0.093	1.487	0.092	1.69	0.1
U238	0.994	0.06	1.018	0.062	1.111	0.061	1.086	0.061

V: Database of major element whole rock chemistry analyses of low-grade Rampsbeck

Schists (Henson, 2000)

Results reported in weight %.

	Girrakool Beds			Transitional Schists						
Sample #	AH11C	AH20C	AH20B	AH02A	AH02qA	AH02B	AH02E	AH06B1	AH06F	AH19G
SiO ₂	66.39	66.79	66.98	74.28	69.23	65.48	74.97	64.80	69.24	72.18
TiO ₂	0.63	0.85	0.83	0.50	0.52	0.76	0.46	0.78	0.72	0.48
Al ₂ O ₃	14.47	14.12	13.68	11.48	14.02	15.07	11.83	14.86	13.74	13.62
Fe ₂ O ₃	0.63	0.74	1.25	1.04	1.34	1.02	1.24	1.30	0.85	1.33
FeO	1.71	2.00	3.37	2.81	3.62	2.75	3.35	3.51	2.29	3.58
MnO	0.07	0.10	0.11	0.06	0.06	0.09	0.06	0.11	0.11	0.05
MgO	1.72	2.14	2.05	0.99	1.58	1.90	0.94	2.30	1.51	1.35
CaO	1.46	2.88	2.53	2.19	2.09	2.26	1.17	2.37	2.59	2.14
Na ₂ O	3.35	3.33	2.67	2.22	3.92	3.38	3.37	2.58	2.33	3.71
K ₂ O	3.99	2.08	3.07	2.88	2.09	2.71	2.63	3.92	3.07	2.10
P ₂ O ₃	0.13	0.23	0.22	0.12	0.10	0.21	0.11	0.20	0.15	0.13
H ₂ O+	2.23	2.21	2.15	1.25	1.34	1.67	1.32	1.46	1.48	1.22
H ₂ O-	0.20	0.02	0.08	0.07	0.15	0.08	0.08	0.02	0.06	0.04
CO ₂	0.53	0.19	0.18	0.75	0.06	0.89	0.41	0.40	0.16	0.23
LOI	4.57	2.41	3.18	1.55	2.64	1.81	1.88	1.70	1.96	1.83
Total	97.51	97.68	99.17	100.64	100.12	98.27	101.94	98.61	98.30	102.16

	Low Grade Rampsbeck Schists					
Sample #	AH03A	AH03B	AH03C	AH03G	AH043	AH045
SiO ₂	74.33	72.98	66.03	68.59	70.35	67.51
TiO ₂	0.50	0.60	0.72	0.68	0.64	0.67
Al ₂ O ₃	12.48	12.82	15.85	14.70	13.33	14.96
Fe ₂ O ₃	1.06	1.45	0.91	0.93	1.21	1.43
FeO	2.87	3.92	2.45	2.52	3.26	3.86
MnO	0.07	0.08	0.10	0.07	0.07	0.08
MgO	1.07	1.18	1.80	1.71	1.42	1.94
CaO	2.40	1.84	2.15	1.50	2.88	2.10
Na ₂ O	3.18	3.50	3.86	3.13	3.47	3.86
K ₂ O	1.36	1.68	2.82	3.22	1.64	2.68
P ₂ O ₃	0.14	0.16	0.15	0.16	0.12	0.16
H ₂ O+	1.01	1.06	1.20	1.37	1.50	1.21
H ₂ O-	0.10	0.08	0.08	0.08	0.06	0.05
CO ₂	0.15	0.17	0.04	0.23	0.27	0.17
LOI	1.31	1.32	1.68	1.83	1.43	1.47
Total	100.72	101.52	98.16	98.89	100.22	100.68

VI: Database of trace and rare earth element whole rock chemistry analyses of low-grade

Rampsbeck Schists (Henson, 2000)

(ppm)		Girrakool Beds			Transitional Schists					
	Sampl e #	AH11C	AH20C	AH20B	AH02A	AH02q A	AH02B	AH02E	AH06B 1	AH06F
Li	7	32.69	12.39	11.05	10.47	24.52	11.73	10.49	10.03	5.84
Be	9	1.43	1.88	1.56	1.69	1.98	2.50	1.31	2.26	2.08
Sc	45	11.14	17.64	16.74	9.33	10.13	15.68	8.49	16.98	15.28
Ti	49	2817.1 8	4271.3 8	4616.7 3	2862.3 7	2736.07	4231.4 0	2547.6 7	4304.1 0	4635.1 8
V	51	58.53	93.47	97.41	45.88	50.39	90.05	39.12	98.52	85.62
Cr	53	27.63	37.78	32.63	29.59	24.54	39.03	22.30	21.33	17.01
Co	59	25.27	30.45	43.00	74.07	37.53	44.67	59.27	36.37	47.48
Ni	60	12.29	17.28	17.52	9.99	10.46	21.15	7.07	21.86	17.27
Cu	65	17.36	10.10	11.31	106.10	22.55	58.34	6.94	35.38	38.54
Zn	66	54.62	76.69	75.40	43.96	61.76	83.56	56.09	96.13	85.71
Ga	71	12.14	15.13	14.86	11.61	11.50	18.18	11.06	19.10	16.04
Rb	85	136.72	62.22	97.50	108.79	68.86	98.09	89.48	143.97	109.44
Sr	88	174.81	253.68	270.95	225.39	251.31	216.38	203.40	222.88	278.55
Y	89	27.65	32.29	32.75	23.83	24.13	32.64	24.74	31.08	30.42
Zr	90	131.15	158.17	156.94	125.36	137.87	160.99	138.22	154.57	170.45
Nb	93	7.63	5.84	6.84	4.04	6.26	7.49	4.94	7.28	8.29
Mo	95	0.27	0.14	0.17	0.32	0.28	0.31	0.12	0.39	0.52
Cd	114	0.17	0.11	0.18	0.18	0.13	0.16	0.46	0.10	0.13
Sn	120	3.02	2.37	2.88	2.28	2.22	2.73	1.54	3.16	1.99
Sb	121	0.58	0.51	0.71	2.48	0.96	1.30	1.42	0.66	1.09
Cs	133	4.90	4.67	6.30	5.57	6.04	8.50	3.14	10.51	6.66
Ba	137	507.38	546.09	661.42	366.90	326.72	556.15	314.16	525.24	604.07
La	139	29.93	23.18	22.90	19.00	26.36	29.46	32.92	24.35	25.06
Ce	140	56.98	47.75	47.86	41.18	57.50	64.74	54.96	50.86	51.47
Pr	141	7.15	6.46	6.34	5.13	7.24	8.06	7.53	6.60	6.57
Nd	146	27.85	25.81	24.88	20.11	28.02	31.43	28.91	25.52	25.30
Sm	147	5.71	6.00	5.85	4.35	5.94	6.71	5.45	5.63	5.28
Eu	151	1.34	1.49	1.51	1.13	1.33	1.57	1.13	1.35	1.31
Tb	159	0.85	0.96	0.93	0.67	0.84	0.99	0.74	0.84	0.78
Gd	160	5.69	6.61	5.45	4.18	5.60	7.76	5.09	5.37	4.15
Dy	163	5.00	5.69	5.64	3.96	4.77	6.40	4.15	4.81	4.64
Ho	165	1.05	1.21	1.17	0.84	0.97	1.19	0.85	1.06	0.99
Er	167	3.04	3.45	3.31	2.41	2.76	3.43	2.40	3.06	2.83
Yb	173	2.84	3.16	3.10	2.18	2.55	3.19	2.23	2.84	2.59
Lu	175	0.42	0.46	0.46	0.32	0.38	0.47	0.33	0.42	0.38
Hf	178	3.94	4.13	4.04	3.54	4.24	4.17	3.75	4.21	4.54
Ta	181	0.92	0.64	1.05	0.88	1.15	1.10	1.15	0.68	1.17
Pb	208	16.40	12.16	12.62	8.26	16.36	12.39	14.97	11.68	14.45
Th	232	9.81	6.03	6.88	5.27	9.99	7.56	6.61	7.00	6.05
U	238	2.30	1.32	1.44	1.24	2.22	1.71	1.35	1.59	1.36

		Transitional Schists	Low-grade Rampsbeck Schists					
Sample #		AH19G	AH03A	AH03B	AH03C	AH03G	AH043	AH045
Li	7	10.22	10.49	14.71	11.66	11.50	10.25	11.59
Be	9	2.31	2.08	1.49	2.40	2.08	1.83	2.37
Sc	45	10.03	9.85	10.88	14.98	13.81	11.82	13.65
Ti	49	2768.05	2821.18	2982.48	3835.28	3677.26	3263.94	3703.32
V	51	46.91	46.38	53.92	75.74	69.84	61.89	70.17
Cr	53	19.16	22.93	28.22	28.26	30.56	26.08	24.73
Co	59	49.72	63.49	54.20	38.17	36.78	48.15	33.26
Ni	60	10.26	10.75	12.06	14.29	16.92	11.51	44.66
Cu	65	17.94	35.91	8.29	20.67	21.00	24.98	18.78
Zn	66	65.84	62.51	62.84	87.66	82.72	65.65	84.98
Ga	71	13.83	11.94	12.43	17.43	16.49	13.29	16.60
Rb	85	65.51	56.79	58.51	94.84	101.10	55.60	94.62
Sr	88	256.18	229.60	191.27	237.76	188.18	256.03	203.72
Y	89	27.25	27.33	23.28	38.26	29.80	24.33	30.00
Zr	90	134.50	161.23	136.06	218.33	171.12	144.14	191.32
Nb	93	6.37	4.82	6.78	9.22	8.32	5.82	7.92
Mo	95	0.14	0.21	0.15	0.19	0.29	0.27	0.38
Cd	114	0.11	0.13	0.11	0.20	0.13	0.07	0.20
Sn	120	2.61	1.76	2.06	3.22	2.95	1.32	3.02
Sb	121	0.91	1.60	1.05	1.25	1.19	1.40	0.87
Cs	133	5.24	6.45	8.33	11.52	12.56	4.17	9.25
Ba	137	501.63	278.21	294.95	537.89	591.41	240.57	574.89
La	139	20.66	28.49	25.11	30.39	30.54	23.60	19.66
Ce	140	45.37	54.86	55.51	77.42	65.06	48.17	42.20
Pr	141	5.67	7.25	6.51	9.04	8.21	6.20	5.36
Nd	146	21.64	28.29	25.11	35.50	31.66	23.67	20.77
Sm	147	4.81	5.86	5.34	8.26	6.55	4.87	4.74
Eu	151	1.11	1.25	1.23	1.65	1.51	1.18	1.25
Tb	159	0.76	0.81	0.80	1.18	0.92	0.71	0.76
Gd	160	3.81	5.43	5.06	10.07	6.45	4.60	4.80
Dy	163	4.50	4.53	4.58	8.25	4.76	3.76	4.88
Ho	165	0.95	0.94	0.96	1.38	1.07	0.86	1.24
Er	167	2.73	2.64	2.74	4.44	3.04	2.45	3.14
Yb	173	2.47	2.34	2.64	3.46	2.82	2.21	2.92
Lu	175	0.36	0.34	0.39	0.51	0.42	0.33	0.44
Hf	178	3.75	4.51	4.03	5.34	4.44	3.58	4.69
Ta	181	1.51	1.41	1.84	0.96	0.95	0.88	0.95
Pb	208	12.90	9.73	13.82	19.37	14.47	12.81	11.44
Th	232	7.34	6.72	6.91	9.20	8.59	6.06	7.26
U	238	1.63	1.57	1.46	2.18	1.89	1.41	1.67

VII: Database of published whole rock chemistry results from quartz-rich rocks

Results reported in weight %.

Reference	Sample type	Notes	SiO ₂	TiO ₂	Al ₂ O ₃	Fe ₂ O ₃	MnO	MgO	CaO	Na ₂ O	K ₂ O	P ₂ O ₅
Thurston, 1972	Green Chert	East Liguria	91.92	0.17	3.19	2.76	0.09	1.08	0.36	0.05	0.49	
Swindon, 1976	Red Chert	Upper Ordovician-Silurian, associated with island-arc type volcanics	79.49	0.24	3.67	9.93	0.33	1.01	2.04		0.68	
Swindon, 1976	Green Chert	Upper Ordovician-Silurian, associated with island-arc type volcanics	74.43	0.27	9.82	4.20	0.13	4.22	5.35		1.64	
Audley-Charles, 1965	Chert	Cretaceous, associated with ophiolitic rocks	95.95	0.01	0.4	0.75	0.1	0.06	0.05			
Leggett and Smith, 1980	Chert	Ordovician ferruginous chert, associated with oceanic basalts	72	0.12	3.2	10.1	0.22		0.46			
Hara et al 2010	Chert	Devonian siliceous succession, Thailand	95.34	0.12	3.87	2.11	0.34	0.24	0.04	<0.1	0.73	0.03
Hara et al 2010	Green Chert	Devonian siliceous succession, Thailand	91.34	0.08	3.56	4.7	1.22	0.38	0.03	<0.1	0.87	0.02
Yongzhang et al 1994	Chert	Averaged bedded cherts, Guangdong, Southern China	92.84	0.11	2.72	1.85	0.07	0.1	0.07	0.03	0.61	0.05
Z.L. Sujkowski, in Cressman, 1962	Ooze	Diatom Ooze, Arctic Ocean	82.36		4.87	2.23	0.1	1.84	1.85	tr.	tr.	
El Wakeel and Riley, 1961	Ooze	Average siliceous ooze from oceanic core samples	67.36	0.59	11.33	4.98	0.19	2.29	1.74	1.64	2.15	
Chudy et al 2008	Quartzite	Limpopo Belt, Southern Africa	76.3	0.02	13.1	1.9	0.16	0.38	1.9	4.1	0.38	0.03

Reference	Sample type	Notes	SiO ₂	TiO ₂	Al ₂ O ₃	Fe ₂ O ₃	MnO	MgO	CaO	Na ₂ O	K ₂ O	P ₂ O ₅
Makrygina and Suvorova 2011	Quartzite	Mn-rich quartzite, Dzhida terrane, Southern Siberia	91.26	0.06	1.51	2.76	0.49	0.58	2.25	0.1	0.04	0.06
Barrett 1981	Radiolarite	North Apennines, Italy	92.52	0.08	2.77	1.77	0.09	0.73	0.05	0.04	0.53	0.04
Leoni, 1974	Radiolarite	Castellina Marittima	90.42	0.12	3.36	2.09	0.16	0.88	0.62		0.79	
Leoni, 1974	Radiolarite	Campeggia Marittima	90.05	0.2	4.7	1.75	0.02	0.6	0.21		1.07	
Audley-Charles, 1965	Radiolarite	Cretaceous, associated with ophiolitic rocks	85.39	0.25	4.57	1.26	0.26	1.12	0.82			

B - Mineral Chemistry Raw Data

I: SEM-EDS raw data

Results presented in wt% oxide.

Mineral	Sample		SiO ₂	TiO ₂	Al ₂ O ₃	Cr ₂ O ₃	FeO	MnO	MgO	CaO	Na ₂ O	K ₂ O	Total (Fe corr)
Biotite	W0903	Small vein	39.68	1.54	21.69		18.66		7.8			10.63	100.00
Biotite	W0903	Host rock	37.42	3.47	19.98		21.44	0.43	7.92			9.33	99.99
Biotite	W0903	Host rock	37.11	2.38	18.76		22.56	0.33	8.96			9.89	99.99
Biotite	W0903	Host rock	37.04	2.67	18.46		23.74	0.3	9.17			8.62	100.00
Biotite	W0903	Host rock	36.58	2.9	19.26		22.68	0.32	8.29			9.96	99.99
Biotite	W0903	Host rock	36.44	2.42	19.48		23.25	0.31	8.76			9.34	100.00
Biotite	W1122	Host rock	35.88	3.01	20.18		22.01	0.62	8.03			10.27	100.00
Biotite	W1122	Host rock	36.04	2.74	20.52		21.2	0.63	8.18			9.96	99.27
Biotite	W1122	Host rock	35.85	3.59	19.77		21.59	0.51	8.43			10.25	99.99
Biotite	W1122	Host rock	36.56	2.42	20.33		21.72	0.61	8.32			10.04	100.00
Biotite	W1122	Host rock	36.22	2.26	20.7		21.18	0.57	8.77			10.31	100.01
Biotite	W1122	Host rock	36.19	3.34	19.79		21.68	0.68	8.35			9.97	100.00
Biotite	W1122	Host rock	36.03	3.47	19.34		22.02	0.53	8.48			10.12	99.99
Biotite	W1122	Host rock	36.3	3.33	20.4		21.3	0.54	8.03			10.09	99.99
Biotite	W1122	Host rock	36.33	3.09	20.12		21.7	0.59	8.2			9.98	100.01
Biotite	W1122	Host rock	35.99	3.35	20.48		21.59	0.57	7.82			10.21	100.01
Biotite	W1122	Host rock	36.96	2.63	20.49		21.01	0.52	8.3			10.08	99.99
Biotite	W1122	Host rock	35.9	3.16	19.64		22.68	0.7	8.09			9.84	100.01
Biotite	W1122	Host rock	36.13	2.4	20.68		21.44	0.72	8.22			10.41	100.00
Biotite	W1122	Host rock	36.2	1.72	21.01		20.91	0.7	9.22			10.24	100.00
Biotite	W1122	Host rock	35.49	2.91	20.14		21.5	0.6	8.16			10.01	98.81
Biotite	W1122	Host rock	36.37	2.73	20.27		21.6	0.48	8.36			10.19	100.00
Biotite	W1122	Host rock	36.19	2.85	20.17		21.34	0.6	8.63			10.22	100.00
Biotite	W1122	Host rock	36.02	3.21	19.53		22.22	0.64	8.42			9.95	99.99
Biotite	W1122	Host rock	36.07	2.72	20.27		21.86	0.61	8.27			10.21	100.01
Biotite	W1122	Host rock	36.43	2.97	20.09		21.23	0.74	8.23			10.3	99.99
Biotite	W1201	Host rock	36.94	1.55	22.64		20.84		8.04			9.98	99.99
Biotite	W1201	Host rock	36.35	2.25	22.21		21.45		7.77			9.98	100.01
Biotite	W1201	Host rock	36.71	2.41	21.82		21.46		7.66			9.94	100.00
Biotite	W1201	Host rock	36.55	2.52	22.31		21.05		7.5			10.07	100.00
Biotite	W1201	Host rock	35.88	3.66	20.96		21.96		7.54			10	100.00
Biotite	W1201	Host rock	35.77	3.8	21.05		21.77		7.27			10.34	100.00
Biotite	W1201	Host rock	36.83	2.1	22.2		21		7.87			10.01	100.01
Biotite	W1201	Host rock	36.84	1.81	22.68		20.81		7.63			10.24	100.01
Biotite	W1201	Host rock	36.55	2.16	22.19		21.28		7.82			10	100.00
Biotite	W1201	Host rock	36.29	2.33	22.56		21.16		7.47			10.19	100.00
Biotite	W1201	Host rock	35.77	3.52	21.3		21.6	0.31	7.48			10.03	100.01
Biotite	W1201	Host rock	36.02	3.61	20.6		21.79		7.85			10.13	100.00
Biotite	W1201	Host rock	36.41	2.19	22.59		20.92		7.78			10.11	100.00
Biotite	W1201	Host rock	36.45	1.74	22.7		21.02		7.9			10.2	100.01
Biotite	W1201	Host rock	36.18	2.63	21.91		21.84		7.49			9.94	99.99
Biotite	W1201	Host rock	36.25	2.51	21.79		21.56		7.55			10.34	100.00
Biotite	W1201	Host rock	36.1	3.64	21.29		21.51		7.25			10.2	99.99

Mineral	Sample		SiO ₂	TiO ₂	Al ₂ O ₃	Cr ₂ O ₃	FeO	MnO	MgO	CaO	Na ₂ O	K ₂ O	Total (Fe corr)
Biotite	W1201	Host rock	36.6	3.53	20.92		21.19		7.72			10.04	100.00
Biotite	W1201	Host rock	36.61	2.09	22.1		21.23		7.98			10	100.01
Biotite	W1201	Host rock	36.76	2	22.26		20.9		7.83			10.26	100.01
Biotite	W1201	Host rock	35.8	2.44	22.23		21.62	0.26	7.89			9.77	100.01
Biotite	W1201	Host rock	36.29	3.28	20.5		21.97		7.63			10.33	100.00
Biotite	W1207 d	Quartzite	40.72	0.91	18.43		9.52	0.71	18.96			10.75	100.00
Biotite	W1207 d	Quartzite	41.39	1.2	16.44		10	0.72	18.76			11.49	100.00
Biotite	W1207 d	Quartzite	41.99	1.17	17.54		8.53	0.75	19.27			10.28	99.53
Biotite	W1207 d	Quartzite	48.38	0.86	15.39		7.35	0.64	18.17			9.21	100.00
Biotite	W1207 d	Quartzite	41.5	1.03	17.39		9.34	0.74	19.51			10.49	100.00
Biotite	W1207 d	Quartzite	41.84	1.07	17.63		8.86	0.66	19.7			10.23	99.99
Biotite	W1207 d	Quartzite	41.23	1.14	17.79		9.47	0.74	19.05			10.58	100.00
Biotite	W1207 d	Quartzite	40.66	0.97	18.56		9.3	0.75	18.94			10.8	99.98
Biotite	W1207 d	Quartzite	40.84	1.04	17.64		9.54	0.92	19.05			10.97	100.00
Biotite	W1207 d	Quartzite	40.37	0.98	18.25		9.5	0.67	18.94			10.62	99.33
Biotite	W1207 d	Quartzite	40.82	0.88	17.75		9.07	0.82	18.96			10.59	98.89
Biotite	W1207 e	Quartzite	42.35	0.76	17.94		7.11	0.45	20.79			10.6	100.00
Biotite	W1207 e	Quartzite	41.23	0.93	19.64		7.08	0.41	20.26			10.46	100.01
Biotite	W1207 e	Quartzite	41.52	0.96	19.32		6.92	0.47	20.16			10.65	100.00
Biotite	W1207 e	Quartzite	48.51	0.92	15.76		5.46	0.44	18.77			8.67	98.53
Biotite	W1207 e	Quartzite	41.55	0.77	17.66		6.38	0.56	20.6			10.02	97.54
Biotite	W1207 e	Quartzite	42.27	0.82	18.23		6.64	0.54	21.15			10.36	100.01
Biotite	W1207 e	Quartzite	40.74	1.21	18.04		8.23	0.54	18.71			11.79	99.26
Biotite	W1207 h	Quartzite	41.42	0.84	19.32		6.29	0.59	20.72			10.3	99.48
Biotite	W1207 h	Quartzite	41.49	1.07	18.84		6.56	0.69	20.43			10.93	100.01
Biotite	W1207 h	Quartzite	42.41	0.8	17.93		6.33	0.55	21.18			10.8	100.00
Biotite	W1209	Host rock	36.5	2.15	21.77		21.31		8.24			10.02	99.99
Biotite	W1209	Host rock	36.35	1.15	22.12		20.99	0.41	9.31			9.67	100.00
Biotite	W1209	Host rock	35.93	1.99	21.06		22.22	0.45	8.13			10.21	99.99
Biotite	W1209	Host rock	36.41	1.95	21.3		20.46	0.35	8.48			9.26	98.21
Biotite	W1209	Host rock	36.05	2.1	21.07		21.82	0.39	8.63			9.95	100.01
Biotite	W1209	Host rock	35.91	2.38	21.19		21.94	0.35	8.02			10.21	100.00
Biotite	W1209	Host rock	36.51	2.11	21.88		20.98		8.62			9.9	100.00

Mineral	Sample		SiO ₂	TiO ₂	Al ₂ O ₃	Cr ₂ O ₃	FeO	MnO	MgO	CaO	Na ₂ O	K ₂ O	Total (Fe corr)
Biotite	W1209	Host rock	36.47	2.37	21.33		21.36	0.31	8.07			10.09	100.00
Biotite	W1209	Host rock	35.95	1.82	21.83		21.9	0.28	8.73			9.49	100.00
Biotite	W1211	Host rock	36.7	2.76	20.16		21.91	0.36	8.36			9.75	100.00
Biotite	W1211	Host rock	36.55	2.78	20.54		21.8	0.34	8.22		0.28	9.49	100.00
Biotite	W1211	Host rock	39.22	2.91	18.43		22.68	0.49	7.3			8.97	100.00
Biotite	W1211	Host rock	36.54	3.08	19.57		22.18	0.54	8.55			9.54	100.00
Biotite	W1211	Host rock	36.32	2.72	20.3		21.7	0.53	8.55			9.88	100.00
Biotite	W1211	Host rock	36.36	3	20.24		21.88	0.49	8.2			9.84	100.01
Biotite	W1211	Host rock	36.02	3.04	20.09		22.19	0.46	8.47			9.74	100.01
Biotite	W1211	Small vein	43.66	2.85	17.47		19.93	0.4	7.24			8.45	100.00
Biotite	W1211	Small vein	38.24	2.61	19.23		21.56	0.48	8.19			9.7	100.01
Biotite	W1211	Small vein	37.96	2.69	19.35		21.59	0.57	8.07			9.75	99.98
Biotite	W1211	Small vein	36.82	2.81	20.25		21.67	0.42	8.28			9.76	100.01
Biotite	W1211	Small vein	36.61	2.86	20.39		21.64	0.44	8.43			9.63	100.00
Biotite	W1211	Small vein	36.29	3.13	19.79		22.15	0.58	8.32			9.73	99.99
Biotite	W1211	Small vein	36.2	2.88	19.84		22.09	0.44	8.27			9.72	99.44
Biotite	W1211	Small vein	36.13	2.83	19.98		22.41	0.49	8.52			9.64	100.00
Biotite	W1211	Small vein	35.75	3.09	20.23		22.63	0.5	8.09			9.71	100.00
Biotite	W1211	Small vein	37.35	2.56	20.4		20.97	0.46	8.57			9.7	100.01
Biotite	W1211	Small vein	36.88	1.59	20.84		22.04	0.48	8.47			9.69	99.99
Biotite	W1211	Small vein	36.69	2.88	20.26		22.37	0.42	7.72			9.66	100.00
Biotite	W1211	Small vein	36.09	2.76	20.24		22.96	0.41	7.76			9.22	99.44
Biotite	W1213	Host rock	35.06	3.83	19.84		23.6	0.35	7.38			9.95	100.01
Biotite	W1213	Host rock	36.31	2.49	21.75		21.79		7.6			10.06	100.00
Biotite	W1213	Host rock	36.23	2.37	21.84		21.93		7.49			10.13	99.99
Biotite	W1213	Host rock	36.2	2.31	21.41		22.66		7.56			9.87	100.01
Biotite	W1213	Host rock	35.83		23.63		21.87		8.52			10.15	100.00
Biotite	W1213	Host rock	36.08	2.12	21.97		22.08	0.26	7.44			10.05	100.00
Biotite	W1213	Host rock	35.9	2.24	21.77		22.24	0.32	7.44			10.09	100.00
Biotite	W1213	Host rock	35.87	2.28	21.17		22.74	0.29	7.48			10.16	99.99
Biotite	W1213	Host rock	35.83	2.42	21.57		22.06	0.34	7.65			10.13	100.00
Biotite	W1213	Host rock	42.5	2.13	19.11		20.6		6.58			9.08	100.00
Biotite	W1213	Host rock	36.46	1.09	22.73		22.38		7.61			9.73	100.00
Biotite	W1213	Host rock	35.72	2.56	21.55		22.14	0.27	7.68			10.07	99.99
Biotite	W1213	Host rock	35.66	2.44	21.74		22.52		7.59			10.04	99.99
Biotite	W1213	Host rock	36.03	2.48	22.04		22.19		7.13			10.14	100.01
Biotite	W1213	Host rock	35.84	1.74	21.93		22.54	0.29	7.59			10.07	100.00
Biotite	W1213	Host rock	35.72	2.6	21.98		22.04		7.71			9.94	99.99
Biotite	W1213	Host rock	35.65	2.35	21.06		23.4	0.31	7.44			9.8	100.01
Biotite	W1213	Host rock	36.47	2.55	21.76		21.96		7.14			10.12	100.00

Mineral	Sample		SiO ₂	TiO ₂	Al ₂ O ₃	Cr ₂ O ₃	FeO	MnO	MgO	CaO	Na ₂ O	K ₂ O	Total (Fe corr)
Biotite	W1213	Host rock	36.06	2.54	21.11		22.55	0.3	7.46			9.98	100.00
Biotite	W1213	Host rock	35.99	2.47	21.69		21.75		8.04			10.06	100.00
Biotite	W1213	Host rock	36.21	2.24	22.52		21.79		7.04			10.19	99.99
Biotite	W1214	Host rock	36.99	2.01	21.56		21.23		8.47			9.74	100.00
Biotite	W1216	Host rock	36.44	3.36	21.1		21.34		7.75			10	99.99
Biotite	W1216	Small vein	38.59	3.4	20.14		21.1		7.71			9.06	100.00
Biotite	W1216	Small vein	37.59	2.58	21.47		20.53		7.91			9.92	100.00
Biotite	W1216	Small vein	34.99	3.1	20.15		24.56		7.06			9.77	99.63
Biotite	W1216	Small vein	37	3.18	21.31		20.93		7.58			10.01	100.01
Biotite	W1216	Small vein	36.27	3.35	20.68		22.06		7.54			10.1	100.00
Biotite	W1216	Small vein	37.14	3.35	20.9		20.81		7.41		0.58	9.8	99.99
Biotite	W1216	Small vein	41.56	2.62	18.8		20.72		7.03			9.27	100.00
Biotite	W1216	Small vein	36.78	2.2	22.04		20.67		8.29			10.01	99.99
Biotite	W1216	Small vein	46.29	2.04	17.78		18.89		6.52			8.47	99.99
Biotite	W1216	Small vein	36.23	3.88	21.8		21.08		6.92			10.1	100.01
Biotite	W1216	Small vein	35.09	2.9	20.68		25.45		8.28			7.6	100.00
Biotite	W1216	Small vein	35.87	3.52	20.31		21.89		7.68			9.91	99.18
Biotite	W1216	Small vein	37.79	3.37	21.72		21.05		7.38			8.7	100.01
Biotite	W1216	Small vein	37.74	3.25	19.67		21.7		7.32		0.3	10.01	99.99
Biotite	W1216	Small vein	37.5	3.68	20.67		20.99		6.68		0.37	10.11	100.00
Biotite	W1216	Small vein	36.48	3.4	21.28		21.06		7.59			10.19	100.00
Biotite	W1217	Host rock	35.89	3.51	20.98		21.97		7.72			9.93	100.00
Biotite	W1218	Host rock	36.02	3.21	20.9		21.81		7.77			10.29	100.00
Biotite	W1218	Host rock	36.57	1.92	22.13		20.97		8.11			10.31	100.01
Biotite	W1218	Host rock	36.61	2.1	22		21.16		7.93			10.21	100.01
Biotite	W1218	Host rock	36.03	2.99	21.68		22.85		7.95			8.5	100.00
Biotite	W1218	Host rock	36.15	1.8	22.43		21.04	0.29	8.15			10.14	100.00
Biotite	W1218	Host rock	35.56	3.43	20.95		23.15		7.26			9.65	100.00
Biotite	W1218	Host rock	36.33	2.09	22.35		20.83		8.15			10.26	100.01
Biotite	W1218	Host rock	35.81	3.55	20.63		22.08	0.32	7.54			10.06	99.99
Biotite	W1218	Host rock	37.83	2.3	21.71		20.57		7.76			9.83	100.00
Biotite	W1218	Host rock	36.07	3.12	21.61		22.17		7.97			9.05	99.99
Biotite	W1218	Host rock	36.39	3.22	21.23		21.21	0.26	7.69			10	100.00
Biotite	W1219	Host rock	36.17	3.33	20.88		21.4		7.8			10.18	99.76
Biotite	W1220	Host rock	37.03	3.54	20.72		21.26		7.55			9.89	99.99
Biotite	W1221	Host rock	35.94	2.86	20.73		22.22		7.67			9.92	99.34
Biotite	W1222	Host rock	38.15	0.91	22.16		23.21	0.21	7.74	0.62	1.58	4.53	99.11

Mineral	Sample		SiO ₂	TiO ₂	Al ₂ O ₃	Cr ₂ O ₃	FeO	MnO	MgO	CaO	Na ₂ O	K ₂ O	Total (Fe corr)
Biotite	W1223	Host rock	36.46	3.22	21.34		20.53		7.97			9.74	99.26
Biotite	W1223	Host rock	38.5	2.28	23.75		17.86	0.37	8.02			9.22	100.00
Biotite	W1223	Host rock	36.54	2.56	22.07		21.47		7.23			10.13	100.00
Biotite	W1223	Host rock	37.87	1.31	22.38		19.93	0.34	8.65			9.52	100.00
Biotite	W1223	Host rock	36.68	2.06	21.98		20.95		8.28			10.05	100.00
Biotite	W1223	Host rock	36.21	3.03	21.49		21.18	0.37	7.91			9.83	100.02
Biotite	W1223	Host rock	35.78	3.41	20.98		21.47	0.35	7.7			10.31	100.00
Biotite	W1223	Host rock	36.63	2.08	22.55		20.76		7.82			10.16	100.00
Biotite	W1223	Host rock	36.42	2.89	21.42		21.67		7.53			10.08	100.01
Biotite	W1223	Host rock	37.07	2.1	22.13		20.41	0.38	8			9.92	100.01
Biotite	W1223	Host rock	36.21	2.58	21.52		21.09	0.43	7.85			10.33	100.01
Biotite	W1223	Host rock	35.98	2.97	21.29		21.22	0.41	7.77			10.36	100.00
Biotite	W1223	Host rock	36.68	3.35	21.64		20.29	0.41	7.71			9.92	100.00
Biotite	W1223	Host rock	37.14	1.92	22.39		19.91		8.52			10.13	100.01
Biotite	W1223	Host rock	35.96	3.08	21.07		21.8		7.69			10.11	99.71
Biotite	W1223	Host rock	36.12	3.36	20.95		21.71	0.3	7.52			10.04	100.00
Biotite	W1223	Host rock	36.8	1.78	22.21		20.58	0.48	8.14			10.01	100.00
Biotite	W1223	Host rock	36.06	3.2	21.18		21.61		7.61			10.34	100.00
Biotite	W1224	Host rock	35.62	3.48	20.63		22.16	0.28	7.54			10.3	100.01
Biotite	W1225	Host rock	36.36	2.8	21.67		22.52		7.81			8.84	100.00
Biotite	W1225	Host rock	35.87	2.33	21.79		23.84		7.59			8.58	100.00
Biotite	W1225	Host rock	39	2.08	20.9	0.65	21.21		6.74			9.43	100.01
Biotite	W1225	Host rock	36.18	1.82	22.28		22.54		7.29			9.89	100.00
Biotite	W1225	Host rock	35.91	3.31	20.3		22.41		7.76			10.31	100.00
Biotite	W1225	Host rock	41.55	1.33	27.07		17.11		7.02			5.91	99.99
Biotite	W1225	Host rock	36.12	3.76	20.74		21.79		7.42			10.17	100.00
Biotite	W1225	Host rock	35.85	2.09	21.95	0.49	22.34	0.29	7.15			9.85	100.01
Biotite	W1225	Host rock	35.39	3.7	19.99		24.02	0.32	7.22			9.36	100.00
Biotite	W1225	Host rock	36.31	2	21.7		22.4		7.27			10.32	100.00
Biotite	W1225	Host rock	36.09	2.31	22.27	0.63	21.81		7			9.9	100.01
Biotite	W1225	Host rock	35.65	1.65	23.15		21.57		8.05			9.93	100.00
Biotite	W1225	Host rock	35.54	3.57	20.48		22.63	0.3	7.2			10.29	100.01
Biotite	W1228	Host rock	36.55	2.04	22.71		21.31		7.28			10.12	100.01
Biotite	W1228	Host rock	36.38	2.1	22.15		22.16		7.07			10.14	100.00
Biotite	W1228	Host rock	36.22	2.11	22.07		22.34		7.36			9.91	100.01
Biotite	W1228	Host rock	36.2	2.42	21.64		22.41		7.15			10.18	100.00
Biotite	W1228	Host rock	36.17	2.37	21.46		22.68		7.14			10.19	100.01
Biotite	W1228	Host rock	36.13	2.7	21.03		22.98		7.65			9.51	100.00
Biotite	W1228	Host rock	36.09	2.32	21.24		22.75		7.34			10.26	100.00
Biotite	W1228	Host rock	35.98	1.9	22.24		22.14		7.75			9.98	99.99
Biotite	W1228	Host rock	35.81	3.15	20.72		22.76		7.34			10.21	99.99
Biotite	W1228	Host rock	35.74	2.7	21.33		22.84		7.24			10.15	100.00
Biotite	W1228	Host rock	35.67	2.58	21.37	0.48	22.78		6.91			10.2	99.99
Biotite	W1228	Host rock	35.62	4.33	20.74		22.47		6.68			10.16	100.00
Biotite	W1229	Host rock	37.64	2.12	21.11		22.68		6.71			9.74	100.00
Biotite	W1229	Host rock	36.99	2.28	22.22	0.33	21.43		7.01			9.74	100.00
Biotite	W1229	Host rock	36.74	1.34	22.18	0.19	20.86		8.27		0.33	9.53	99.44
Biotite	W1229	Host rock	36.42	3.08	21.19		22.1		7.14			10.07	100.00
Biotite	W1229	Host rock	43.05	1.92	20.47		19.37		6.46			8.74	100.01
Biotite	W1229	Host rock	36.92	1.05	22.63		21.21		8.3			9.89	100.00
Biotite	W1229	Host rock	35.97	2.24	21.67		22.77		7.29			10.07	100.01
Biotite	W1229	Host rock	35.63	2	21.77		23.2		7.13			10.27	100.00

Mineral	Sample		SiO ₂	TiO ₂	Al ₂ O ₃	Cr ₂ O ₃	FeO	MnO	MgO	CaO	Na ₂ O	K ₂ O	Total (Fe corr)
Biotite	W1229	Host rock	36.97	2.28	21.69		21.42		8.12			9.52	100.00
Biotite	W1229	Host rock	36.11	2.57	21.67	0.25	22.28		7.46			9.65	99.99
Biotite	W1229	Host rock	35.95	2.14	21.55		22.79		7.23			10.34	100.00
Biotite	W1229	Host rock	36.79	2.51	21.67		22.53		6.9			9.59	99.99
Biotite	W1229	Host rock	36.45	2.29	21.57		22.44		7.27			9.97	99.99
Biotite	W1229	Host rock	36	2.08	22.14		22.18		7.65			9.94	99.99
Biotite	W1229	Host rock	41.96	1.8	19.54		21.2		6.22			9.27	99.99
Biotite	W1229	Host rock	37.37	2.43	21.9	0.3	20.89		7.71			9.41	100.01
Biotite	W1229	Host rock	38.58	2.22	23.18		18.47		8.65			8.92	100.02
Biotite	W1229	Host rock	36.28	2.4	21.8		22.45		6.76			10.32	100.01
Muscovite	W1201	Host rock	47.68	0.6	38.28		0.93		0.54		0.49	11.49	100.01
Muscovite	W1201	Host rock	46.84	0.53	38.53		0.91		0.48			11.78	99.07
Muscovite	W1201	Host rock	47.52	0.41	38.58		0.92		0.53		0.53	11.51	100.00
Muscovite	W1211	Host rock	47.83	0.93	37.63		1.05		0.61		0.45	11.51	100.01
Muscovite	W1211	Host rock	48.37	0.86	37.08		1.2		0.77		0.5	11.22	100.00
Muscovite	W1211	Host rock	47.47	0.85	36.55		2.82		0.78		0.51	11.02	100.00
Muscovite	W1211	Host rock	48.77	0.68	36.3		1.57		0.75		0.47	10.84	99.38
Muscovite	W1211	Host rock	47.93	0.89	37.51		1.4		0.58		0.49	11.2	100.00
Muscovite	W1213	Host rock	47.77	0.45	38.67		0.82				0.58	11.71	100.00
Muscovite	W1213	Host rock	47.45	0.59	38.41		0.87		0.38		0.54	11.76	100.00
Muscovite	W1213	Host rock	47.23	0.97	38.22		0.9		0.4		0.5	11.78	100.00
Muscovite	W1213	Host rock	47.09	0.85	38.28		1.1		0.49		0.53	11.67	100.01
Muscovite	W1213	Host rock	47.26	0.49	38.64		1.11		0.43		0.52	11.55	100.00
Muscovite	W1213	Host rock	47.82	0.46	38.93		1.02					11.77	100.00
Muscovite	W1213	Host rock	47.78	0.6	38.51		1.02		0.61			11.48	100.00
Muscovite	W1213	Host rock	47.39	0.63	38.58		0.82		0.35		0.58	11.65	100.00
Muscovite	W1216	Host rock	47.15	0.9	38.31		0.83		0.36		0.48	11.66	99.69
Muscovite	W1216	Host rock	47.6	0.48	38.21		0.82		0.5		0.4	12	100.01
Muscovite	W1216	Host rock	47.75	0.58	37.94		1.21		0.62		0.47	11.43	100.00
Muscovite	W1216	Host rock	47.52	0.42	38.44		0.96		0.49		0.6	11.58	100.01
Muscovite	W1218	Host rock	47.82	0.58	38.39		0.65		0.53		0.4	11.63	100.00
Muscovite	W1218	Host rock	47.18	0.96	38.33		0.84		0.42		0.44	11.84	100.01
Muscovite	W1218	Host rock	47.75	0.39	38.38		0.83		0.49		0.49	11.66	99.99
Muscovite	W1218	Host rock	47.36	1.47	37.49		0.8		0.57		0.48	11.84	100.01
Muscovite	W1218	Host rock	47.72	0.58	38.49		0.75		0.52		0.43	11.52	100.01
Muscovite	W1223	Host rock	47.65	0.5	38.93		0.88					12.04	100.00
Muscovite	W1223	Host rock	47.51	0.77	38.02		1.03		0.57		0.36	11.73	99.99
Muscovite	W1223	Host rock	47.93	0.43	39.02		0.91					11.7	99.99
Muscovite	W1223	Host rock	47.38	0.74	38.46		0.87		0.51		0.47	11.56	99.99
Muscovite	W1223	Host rock	47.46	0.69	38.37		0.83		0.55			11.8	99.70
Muscovite	W1223	Host rock	47.46	0.37	38.56		0.97		0.53		0.51	11.6	100.00
Muscovite	W1223	Host rock	48	0.48	38.17		0.88		0.48		0.52	11.46	99.99
Muscovite	W1223	Host rock	47.61	0.27	38.47		0.77		0.49		0.49	11.62	99.72
Muscovite	W1223	Host rock	47.61	0.76	38.03		0.81		0.56		0.51	11.72	100.00
Muscovite	W1223	Host rock	47.3	0.69	38.55		1.16		0.43		0.44	11.44	100.01
Muscovite	W1229	Host rock	47.14		35.96		3.97		1.62			11.31	100.00
Muscovite	W1229	Host rock	47.55	1.33	36.94		1.08		0.82		0.45	11.09	99.26
Muscovite	W1211	Small vein	49.1	0.8	36.87		0.96		0.49		0.46	11.32	100.00
Muscovite	W1211	Small vein	48.75	0.79	37.08		1.13		0.63		0.52	11.11	100.01
Muscovite	W1211	Small	48.44	0.97	37.53		0.86		0.56		0.47	11.18	100.01

Mineral	Sample		SiO ₂	TiO ₂	Al ₂ O ₃	Cr ₂ O ₃	FeO	MnO	MgO	CaO	Na ₂ O	K ₂ O	Total (Fe corr)
Muscovite	W1211	vein Small vein	47.52	1.05	36.35		2.21		1.09		0.46	11.32	100.00
Muscovite	W1211	Small vein	47.65	0.67	38.08		1.11		0.58		0.51	11.4	100.00
Muscovite	W1216	Small vein	46.96	1	37.19		2.93		0.76		0.48	10.67	99.99
Muscovite	W1221	Large vein	47.69	0.48	38.16		0.57		0.26		0.57	11.35	99.08
Muscovite	W1207 d	Quartzite	47.66	0.45	35.02		3.85		1.05		1.11	10.17	99.31
Muscovite	W1207 d	Quartzite	48.14	0.38	34.81		3.43		1.18		1.06	10.1	99.10
Muscovite	W1207 d	Quartzite	49.31	0.58	33.67		3.89		1.24		1.13	9.95	99.77
Muscovite	W1207 d	Quartzite	47.16		35.04		3.76		1.06		1.2	9.79	98.01
Muscovite	W1207 d	Quartzite	47.31	0.31	33.43		4.51		1.31		1.01	8.57	96.45
Muscovite	W1207 d	Quartzite	48.21		33.46		3.53		1.48		0.83	10.27	97.78
Muscovite	W1207 d	Quartzite	49.52	0.49	32.79		3.47		1.42		0.68	10.41	98.78
Muscovite	W1207 d	Quartzite	49.6	0.4	33.59		3.82		1.04		1.56	9.45	99.46
Muscovite	W1207 d	Quartzite	49.67		34.49		3.32		1.08		0.73	10.72	100.01
Muscovite	W1207 d	Quartzite	47.67	0.39	34.67		3.93		0.99		1.04	10.75	99.44
Muscovite	W1207 d	Quartzite	47.93	0.38	34.34		3.66		1.52		0.86	10.58	99.27
Muscovite	W1207 e	Quartzite	48.58	0.97	35.04		3.25		1		1.13	10.03	100.00
Muscovite	W1207 e	Quartzite	48.7	0.57	34.89		3.17		1.14		0.8	10.73	100.00
Muscovite	W1207 e	Quartzite	48.07	1.16	34.73		3.52		1.1		1.13	10.29	100.00
Muscovite	W1207 e	Quartzite	47.95	0.93	34.48		3.61		1.11		1.2	10.14	99.42
Muscovite	W1207 e	Quartzite	47.75	0.98	34.84		3.5		0.97		1.05	10.21	99.30
Muscovite	W1207 e	Quartzite	49.54	0.4	35.32		3.15		1.3		0.74	9.55	100.00
Muscovite	W1207 e	Quartzite	48.07	0.74	34.99		3.56		0.96		1.12	10.56	100.00
Muscovite	W1207 e	Quartzite	47.84	0.46	35.37		3.7		1.11		1.16	9.81	99.45
Muscovite	W1207 h	Quartzite	48.14	0.48	35.09		3.38		1.17		0.96	10.79	100.01
Muscovite	W1207 h	Quartzite	48.05	0.62	35.14		3.4		1.09		1.01	10.68	99.99
Muscovite	W0903	Host rock	47.54	0.98	37.11		1.3		0.76		0.29	12.02	100.00
Muscovite	W0903	Host rock	47.45	1.23	36.33		2.14		0.78		0.32	11.75	100.00
Muscovite	W1122	Host rock	47.55	0.92	38.11		0.97		0.45		0.6	11.41	100.01

Mineral	Sample		SiO ₂	TiO ₂	Al ₂ O ₃	Cr ₂ O ₃	FeO	MnO	MgO	CaO	Na ₂ O	K ₂ O	Total (Fe corr)
Muscovite	W1122	Host rock	47.78	0.95	37.86		0.79		0.5		0.46	11.66	100.00
Muscovite	W1122	Host rock	47.84	0.94	38.07		1.03		0.56			11.55	99.99
Muscovite	W1122	Host rock	48.1		38.15		1.07		0.64			12.05	100.01
Muscovite	W1122	Host rock	47.38	1.11	37.55		1.32		0.56		0.45	11.63	100.00
Muscovite	W1122	Host rock	47.38	1.21	37.43		1.2		0.63			12.15	100.00
Muscovite	W1122	Host rock	47.72	1.07	37.84		1.09		0.56			11.72	100.00
Muscovite	W1122	Host rock	48.03	1.16	37.69		1					12.12	100.00
Muscovite	W1122	Host rock	47.28	0.99	38.19		0.92		0.51		0.44	11.67	100.00
Muscovite	W1122	Host rock	47.13	0.84	38.03		0.94		0.46		0.43	12.16	99.99
Muscovite	W1122	Host rock	47.85		38.63		0.98		0.63			11.92	100.01
Muscovite	W1122	Host rock	47.47	0.93	37.72		0.99		0.46		0.42	12.02	100.01
Muscovite	W1122	Host rock	47.81	1.03	38.12		1.16					11.88	100.00
Muscovite	W1122	Host rock	47.86	1.04	37.57		0.92		0.62			12	100.01
Muscovite	W1122	Host rock	47.04	1.26	38.15		1.09		0.5			11.97	100.01
Muscovite	W1122	Host rock	47.79	0.59	38.03		1.03		0.6			11.96	100.00
Muscovite	W1122	Host rock	47.81		38.51		1.15		0.59			11.95	100.01
Muscovite	W1122	Host rock	47.57	0.95	37.74		1.05		0.48		0.46	11.74	99.99
Muscovite	W1122	Host rock	47.86	1.06	37.74		1.26					12.09	100.01
Muscovite	W1122	Host rock	47.26	1.14	37.95		0.95		0.57			12.14	100.01
Muscovite	W1122	Host rock	47.44	0.98	38.07		0.99					12.53	100.01
Muscovite	W1122	Host rock	48.28		38.13		1.09		0.58			11.92	100.00
Muscovite	W1122	Host rock	47.66	0.98	37.76		1.08		0.6			11.93	100.01
Muscovite	W1122	Host rock	47.6	0.52	38.04		1.05		0.51		0.44	11.83	99.99
Muscovite	W1122	Host rock	48.16		38.41		1.2		0.62			11.62	100.01
Muscovite	W1122	Host rock	47.77	0.98	38.46		0.97					11.81	99.99
Muscovite	W1221	Host rock	48.17	0.56	36.73		1.49		0.71		0.44	11.32	99.42
Muscovite	W1225	Host rock	47.01	0.73	38.65		0.78		0.53		0.53	11.77	100.00
Muscovite	W1225	Host rock	46.93	0.57	38.77		0.9		0.34		0.55	11.94	100.00
Muscovite	W1225	Host rock	47.01	0.74	38.9		0.79				0.57	11.99	100.00
Muscovite	W1228	Host rock	47.68	0.55	38.77		1.16		0.4		0.44	10.99	99.99
Muscovite	W1228	Host rock	47.49	0.39	38.6		1.13		0.62			11.77	100.00
Muscovite	W1228	Host rock	47.21	0.64	38.27		0.96		0.52		0.4	12.01	100.01
Muscovite	W1228	Host rock	47.17	0.8	38.38		0.9		0.48		0.4	11.86	99.99
Muscovite	W1228	Host rock	47.16	0.5	38.5		1.13		0.5		0.52	11.67	99.98
Muscovite	W1228	Host rock	47.1	0.44	38.46		1.04		0.49		0.54	11.92	99.99
K-feldspar	W0903	Host rock	63.82		19.11		0.26				0.82	14.67	98.68
K-feldspar	W0903	Small vein	63.58		18.76						0.79	15.72	98.85
K-feldspar	W0903	Small vein	65.51		18.55						0.2	15.75	100.01
K-feldspar	W0903	Small vein	65.09		18.34		0.49					16.08	100.00
K-feldspar	W1122	Host rock	64.79		18.55						1.05	14.83	99.22
K-feldspar	W1122	Host rock	63.65		18.46						0.78	14.85	97.74
K-feldspar	W1122	Host rock	61.26		18.27					2.31	0.73	14.99	97.56
K-feldspar	W1122	Host rock	62.73	2.65	18.49						0.95	15.18	100.00
K-feldspar	W1122	Host rock	63.98		18.8		0.27				0.94	15.31	99.30
K-feldspar	W1122	Host rock	63.72		19.06						0.94	15.35	99.07
K-feldspar	W1122	Host rock	63.98		19.03						0.86	15.38	99.25
K-feldspar	W1122	Host rock	63.88		18.88						0.99	15.4	99.15
K-feldspar	W1122	Host rock	63.72		18.88		0.28				0.86	15.41	99.15
K-feldspar	W1122	Host rock	63.79		18.87						0.96	15.41	99.03

Mineral	Sample		SiO ₂	TiO ₂	Al ₂ O ₃	Cr ₂ O ₃	FeO	MnO	MgO	CaO	Na ₂ O	K ₂ O	Total (Fe corr)
K-feldspar	W1122	Host rock	63.95		18.9						0.71	15.48	99.04
K-feldspar	W1122	Host rock	63.99		18.92						0.83	15.49	99.23
K-feldspar	W1122	Host rock	63.46		18.95		0.28				0.93	15.5	99.12
K-feldspar	W1122	Host rock	63.21		18.54						0.86	15.56	98.17
K-feldspar	W1122	Host rock	63.62		19						0.94	15.58	99.14
K-feldspar	W1122	Host rock	63.94		18.8						0.91	15.58	99.23
K-feldspar	W1122	Host rock	63.49		18.82		0.42				0.66	15.59	98.98
K-feldspar	W1122	Host rock	63.78		18.94						0.75	15.63	99.10
K-feldspar	W1122	Host rock	63.87		18.79						0.81	15.69	99.16
K-feldspar	W1201	Host rock	47.65		39.09		0.92				0.71	11.63	100.00
K-feldspar	W1201	Host rock	48.05		39.08		0.99					11.88	100.00
K-feldspar	W1201	Host rock	64.06		19.29						1.45	14.19	98.99
K-feldspar	W1201	Host rock	63.81		19.35						1.79	14.31	99.26
K-feldspar	W1201	Host rock	63.11		19.06						1.36	14.42	97.95
K-feldspar	W1201	Host rock	64.06		19.06						1.56	14.44	99.12
K-feldspar	W1201	Host rock	63.67		19.09						1.52	14.57	98.85
K-feldspar	W1201	Host rock	63.36		19.35						1.3	14.68	98.69
K-feldspar	W1201	Host rock	63.64		19.1						1.24	14.87	98.85
K-feldspar	W1201	Host rock	63.94		19						1.15	14.92	99.01
K-feldspar	W1201	Host rock	63.35		19.34						1.07	15.04	98.80
K-feldspar	W1201	Host rock	63.97		19.17						1.18	15.08	99.40
K-feldspar	W1201	Host rock	63.08		18.92						1.4	15.25	98.65
K-feldspar	W1211	Small vein	68.04	0.36	22.8		0.66		0.41		0.29	7.44	100.00
K-feldspar	W1211	Small vein	64.85	0.46	25.02		0.83		0.54		0.36	7.95	100.01
K-feldspar	W1211	Small vein	54.33	0.66	32.38		1.2		0.65		0.47	9.48	99.17
K-feldspar	W1211	Small vein	55.3	0.73	32.11		0.87		0.59		0.47	9.91	99.98
K-feldspar	W1211	Small vein	53.17	0.78	33.62		1.02		0.6		0.46	10.36	100.01
K-feldspar	W1213	Host rock	63.93		19.28						1.62	14.25	99.08
K-feldspar	W1213	Host rock	63.88		19.04						1.68	14.4	99.00
K-feldspar	W1213	Host rock	63.84		19.28						1.43	14.45	99.00
K-feldspar	W1213	Host rock	63.96		18.92						1.28	14.83	98.99
K-feldspar	W1216	Host rock	35.62	3	20.65		22.32		7.78			9.77	99.14
K-feldspar	W1216	Host rock	64.04		18.86						1.9	13.42	98.22
K-feldspar	W1216	Small vein	65.25		17.98						1.19	13.57	97.99
K-feldspar	W1216	Host rock	65.97		18.14		0.3				1.25	14.35	100.01
K-feldspar	W1216	Host rock	64.12		18.73						1.21	14.56	98.62
K-feldspar	W1218	Host rock	62.42		19.15						1.41	13.85	96.83
K-feldspar	W1218	Host rock	63.68		19.33						1.28	14.46	98.75
K-feldspar	W1218	Host rock	63.12		19.36						1.34	14.54	98.36
K-feldspar	W1218	Host rock	63.56		18.98						1.15	14.82	98.51
K-feldspar	W1218	Host rock	63.31		19.28						1.33	14.82	98.74
K-feldspar	W1218	Host rock	63.41		19.33						1.14	14.88	98.76
K-feldspar	W1218	Host rock	63.2		19.16						1.16	15.16	98.68
K-feldspar	W1221	Host rock	62.92		19.05						0.89	14.57	97.43
K-feldspar	W1221	Large vein	62.19		19.22						0.73	14.61	96.75
K-feldspar	W1221	Host rock	62.71		18.97		0.42				0.81	14.69	97.60

Mineral	Sample		SiO ₂	TiO ₂	Al ₂ O ₃	Cr ₂ O ₃	FeO	MnO	MgO	CaO	Na ₂ O	K ₂ O	Total (Fe corr)
K-feldspar	W1221	Host rock	63.11		19.09						0.75	14.76	97.71
K-feldspar	W1221	Host rock	62.2		19.1						0.89	14.78	96.97
K-feldspar	W1221	Large vein	62.53		19.14						0.86	14.9	97.43
K-feldspar	W1221	Host rock	62.99		19.06						0.89	15.01	97.95
K-feldspar	W1221	Host rock	62.81		19						0.84	15.03	97.68
K-feldspar	W1221	Host rock	62.71		19.23						0.88	15.22	98.04
K-feldspar	W1221	Large vein	62.23		19.24						0.66	15.64	97.77
K-feldspar	W1221	Large vein	63.21		18.95						0.27	15.74	98.17
K-feldspar	W1223	Host rock	64.27		19.05						1.76	14.18	99.26
K-feldspar	W1223	Host rock	64		18.84		0.28				1.21	14.86	99.19
K-feldspar	W1223	Host rock	64.09		18.97						1.28	15.07	99.41
K-feldspar	W1223	Host rock	63.86		18.93						1.32	15.12	99.23
K-feldspar	W1223	Host rock	64.2		18.89						1.07	15.29	99.45
K-feldspar	W1223	Host rock	63.84		19.01						1.18	15.3	99.33
K-feldspar	W1223	Host rock	63.62		18.99						1.26	15.34	99.21
K-feldspar	W1225	Host rock	70.51		15.42						1.17	11.9	99.00
K-feldspar	W1225	Host rock	63.48		19.26		0.25				1.29	14.89	99.17
K-feldspar	W1225	Host rock	63.69		19.17						1.22	14.98	99.06
K-feldspar	W1225	Host rock	63.98		19.13						1.11	15.07	99.29
K-feldspar	W1225	Host rock	63.86		18.96						1.42	15.07	99.31
K-feldspar	W1225	Host rock	64.16		18.83						1.2	15.32	99.51
K-feldspar	W1225	Host rock	63.6		18.93						1.05	15.66	99.24
K-feldspar	W1228	Host rock	63.21		19.39						2.08	13.59	98.27
K-feldspar	W1228	Host rock	64.08		18.67						1.41	14.79	98.95
K-feldspar	W1228	Host rock	63.31		19.22						1.31	14.88	98.72
K-feldspar	W1228	Host rock	63.46		19.22						1.24	14.93	98.85
K-feldspar	W1228	Host rock	63.67		18.97						1.26	15.17	99.07
K-feldspar	W1228	Host rock	63.51		19.07						0.97	15.45	99.00
K-feldspar	W1228	Host rock	63.86		18.63						1.18	15.46	99.13
K-feldspar	W1228	Host rock	63.68		18.9						1.02	15.49	99.09
K-feldspar	W1228	Host rock	63.35		19.18						1.06	15.57	99.16
K-feldspar	W1229	Host rock	65.06		18.75						1.42	14.77	100.00
Plagioclase feldspar	W0903	Host rock	63.92		22.86					4.02	9.08	0.13	100.01
Plagioclase feldspar	W0903	Host rock	62.91		23.36		0.22			4.17	9.17	0.18	100.01
Plagioclase feldspar	W0903	Host rock	63.7		23.25					3.5	8.91	0.64	100.00
Plagioclase feldspar	W0903	Host rock	67.14		20.54					1.39	9.81	1.11	99.99
Plagioclase feldspar	W0903	Host rock	64.05		22.97					3.68	9.3		100.00
Plagioclase feldspar	W1122	Host rock	62.91		23.57		0.25			4.27	8.85	0.15	100.00
Plagioclase feldspar	W1122	Host rock	63.21		23.33					4.41	8.9	0.15	100.00
Plagioclase feldspar	W1122	Host rock	63.02		23.51					4.4	8.85	0.21	99.99
Plagioclase feldspar	W1122	Host rock	62.71		23.64					4.45	8.99	0.21	100.00

Mineral	Sample		SiO ₂	TiO ₂	Al ₂ O ₃	Cr ₂ O ₃	FeO	MnO	MgO	CaO	Na ₂ O	K ₂ O	Total (Fe corr)
Plagioclase feldspar	W1122	Host rock	62.63		23.36		0.28			4.66	8.86	0.22	100.01
Plagioclase feldspar	W1122	Host rock	64.18		22.81					3.76	9.25		100.00
Plagioclase feldspar	W1122	Host rock	63		23.61					4.41	8.98		100.00
Plagioclase feldspar	W1201	Host rock	41.46		14.87					2.5	6.05	0.1	64.98
Plagioclase feldspar	W1201	Host rock	63.17		23.56					3.9	9.23	0.14	100.00
Plagioclase feldspar	W1201	Host rock	63.39		23.28					3.95	9.21	0.16	99.99
Plagioclase feldspar	W1201	Host rock	64.03		22.82					3.74	9.25	0.17	100.01
Plagioclase feldspar	W1201	Host rock	63.77		23.02					3.91	9.12	0.17	99.99
Plagioclase feldspar	W1201	Host rock	63.77		23.09					3.8	9.14	0.19	99.99
Plagioclase feldspar	W1201	Host rock	63.42		23.04		0.29			3.85	9.19	0.21	100.00
Plagioclase feldspar	W1201	Host rock	63.55		23.17					3.88	9.17	0.23	100.00
Plagioclase feldspar	W1201	Host rock	63.32		23.39					3.84	9.19	0.26	100.00
Plagioclase feldspar	W1201	Host rock	63.98		22.82					3.72	9.48		100.00
Plagioclase feldspar	W1201	Host rock	64.17		22.87					3.73	9.23		100.00
Plagioclase feldspar	W1201	Host rock	63.62		23.16					3.95	9.27		100.00
Plagioclase feldspar	W1201	Host rock	63.69		23.1		0.27			3.97	8.97		100.00
Plagioclase feldspar d	W1207	Quartzite	68.3		20.06					0.26	11.38		100.00
Plagioclase feldspar d	W1207	Quartzite	67.67		20.76					1.42	10.15		100.00
Plagioclase feldspar d	W1207	Quartzite	67.7		20.53					1.44	10.34		100.01
Plagioclase feldspar d	W1207	Quartzite	66.96		20.66					1.59	10.79		100.00
Plagioclase feldspar d	W1207	Quartzite	66.63		21.08					1.7	10.59		100.00
Plagioclase feldspar d	W1207	Quartzite	66.02		21.64					2.01	10.33		100.00
Plagioclase feldspar d	W1207	Quartzite	64.23		23.81				0.28	2.06	9.62		100.00
Plagioclase feldspar d	W1207	Quartzite	66.43		21.47					2.12	9.98		100.00
Plagioclase feldspar d	W1207	Quartzite	66.55		21.24					2.15	10.06		100.00
Plagioclase feldspar d	W1207	Quartzite	65.23		22.05					2.6	9.99		99.87
Plagioclase feldspar d	W1207	Quartzite	66.84		20.84					2.8	9.09		99.57

Mineral	Sample		SiO ₂	TiO ₂	Al ₂ O ₃	Cr ₂ O ₃	FeO	MnO	MgO	CaO	Na ₂ O	K ₂ O	Total (Fe corr)
Plagioclase feldspar	W1207 e	Quartzite	65.12		22.03					2.86	9.99		100.00
Plagioclase feldspar	W1207 e	Quartzite	65.46		22.06					2.89	9.59		100.00
Plagioclase feldspar	W1207 e	Quartzite	64.96		22.05			0.24		2.92	9.82		99.99
Plagioclase feldspar	W1207 e	Quartzite	64.72		22.44					3.06	9.78		100.00
Plagioclase feldspar	W1207 e	Quartzite	65.23		21.95					3.33	8.91		99.42
Plagioclase feldspar	W1207 e	Quartzite	64.6		22.47					3.36	9.57		100.00
Plagioclase feldspar	W1209	Host rock	61.66		24.41					5.55	8.23	0.15	100.00
Plagioclase feldspar	W1209	Host rock	61.98		24.27					5.48	8.27		100.00
Plagioclase feldspar	W1209	Host rock	62.02		24.11					5.59	8.28		100.00
Plagioclase feldspar	W1209	Host rock	60.31		25.42					6.46	7.81		100.00
Plagioclase feldspar	W1211	Host rock	63.11		23.22		0.28			4.39	8.88	0.12	100.00
Plagioclase feldspar	W1211	Small vein	63.14		23.51					4.27	8.93	0.14	99.99
Plagioclase feldspar	W1211	Host rock	63.17		23.5					4.3	8.88	0.15	100.00
Plagioclase feldspar	W1211	Small vein	63.12		23.49					4.46	8.78	0.15	100.00
Plagioclase feldspar	W1211	Host rock	62.84		23.65					4.53	8.82	0.15	99.99
Plagioclase feldspar	W1211	Small vein	63.24		23.3					4.63	8.68	0.15	100.00
Plagioclase feldspar	W1211	Host rock	62.96		23.36					4.58	8.94	0.16	100.00
Plagioclase feldspar	W1211	Host rock	63.07		23.32					4.25	9.1	0.26	100.00
Plagioclase feldspar	W1211	Host rock	62.59		23.44		0.45			4.34	8.92	0.26	100.00
Plagioclase feldspar	W1211	Small vein	62.64		23.03		0.95			4.15	8.74	0.48	99.99
Plagioclase feldspar	W1211	Small vein	62.89		23.35					4.16	8.75	0.85	100.00
Plagioclase feldspar	W1211	Host rock	68.25		19.93					3.68	8.14		100.00
Plagioclase feldspar	W1211	Small vein	69.62		19.12					3.78	7.48		100.00
Plagioclase feldspar	W1211	Small vein	61.95		23.2		0.42			3.93	9.11		98.61
Plagioclase feldspar	W1211	Small vein	63.75		23.12					4	9.12		99.99
Plagioclase feldspar	W1211	Small vein	64.01		23.08					4.1	8.81		100.00
Plagioclase feldspar	W1211	Small vein	65.2		22.2					4.19	8.4		99.99

Mineral	Sample		SiO ₂	TiO ₂	Al ₂ O ₃	Cr ₂ O ₃	FeO	MnO	MgO	CaO	Na ₂ O	K ₂ O	Total (Fe corr)
Plagioclase feldspar	W1211	Host rock	63.03		23.38		0.35			4.21	9.02		99.99
Plagioclase feldspar	W1211	Host rock	62.97		23.3		0.29			4.22	9.23		100.01
Plagioclase feldspar	W1211	Host rock	63.63		23.1					4.22	9.05		100.00
Plagioclase feldspar	W1211	Host rock	63.61		23.39					4.36	8.64		100.00
Plagioclase feldspar	W1211	Host rock	63.27		23.14		0.4			4.38	8.82		100.01
Plagioclase feldspar	W1211	Small vein	63.13		23.64					4.39	8.83		99.99
Plagioclase feldspar	W1211	Host rock	63.37		23.26					4.49	8.88		100.00
Plagioclase feldspar	W1211	Small vein	63.16		23.55					4.49	8.8		100.00
Plagioclase feldspar	W1211	Host rock	63.29		23.36					4.51	8.84		100.00
Plagioclase feldspar	W1211	Small vein	63.25		23.35					4.52	8.89		100.01
Plagioclase feldspar	W1211	Small vein	62.69		23.58		0.35			4.54	8.84		100.00
Plagioclase feldspar	W1211	Host rock	63.19		23.2		0.26			4.58	8.77		100.00
Plagioclase feldspar	W1211	Small vein	62.82		23.63					4.81	8.74		100.00
Plagioclase feldspar	W1211	Small vein	61.87		24.36					5.57	8.19		99.99
Plagioclase feldspar	W1213	Host rock	63.34		23.28					4.52	8.86		100.00
Plagioclase feldspar	W1213	Host rock	63.19		23.4					4.62	8.79		100.00
Plagioclase feldspar	W1213	Host rock	63.19		23.57					4.67	8.58		100.01
Plagioclase feldspar	W1214	Host rock	61.79		24.24		0.25			5.39	8.33		100.00
Plagioclase feldspar	W1216	Host rock	60.22	0.24	23.2		1.8		0.61	4.24	7.76	1.01	99.08
Plagioclase feldspar	W1216	Small vein	63.31		23.52					4.37	8.81		100.01
Plagioclase feldspar	W1216	Host rock	65.18		22.2		0.22			4.48	7.92		100.00
Plagioclase feldspar	W1216	Host rock	63.03		23.52					4.52	8.93		100.00
Plagioclase feldspar	W1216	Small vein	62.87		23.4					4.68	8.64		99.59
Plagioclase feldspar	W1216	Small vein	62.03		23.31		1.5			4.71	8.45		100.00
Plagioclase feldspar	W1216	Host rock	62.66		23.68		0.21			4.79	8.67		100.01
Plagioclase feldspar	W1216	Small vein	62.37		23.84					4.79	8.6		99.60
Plagioclase feldspar	W1216	Host rock	62.86		23.72					4.82	8.61		100.01

Mineral	Sample		SiO ₂	TiO ₂	Al ₂ O ₃	Cr ₂ O ₃	FeO	MnO	MgO	CaO	Na ₂ O	K ₂ O	Total (Fe corr)
Plagioclase feldspar	W1216	Small vein	62.17		23.96					4.83	8.5		99.46
Plagioclase feldspar	W1216	Small vein	61.46		23.48		1.13			4.85	8.57		99.49
Plagioclase feldspar	W1216	Small vein	62.15		23.96					4.87	8.52		99.50
Plagioclase feldspar	W1216	Host rock	62.43		24.03					4.93	8.61		100.00
Plagioclase feldspar	W1216	Small vein	62.04		24.13					4.93	8.54		99.64
Plagioclase feldspar	W1216	Host rock	62.65		23.77					4.95	8.63		100.00
Plagioclase feldspar	W1216	Small vein	62.55		23.92		0.39			5	8.14		100.00
Plagioclase feldspar	W1216	Small vein	61.45		23.89		0.5			5.02	8.29		99.15
Plagioclase feldspar	W1216	Small vein	62.6		23.85					5.02	8.52		99.99
Plagioclase feldspar	W1216	Small vein	62.41		24.08					5.04	8.46		99.99
Plagioclase feldspar	W1216	Small vein	61.92		23.99					5.18	8.39		99.48
Plagioclase feldspar	W1216	Small vein	61.84		24.04					5.2	8.6		99.68
Plagioclase feldspar	W1216	Small vein	60.92		23.67		0.7			5.25	8.24		98.78
Plagioclase feldspar	W1216	Small vein	62.28		24.05					5.33	8.34		100.00
Plagioclase feldspar	W1216	Small vein	61.63		24.57					5.7	8.11		100.01
Plagioclase feldspar	W1216	Small vein	61.57		24.55					5.72	8.15		99.99
Plagioclase feldspar	W1216	Small vein	61.75		24.09		0.36			5.77	8.03		100.00
Plagioclase feldspar	W1216	Small vein	61.47		24.39		0.32			5.93	7.89		100.00
Plagioclase feldspar	W1216	Small vein	60.54		24.84					6.4	7.76		99.54
Plagioclase feldspar	W1216	Host rock	58.8		26.35					7.69	7.16		100.00
Plagioclase feldspar	W1218	Host rock	63.45		22.79					3.9	9.13	0.13	99.40
Plagioclase feldspar	W1218	Host rock	64.09		22.73					3.63	9.38	0.17	100.00
Plagioclase feldspar	W1218	Host rock	64.01		22.94					3.56	9.31	0.18	100.00
Plagioclase feldspar	W1218	Host rock	63.78		23.03					3.72	9.26	0.21	100.00
Plagioclase feldspar	W1218	Host rock	63.82		22.95					3.68	9.35	0.22	100.02
Plagioclase feldspar	W1218	Host rock	63.98		23.03					3.71	9.29		100.01
Plagioclase feldspar	W1218	Host rock	63.85		23.12					3.73	9.29		99.99

Mineral	Sample		SiO ₂	TiO ₂	Al ₂ O ₃	Cr ₂ O ₃	FeO	MnO	MgO	CaO	Na ₂ O	K ₂ O	Total (Fe corr)
Plagioclase feldspar	W1221	Host rock	66.8		20.96		0.44			1.36	10.21	0.22	99.99
Plagioclase feldspar	W1221	Host rock	65.68		23.06		0.4		0.23	1.52	8.59	0.53	100.01
Plagioclase feldspar	W1221	Host rock	65.5		21.93					2.41	9.6	0.56	100.00
Plagioclase feldspar	W1221	Host rock	68.76		20.05					0.43	10.76		100.00
Plagioclase feldspar	W1221	Host rock	67.72		20.07					0.81	10.99		99.59
Plagioclase feldspar	W1221	Host rock	67.24		20.45		0.39			1.47	10.45		100.00
Plagioclase feldspar	W1221	Large vein	66.88		21.21					1.58	10.32		99.99
Plagioclase feldspar	W1223	Host rock	61.96		24.31					4.96	8.55	0.21	99.99
Plagioclase feldspar	W1223	Host rock	61.85		24.26					5.22	8.45	0.22	100.00
Plagioclase feldspar	W1223	Host rock	62.18		23.99					4.8	8.77	0.26	100.00
Plagioclase feldspar	W1223	Host rock	61.63		24.42					5.09	8.58	0.27	99.99
Plagioclase feldspar	W1223	Host rock	62.27		24.21					5.1	8.42		100.00
Plagioclase feldspar	W1223	Host rock	62.18		24.17					5.12	8.52		99.99
Plagioclase feldspar	W1223	Host rock	62.12		24.16					5.15	8.57		100.00
Plagioclase feldspar	W1225	Host rock	64.14		22.77					2.67	8.31	2.11	100.00
Plagioclase feldspar	W1225	Host rock	62.45		23.94					4.71	8.9		100.00
Plagioclase feldspar	W1225	Host rock	62.68		23.79					4.76	8.77		100.00
Plagioclase feldspar	W1225	Host rock	62.63		23.91					4.83	8.64		100.01
Plagioclase feldspar	W1225	Host rock	62.09		24.2					4.87	8.84		100.00
Plagioclase feldspar	W1225	Host rock	62.55		23.88					5.07	8.5		100.00
Plagioclase feldspar	W1228	Host rock	61.07		24.99		0.38			5.74	7.62	0.2	100.00
Plagioclase feldspar	W1228	Host rock	57.16		23.68		2.99			5.45	7.58	0.84	97.70
Plagioclase feldspar	W1228	Host rock	61.14		24.8					6.01	8.04		99.99
Cordierite	W1201	Host rock	31.88		22.12		6.52	0.44	4.82		0.25		66.03
Cordierite	W1201	Host rock	48.52		33.56		9.67	0.53	7.38		0.34		100.00
Cordierite	W1201	Host rock	48.49		33.21		9.73	0.55	6.89		0.53	0.6	100.00
Cordierite	W1201	Host rock	48.67		33.47		10.02	0.61	6.85		0.38		100.00
Cordierite	W1201	Host rock	32.18		21.18		6	0.34	4.61		0.25		64.56
Cordierite	W1201	Host rock	48.42		33.41		10.08	0.7	6.99		0.4		100.00
Cordierite	W1201	Host rock	48.84		33.19		9.9	0.51	6.91		0.64		99.99
Cordierite	W1201	Host rock	48.43		33.59		9.75	0.57	7.22		0.44		100.00

Mineral	Sample		SiO ₂	TiO ₂	Al ₂ O ₃	Cr ₂ O ₃	FeO	MnO	MgO	CaO	Na ₂ O	K ₂ O	Total (Fe corr)
Cordierite	W1201	Host rock	31.74		22.02		6.55	0.45	4.69		0.26		65.71
Cordierite	W1201	Host rock	48.54		33.37		9.91	0.66	7.06		0.46		100.00
Cordierite	W1201	Host rock	48.59		33.19		10.11	0.57	6.81		0.73		100.00
Cordierite	W1201	Host rock	48.88		33.46		9.87	0.48	6.66	0.25	0.4		100.00
Cordierite	W1201	Host rock	31.59		21.84		6.54	0.38	4.64				64.99
Cordierite	W1201	Host rock	48.4		33.75		9.63	0.68	7.12		0.42		100.00
Cordierite	W1201	Host rock	48.54		32.9		10.19	0.57	6.99		0.81		100.00
Cordierite	W1201	Host rock	48.96		33.38		9.42	0.56	7.27		0.4		99.99
Cordierite	W1201	Host rock	31.88		21.82		6.43	0.4	4.75				65.28
Cordierite	W1201	Host rock	48.53		33.21		9.8	0.8	7.15		0.5		99.99
Cordierite	W1201	Host rock	49.14		32.57		9.78	0.57	7.12		0.83		100.01
Cordierite	W1201	Host rock	48.3		33.22		9.95	0.56	6.76		0.44	0.78	100.01
Cordierite	W1201	Host rock	31.83		21.93		6.21	0.39	4.72		0.23		65.31
Cordierite	W1201	Host rock	48.82		33.24		9.72	0.58	7.26		0.38		100.00
Cordierite	W1201	Host rock	48.6		32.7		10.44	0.68	6.64		0.94		100.00
Cordierite	W1201	Host rock	48.62		33.36		9.94	0.39	7.37		0.32		100.00
Cordierite	W1201	Host rock	48.6		33.27		9.98	0.55	7.07	0.2	0.33		100.00
Cordierite	W1201	Host rock	48.78		32.88		10.1	0.66	6.71		0.87		100.00
Cordierite	W1201	Host rock	48.47		33.59		9.92	0.56	7.02		0.44		100.00
Cordierite	W1201	Host rock	48.54		33.51		9.78	0.62	7.2		0.35		100.00
Cordierite	W1201	Host rock	48.67		33.4		10.06	0.56	7		0.31		100.00
Cordierite	W1201	Host rock	46.07	0.46	32.26		11.5	0.52	6.99		0.36	1.84	100.00
Cordierite	W1201	Host rock	48.63		33.81		10.01	0.55	7				100.00
Cordierite	W1201	Host rock	50.04		32.53		9.86	0.57	7.01				100.01
Cordierite	W1201	Host rock	48.45		33.81		10.1	0.7	6.94				100.00
Cordierite	W1201	Host rock	42.39	0.49	38.28		9.95		6.43	0.35	2.1		99.99
Cordierite	W1201	Host rock	48.59		33.72		10.06	0.6	7.03				100.00
Cordierite	W1201	Host rock	50.08		32.77		9.61	0.59	6.96				100.01
Cordierite	W1201	Host rock	48.82		33.38		10.08	0.61	7.11				100.00
Cordierite	W1201	Host rock	49.34		32.9		9.57	0.69	7.12			0.39	100.01
Cordierite	W1201	Host rock	44.46	0.62	36.79		9.57		6.1	0.56	1.9		100.00
Cordierite	W1201	Host rock	48.64		33.78		9.88	0.6	7.1				100.00
Cordierite	W1201	Host rock	48.58		33.75		9.96	0.56	7.14				99.99
Cordierite	W1201	Host rock	48.5		34.14		9.44	0.65	7.26				99.99
Cordierite	W1201	Host rock	49.6		33.08		9.53	0.64	7.14				99.99
Cordierite	W1201	Host rock	48.03		33.89		10.05	0.68	7.35				100.00
Cordierite	W1201	Host rock	48.56		33.69		10.19	0.64	6.91				99.99
Cordierite	W1201	Host rock	48.59		33.71		9.98	0.58	7.13				99.99
Cordierite	W1201	Host rock	48.36		33.8		9.68	0.65	7.11				99.60
Cordierite	W1201	Host rock	48.8		33.61		9.62	0.53	7.26			0.18	100.00
Cordierite	W1201	Host rock	48.58		33.78		9.64	0.75	7.25				100.00
Cordierite	W1201	Host rock	48.84		33.53		10.02	0.57	7.03				99.99
Cordierite	W1213	Host rock	48.59		33.46		10.09	0.74	7.13				100.01
Cordierite	W1213	Host rock	48.45		33.46		10.25	0.65	7.2				100.01
Cordierite	W1213	Host rock	48.38		33.62		10.31	0.64	7.06				100.01
Cordierite	W1213	Host rock	48.36		33.1		10.32	0.81	7.14		0.26		99.99
Cordierite	W1213	Host rock	48.07		33.79		10.45	0.78	6.91				100.00
Cordierite	W1213	Host rock	47.99		33.73		10.23	0.8	7.26				100.01
Cordierite	W1213	Host rock	47.98		33.58		10.6	0.71	7.13				100.00
Cordierite	W1213	Host rock	47.94		32.61		10.09	0.7	6.99		0.19		98.52
Cordierite	W1213	Host rock	48.61		33.39		10.28	0.69	7.03				100.00
Cordierite	W1213	Host rock	48.49		33.47		10.17	0.83	7.03				99.99

Mineral	Sample		SiO ₂	TiO ₂	Al ₂ O ₃	Cr ₂ O ₃	FeO	MnO	MgO	CaO	Na ₂ O	K ₂ O	Total (Fe corr)
Cordierite	W1213	Host rock	48.37		33.56		10.08	0.86	7.12				99.99
Cordierite	W1213	Host rock	48.36		33.38		10.44	0.79	7.03				100.00
Cordierite	W1213	Host rock	48.27		33.61		9.94	0.8	7.12			0.27	100.01
Cordierite	W1213	Host rock	48.2		33.53		10.4	0.68	7.18				99.99
Cordierite	W1213	Host rock	48.17		33.72		10.23	0.67	7.2				99.99
Cordierite	W1213	Host rock	47.98		33.89		10.49	0.65	6.99				100.00
Cordierite	W1213	Host rock	48.33		33.43		10.11	0.85	7.29				100.01
Cordierite	W1213	Host rock	48.2		33.64		10.29	0.71	7.16				100.00
Cordierite	W1213	Host rock	48.14		33.63		9.97	0.71	7.24		0.31		100.00
Cordierite	W1213	Host rock	48.06		33.71		10.46	0.64	7.12				99.99
Cordierite	W1213	Host rock	48.53		33.67		9.86	0.64	7.29				99.99
Cordierite	W1213	Host rock	48.16		33.62		10.36	0.63	7.23				100.00
Cordierite	W1214	Host rock	49.17		33.25		9.61	0.89	7.08				100.00
Cordierite	W1214	Host rock	48.74		33.35		9.74	0.87	7.3				100.00
Cordierite	W1214	Host rock	48.74		33.47		9.86	0.76	7.17				100.00
Cordierite	W1214	Host rock	48.73		33.78		9.43	0.91	7.15				100.00
Cordierite	W1214	Host rock	48.72		33.4		9.78	0.88	7.22				100.00
Cordierite	W1214	Host rock	48.71		33.62		9.61	0.85	7.21				100.00
Cordierite	W1214	Host rock	48.62		33.53		10.01	0.8	7.05				100.01
Cordierite	W1214	Host rock	48.61		33.5		9.75	0.96	7.19				100.01
Cordierite	W1214	Host rock	48.53		33.56		9.32	0.98	7.39		0.23		100.01
Cordierite	W1214	Host rock	48.46		33.33		9.96	0.92	7.02		0.31		100.00
Cordierite	W1214	Host rock	48.46		33.44		10.02	0.87	6.94		0.28		100.01
Cordierite	W1214	Host rock	48.43		33.46		10.12	0.75	6.99		0.25		100.00
Cordierite	W1214	Host rock	48.35		33.43		10	0.84	7.15		0.24		100.01
Cordierite	W1214	Host rock	48.12		33.54		10.1	0.88	7.03		0.34		100.01
Cordierite	W1216	Host rock	48.42		33.48		9.81	0.5	7.49		0.31		100.01
Cordierite	W1216	Host rock	48.25		33.24		10.23	0.52	7.76				100.00
Cordierite	W1216	Host rock	48.54		33.35		9.85	0.46	7.5		0.3		100.00
Cordierite	W1216	Host rock	48.53		33.54		9.84	0.41	7.4		0.27		99.99
Cordierite	W1216	Host rock	48.59		33.39		10.19	0.49	7.33				99.99
Cordierite	W1218	Host rock	48.53		33.69		9.95	0.64	7.2				100.01
Cordierite	W1218	Host rock	48.5		33.69		9.67	0.74	7.4				100.00
Cordierite	W1218	Host rock	48.98		33.69		9.51	0.51	7.31				100.00
Cordierite	W1218	Host rock	48.67		33.68		9.94	0.85	6.86				100.00
Cordierite	W1218	Host rock	48.62		33.71		9.83	0.66	7.18				100.00
Cordierite	W1218	Host rock	48.77		33.64		9.48	0.91	7.21				100.01
Cordierite	W1218	Host rock	48.88		33.58		9.86	0.59	7.09				100.00
Cordierite	W1218	Host rock	48.7		33.29		9.61	0.7	7.02			0.35	99.67
Cordierite	W1218	Host rock	48.17		33.79		9.95	0.7	7.39				100.00
Cordierite	W1218	Host rock	48.76		33.85		9.49	0.84	7.06				100.00
Cordierite	W1218	Host rock	48.03		33.67		9.78	0.66	6.9		0.51		99.55
Cordierite	W1218	Host rock	48.48		33.76		9.94	0.84	6.98				100.00
Cordierite	W1218	Host rock	48.61		33.61		9.96	0.83	6.98				99.99
Cordierite	W1218	Host rock	48.35		33.75		9.82	0.88	7.2				100.00
Cordierite	W1218	Host rock	48.54		33.87		9.9	0.61	7.08				100.00
Cordierite	W1218	Host rock	48.1		33.92		9.82	0.64	7.07		0.45		100.00
Cordierite	W1218	Host rock	48.75		33.89		9.42	0.67	7.28				100.01
Cordierite	W1218	Host rock	48.58		33.91		9.55	0.57	7.39				100.00
Cordierite	W1218	Host rock	48.65		33.58		9.78	0.74	7.26				100.01
Cordierite	W1223	Host rock	48.47		33.79		9.68	1.14	6.92				100.00
Cordierite	W1223	Host rock	48.5		33.64		10.1	1.04	6.72				100.00

Mineral	Sample		SiO ₂	TiO ₂	Al ₂ O ₃	Cr ₂ O ₃	FeO	MnO	MgO	CaO	Na ₂ O	K ₂ O	Total (Fe corr)
Cordierite	W1223	Host rock	48.69		33.56		9.03	1.09	7.09		0.53		99.99
Cordierite	W1223	Host rock	48.61		33.37		9.57	1.25	6.84		0.35		99.99
Cordierite	W1223	Host rock	48.29		33.61		9.96	1.25	6.9				100.01
Cordierite	W1223	Host rock	48.39		33.48		10.25	1.02	6.37		0.5		100.01
Cordierite	W1223	Host rock	48.4		33.78		9.8	1.1	6.91				99.99
Cordierite	W1223	Host rock	48.08		33.91		9.57	1.18	6.84		0.41		99.99
Cordierite	W1223	Host rock	48.54		33.61		9.67	0.97	6.73		0.49		100.01
Cordierite	W1223	Host rock	48.11		33.41		10.06	1.01	6.83		0.58		100.00
Cordierite	W1223	Host rock	48.69		33.67		9.62	0.92	7.1				100.00
Cordierite	W1223	Host rock	48.65		33.79		9.6	1.18	6.78				100.00
Cordierite	W1223	Host rock	48.58		33.54		9.73	1.05	7.09				99.99
Cordierite	W1223	Host rock	48.61		33.45		10.07	1.1	6.77				100.00
Cordierite	W1223	Host rock	48.4		33.92		9.76	1.1	6.82				100.00
Cordierite	W1223	Host rock	48.62		33.35		10	1.29	6.74				100.00
Cordierite	W1223	Host rock	48.28		33.71		9.5	1.28	6.68		0.54		99.99
Cordierite	W1229	Host rock	48.75		33.62		10.64		6.99				100.00
Cordierite	W1229	Host rock	48.44		33.63		10.71	0.33	6.88				99.99
Cordierite	W1229	Host rock	48.27		33.55		10.9	0.42	6.86				100.00
Cordierite	W1229	Host rock	49		33.37		10.54		7.09				100.00
Cordierite	W1229	Host rock	48.23		33.8		10.67		7.3				100.00
Cordierite	W1229	Host rock	48.16		33.63		10.83	0.3	7.08				100.00
Cordierite	W1229	Host rock	48.51		33.6		10.78	0.27	6.84				100.00
Cordierite	W1229	Host rock	48.39		33.72		10.61	0.27	7.01				100.00
Cordierite	W1229	Host rock	48.35		33.7		10.5	0.38	7.06				99.99
Cordierite	W1229	Host rock	48.41		33.87		10.77		6.95				100.00
Cordierite	W1229	Host rock	48.33		33.11		11.11	0.32	7.14				100.01
Cordierite	W1229	Host rock	48.27		33.49		10.9	0.27	7.07				100.00
Cordierite	W1229	Host rock	48.93		33.37		10.7		7				100.00
Cordierite	W1229	Host rock	48.7		33.55		10.73		7.03				100.01
Cordierite	W1229	Host rock	48.18		33.43		11.17	0.31	6.92				100.01
Cordierite	W1229	Host rock	48.59		33.4		11.03		6.98				100.00
Cordierite	W1229	Host rock	48.53		33.33		10.75	0.29	7.1				100.00
Cordierite	W1229	Host rock	48.34		33.64		11.31		6.72				100.01
Cordierite	W1229	Host rock	48.52		33.76		10.62		7.11				100.01
Cordierite	W1229	Host rock	48.08		33.68		10.86	0.29	7.1				100.01
Cordierite	W1229	Host rock	48.67		33.43		11.04		6.86				100.00
Cordierite	W1229	Host rock	48.22		33.51		11.12		7.15				100.00
Garnet	W1204	Large vein	37.85	0	19.96	0	14.67	24.88	0	2.63			99.990
Garnet	W1204	Large vein	35.93	0	20.24	0.44	9.65	30.9	0	2.84			100.00 0
Garnet	W1204	Large vein	35.87	0	19.43	0	10.07	31.22	0	3.41			100.00 0
Garnet	W1204	Large vein	35.8	0	19.38	0	16.39	26.06	0	2.37			100.00 0
Garnet	W1204	Large vein	35.78	0	19.84	0	15.69	26.45	0	2.24			100.00 0
Garnet	W1204	Large vein	35.67	0.36	19.18	0	11.2	31.25	0	2.35			100.01 0
Garnet	W1204	Large vein	35.63	0	19.74	0	16.49	25.51	0	2.64			100.01 0
Garnet	W1204	Large vein	35.56	0.52	19.46	0	16.22	25.25	0	3			100.01 0

Mineral	Sample		SiO ₂	TiO ₂	Al ₂ O ₃	Cr ₂ O ₃	FeO	MnO	MgO	CaO	Na ₂ O	K ₂ O	Total (Fe corr)
Garnet	W1204	Large vein	35.56	0.5	19.16	0	16.21	25.46	0	3.11			100.00 0
Garnet	W1204	Large vein	35.55	0	19.93	0	14.85	27.84	0	1.84			100.01 0
Garnet	W1204	Large vein	35.55	0	20.19	0	15.04	27.25	0	1.96			99.990
Garnet	W1204	Large vein	35.54	0	19.78	0	16.39	25.9	0	2.38			99.990
Garnet	W1204	Large vein	35.53	0.36	19.5	0	15.38	26.39	0	2.83			99.990
Garnet	W1204	Large vein	35.47	0	19.86	0	16.17	26.03	0	2.47			100.00 0
Garnet	W1204	Large vein	35.47	0.55	18.92	0	16.79	25.78	0	2.5			100.01 0
Garnet	W1204	Large vein	35.44	0	19.83	0	16.54	25.55	0	2.63			99.990
Garnet	W1204	Large vein	35.43	0.44	18.74	0	11.05	31.68	0	2.67			100.01 0
Garnet	W1204	Large vein	35.41	0.43	19.3	0	15.61	26.37	0	2.87			99.990
Garnet	W1204	Large vein	35.35	0.47	19.22	0	16.11	25.87	0	2.98			100.00 0
Garnet	W1204	Large vein	35.22	0	19.56	0	15.79	26.66	0	2.78			100.01 0
Garnet	W1204	Large vein	35.2	0.42	19.65	0	16.26	25.89	0	2.58			100.00 0
Garnet	W1204	Large vein	35.19	0	19.38	0.63	15.96	25.77	0	3.07			100.00 0
Garnet	W1204	Large vein	35.19	0.56	18.67	0	10.8	32.21	0	2.57			100.00 0
Garnet	W1204	Large vein	35.16	0.38	19.39	0.57	15.99	25.56	0	2.94			99.990
Garnet	W1204	Large vein	35.1	0.32	19.7	0	14.87	27.69	0	2.34			100.02 0
Garnet	W1204	Large vein	35.01	0	19.55	0	15.78	27.57	0	2.09			100.00 0
Garnet	W1204	Large vein	34.91	0.42	18.73	0	15.08	27.31	0	2.58			99.030
Garnet	W1204	Large vein	34.84	0.49	19.11	0	16.39	25.19	0.45	3.26			99.730
Garnet	W1204	Large vein	34.79	0.38	18.9	0	10.4	30.85	0	2.79			98.110
Garnet	W1204	Large vein	34.53	0	18.91	0	15.52	25.58	0	3.51			98.050
Garnet	W1204	Large vein	34.32	0	19.06	0	13.12	27.59	0	3.02			97.110
Garnet	W1204	Large vein	34.3	0	19.13	0	14.89	29.67	0	2.01			100.00 0
Garnet	W1207 d	Quartzite	38.37	0	19.12	0	9.75	30.28	1.55	0.93			100.00 0
Garnet	W1207 d	Quartzite	36.85	0	20.28	0	10.02	30.08	2.18	0.58			99.990
Garnet	W1207 d	Quartzite	36.09	0	19.19	0	11.03	31.03	1.71	0.94			99.990

Mineral	Sample		SiO ₂	TiO ₂	Al ₂ O ₃	Cr ₂ O ₃	FeO	MnO	MgO	CaO	Na ₂ O	K ₂ O	Total (Fe corr)
Garnet	W1207 d	Quartzite	36.11	0	19.65	0	10.77	31.11	1.45	0.9			99.990
Garnet	W1207 d	Quartzite	41.02	0	23.2	0	7.31	23.3	1.78	0.8			97.410
Garnet	W1207 d	Quartzite	36.26	0	20.2	0	9.71	30.68	1.84	0.61			99.300
Garnet	W1207 d	Quartzite	35.67	0.26	19.58	0	10.21	30.72	2.08	0.89			99.410
Garnet	W1207 d	Quartzite	36.55	0	20.03	0	10.69	30.03	1.88	0.83			100.01 0
Garnet	W1207 d	Quartzite	34.79	0	18.14	0	11.36	32.14	1.61	1.16			99.200
Garnet	W1207 d	Quartzite	36.66	0	19.76	0	10.66	29.89	1.89	1.14			100.00 0
Garnet	W1207 d	Quartzite	37.46	0	19.65	0	9.6	30.69	1.73	0.87			100.00 0
Garnet	W1207 d	Quartzite	36.12	0	19.88	0	11.03	30.49	1.74	0.74			100.00 0
Garnet	W1207 d	Quartzite	36.56	0.14	19.56	0	10.85	30	1.91	0.98			100.00 0
Garnet	W1207 d	Quartzite	35.83	0	19.62	0	10.64	31.23	1.84	0.84			100.00 0
Garnet	W1207 d	Quartzite	36.3	0	20.44	0	9.94	30.82	1.74	0.76			100.00 0
Garnet	W1207 e	Quartzite	36.2	0.32	20	0	9.48	31.05	2.07	0.88			100.00 0
Garnet	W1207 e	Quartzite	36.73	0	20.21	0	8.66	31.31	2.2	0.89			100.00 0
Garnet	W1207 e	Quartzite	36.92	0	20.21	0	8.63	30.96	2.26	1.02			100.00 0
Garnet	W1207 e	Quartzite	37.49	0	21.19	0	8.23	29.87	2.47	0.76			100.01 0
Garnet	W1207 e	Quartzite	36.52	0	20.75	0	8.46	31.39	2.21	0.66			99.990
Garnet	W1207 e	Quartzite	36.16	0.23	19.53	0	9.36	30.53	2.16	1.37			99.340
Garnet	W1207 e	Quartzite	36	0.24	20.06	0	8.51	32.33	1.96	0.89			99.990
Garnet	W1207 e	Quartzite	36.35	0	19.68	0	9.76	30.91	2.09	1.2			99.990
Garnet	W1207 e	Quartzite	36.21	0	20.47	0	7.65	31.96	2.37	0.63			99.290
Garnet	W1207 e	Quartzite	36.55	0	20.46	0	8.98	30.71	2.27	1.03			100.00 0
Garnet	W1207 e	Quartzite	36.4	0	19.96	0	8.96	31.42	2.3	0.97			100.01 0
Garnet	W1207 h	Quartzite	35.67	0	20.27	0	7.49	32.69	2.35	0.56			99.030
Garnet	W1207 h	Quartzite	36.13	0	20.54	0	7.64	32.7	2.47	0.52			100.00 0
Garnet	W1207 h	Quartzite	36.59	0	20.31	0	8.18	34.23		0.69			100.00 0
Garnet	W1207 h	Quartzite	36.27	0	19.71	0	7.88	33.23	2.2	0.71			100.00 0

Mineral	Sample		SiO ₂	TiO ₂	Al ₂ O ₃	Cr ₂ O ₃	FeO	MnO	MgO	CaO	Na ₂ O	K ₂ O	Total (Fe corr)
Garnet	W1207 h	Quartzite	36.17	0	20.63	0	7.52	32.8	2.3	0.58			100.00 0
Garnet	W1207 h	Quartzite	36.11	0	19.82	0	8.27	32.89	2.22	0.7			100.01 0
Garnet	W1207 h	Quartzite	35.49	0.26	20.18	0	8.02	32.94	2.37	0.75			100.01 0
Garnet	W1207 h	Quartzite	34.43	0	18.97	0	7.79	32.13	2.28	0.85			96.450
Garnet	W1207 h	Quartzite	36.25	0	20.48	0	7.44	32.94	2.36	0.53			100.00 0
Garnet	W1207 h	Quartzite	35.6	0.34	19.92	0	8.09	33.07	2.15	0.84			100.01 0
Garnet	W1207 h	Quartzite	36.09	0	20.42	0	7.46	33.48	1.89	0.65			99.990
Garnet	W1207 h	Quartzite	36.11	0	20.37	0	7.6	32.99	2.4	0.53			100.00 0
Garnet	W1207 h	Quartzite	36.5	0	20.25	0	7.38	33.14	2.15	0.58			100.00 0
Garnet	W1207 h	Quartzite	35.8	0	20.25	0	7.69	33.53	2.05	0.69			100.01 0
Garnet	W1207 h	Quartzite	36.48	0	20.48	0	7.27	32.88	2.23	0.66			100.00 0
Garnet	W1207 h	Quartzite	35.81	0	20.15	0	8	33.47	1.91	0.65			99.990
Garnet	W1207 h	Quartzite	36.79	0	20.3	0	8.22	33.87		0.77			99.950
Garnet	W1207 h	Quartzite	35.93	0	20.34	0	7.79	33.21	2.09	0.64			100.00 0
Garnet	W1207 h	Quartzite	36.29	0	19.96	0	7.84	32.92	2.24	0.75			100.00 0
Garnet	W1207 h	Quartzite	34.01	0	19.28	0	7.23	32.08	2.28	0.68			95.560
Garnet	W1207 h	Quartzite	35.8	0	20.35	0	7.96	32.85	2.43	0.62			100.01 0
Garnet	W1207 h	Quartzite	36.14	0	20.25	0	7.7	32.99	2.36	0.56			100.00 0
Garnet	W1207 h	Quartzite	36.15	0	20.16	0	7.8	33.06	2.07	0.76			100.00 0
Garnet	W1207 h	Quartzite	35.87	0	20.36	0	7.21	32.57	2.02	0.47			98.500
Garnet	W1207 h	Quartzite	35.77	0	20.36	0	7.64	33.52	2.18	0.54			100.01 0
Garnet	W1207 h	Quartzite	36.1	0	19.75	0	7.99	32.95	2.38	0.83			100.00 0
Garnet	W1209	Host rock	39.05	0	18.9	0	27.43	12.4	1.46	0.77			100.01 0
Garnet	W1209	Host rock	37.85	0	21.53	0	26.88	11.36	1.56	0.81			99.990
Garnet	W1209	Host rock	36.57	0	20.65	0	28.84	12.68	0	0.78			99.520
Garnet	W1209	Host rock	36.29	0	21.04	0	28.56	12.97	0	1.14			100.00 0
Garnet	W1209	Host rock	36.24	0	20.89	0	29.16	12.6	0	1.1			99.990
Garnet	W1209	Host rock	36.2	0	20.49	0	28.92	12.85	0	1.05			99.510
Garnet	W1209	Host rock	36.17	0	20.93	0	29.1	12.8	0	0.99			99.990

Mineral	Sample		SiO ₂	TiO ₂	Al ₂ O ₃	Cr ₂ O ₃	FeO	MnO	MgO	CaO	Na ₂ O	K ₂ O	Total (Fe corr)
Garnet	W1209	Host rock	36.13	0	20.39	0	28.6	12.56	1.37	0.96			100.01 0
Garnet	W1209	Host rock	36.13	0	20.74	0	29.23	12.82	0	0.91			99.830
Garnet	W1209	Host rock	36.12	0	20.76	0	28.96	13	0	1.1			99.940
Garnet	W1209	Host rock	35.9	0	20.35	0	28.17	12.74	1.72	1.13			100.01 0
Garnet	W1209	Host rock	35.87	0.33	20.35	0	28.64	12.33	1.44	1.03			99.990
Garnet	W1209	Host rock	35.82	0	21.15	0	29.18	12.78	0	1.08			100.01 0
Garnet	W1209	Host rock	35.8	0	20.55	0	28.51	12.73	1.39	1.03			100.01 0
Garnet	W1209	Host rock	35.79	1.61	20.74	0	28.26	12.47	0	1.13			100.00 0
Garnet	W1209	Host rock	35.76	0	20.6	0	28.71	12.45	1.43	1.05			100.00 0
Garnet	W1209	Host rock	35.74	0	20.43	0	28.83	12.45	1.46	1.08			99.990
Garnet	W1209	Host rock	35.69	0	20.81	0	28.73	12.33	1.43	1			99.990
Garnet	W1209	Host rock	35.62	0.32	20.43	0	28.2	12.63	1.76	1.04			100.00 0
Garnet	W1209	Host rock	35.62	0.29	20.45	0	28.67	12.29	1.76	0.92			100.00 0
Garnet	W1209	Host rock	35.58	0	20.31	0	28.81	12.63	1.51	1.15			99.990
Garnet	W1209	Host rock	35.55	0	20.71	0	28.12	12.88	1.72	1.01			99.990